

The study of atmospheric reaction chemistry of cloud droplets and aerosol by application of optical trapping & neutron and x-ray scattering

Rosalie Helen Shepherd



A thesis submitted for the degree of Doctor of Philosophy at the University of London

Royal Holloway, University of London

Declaration of Authorship

I, Rosalie Helen Shepherd, hereby declare that this thesis and the work presented in it is entirely my own.

My contributions to the six co-authored papers that make up the body of the thesis, is clearly stated on the cover page for each paper.

Signed:

Dated: 29.08.2017

Acknowledgments

I would like to thank my two supervisors, Martin King and Andy Ward. I am grateful for their continued support, motivation and guidance over the last few years. I am fortunate to have worked alongside two people whose methods of working compliment each other, and from which I have experienced different methods of tackling and overcoming a problem.

Additionally, I would like to thank Adrian Rennie for his assistance with the neutron reflectivity experiments. Adrian not only supported work conducted during an experiment, but always took time to answer my questions once an experiment was completed.

The Central Laser Facility, ISIS Neutron Source and Diamond Light Source provided numerous access weeks to the facilities they offer, for which I am grateful.

Lastly, I would like to thank my friends and family for their support and encouragement over the last few years.

Abstract

Atmospheric aerosols affect global temperatures by scattering or absorbing solar radiation. Aerosols are often coated in a film of organic or inorganic material. To correctly understand atmospheric aerosols and their influence on climate, it is paramount that atmospheric aerosols are correctly understood. In the thesis, optical trapping techniques were applied alongside neutron and x-ray reflectivity methods to study atmospheric aerosol and atmospheric aerosol thin films.

Optical trapping applied simultaneously with Mie spectroscopy determined the refractive index of an aerosol. Optical trapping was applied to extracts sourced from atmospheric aerosol collected at urban, remote and wood burning sources: the refractive index of the extracts ranged from 1.450 to 1.588 at 589 nm. Optical trapping techniques were also successfully applied to changing systems: the refractive index of squalene upon exposure to ozone or oxygen changed by 0.0169 ± 0.0026 or 0.0173 ± 0.0026 respectively.

All three experimental techniques were applied to study thin films. Optical trapping demonstrated the consequence of film formation upon aerosol light scattering. When a $0.190 \mu\text{m}$ thick film of sulfuric acid formed on a silica particle with a diameter of $1.930 \mu\text{m}$, the refractive index resembled sulfuric acid.

Application of neutron and x-ray experiments extended thin film studies by allowing the oxidation of thin films to be followed. The scattering length density and film thickness of aerosol extract films composed of urban, remote and wood burning aerosol extracts at the air water interface were determined. Subsequently, continuous collection of reflectivity data during exposure to gas-phase OH radicals allowed the oxidation kinetics to be studied and film lifetime to be estimated. Film lifetime was on the timescale of minutes for all samples.

Additionally, neutron reflectivity was applied to determine the oxidation kinetics of an aerosol proxy film at the silica-water interface. The film demonstrated degradation decay upon exposure to aqueous-phase OH radicals.

Contents

1. Introduction	15
1.1 The atmosphere	15
1.2 Atmospheric aerosols & cloud droplets	17
1.2.1 Size distribution of atmospheric aerosols	22
1.2.2 Source of atmospheric aerosols	23
1.2.3 Composition of atmospheric aerosols	27
1.2.3.1 Composition of the troposphere	27
1.2.3.2 Composition of the stratosphere	29
1.3 Atmospheric aerosol thin films	30
1.4 Atmospheric aerosol chemical reactions	30
1.4.1 Aerosol chemical reactions	34
1.4.2 Aerosol thin film chemical reactions	35
1.5. Summary and strategy applied to study atmospheric aerosols and thin films	37
Introduction references	39
2. Methodology	44
2.1 Optical trapping	44
2.1.1 Optical trapping introduction	44
2.1.2 Optical trapping procedure	48
2.1.3 Mie spectroscopy	49
2.1.3.1 Theory of Mie spectroscopy	50
2.1.3.2 Collection of Mie spectra	52
2.1.3.3 Analysis of the Mie spectra	53
2.1.4 Optical trapping experiments conducted	55
2.1.5 Limitations of optical trapping	56
2.2 Neutron and x-ray scattering	58
2.2.1 Neutron and x-ray scattering introduction	58
2.2.2 Neutron and x-ray scattering data analysis	61
2.2.3 Neutron and x-ray scattering experiments conducted	63
2.2.4 Comparison between neutron and x-ray scattering experiments	64
2.2.5 Limitations of neutron and x-ray scattering	66
2.3 Sample collection	67

2.4 Formation of OH radicals	70
2.4.1 Formation of gas-phase OH radicals	70
2.4.2 Formation of aqueous-phase OH radicals	72
2.5 Summary	73
Methodology references	75
Paper 1: Mie scattering from optically levitated mixed sulfuric acid-silica core-shell aerosols: confirmation of core-shell morphology for atmospheric science	78
Paper 2: Following the refractive index of squalene droplets during oxidative ageing	79
Paper 3: Determination of the refractive index of insoluble organic extracts from atmospheric aerosol over the visible wavelength range using optical tweezers	80
Paper 4: Gas-phase OH radical oxidation of an organic film at the air-water interface using material extracted from urban, remote and wood smoke aerosol	81
Paper 5: The reaction between gas-phase OH radicals and organic films extracted from atmospheric aerosol at the air-water interface: an x-ray reflectivity and atmospheric lifetime study	82
Paper 6: Oxidation of a bilayer of DPPC on a mineral interface by aqueous-phase OH radicals to replicate atmospheric aerosol behaviour	83
3. Critical Evaluation	84
3.1 Optical Trapping	84
3.1.1 Evaluation of Paper 1	84
3.1.2 Evaluation of Paper 2	87
3.1.3 Evaluation of Paper 3	89
3.1.4 Future work	90
3.1.5 Summary	92
3.2 Neutron and x-ray scattering	93
3.2.1 Evaluation of Paper 4	93
3.2.2 Evaluation of Paper 5	96
3.2.3 Evaluation of Paper 6	98
3.2.4 Future work	100
3.2.5 Summary	101

Critical evaluation references	103
4. Summary and Conclusion	104

List of Figures

Introduction

Figure 1.1. The layers of the atmosphere.

Figure 1.2. Contribution to climate change by atmospheric aerosol.

Figure 1.3. Curves depicting the Kelvin effect, the Raoult effect and Köhler theory.

Figure 1.4. A depiction of the different modes that characterise atmospheric aerosol.

Figure 1.5. The lifetime of atmospheric aerosols.

Figure 1.6. The possible geometries of two-phase atmospheric aerosols.

Methodology

Figure 2.1. The scattering forces that an aerosol in a counter-propagating trap experiences.

Figure 2.2. Depiction of the gradient forces that act upon an aerosol in a single gradient trap.

Figure 2.3. A simplified schematic of the optical trapping setup.

Figure 2.4. Experimental Mie spectrum for a concentrated sulfuric acid aerosol droplet.

Figure 2.5. The instruments used at ISIS Neutron and Muon Source.

Figure 2.6. The reflectometer used at Diamond Light Source.

Figure 2.7. The experimental and corresponding simulated fit for a bare deuterium oxide air-water interface.

Figure 2.8. A diagram of the layers simulated to reproduce the reflectivity profiles for the experiments conducted at ISIS.

Figure 2.9. Comparison between neutron and x-ray reflectivity profiles for atmospheric aerosol extract sourced from the campus of Royal Holloway, University of London.

Paper 1: Mie scattering from optically levitated mixed sulfuric acid-silica core-shell aerosols: confirmation of core-shell morphology for atmospheric science

Figure 1. Measured and simulated Mie spectra for optically trapped sulfuric acid droplets.

Figure 2. Experimental refractive index of trapped sulfuric acid droplets as a function of wavelength compared to literature values.

Figure 3. Mie spectra showing how the Mie scattering of silica aerosol alters upon growth of a film of sulfuric acid.

Figure 4. Experimentally collected Mie spectra from the collision of sulfuric acid on silica, with overlaying Mie spectra simulations of pure sulfuric acid droplets.

Figure 5. Simulated and experimental Mie spectra for sulfuric acid film formation on polystyrene.

Figure 6. The scattering efficiency for atmospheric silica, sulfuric acid and core-shell silica-sulfuric acid aerosol as a function of aerosol diameter.

Figure 7. Typical Mie spectra for alumina and titania aerosols.

Paper 2: Following the refractive index of squalene droplets during oxidative ageing

Figure 1. Experimentally collected Mie spectrum of an optically trapped squalene droplet.

Figure 2. Refractive index dispersions for optically trapped squalene droplets before and after oxidative ageing.

Figure 3. Continuous collection of Mie spectra whilst a squalene droplet was exposed to 0.4 ppm ozone.

Figure 4. Brightfield illumination images of squalene droplets post exposure to oxidative gases.

Figure 5. The refractive index and radius change of an optically trapped squalene droplet upon exposure to gas-phase oxygen.

Paper 3: Determination of the refractive index of insoluble organic extracts from atmospheric aerosol over the visible wavelength range using optical tweezers

Figure 1. The typical Mie spectra as a function of wavelength obtained for urban and remote atmospheric aerosol extracts.

Figure 2. Typical Mie spectrum for the wood smoke aerosol extracts B and humic acid aerosol.

Figure 3. The absorption Ångstrom exponent and imaginary component of the refractive index for the optically trapped wood smoke aerosol extract and humic acid aerosol.

Figure 4. Refractive index dispersions for urban, remote and wood smoke atmospheric aerosol extracts and humic acid aerosol, compared to refractive index values from literature.

Figure 5. The total aerosol radiative effect for core-shell morphology aerosols.

Paper 4: Gas-phase OH radical oxidation of an organic film at the air-water interface using material extracted from urban, remote and wood smoke aerosol

Figure 1. Neutron reflectivity profile for films of urban, remote, wood smoke and remote seawater extract at the air-water interface.

Figure 2. The neutron scattering length density of pure compounds compared to the neutron scattering length density of films of the aerosol and seawater extracts collected in the present study.

Figure 3. The change in film thickness of a film composed of urban aerosol extract at the air-water interface as the surface pressure of the trough is increased and decreased by changing the barrier position.

Figure 4. Oxidation of urban aerosol extract at the air-water interface for aerosol extract collected during May 2015 and January 2016.

Figure 5. The reaction of a film of remote aerosol extract collected in 2015 and 2016 with gas-phase OH radicals.

Figure 6. The reaction of wood smoke aerosol extracts with gas-phase OH radicals.

Figure 7. A typical decay profile for the head and tail region when added together for a film of DSPC at the air-water interface when exposed to OH radicals.

Figure 8. A χ^2 test was executed to determine the number of steps required to represent the oxidation of DSPC thin films.

Figure 9. To study the level of accuracy in the simulation of the neutron reflection profile a χ^2 test was executed.

Paper 5: The reaction between gas-phase OH radicals and organic films extracted from atmospheric aerosol at the air-water interface: an x-ray reflectivity and atmospheric lifetime study

Figure 1. Depiction of the typical x-ray reflection profiles for urban and remote atmospheric aerosol extract at the air-water interface.

Figure 2. An investigation into the robustness of the fitting procedure to find values of ρ and δ using the fitting metric χ^2 .

Figure 3. X-ray reflection profile of two films upon exposure to gas-phase OH radicals.

Figure 4. Urban atmospheric aerosol extract collected during September 2015 and January 2016 decayed when exposed to $[\text{OH}\cdot] = 7.0 \times 10^6 \text{ molecule cm}^{-3}$.

Figure 5. Remote atmospheric aerosol extract collected during 2015 Antarctic summer and 2016 Antarctic summer when exposed to $[\text{OH}\cdot] = 7.0 \times 10^6 \text{ molecule cm}^{-3}$.

Figure 6. The decay in $\frac{\rho_t \delta_t}{\rho_{t=0} \delta_{t=0}}$ for urban and remote atmospheric aerosol extracts at the air-water interface reacts with gas-phase OH radicals as a function of time.

Paper 6: Oxidation of a bilayer of DPPC on a mineral interface by aqueous-phase OH radicals to replicate atmospheric aerosol behaviour

Figure 1. Depiction of the layers of the system under study.

Figure 2. The decay in the concentration of H_2O_2 in H_2O owing to photolysis by the UV illumination.

Figure 3. The loss in neutron reflectivity as a film of DPPC at the air-water interface was exposed to OH radicals.

Figure 4. The step-wise degradation mechanism for each layer used to represent the DPPC bilayer at the silica-water interface.

Figure 5. To quantify the quality of fit between simulated and experimental reflection profiles, χ^2 as a function of neutron scattering length density and film thickness was calculated for each layer.

Figure 6. The requirement for 7 to 9 steps in the degradation decay was investigated by applying a χ^2 test.

Figure 7. The DPPC bilayer at the silica-water interface simulated as a one-layer system.

List of Tables

Introduction

Table 1.1. Aerosol emissions from natural and anthropogenic aerosol.

Paper 1: Mie scattering from optically levitated mixed sulfuric acid-silica core-shell aerosols: confirmation of core-shell morphology for atmospheric science

Table 1. The refractive index of optically trapped sulfuric acid droplets.

Paper 2: Following the refractive index of squalene droplets during oxidative ageing

Table 1. Diffusion constants and reaction timescales for squalene.

Paper 3: Determination of the refractive index of insoluble organic extracts from atmospheric aerosol over the visible wavelength range using optical tweezers

Table 1. The determined Cauchy coefficients, refractive index and radius for the atmospheric aerosol extracts.

Paper 4: Gas-phase OH radical oxidation of an organic film at the air-water interface using material extracted from urban, remote and wood smoke aerosol

Table 1. A list of the neutron scattering length density and thickness of the each film studied at the air-water interface, as well as listing the oxidation kinetics of the film if exposed to OH radicals.

Table 2. The steady-state rate constants (k'_{1-10}) for the degradation mechanism comprising of ten kinetic steps fitted to the film of DSPC at the air-water interface when exposed to OH radicals.

Paper 5: The reaction between gas-phase OH radicals and organic films extracted from atmospheric aerosol at the air-water interface: an x-ray reflectivity and atmospheric lifetime study

Table 1. Table of the x-ray scattering length density (ρ) and film thickness (δ) for urban and remote atmospheric aerosol extract thin films at the air-water interface.

Table 2. Pseudo first-order and bimolecular rate constants as well as atmospheric film lifetime for the reaction between atmospheric aerosol extract and gas-phase OH radicals.

Paper 6: Oxidation of a bilayer of DPPC on a mineral interface by aqueous-phase OH radicals to replicate atmospheric aerosol behaviour

Table 1. The scattering length density (ρ) and thickness (δ) of the layers used to fit the neutron reflection profile of a bilayer of DPPC at the air water interface.

Table 2. The bimolecular rate constant (k) and lifetime with regard to atmospheric conditions (τ) for each kinetic step of the three-layers used to depict the DPPC bilayer at the silica-water interface.

Table 3. The pseudo first-order rate constants (k') for each step of the step-wise degradation decay of each layer of the DPPC bilayer at the silica-water interface when exposed to OH radicals.

Introduction

1.1. The atmosphere

The Earth's atmosphere is a collection of gases retained by gravity that surround the Earth. The Earth's atmosphere can be characterised in terms of temperature and pressure variations, which leads to the atmosphere being characterised into layers, as displayed in Figure 1.1. Figure 1.1 depicts the "standard atmosphere" with temperature and pressure altering with altitude. Figure 1.1 would also alter with season and latitude, however these alterations are not depicted in Figure 1.1.

The lower regions of the atmosphere include the troposphere layer that extends from the Earth's surface to 15 km altitude, within the troposphere is the planetary boundary layer where the Earth's surface strongly influences turbulence, temperature and humidity. Transport of air in the troposphere will move vertical upwards owing to the decreasing pressure, as the air rises it will expand and cool. The cooling of the air is called adiabatic cooling owing to no heat being added or taken away from the air. The stratosphere layer follows the troposphere and is situated at an altitude of 15 to 55 km. Stratospheric air is very stable, and consequently vertical motion is quite slow. Stratospheric air is stable owing to temperature increasing with altitude: warmer air lies over colder air and as a result convection rarely happens in the stratosphere. A consequence occurring from the lack of movement in the stratosphere is "the ozone hole", chlorine-containing gases such as CFCs and other related hydrocarbons pass through the troposphere into the stratosphere. Owing to the vertical movement of air in the troposphere, the chlorine-containing gases do not react with material in the troposphere, contrastingly the gases do not move so quickly through the stratosphere owing to minimal air movement. The chlorine-containing compounds subsequently undergo photochemical process that catalyses ozone destruction.

The upper atmosphere includes the mesosphere extending from 55 km to 90 km and the thermosphere layer situated from 90 km to 500 to 1000 km. The ionosphere layer is the region of the atmosphere

Introduction

where ions are produced by photoionisation, and extends from the upper region of the mesosphere layer into the lower regions of the thermosphere layer. The exosphere layer is the outermost region of the atmosphere and is where gaseous molecules with sufficient energy escape from the atmosphere e.g. Seinfeld and Pandis (2006). Interestingly, Figure 1.1 depicts the atmospheric temperature varying by less than a factor of two, whilst the pressure changes by six orders of magnitude. Alteration in temperature and pressure with altitude will affect atmospheric chemistry and the kinetics of the reactions occurring.

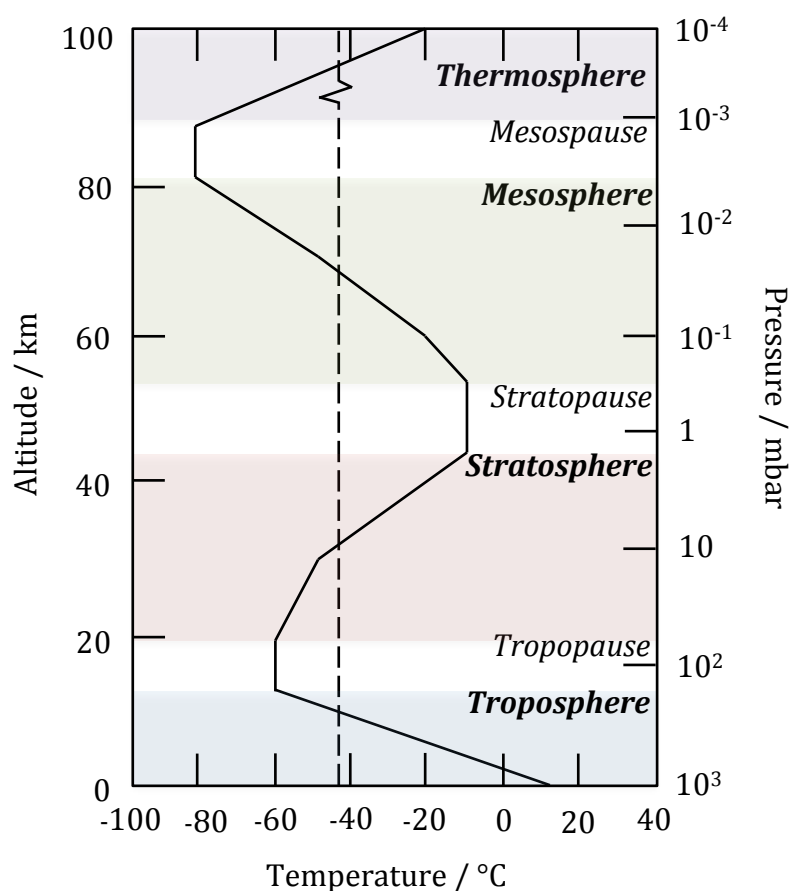


Figure 1.1. The layers of the atmosphere, redrawn from Seinfeld and Pandis (2006).

Studies that have focused on atmospheric chemistry reach as far back as the eighteenth century when scientists such as Henry Cavendish and Joseph Priestly undertook experiments to determine the chemical composition of the atmosphere. The composition of the atmosphere is understood to be predominantly nitrogen gas (78

Introduction

percent), oxygen gas (21 percent) and argon (1 percent). The concentration of such gases is mainly controlled by the biosphere, uptake and release from the Earth's crust and degassing of the interior of the Earth e.g. Seinfeld and Pandis (2006).

Water vapour is the next most abundant component, followed by trace gases such as carbon dioxide and methane at low concentrations; however there has been an extraordinary increase in the concentration of such trace gases in comparison to historical levels owing to the increase of human activity releasing such compounds. Present-day measurements have enabled identification of atmospheric trace species, including atmospheric aerosols, down to levels of 10^{-12} parts per air e.g. Seinfeld and Pandis (2006).

1.2. Atmospheric aerosols & cloud droplets

Atmospheric aerosols are solid or liquid micron-sized particles dispersed throughout the atmosphere. Atmospheric aerosols are most easily noticed when they scatter or absorb solar radiation, and their consequent effects on global climate and human health are current environmental hot topics e.g. Pöschl (2005).

Atmospheric aerosols have a crucial role in contributing to global temperatures and current climate through directly scattering or absorbing solar radiation, or by acting as cloud condensation nuclei. Figure 1.2 depicts the total contribution to the global radiative forcing from atmospheric aerosol based on data sourced from Stocker et al. (2013), where radiative forcing can be described as an aerosol's or cloud droplet's ability to affect the energy balance, thereby contributing to climate change.

Introduction

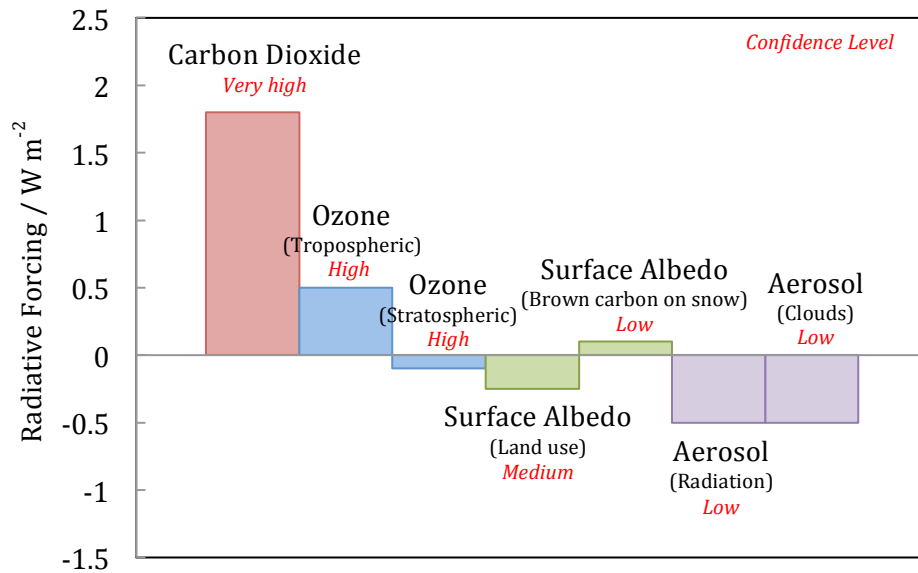


Figure 1.2. Diagram redrawn from a graph featured in the Intergovernmental Panel on Climate Change (IPCC) assessment on climate change written by Stocker et al.(2013). The diagram highlights the radiative forcing contribution from different atmospheric aerosol.

From Figure 1.2, it can be observed that atmospheric aerosols are not the only agents that contribute to climate change; greenhouse gases absorb outgoing radiation and hence have a positive radiative forcing effect. Greenhouse gases currently have a radiative forcing of 2.4 W m^{-2} (as calculated by Ramanathan et al., 2001). Greenhouse gases radiative forcing contributions are described with a high level of confidence in Figure 1, however the certainty regarding atmospheric aerosols contribution is currently regarded as low.

Figure 1.2 shows that aerosol-cloud interactions contribute to the radiative forcing of climate. Cloud droplets form from rising air in the atmosphere that adiabatically cools owing to decreasing pressure. Cooling air has a reducing capacity for holding water and subsequently the air becomes supersaturated with water. Water in the atmosphere exists in two phases: as water vapour in the gas-phase and droplets or wet aerosol particles in the aqueous-phase, conversion between the two phases is complicated. Gas-phase water will condense out of the atmosphere in the presence of cloud condensation nuclei. The point where condensation occurs is called the air's dew point. The altitude at

Introduction

which the dew point is reached and clouds form is known as the condensation level.

Aerosols are cloud condensation nuclei. Cloud condensation nuclei are not a specific type of aerosol, but can form from a variety of aerosol depending on its size, content, wettability and presence of surface-active substances. Cloud condensation nuclei aerosols act as initial sites for the condensation of water vapour into droplets or cloud ice droplets. The water vapour saturation level of the cloud condensation nuclei's surrounding environment needs to be considered to determine if a cloud droplet will form.

Cloud condensation nuclei typically have a curved surface. The water saturation vapour pressure over a curved surface is larger than the water saturation vapour pressure over a flat surface, as summarised in the Kelvin equation:

$$\ln \frac{p}{p_0} = \frac{2\gamma V_m}{rRT}, \quad (\text{Eq.1.1})$$

where p is the actual vapour pressure, p_0 is the saturation vapour pressure, γ surface tension, V_m is the molar volume, r is the radius of the droplet, R is the universal gas constant and T is temperature. An important aspect of the Kelvin equation is the consideration of the droplet's surface tension in relation to the droplet's size: as a droplet's radius increases the surface tension will decrease reducing the likelihood of evaporation occurring. Subsequently, the Kelvin equation is very important when considering the growth of a cloud droplet.

Interestingly, from equation 1.1 it can be observed that as r reaches infinity, the curvature effect on the saturation vapour pressure will become insignificant and the droplet can be considered a flat surface, aerosols with a radius of 1 μm or more are considered to be in this regime. However, for extremely small droplets large supersaturations are required for the droplet to be in equilibrium with its environment. Large supersaturations with a relative humidity in excess of 100 percent rarely occur in the atmosphere and therefore cloud condensation will not occur. Aerosols with a radius of 0.1 μm fit into this regime.

Introduction

A second scenario to consider is the presence of dissolved material that may alter the vapour pressure of the droplet. The effect arising from the presence of solutes upon the saturation vapour pressure is summarised by the Raoult effect (Equation 1.2):

$$p_i = p_i^* x_i , \quad (\text{Eq.1.2})$$

where p_i is the partial vapour pressure of component i in a gaseous mixture and x_i the mole fraction of component i , whilst p_i^* is the vapour pressure of the pure component i . The presence of a solute would lower the vapour pressure of the solution compared to the vapour pressure of a pure solvent. Consequently, a cloud droplet containing a dissolved material will favour condensation more than a pure droplet without the presence of the dissolved material. It ought to be noted that the Raoult effect only works for ideal solutions and in practice there is no such thing; in an ideal solution the forces between solvent molecules and solute molecules are exactly the same.

The combined effects resulting from curvature of the aerosol droplet and solute content of the droplet are combined by Köhler theory (Equation 1.3). Köhler theory describes the critical dependence between diameter of a droplet and the solute content upon formation of cloud droplets from the condensation of water vapour:

$$\ln \left(\frac{p_w(D_p)}{p_0} \right) = \frac{4M_w \sigma_w}{RT \rho_w D_p} - \frac{6n_s M_w}{\pi \rho_w D_p^3} , \quad (\text{Eq.1.3})$$

where p_w is the droplet water vapour pressure, p_0 the corresponding saturation vapour pressure over a flat surface, D_p the cloud droplet diameter, M_w the molecular weight of water, ρ_w the density of pure water, and n_s the moles of solute. Figure 1.3 depicts the relationship between the Kelvin effect, the Raoult effect and Köhler theory.

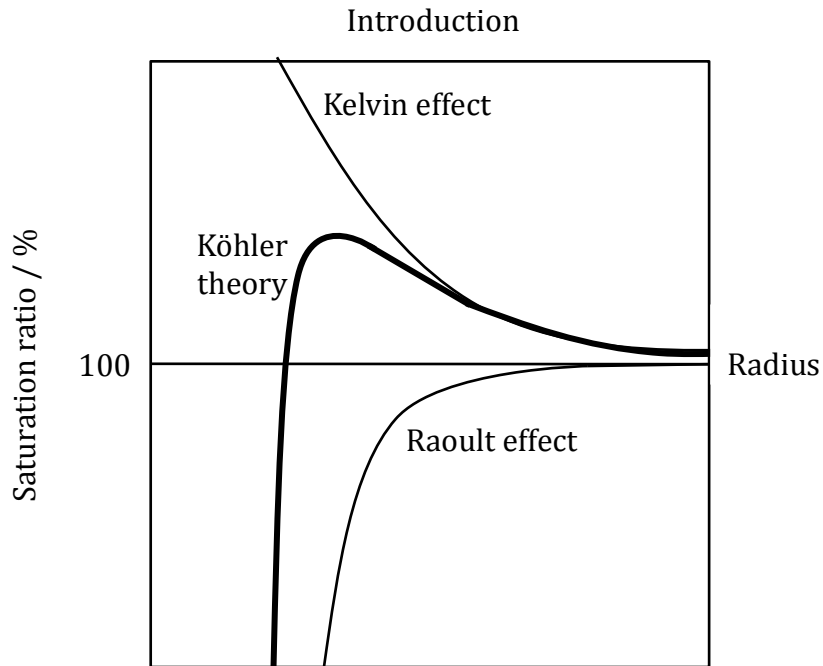


Figure 1.3. Curves depicting the Kelvin effect, the Raoult effect and Köhler theory.

The peak of the Köhler curve depicts the radius required for an aerosol to be a cloud condensation nuclei, the peak of the curve is called the critical supersaturation point. An activated cloud droplet will grow by vapour condensing onto its surface, providing the vapour pressure of the surrounding environment exceeds the vapour pressure adjacent to the cloud droplet. Condensation will occur up to the critical supersaturation point, with the effect from the dissolved solute being the governing factor in droplet growth. Thereafter evaporation will occur, and the surface tension of the droplet will be the governing factor in droplet growth.

The impact of anthropogenic aerosols upon cloud formation has featured in a number of studies. For example, Reid (1999) and Andreae (2004) studied aerosols produced from forest fires in the Amazon basin. The forest fires were shown to cause an increase in the number of cloud condensation nuclei and consequently a decrease in cloud droplet size. The effect is called the Twomey effect e.g. Charlson et al. (2001) and Lohmann and Feichter (2005): the increase in aerosol number in a cloud with the same water content leads to smaller cloud droplets forming, resulting in more solar radiation being reflected.

Introduction

In addition, several studies have concentrated on examining the effects of cloud condensation nuclei composition, for example work conducted by Randles et al. (2004) demonstrated that the presence of internal mixtures may affect water uptake whilst studies conducted by Mircea et al. (2005) showed the importance of the presence of organic material in the activation of aerosols sourced from biomass burning aerosols to become cloud condensation nuclei. However, owing to atmospheric aerosols having a complex composition, current understanding is far from complete.

1.2.1. Size distribution of atmospheric aerosols

The size of atmospheric aerosols ranges from a few nanometres to approximately 100 micrometres. Resulting from the wide variety of aerosol sources and in situ formation of aerosol and atmospheric processing, the size of atmospheric aerosol is characterised by a number of modes, as displayed in Figure 1.4.

Aerosol size is firstly split into fine or coarse modes. The separation of aerosol size is a distinct separation owing to the two modes differing in their origins, chemical composition, atmospheric processing and atmospheric removal processes. For example, common sinks for a fine mode aerosol includes rainout and washout, whilst a sink for coarse aerosol is sedimentation.

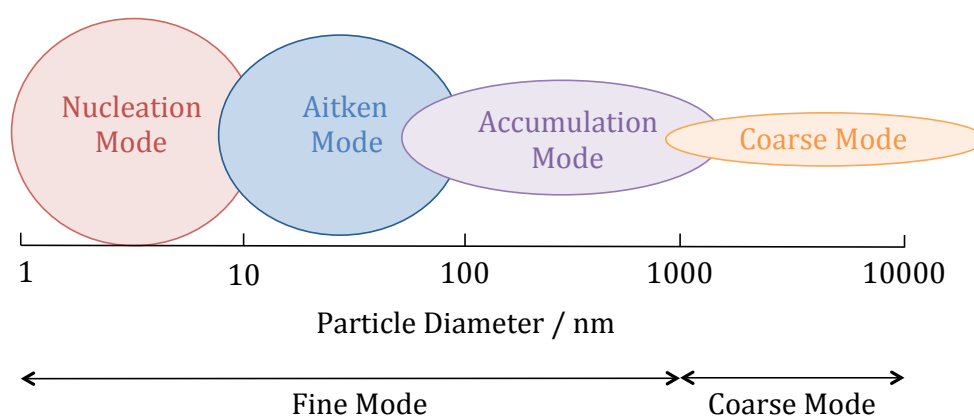


Figure 1.4. A depiction of the different modes that characterise atmospheric aerosol.

Within the two modes, there are four main aerosol size modes: nucleation, Aitken, accumulation and coarse mode. Each mode can be

Introduction

characterised by its specific source. For example, nucleation mode aerosols form from the condensation of super-saturated gases, whilst Aitken aerosols from the condensation of nucleation mode aerosols or the incomplete combustion of soot. Nucleation and Aitken mode aerosols account for the greatest number quantity of atmospheric aerosols, however owing to their small size the aerosols are only a few percent of the total mass of atmospheric aerosols.

Aerosols that fit into the accumulation mode are of the size 0.1 to 2 micrometres with volumes reaching $40 \mu\text{m}^3$ e.g. Seinfeld and Pandis (2006). Accumulation mode aerosols are sourced from the condensation or coagulation of Aitken mode aerosols or intensive mechanical processes. An example of accumulation mode aerosols includes the condensation of secondary sulphates, nitrates and organics from the gas-phase. Coarse mode aerosols are much larger, ranging in size from 2 to 100 micrometres with aerosol volumes reaching $30 \mu\text{m}^3$ e.g. Seinfeld and Pandis (2006). Coarse modes are sourced from the condensation or coagulation of accumulation mode aerosols or mechanical processes such as abrasion of mineral dust. Examples of coarse mode aerosols include primary aerosols such as seasalt, volcanic ash and mineral dust.

1.2.2. Sources and sinks of atmospheric aerosols

Direct emission of aerosols into the atmosphere is a primary source of atmospheric aerosol, whilst further reactions involving atmospheric aerosols are a source of secondary atmospheric aerosol. Primary atmospheric aerosol sources are predominantly mechanical in nature, for example emissions from volcanic eruption, seasalt and desert dust. However, anthropogenic emissions account for approximately ten percent by mass of primary aerosol. Examples of primary anthropogenic aerosol sources includes fossil fuel combustion and biomass burning, such sources emit organic and black carbon as well as sulfur dioxide into the atmosphere. Sulfur dioxide will react with water vapour and other gases once in the atmosphere, producing sulphate particles.

Introduction

The source of the atmospheric aerosols can be used to categorise the aerosol, for example urban aerosol, marine aerosol, rural aerosol and remote aerosol. Urban aerosols are mixtures of primary particulate emissions from industries, transportation, power generation and secondary material formed vapours that condense onto an existing aerosol e.g. Seinfeld and Pandis (2006). Zhu et al. (2002) reported a decrease in aerosol concentration away from major highways, owing to roads being the sites where fresh combustion aerosols are produced.

In contrast, rural aerosols are predominantly natural in origin containing naturally sourced aerosols from dust, pollen and plant waxes e.g. Deepak and Gali (1991). However, Hobbs et al. (1985) discovered that when nearing inhabited areas rural aerosols begin to have urban aerosol qualities. Interestingly, polar aerosols also show an anthropogenic influence during the winter and early spring as demonstrated by work conducted by Barrie (1986).

Aerosol sources differ regionally: carbonaceous aerosol is most prominent over the mid-latitudes of the Northern hemisphere owing to the consumption of fossil fuels and agricultural practices, whilst aerosols formed from biomass burning are most prominent in southern Africa and South America. Naturally high concentrations of mineral aerosol are seen over the desert in the form of desert dust and over the oceans owing to sea salt e.g. Takemura et al. (2005). Interestingly, desert dust sourced from the Saharan desert has been found in the Amazon. The trans-continental transport of the desert dust is important to the Amazon because of the high phosphorus content: some nutrients are low in content in Amazonian soils owing to the high level of nutrients being washed away by heavy rainfall and thus desert dust may play a fertilising role in the Amazon e.g. Yu et al. (2015). Table 1.1 outlines the emissions from both natural and anthropogenic sources.

Table 1.1. Emissions from natural and anthropogenic primary sources of atmospheric aerosol. Data sourced from Boucher (2013).

Source	Global Min	Global Max
<i>Natural</i>		
Sea spray	1400 Tg yr ⁻¹	6800 Tg yr ⁻¹
Mineral dust	2 Tg yr ⁻¹	20 Tg yr ⁻¹
Terrestrial primary biological aerosol	1000 Tg yr ⁻¹	4000 Tg yr ⁻¹
Dimethylsulphide	10 TgS yr ⁻¹	40 TgS yr ⁻¹
Monoterpenes (C ₁₀ H ₁₆)	30 TgC yr ⁻¹	120 TgC yr ⁻¹
Isoprene (C ₅ H ₈)	410 TgC yr ⁻¹	600 TgC yr ⁻¹
<i>Anthropogenic</i>		
Black carbon	3.6 Tg yr ⁻¹	6.0 Tg yr ⁻¹
Primary organic aerosol	6.3 Tg yr ⁻¹	15.3 Tg yr ⁻¹
SO ₂	43.3 Tg yr ⁻¹	77.9 Tg yr ⁻¹
NH ₃	41.6 Tg yr ⁻¹	34.5 Tg yr ⁻¹
Biomass burning	29.0 Tg yr ⁻¹	85.3 Tg yr ⁻¹

Table 1.1 illustrates that the largest source of atmospheric aerosol is sea spray. Sea spray produces sea salt as well as organic aerosol. The sea surface microlayer contains a high concentration of organic material that will enter the atmosphere through bubbles forming when waves break e.g. Blanchard (1964), Blanchard and Woodcock (1957), Cochran (2016) and Donaldson and George (2012).

Primary organic aerosols such as those produced from tree or industrial emissions likely undergo complex interactions with other aerosols or sunlight to form secondary organic aerosols. Secondary organic aerosols likely form by one of the following pathways: (a) new particle formation from the formation of semi-volatile organic compounds which partake in the nucleation and growth of new aerosol, (b) gas-phase partitioning where pre-existing aerosol uptake newly formed semi-volatile organic compounds or (c) formation of non-volatile compounds through heterogeneous reactions e.g. Pösch(2005).

Aerosols will leave the atmosphere via a variety of pathways, which can be split into two sub-categories: wet deposition or dry deposition e.g. Petroff and Zhang (2010) and Sportisse (2007). Dry deposition is the movement of atmospheric aerosols out of the atmosphere without the aid of precipitation, whilst wet deposition is the scavenging of atmospheric aerosols by cloud, fog, rain and snow droplets, which are consequently deposited onto the surface of Earth

Introduction

e.g. Seinfeld and Pandis (2006). Examples of wet deposition include in-cloud or below-cloud scavenging, whilst turbulent diffusion or gravitational settling are examples of dry deposition.

Deposition will determine the lifetime of an atmospheric aerosol. Figure 1.5 depicts the typical lifetime of aerosol in the lower layers of the atmosphere. Many factors play a role in the likelihood of deposition occurring. For example, the level of turbulence, the chemical and physical properties of an aerosol (for example size, mass, density or shape) as well as the surface the aerosols are deposited onto. For example, a nonreactive surface may not absorb certain gases thereby limiting dry deposition.

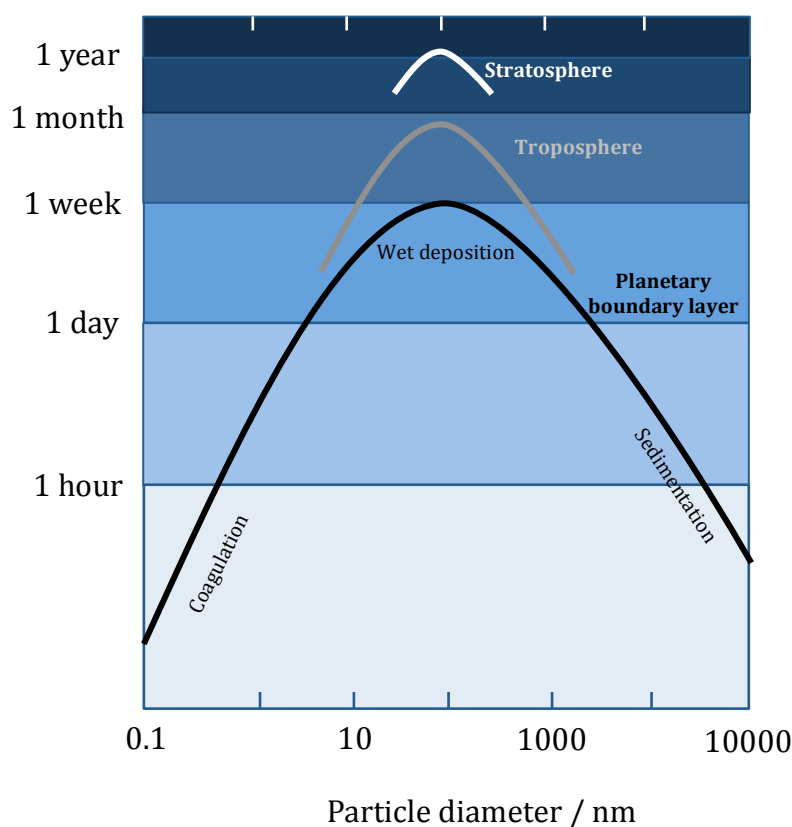


Figure 1.5. The lifetime of atmospheric aerosols with regard to particle diameter and location in the atmosphere. The diagram is adapted from a schematic from the book written by Georgii and Jaenicke (1981).

For successful wet deposition, three parameters are important: (1) the aerosol must be in near proximity to condensed water, (2) the condensed water must scavenge the aerosol and (3) the water and aerosol must be deposited, normally in the form of rain or snow. Each of the three steps are reversible processes. During wet deposition, the

Introduction

aerosol will more than likely change e.g. Seinfeld and Pandis (2006). In an annual mean, 80 to 90 percent of aerosol particles are removed by wet deposition. The majority of clouds are formed in the troposphere, and hence the lifetime of tropospheric aerosols is shorter (days) in comparison to aerosols residing at higher altitudes, for example stratospheric aerosols often exist for years.

1.2.3. Composition of atmospheric aerosols

Atmospheric aerosol particles are known to be chemically complex, containing organic material in varying amounts e.g. Li et al. (2011). Unfortunately owing to the richness of the organic chemistry and variable physical properties associated with natural and anthropogenic organic aerosol there is currently great difficulties in sampling and obtaining complete chemical information on aerosols e.g. Jacobson and Hansson (2000). However, it is understood that the composition of atmospheric aerosols is temporally and spatially variable. The main constituents of atmospheric aerosol are sulphate, nitrate, ammonium, sea salt, mineral dust, organic compounds and carbonaceous aerosol e.g. Pöschl (2005).

1.2.3.1. Composition of the troposphere

The troposphere is a relatively separate chemical reservoir to the stratosphere, owing to transport between the two atmospheric layers being relatively slow e.g. Seinfeld and Pandis (2006). Key gaseous components include water vapour, NO_x species, carbon monoxide, methane and ozone. Owing to approximately 35 out of every billion molecules being ozone, ozone production and subsequent removal is important for tropospheric science.

Another large component of the troposphere is organic compounds. Organic compounds are the sum of primary and secondary aerosol and are approximately 10 to 70 percent of the total dry fine particle mass in the troposphere e.g. Eliason et al. (2004). A number of studies have been carried out to try and identify the content of organic aerosol. For example, Rogge et al. (1993) analysed the organic content

Introduction

collected over a year from ten sites in southern California, whilst Kendall et al. (2001) analysed particulate matter collected from two sites in central and north London. Both found a high level of organic containing compounds. Rogge et al. (1993) discovered that the organic material was approximately two thirds of the total fine particle mass, whilst Kendall et al. (2001) discovered that the total organic content lay between 7 to 45 percent of the total particulate matter analysed.

Classes of atmospheric organic aerosols that have been measured in atmospheric particles or are predicted to be presented include the following: alkanes, alkanolic acids, aromatic polycarboxylic acids, polyols, amino acids and polycyclic aromatic ketones to list a few e.g. Rogge et al. (1993) and Saxena and Hildemann (1996). It is important to understand the saturated or unsaturated content of organic aerosols with regard to their reaction potential. The total saturated content has been reported to be larger than the unsaturated content of aerosols e.g. Jones et al. (2017) and is likely because the unsaturated parts of the atmospheric aerosol are unstable with regard to oxidation e.g. Kawamura and Gagosian (1987) and Nah et al. (2013) or decomposition e.g. Abas and Simoneit (1996). Owing to the complexity of organic compounds in the atmosphere, it is estimated that only 10 to 40 percent organic compounds have been identified at the molecular level e.g. Pöschl (2005).

Furthermore, to add to the complexity in composition of tropospheric aerosols, tropospheric aerosols may also contain inorganic ions such as sulphates or nitrates e.g. Turpin (2000) as well as mineral dust, sea salt and carbonaceous components. Carbonaceous aerosol makes up a large fraction of tropospheric aerosol. Carbonaceous aerosol can be classified into three categories: organic carbon (which has already been covered above), elemental carbon and black carbon. There is no distinct classification between the three carbon categories, more a continuous change in refractive index and optical absorption e.g. Pöschl (2005). Interestingly, investigation into the atmospheric concentration of carbonaceous aerosol shows that the total carbon content decreases by a factor of 1.3 between urban to rural

Introduction

environments demonstrating the anthropogenic influence on carbonaceous aerosol concentrations.

1.2.3.2. Composition of the stratosphere

Ozone is the most prominent chemical in the stratosphere. The majority of atmospheric ozone (90 percent by mass) is found in the stratosphere, whilst tropospheric ozone levels are small: stratospheric ozone has a concentration of 10000 ppb versus tropospheric levels of 10 ppb e.g. Seinfeld and Pandis (2006). The majority of ozone is found in the “ozone layer” lying at 10 to 17 km above the Earth’s surface and extending up to 50 km. Other chemical families found in the stratosphere include nitrogen oxides (e.g. NO, N₂O₅ and HOONO₂) hydrogen radicals (e.g. OH or HO₂), and chlorine or bromine containing compounds (e.g. ClO, CF₂Cl₂, HOBr or BrONO₂).

The stratosphere also contains the natural stratospheric aerosol layer predominantly containing sulfur-based aerosols. Sulfur containing compounds can enter the stratosphere by volcanic eruption; recent major eruptions include Agung in 1963, El Chichón in 1982 and Pinatubo in 1991. The Pinatubo eruption added 30 Tg of sulfur dioxide into the stratosphere enhancing the sulfur dioxide content in the stratosphere for the next two years e.g. Seinfeld and Pandis (2006). Apart from volcanic eruption, carbonyl sulphide makes the second largest contribution to the stratospheric aerosol layer e.g. Kremser (2016). The oceans and deep-sea vents produce carbonyl sulphide. Once in the stratosphere, sulfur dioxide and carbonyl sulfide convert into sulfur dioxide by reacting with OH radicals e.g. Solomon (2011) and Crutzen (1976). Carbonyl sulfide is relatively inert and therefore survives in the troposphere and can be transported into the stratosphere, where it photodissociates and is attacked by OH radicals.

Non-sulfur components of the stratospheric aerosol layer include black carbon, organic aerosols, volcanic ash and meteoric and extra-terrestrial aerosol material. Black carbon and organic aerosols enter the lower levels of the stratosphere from the troposphere, and the aerosols relative abundance decrease with altitude. Contrastingly, meteoric and

extra-terrestrial material enters from space. The upper stratosphere is where the majority of such aerosols exist, though they can partition down to lower altitudes e.g. Kremser et al. (2016).

1.3. Atmospheric aerosol thin films

There is considerable evidence proving that atmospheric aerosol and cloud droplets are coated in a thin film of organic or inorganic material. Husar and Shu (1975) provide one of the first studies on thin film coated atmospheric aerosols, which was followed by thin films studies conducted by Posfai et al. (1998) and Capel et al. (1990).

The presence of a thin film may alter the chemical and physical properties of the aerosol or cloud droplet by (a) reducing the rate of evaporation from the particle or droplets e.g. Davies et al. (2013), Eliason et al. (2003), Gill et al. (1983), Kaiser et al. (1996) and McFiggans et al. (2005), (b) inhibiting the transport of chemicals from the gas to the liquid phase of the droplet or particle e.g. Donaldson et al. (1999) and Donaldson and Valsaraj (2010), (c) reducing the scavenging of the droplet or particle by larger cloud and ice particles e.g. Andreaea and Rosenfeld (2008) and Feingold and Chuang (2002), (d) alter the cloud condensation nuclei activation potential of the droplet or particle e.g. Cruz and Pandis (1998) and Ruehl and Wilson (2014), (e) change the optical properties of the droplet or particle e.g. Eliason et al. (2004) and Jones et al. (2014) and (f) alter the reactive uptake ability of the droplet or particle e.g. Enami et al. (2010). The thin film that surrounds the particle or droplet determines the atmospheric chemical properties of the aerosol e.g. Donaldson and Valsaraj (2010); hence it is paramount that the thin film is well defined.

Atmospheric thin films are predominantly organic in composition owing to organic aerosols having the ability to attach to almost any particle they collide with e.g. Eliason et al. (2004). A large number of sources emit organic aerosol into the atmosphere, including vegetation waxes, fossil fuel consumption and photochemical oxidation of primary emissions in the gas-phase.

Introduction

The sea-surface microlayer additionally contributes to the atmospheric organic aerosol concentration: oceans are covered in a sea-surface microlayer of organic compounds including humic substances and fatty acids that reside in the top 1000 μm of the ocean e.g. Ciuraru et al. (2015). Sea-to-air transport results in the film forming material entering the atmosphere through bursting bubbles at the air-water interface causing the sea-surface microlayer to become airborne e.g. Blanchard and Woodcock (1957) and Marty et al. (1979). Chemical analysis of the sea-surface microlayer has shown that the layer consists of amphiphiles sourced from oceanic biota e.g. Donaldson and Vaida (2006).

Thin films are surface-active in varying degrees, according to their chemical structure and similar physical properties to water e.g. Gill et al. (1983). Thin films can be separated into two categories: water-insoluble films and water-soluble films. Water-insoluble films are predominantly made up of amphiphilic compounds such as carboxylic acids, (stearic or oleic acids are commonly used as atmospheric carboxylic acid proxies e.g. Pfrang et al., 2010 and George et al., 2009) and phospholipids e.g. Donaldson and Vaida (2006) and can be described as surface-active films e.g. Gill et al. (1983). Thin films composed of water-soluble material form when the water phase is saturated.

A thin film can be considered as a continuous layer around the periphery of an atmospheric aerosol or cloud droplet, the ensemble is often modelled as core-shell. Core-shell morphology is when a core atmospheric aerosol or cloud droplet is encased within a shell of a different material. Figure 1.6 depicts the different morphology atmospheric aerosol may have.

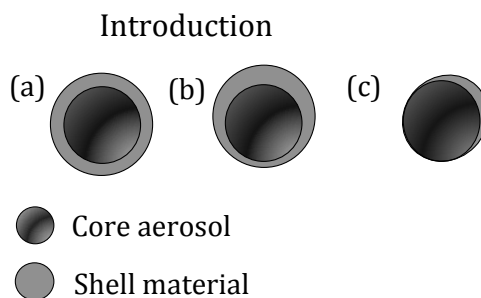


Figure 1.6. Possible geometries of a two-phase aerosol. The geometries are: (a) core-shell, (b) core aerosol displacement and (c) lens formation.

However, when compounds contain hydrophobic and hydrophilic functional groups, the competition between the compounds to form either core-shell or partially engulfed (where the hydrophobic compound forms a lens on the surface) morphology needs to be considered e.g. Reid et al. (2011). Phase separation between contrasting liquids has been studied, in particular Reid et al. (2011) applied optical trapping techniques to demonstrate that core-shell morphology is not necessarily the morphology for an aerosol containing hydrophobic and hydrophilic liquids.

A number of studies have focused on understanding the thin films on atmospheric aerosol and cloud droplets. Studies date back to 1975 when Husar and Shu (1975) used electron microscopy to study smog and haze aerosol particles collected from the atmosphere above Los Angeles. The smog and haze aerosol demonstrated different light scattering abilities, representative of difference chemical compositions or morphology. Additionally, electron microscopy showed the smog aerosol to be a solid sphere, whilst the haze aerosol could be described as a hollow structure – providing indirect evidence for the presence of thin film morphology atmospheric aerosol.

In later years, Posfai et al. (1998) applied electron microscopy techniques with atomic force microscopy to study organic coatings on ammonium sulphate aerosol collected from above the North Atlantic ocean, whilst Capel et al. (1990) applied surface tension techniques to determine the presence of an organic coating in fog droplets collected from the urban area of Zurich, Switzerland: the surface tension for the measured samples was less than pure water. Since the dissolved organic material probably provided the measured surface properties, it

Introduction

was presumed the air-water interface was covered with organic chemicals.

More recent studies have been conducted by Tervahattu et al. (2002) who applied scanning electron microscopy coupled with an energy dispersive x-ray micro-analyser to study aerosol collected from over Helsinki, Finland. The air mass from which the aerosol had been collected from originated from the North Atlantic Ocean, and had subsequently passed over France, Germany and southern Scandinavia. Tervahattu concluded that the aerosols studied were marine sea-salt with a layer of organic aerosol sourced from anthropogenic emissions. Additionally, Tervahattu et al. (2005) demonstrated the prominence of the presence of fatty acid films on aerosol collected from forest fires or the emissions from coal and straw burning through applying time of flight secondary particle mass spectrometry.

Current research is focusing on trying to determine the chemical composition of thin films. Russell et al. (2002) drew organic maps to elucidate the organic compounds present, whilst Takahama et al. (2010) applied scanning transmission x-ray microscopy coupled with near edge x-ray absorption fine structure spectroscopy to characterise the chemical structure of 636 aerosol samples that were collected from the western hemisphere. Takahama et al. (2010) discovered that the majority of the aerosols were heterogeneous in composition and many had one of the following morphologies: (a) black carbon aerosol coated in an aqueous phase, (b) dust aerosol with an organic coating, (c) an organic aerosol enriched with a carboxylic acid film or (d) an inorganic aerosol encapsulated by a organic layer. All the coatings were determined to be less than 0.6 μm thick.

1.4. Atmospheric aerosol chemical reactions

The atmosphere is chemically complex and atmospheric aerosols and cloud droplets often partake in heterogeneous reactions. The most important atmospheric oxidants are ozone, OH radicals and nitrate owing to their abundance and negative effects on human health e.g. Chapleski et al. (2016). The oxidants have a central role in regulating

Introduction

atmospheric gas concentrations, aerosol processing and aerosol ageing e.g. Chapleski et al. (2016).

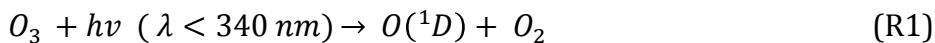
1.4.1. Aerosol chemical reactions

It has long been recognised that reactions between ozone and organic aerosols is critical to the overall chemistry of the atmosphere, and consequently there are numerous studies investigating the heterogeneous chemistry between ozone and a range of organic aerosols e.g. Chapleski et al. (2016), Mmereki and Donaldson (2003), Nieto-Gligorovski et al. (2008) and Smith et al. (2002) to highlight a few. A number of studies have investigated the possible products produced from ozone uptake by atmospheric aerosol. Wisthaler and Weschler (2010) used proton transfer reaction mass spectrometry for direct air analysis of volatile products produced from the reaction between ozone and human skin lipids and detected products include carbonyls, carboxyl or α -hydroxy ketone groups. Additionally, Wells et al. (2008) determined reaction products of ozone and squalene, whilst King et al. (2008) applied Raman spectroscopy to follow the reaction of ozone with carbonate ions: a product peak suggested the reaction between ozone and α -pinene resulted in the formation of carbonyl containing compounds.

The reaction kinetics of ozone with atmospheric aerosols has additionally been investigated. For example, Pfrang et al. (2010) presents a kinetic double layer model based on the interactions between oleic acid and ozone, coupling aerosol surface and bulk chemistry, whilst Morris et al. (2002) applied mass spectroscopy to determine the reaction kinetics between submicron oleic acid aerosols with ozone.

Atmospheric ozone has a key role in converting atmospheric odd nitrogen (e.g. NO, NO₂ and NO₃), hydrogen (e.g. OH and HO₂), halogens and sulfur containing molecules e.g. Thompson (1992). One loss process for ozone in the atmosphere is the formation of the OH radical by way of reaction between O(¹D) and water vapour after formation of O(¹D) from ozone by photo-dissociation e.g. Thompson (1992):

Introduction



The above reaction process does not lead to a significant loss of ozone from the atmosphere as only a small proportion of $O(^1D)$ participate in R2. Once formed, $O(^1D)$ will more likely interact with nitrogen molecules. Photolytic processes largely produce atmospheric OH radicals, however non-light induced reactions can also resulting in the production of OH radicals, for example the Fenton reaction. The Fenton reaction requires a low-valence transition metal such as Fe(II), Fe(III), Cu(I) or Mn(III) to catalyse the decomposition of H_2O_2 e.g. Herrmann et al. (2015).

Resulting from the prominent presence of OH radicals in the atmosphere, a number of studies have used OH radicals as the oxidant. For example, Nah et al. (2013) studied OH radical initiated oxidation of sub-micron unsaturated fatty acid particles to explore how surface OH radical addition reactions initiate chain reactions that have the potential to rapidly transform the chemical composition of an aerosol, whilst Ruehl et al. (2013) determined the oxidation products produced from the heterogeneous oxidation of OH radical with atmospheric aerosol proxies n-octacosane and squalane. Additionally, Slade and Knopf (2013) determined reactive uptake coefficients of OH radicals by levoglucosan, abietic acid and nitroguaiacol (common atmospheric aerosol proxies), and Kolesar et al. (2014) studied OH radical initiated oxidation of internally mixed squalane and secondary organic aerosol.

Studies involving other atmospheric oxidants include the work conducted by Zhang et al. (2014) who used the nitrate radical to investigate the reaction kinetics and determine the probable reaction mechanism of the radicals reacting with vinyl-terminated self-assembled monolayers, whilst Gross et al. (2009) studied the heterogeneous reactions between nitrate and dinitrogen pentoxide on a range of proxy atmospheric aerosol to understand night time aerosol chemistry.

Introduction

1.4.2. Aerosol thin film chemical reactions

The species at the surface of any organic-coated atmospheric aerosol or cloud droplet are susceptible to atmospheric oxidation e.g. Eliason et al. (2003), and consequently a number of studies have investigated the effect of atmospheric oxidants on aerosols thin films. Oxidants such as OH, halogen atoms, ozone and nitrate radicals have all featured in the studies. For example, Nieto-Gligorovski et al. (2008) exposed aerosol proxies phenoxyphenol and catechol to ozone, whilst Eliason et al. (2003) compared the mechanisms of oxidative processing for organic aerosol and thin films composed of octenoic acid when exposed to ozone. Vlasenko et al. (2008) used a different atmospheric oxidant, gas-phase OH, to study the heterogeneous oxidation of organic films formed from aerosols sourced from soot.

Thin films composed of amphiphilic compounds at the air-water interface of cloud droplets or aqueous atmospheric aerosol are exposed to dissolved inorganic chemical species from within the aerosol or droplet, and gas-phase reactive radicals and solar radiation. Subsequently thin films often display different reactivity to bulk atmospheric aerosol e.g. Donaldson and Vaida (2006).

Examples of studies involving the oxidation of a thin film at the air-water interface includes the work conducted by Pfrang et al. (2014), King et al. (2009), Voss et al. (2007), Wadia et al. (2003) and González-Labrada et al. (2006). Pfrang et al. (2014), King et al. (2009) and Voss et al. (2007) applied neutron scattering techniques to monitor the alteration in a film of oleic acid at the air-water interface when exposed to ozone, whilst González-Labrada et al. (2006) used a surface tensiometer to record changes in surface tension of a film of oleic acid at the air-water interface upon exposure to ozone. Wadia et al. (2003) additionally studied the effect of ozone to thin films at the air-water interface, however Wadia et al. (2003) used atmospheric pressure ionization mass spectrometry to study unsaturated and saturated phospholipids.

The above studies have focused on the oxidation of thin films at the air-water interface by gas-phase oxidants, however aqueous-phase

oxidants may also exist: Karagulian et al. (2008) reported a new bottom-up mechanism of oxidation for organics on surfaces involving the photochemical formation of OH radicals from the substrates NaNO_2 and NaCl .

1.5. Summary and strategy applied to study atmospheric aerosols and thin films

Research in the field of atmospheric aerosol focuses upon the role aerosol has upon air pollution, climate and remote sensing. However, owing to the huge complexity of atmospheric aerosol's composition, there is not a single inventory of the chemical compounds which make up atmospheric aerosols or a complete understanding of atmospheric aerosol sources, reactions or their effects upon life on Earth e.g. Jacobson and Hansson (2000).

Within the thesis presented a number of projects have been carried out with the aim of addressing the current uncertainty regarding atmospheric aerosol. Optical trapping techniques have been applied alongside neutron and x-ray reflectivity techniques. The use of the optical trapping technique used simultaneously with Mie spectroscopy provided a non-contact method of studying atmospheric aerosols in a gaseous environment, semi-representative of the atmosphere, whilst reflectometry techniques provided a surface sensitive method of studying thin films that form upon atmospheric aerosol or cloud droplets. The complimentary use of neutron and x-ray reflectometry provided an insight into film thickness, film structure and change of the film upon exposure to atmospheric oxidants.

In the thesis presented, six experiments focusing on the study of atmospheric aerosol and atmospheric aerosol or cloud droplet thin films have been carried out. A number of projects are applied to thin film systems owing to the prevalence of such systems in the atmosphere, whilst considerable work has concentrated on understanding the reaction chemistry of atmospheric aerosols. In the thesis presented work has been carried out to understand (a) the change in refractive index and (b) the kinetics for different oxidising

Introduction

proxy atmospheric aerosol system. The methodology section outlines the background, theory and procedure applied to use the optical trapping and reflectometry techniques.

Hopefully the work presented in the thesis, when combined with other and future research, will help elucidate atmospheric aerosols and aid others in the compilation of an accurate description of atmospheric aerosol.

Introduction references

- Abas R. B. and B. R. T. Simoneit, *Atmospheric Environment* **30**(15), 2779–2793 (1996).
- Andreae M. O. et al., *Science* **303**(5662): 1337–1342 (2004).
- Andreae M.O. and D. Rosenfeld, *Earth Science Reviews* **89**(1–2), 13–41 (2008).
- Barrie L. A., *Atmospheric Environment* **20**(4), 643–663 (1986).
- Blanchard D. C., *Science* **146**, 396–397 (1964).
- Blanchard D. C. and A. H. Woodcock, *Tellus* **9**(2), 145–158 (1957).
- Boucher O. et al., *Climate Change 2013: The Physical Science Basis*, 571–657 (2013).
- Capel P. D. et al., *Environmental Science & Technology* **24**(5): 722–727 (1990).
- Chapleski R. C. et al., *Chemical Society Reviews* **45**(3), 3731–3746 (2016).
- Charlson R J et al., *Science* **292**(5524), 2025–2026 (2001).
- Ciuraru R. et al., *Scientific Reports* **5**(August), 12741 (2015).
- Cochran R. E. et al., *Environmental Science and Technology* **50**(5), 2477–2486 (2016).
- Crutzen P J., *Geophysical Research Letters* **3**(2), 73–76 (1976).
- Cruz C N, and S N Pandis, *Journal Of Geophysical Research* **103**, 13111–13123 (1998).
- Davies J. F. et al., *Proceedings of the National Academy of Sciences of the United States of America* **110**(22), 8807–8812 (2013).
- Deepak A. and G. Gali, Deepak Publishing (1992).
- Donaldson D. J. and V. Vaida, *Chemical Reviews* **106**(4), 1445–1461 (2006).
- Donaldson D. J. and K. T. Valsaraj, *Environmental Science and Technology* **44**(3), 865–873 (2010).
- Donaldson D. J., *Journal of Physical Chemistry A* **103**(1), 62–70 (1999).
- Donaldson D. J. and C. George, *Environmental Science & Technology* **46**(19), 10385–10389 (2012).
- Eliason T. L. et al., *Atmospheric Environment* **37**(16), 2207–19 (2003).
- Eliason T. L., J. B. Gilman, and V. Vaida, *Atmospheric Environment*

Introduction

- 38**(9), 1367–1378 (2004).
- Enami S., M. R. Hoffmann, and A. J. Colussi, *Journal of Physical Chemistry A* **114**(18), 5817–5822 (2010).
- Feingold G. and P. Y. Chuang, *Journal of the Atmospheric Sciences* **59**(12), 2006–2018 (2002).
- George et al., *Atmospheric Environment* **43**(32): 5038-5045 (2009).
- Georgii E. and R. Jaenicke, D. Reidel Publishing (1981).
- Gill P. S., T. E. Graedel, and C. J. Weschler, *Reviews of Geophysics* **21**(4), 903 (1983).
- González-Labrada E., R. Schmidt and C. E. DeWolf, *Chemical Communications* **23**, 2471–2473 (2006)
- Gross S., R. Iannone, and S Xiao, *Physical Chemistry Chemistry Physics* **11**(36): 7792–7803 (2009).
- Herrmann H. et al., *Chemical Reviews* **115**(10), 4259–4334 (2015).
- Hobbs P. V., D. A. Bowdle and L. F. Radke, *Journal of Climate and Applied Meteorology* **24**(12), 1344–1356 (1985).
- Husar R.B. and W. R. Shu. *Journal of Applied Meteorology* **14**, 1558–1565 (1975).
- Jacobson M C and H Hansson, *Reviews of Geophysics* **38**, 267–294 (2000).
- Jones S. H. et al., *Atmospheric Environment* **161**, 274-287, (2017).
- Jones S. H., M. D. King and A. D. Ward, *Chemical Communincations* **51**, 4914 (2015).
- Kaiser T. G. R. and G. Schweiger, *Applied Optics* **35**(30), 5918–5924 (1996).
- Karagulian F., C. W. Dilbeck and B. J. Finlayson-Pitts, *Journal of the American Chemical Society* **130**(34): 11272–11273 (2008).
- Kawamura K., and R. B. Gagosian, *Nature* **325**(6102), 330–332 (1987)
- Kendall M. et al. *Atmospheric Environment* **35**(14), 2483–2495 (2001).
- King M. D. et al., *Physical Chemistry Chemical Physics* **11**(35), 7699–7707 (2009).
- King M. D. et al., *Faraday Discuss.* **137**, 173–192 (2008).
- Kolesar K. R. et al., *Environmental Science and Technology* **48**(6), 3196–3202 (2014).

Introduction

- Kremser S. et al., Reviews of Geophysics **54**, 278-335 (2016).
- Li Y., M. J. Ezell, and B. J. Finlayson-Pitts, Atmospheric Environment **45**(25), 4123–4132 (2011).
- Lohmann U., and J. Feichter, Atmospheric Chemistry and Physics **5**, 715–737 (2005).
- Marty J. C. et al., Journal of Geophysical Research: Oceans **84**(C9), 5707–5716 (1979).
- McFiggans G. et al., Atmospheric Chemistry and Physics Discussions **5**(5), 8507–8646 (2005).
- Mircea M. et al., Atmospheric Chemistry Physics **5**, 3111–3126 (2005).
- Mmereki B. T. and D. J. Donaldson, Journal of Physical Chemistry A **107**(50), 11038–11042 (2003).
- Morris J. W. et al., Geophysical Research Letters **29**(9), 1357-1360 (2002).
- Nah T. et al., Physical Chemistry Chemical Physics **15**(42), 18649–18663 (2003).
- Nieto-Gligorovski L. et al. 2008. Physical Chemistry Chemical Physics **10**(20): 2964–2971.
- Petroff A. and L. Zhang, Geoscientific Model Development **3**(2), 753–769 (2010).
- Pfrang C., M. Shiraiwa, and U. Pöschl, Atmospheric Chemistry and Physics **10**(10), 4537–4557 (2010).
- Pfrang C. et al., Physical Chemistry Chemical Physics **16**(26), 13220–13228 (2014).
- Pöschl U., Angewandte Chemie **44**(46), 7520–7540 (2005).
- Posfai M. et al., Geophysical Research Letters **25**(11), 1907–1910 (1998).
- Ramanathan V. et al., Science **294**(December), 2119–2125 (2001)
- Randles C. A., L. M. Russell and V. Ramaswamy, Geophysical Research Letters **31**(16): 4–7 (2004).
- Reid J. S. et al., Journal of Geophysical Research: Atmospheres **104**(D22): 27473–26489 (1999).
- Reid J. P et al., Physical Chemistry Chemical Physics **13**(34), 15559–15572 (2011).

Introduction

- Rogge W. F. et al., Atmospheric Environment Part A, General Topics **27**(8), 1309–1330 (1993).
- Ruehl C. R. et al., Journal of Physical Chemistry A **117**(19), 3990–4000 (2013).
- Ruehl C. R., and Kevin R. Wilson, Journal of Physical Chemistry A **118**(22), 3952–66 (2014).
- Russell L. M., M. F. Steven and M. C. B. Satish, Geophysical Research Letters **29**(16), 1–4 (2002).
- Saxena P. and L. M. Hildemann, Journal of Atmospheric Chemistry **24**(1), 57–109 (1996).
- Seinfeld J. H. and S. N. Pandis, Wiley, (2006).
- Slade J. H. and D. A. Knopf, Physical Chemistry Chemistry Physics **15**(16), 5898–5915 (2013).
- Smith G. D. et al., Journal of Physical Chemistry A **106**(35), 8085–95 (2002).
- Solomon S. et al., Science **333**(6044), 866–870 (2011).
- Sportisse B., Atmospheric Environment **41**(13), 2683–2698 (2007).
- Stocker T. F., D. Qin and G. K. Plattner, Climate Change 2013: The Physical Science Basis, 33–115 (2013).
- Takahama S., S. Liu and L. M. Russell, Journal of Geophysical Research Atmospheres **115**(1), 1–21 (2010).
- Takemura T. et al., Journal of Geophysical Research D: Atmospheres **110**(2), 1–16 (2005).
- Tervahattu H. et al., Journal of Geophysical Research **107**(D7), 4053–4061 (2002).
- Tervahattu H. et al., Journal of Geophysical Research D: Atmospheres **110**(6), 1–9 (2005).
- Thompson A. M., Science **256**(5060), 1157–1165 (1992).
- Turpin B. J., P. Saxena and E. Andrews, Atmospheric Environment **34**(18), 2983–3013 (2000).
- Vlasenko A., I. J. George and J. P. D. Abbatt, Journal of Physical Chemistry A **112**(7), 1552–1560 (2008).
- Voss Laura. F. et al., Journal of Geophysical Research Atmospheres **112**(6), 1–9 (2007).

Introduction

Wadia Y. et al., *Langmuir* **16**(3), 9321–9330 (2003).

Wells J. R. et al., *Journal of ASTM International* **5**(7), 1-8 (2008).

Wisthaler A. and C. J. Weschler, *Proceedings of the National Academy of Sciences* **107**(15), 6568–6575 (2010).

Yu, H. et al., *Geophysical Research Letters*, 1-8 (2015).

Zhang Y. et al., *Physical Chemistry Chemical Physics* **16**(31), 16659–16670 (2014).

Zhu Y. et al., *Atmospheric Environment* **36**(27), 4323–4335 (2002).

Methodology

To study the morphology of atmospheric aerosol, a contact free technique where the natural environment of the aerosol could be created was used. Use of non-invasive techniques is paramount in the study of atmospheric aerosols owing to the need for the aerosol to resemble its atmospheric state to enable accurate understanding of atmospheric aerosols. Optical trapping is a non-invasive technique e.g. McGloin (2006) that allows individual aerosol particles to be levitated and manipulated in a gaseous environment.

In addition, x-ray and neutron scattering techniques were applied. X-ray and neutron scattering techniques are surface analysis experimental techniques that provide an excellent method to study layered media, surfaces and buried interfaces. The scattering techniques were applied to study oxidation of thin films composed of atmospheric aerosol at the air-water interface or proxy atmospheric aerosol thin films at the silica-water interface. X-ray scattering techniques are sensitive to electron density, whilst neutron scattering techniques are sensitive to the isotopic nature of nuclei. Therefore, application of neutron and x-ray techniques to similar interfaces provided a complementary method to probe the structure and reaction kinetics of a thin film before and during the oxidative process.

The section describes the background and theory required to understand the techniques and data analysis methods applied in the following papers.

2.1. Optical trapping

2.1.1. Optical trapping introduction

Optical trapping occurs when light exerts a force on microscopic aerosols. To understand the phenomena, light needs to be considered as photons that possess momentum. When an aerosol passes into the beam of light, the light will scatter from the aerosol: the momentum of the light has changed, and consequently a force is associated with the change in light momentum (as according to Newton's second law).

Methodology

Lebedev (1901) first demonstrated the ability of light to exert a force by using a focused arc lamp in 1901. However, this particular area of science did not see a resurgence until 1970 when Ashkin (1970) demonstrated the first use of light to manipulate aerosols. Ashkin dominated optical manipulation discoveries over the next few decades. From initially demonstrating the ability of light to guide aerosols e.g. Ashkin (1970), Ashkin and colleagues proved the ability of light to levitate solid aerosols in a radiation-pressure gravity trap and optically trap airborne droplets e.g. Ashkin and Dziedzic (1971) and Ashkin and Dziedzic (1975). Finally, Ashkin and Dziedzic proved the ability of light to trap not only large Mie aerosols of 10 μm diameter, but also small Rayleigh aerosols in a single-beam radiation pressure trap e.g. Ashkin et al. (1986).

Current optical traps use lasers; tightly focused, high intensity lasers allow the manipulation of small particles. Over the past forty years, the ability to measure position and forces to high precision through application of optical trapping techniques has predominantly been used in biology, but also in colloid interaction studies and hydrodynamics. Examples of key studies that have used optical trapping techniques includes the work conducted by Chu (1997) on the cooling and trapping of neutral atoms: the work conducted by Chu earned him the 1997 Nobel prize in Physics. Additionally, work conducted by MacDonald et al. (2003) applied optical trapping techniques in the field of cell sorting.

Depending on the size of aerosol trapped, the process involved with optical trapping can be considered differently. For example, when the aerosol is much larger than the trapping wavelength, Ray optics are considered, contrastingly when an aerosol is much smaller than the wavelength of light then the aerosol is considered a Rayleigh aerosol. In the thesis presented, a third process is considered: when a spherical aerosol is similar in size to the wavelength of light, then Mie scattering is valid e.g. Bowman and Padgett (2013). Hence, the wavelength of light has a significant impact on an optical traps performance.

Methodology

To understand the mechanics behind optical trapping, Snell's law must be considered. When a beam of light passes through a boundary separating two media with different indices of refraction then the beam will be diffracted according to Snell's law:

$$n_a \sin \theta_a = n_b \sin \theta_b, \quad (\text{Eq.2.1})$$

where n_a and n_b represent the refractive index of the two media and θ_a and θ_b represent the angle of the incidence and resulting beam. When a laser beam passes into an aerosol, it is refracted resulting in a transfer of momentum from the refracted photons to the aerosol. The momentum transfer results in a force. The force an aerosol feels can be split into two: the scattering force and the gradient force. The interplay between the two forces will result in aerosol levitation. The interplay between the two forces will change whether a single or dual counter-propagating optical trap is used.

Both single and dual beam optical traps experience a scattering force that acts in the direction of the laser. The scattering force is proportional to the light intensity; the scattering force has been described by Neuman and Block (2004) as a "photon hose that will push the aerosol in the direction of light propagation". However, in a single beam optical trap the gradient force dominates the trapping of the aerosol.

The gradient force acts in the direction perpendicular to the scattering force and draws the aerosol towards the focus of the laser beam. The gradient force can be separated into two forces: the transverse-gradient force and the axial-gradient force. The transverse-gradient force occurs if the focal point of a light beam is not central onto the aerosol, the light is refracted when it passes through the aerosol causing a change in momentum for the incident photons. A restoring force then acts upon the sphere. The axial-gradient force occurs upon the displacement of the aerosol from the focus of the light beam that results in the divergence of the emerging light. By changing the divergence of the light beam, the position of the aerosol in the axial direction can be altered, for example if the aerosol is placed in the light beam before the point of focus, it increases the divergence of the light

Methodology

and is pushed towards the focus point. Figure 2.1 depicts the two gradient forces an optical trap feels in a single beam optical trap.

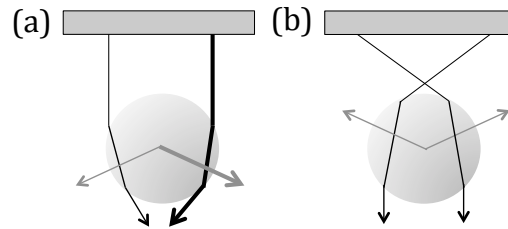


Figure 2.1. The two gradient forces that act on an aerosol in a single-beam gradient trap. The transverse-gradient force is depicted in (a), whilst (b) depicts the axial gradient force. Diagram is adapted from Neuman and Block (2004).

Interestingly, for stable single-beam optical trapping the gradient force must exceed the scattering force, achieved by focussing the incident laser light and slightly overfilling the back aperture of a high numerical aperture microscope objective lens. If the scattering force exceeds the gradient force then the particle will be pushed out of the focal point.

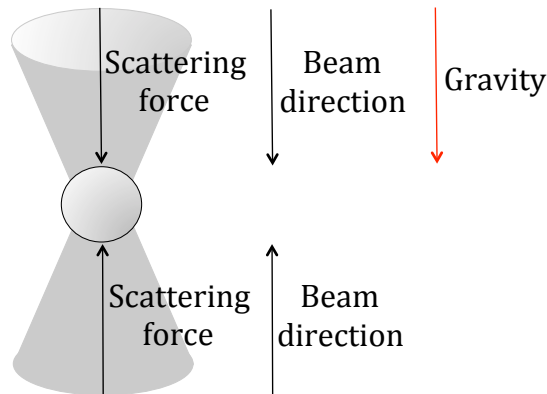


Figure 2.2. The scattering forces that an aerosol in a counter-propagating trap experiences.

A counter-propagating optical trap also experiences the scattering and gradient force. The optical trap had two beams that focus just before the aerosol so that the aerosol can be positioned between the foci of the two beams, resulting in the aerosol being pushed back towards the focus of the one laser beam as it approaches the focus of the other laser. The scattering force for the two laser beams will cancel

Methodology

in the centre. Figure 2.2. depicts the scattering force an aerosol will feel in a counter-propagating trap.

The aerosol is confined in the transverse plane predominantly by the transverse gradient force; the counter-propagating force has essentially zero axial-gradient force. A counter-propagating optical trap was used for all optical trapping experiments conducted in the thesis. The optical trap allowed liquid or solid aerosols to be trapped in air easily.

2.1.2. Optical trapping procedure

The optic setup used in the presented thesis used a 1064 nm, continuous wave Nd:YAG laser beam (Ventus, Laser Quantum) e.g. Jones et al. (2013). The laser beam passed into a 50:50 beamsplitter that split the laser into two equal beams. Each beam passed through an array of beam expansion optics before entering two vertically opposing microscope objective lenses (Mitutoyo NIR $\times 50$ NA 0.42) that controlled the focus of the laser beam. Use of beam expansion optics was essential to ensure the beam was the correct size for the numerical aperture of the microscope objective. The optic setup was arranged to allow full control of the bottom laser pathway in the x, y and z dimensions e.g. Fällman and Axner (1997). The position of the upper pathway laser beam in the x, y and z positions could be controlled to sub-micron accuracy by a piezo-stage (Physik-Instrumente). Precise control of the separation is critical for the configuration of the optical trap e.g. Rkiouak et al. (2014). Vibration of the optical setup was minimised by the use of anti-vibration tables. Figure 2.3 depicts a simplified schematic of the optical trapping setup.

All aerosols were optically levitated within an aluminium cell. The purpose of trapping within the cell was two-fold: (1) the cell created minimised turbulence and (2) the environment of the trap could be controlled in terms of relative humidity and gas-flow. The cell had two quarter-inch inlets and one quarter-inch outlet. The inlets were used for aerosol and gas entry, and could be closed if required. MassView mass flow metres controlled gas entry. The outlet behaved as

Methodology

an exhaust. Two borosilicate windows were positioned on the top and bottom of the cell to allow the lasers to enter the cell unattenuated.

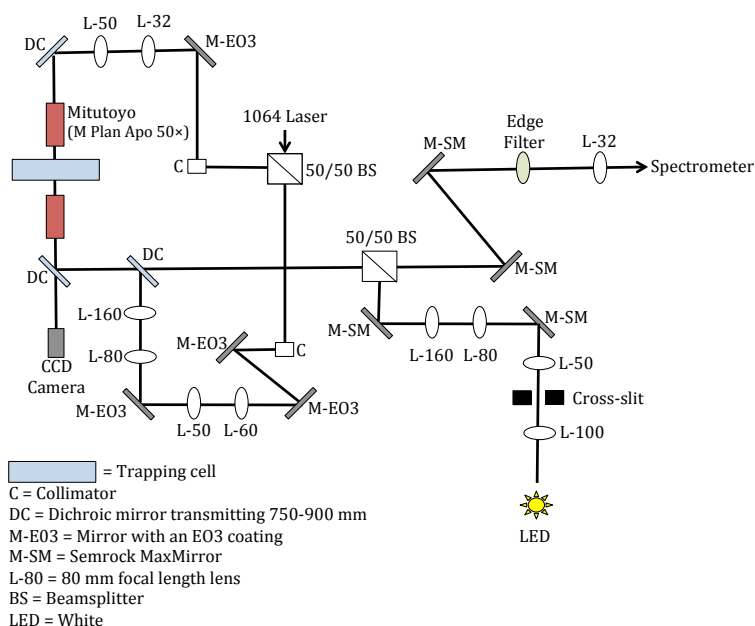


Figure 2.3. A simplified schematic of the optical trapping setup. A white LED is included in the diagram, the white LED was used to analyse the optically trapped aerosol, as described in section 2.1.3.

Brightfield illumination is a common and simple method applied in the field of microscopy, allowing a sample to be illuminated and then viewed. The sample is often viewed dark, surrounded by a bright viewing field. Brightfield illumination was configured along the same axis as the lower laser pathway, allowing an image of the trapped aerosol to be obtained and an estimate of the aerosol size, to the nearest $0.5 \mu\text{m}$ to be calculated.

2.1.3. Mie spectroscopy

Optical trapping has been applied to a range of research fields, and consequently a large number of analytical techniques have developed in the field. A prevalent technique is Raman spectroscopy because of the relative ease in which a Raman laser can be focused onto the trapped particle, for example Hunt et al. (2015) applied Raman spectroscopy to study the oxidation of aqueous nitrite anions, Tang et al. (2014) studied the interaction between SiO_2 and N_2O_2 aerosols with Raman

Methodology

spectroscopy and Mitchem et al. (2006) studied the growth and evaporation of a water droplet by applying Raman spectroscopy. Other analytical techniques that have been coupled with optical trapping include fluorescent imaging microscopy e.g. Athanasiadis et al. (2016) and x-ray elemental imaging e.g. Vergucht et al. (2015).

Mie spectroscopy has frequently been coupled with optical trapping techniques, e.g. Jauffred et al. (2015) studied the absorption and scattering cross sections of gold nanoparticles, Fontes et al. (2005) performed force spectroscopy upon single isolated particles whilst Moore et al. (2013) studied ionic liquid droplets. In the study presented, Mie spectroscopy has been coupled with optical trapping to allow the wavelength dependent refractive index and radius of an optically trapped aerosol to be determined and core-shell aerosol morphology to be studied.

2.1.3.1. Theory of Mie spectroscopy

Gustav Mie pioneered the field of Mie spectroscopy by solving Maxwell's equations for the electromagnetic scattering from a homogenous sphere by expressing the electric field inside and outside a sphere as a vector spherical harmonic expansion e.g. Mie (1908). Mie theory has since been expanded to involve calculations based on interstellar dust, near-field optics, atmospheric science, medical optics and optical particle characterisation e.g. Hergert and Wriedt (2012).

Mie theory involves the application of Maxwell's equations to describe the scattering and absorption of an electromagnetic plane wave by a homogeneous sphere. Mie scattering and computer algorithms have evolved rapidly in recent years, resulting in scattering computations for spheres of similar size to the incident wavelength being performed easily. To begin deriving the Mie formulas, the incident plane wave has to be described as a series of spherical waves. The scattered field can be described by the following spherical waves:

$$E_{s\theta} = \frac{e^{ikr}}{-ikr} \cos \varphi \cdot S_2(\cos \theta), \quad (\text{Eq.2.2})$$

$$E_{s\varphi} = \frac{e^{ikr}}{-ikr} \sin \varphi \cdot S_1(\cos \theta), \quad (\text{Eq.2.3})$$

with the scattering amplitudes S_1 and S_2 :

Methodology

$$S_1(\cos \theta) = \sum_{n=1}^{\infty} \frac{2n+1}{n(n+1)} (A_n \pi_n + B_n \tau_n), \quad (\text{Eq.2.4})$$

$$S_2(\cos \theta) = \sum_{n=1}^{\infty} \frac{2n+1}{n(n+1)} (A_n \tau_n + B_n \pi_n), \quad (\text{Eq.2.5})$$

where φ is the angle between the incident electric field, r is distance in spherical coordinates, k is the frequency of the incident field and the scattering plane, and π_n and τ_n describe the angular scattering patterns of the spherical harmonics used to describe S_1 and S_2 . A_n and B_n are the Mie coefficients used to compute the amplitudes of the scattered field and are key parameters for Mie calculations. The parameters can be determined by imposing boundary conditions between the sphere and surrounding medium.

$$A_n = \frac{m\psi_n(mx)\psi'_n(x) - \psi_n(x)\psi'_n(mx)}{m\psi_n(mx)\chi'_n(x) - \chi_n(x)\psi'_n(mx)}, \quad (\text{Eq.2.6})$$

$$B_n = \frac{\psi_n(mx)\psi'_n(x) - m\psi_n(x)\psi'_n(mx)}{\psi_n(mx)\chi'_n(x) - m\chi_n(x)\psi'_n(mx)}, \quad (\text{Eq.2.7})$$

where x is the size parameter:

$$x = \frac{2\pi r}{\lambda}, \quad (\text{Eq.2.8})$$

where r is radius of the sphere, λ is wavelength, m is refractive index of the sphere relative to its surrounding medium and ψ_n and χ_n are Riccati-Bessel functions:

$$\psi_n(x) = x j_n(x), \quad (\text{Eq.2.9})$$

$$\chi_n(x) = x h_n^{(1)}(x), \quad (\text{Eq.2.10})$$

where $j_n(x)$ is a spherical Bessel function and $h_n^{(1)}(x)$ is a spherical Hankel function e.g. Bohren and Huffman (1983).

One solution to Maxwell's equations includes the calculation of the extinction (Q_{ext}) and scattering (Q_{sca}) efficiencies of a homogeneous sphere:

$$Q_{ext} = \frac{2}{x^2} \sum_{n=1}^{\infty} (2n+1) \mathcal{R}(A_n + B_n), \quad (\text{Eq.2.11})$$

$$Q_{sca} = \frac{2}{x^2} \sum_{n=1}^{\infty} (2n+1) (|A_n|^2 + |B_n|^2), \quad (\text{Eq.2.12})$$

where n denotes the term and \mathcal{R} indicates the real part of the refractive index. Finally, the backscattering efficiency, Q_b :

$$Q_b = \frac{1}{x^2} \sum_{n=1}^{\infty} (2n+1) (-1)^n (A_n + B_n)^2, \quad (\text{Eq.2.13})$$

Q_b can be plotted as a function of the size parameter. The plot will consist of a series of resonances that hereafter will be called Mie

Methodology

resonances in the thesis. Other names for the Mie resonances include whispering gallery modes or morphology dependent resonances e.g. David et al. (2016).

2.1.3.2. Collection of Mie spectra

The method of determining the Mie resonances in the thesis presented required the optically trapped aerosol to be illuminated with white light. Figure 2.3 shows a LED used as the white light source (Comar 01 LD 555, 6V), the white light is focused onto the optically trapped aerosol and the elastic, backscattered light collected using the microscope objective. The light was dispersed by a spectrometer (Acton SP2500i) onto a charge-coupled device detector (Princeton Instruments) that had a quantum efficiency of 92 to 95 percent. The resultant spectrum is a Mie spectrum plotted as a function of intensity versus wavelength. Figure 2.4 shows an example of a Mie spectrum.

The wavelength range that a Mie spectrum is plotted over depends on the optics used and the grating setting of the spectrometer. In the thesis, a 600 lines mm^{-1} groove grating was typically used which produced a Mie spectrum over the wavelength range 520 to 600 nm with a resolution of 0.06 nm per pixel. Other gratings (300, 600 and 1200 lines mm^{-1}) could be used if needed or a grating scanned to produce a Mie spectrum that covered a broader wavelength range (typically ~ 450 to 650) nm. The wavelength range was calibrated by using the spectral lines from an Argon gas lamp.

The resonances depicted in Figure 2.4 are called morphology-dependent resonances and are a manifestation of the scattering resonances formed when electromagnetic energy is temporarily trapped inside a spherical aerosol. The electromagnetic energy is trapped by almost total internal reflection as it propagates around the inside surface of the aerosol. A number of wavelengths can propagate around the inside surface of the aerosol at one time, resulting in the formation of a standing wave.

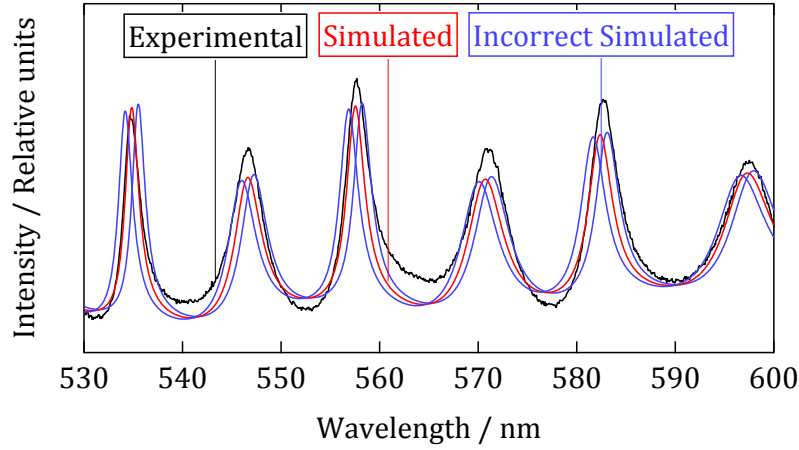


Figure 2.4. Experimental Mie spectrum, and the correct and incorrect Mie spectrum simulations, for a concentrated sulfuric acid aerosol droplet with a radius of 1.605 μm trapped in air.

The wavelength positions of the resonances depicted in Figure 2.4 are typically dependent on size and refractive index of the trapped aerosol. A large optically trapped aerosol will have a greater number of resonances with fine structure than a smaller aerosol, owing to the difference in the number of wavelengths than can form a standing wave around the circumference of the aerosol.

2.1.3.3. Analysis of the Mie spectra

To determine the refractive index and radius of the optically trapped aerosol, the experimentally obtained Mie spectrum was compared to a calculated Mie spectrum. To ensure the simulated Mie spectrum accurately represented the experimental data, a minimum of four resonances were required. The Mie spectrum could be accurately calculated through application of Bohren and Huffman formalism in conjunction with the Cauchy equation:

$$n = A + \frac{B}{\lambda^2} + \frac{C}{\lambda^4}, \quad (\text{Eq.2.14})$$

where n is the real refractive index, A , B and C are the Cauchy empirical coefficients to be determined and λ is wavelength e.g. Bohren and Huffman (1983). The empirical coefficients (A , B and C) were initially estimated from literature, and then adjusted along with the aerosol radius until a fit between the experimental and calculated spectra,

Methodology

which concentrated on peak position, shape and intensity, was obtained.

For Mie spectra containing a significant number of resonances, the empirical coefficients (A , B and C) and aerosol radius were adjusted until a global minimum was determined with the least squares fitting residual between experimental and theoretical peak positions e.g. Jones (2013). Owing to the position of the resonances being extremely important in the fitting procedure, a greater number of resonances would increase the accuracy of the fitting. A Mie spectrum consisting of six resonances had an uncertainty of ± 0.0026 in refractive index and ± 2 nm in radius.

In the thesis presented, one paper involves the optical trapping of a core-shell aerosol. The characterisation of a homogeneous aerosol in terms of refractive index and radius can be executed in the procedure outlined above, however for core-shell aerosol A and B have a different functional form than A_n and B_n for a homogeneous aerosol (see Equations 4 and 5). The scattering coefficients for a core-shell aerosol are displayed in Equations 2.15 and 2.16:

$$A_n = \frac{m_2 \psi_n(m_2 x) \psi'_n(m_1 x) - m_1 \psi'_n(m_2 x) \psi_n(m_1 x)}{m_2 \chi_n(m_2 x) \psi'_n(m_1 x) - m_1 \chi'_n(m_2 x) \psi_n(m_1 x)}, \quad (\text{Eq.2.15})$$

$$B_n = \frac{m_2 \psi_n(m_1 x) \psi'_n(m_2 x) - m_1 \psi_n(m_2 x) \psi'_n(m_1 x)}{m_2 \chi'_n(m_2 x) \psi'_n(m_1 x) - m_1 \psi'_n(m_1 x) \chi_n(m_2 x)}, \quad (\text{Eq.2.16})$$

where two refractive indices are used to describe the refractive index of the core (m_1) and shell (m_2) relative to their surrounding medium instead of using only one refractive index e.g. Bohren and Huffman (1983).

To accurately simulate a core-shell aerosol Mie spectrum, a droplet consisting purely of the shell material was optically trapped and its refractive index as a function of wavelength determined by the method outlined above. Secondly, the core aerosol particle was optically trapped on its own and characterised in terms of wavelength dependent refractive index and radius. Finally, the core aerosol particle was coated in a film of the shell material and the Mie spectrum of the resultant aerosol collected. Application of core-shell Mie theory e.g. Aden and Kerker (1951) and Toon and Ackerman (1981) was applied

Methodology

to calculate the Mie spectra of the core aerosol with a shell of varying thickness. The refractive indices of the core and shell material were fixed, and the film thickness adjusted until a good fit between the experimental core-shell aerosol and the calculated core-shell aerosol was determined.

2.1.4. Optical trapping experiments conducted

Optical trapping experiments were conducted at the Central Laser Facility at Rutherford Appleton Laboratories in Oxfordshire, UK. Three of the six papers outlined in the thesis applied optical trapping techniques and a brief description of each project is outlined here.

Paper 1 involved the development of a core-shell aerosol using the proxy atmospheric aerosol silica as the core and concentrated sulfuric acid as the shell forming material. Owing to the abundance of sulfuric acid in the stratospheric aerosol layer, sulfuric acid may condense onto aerosols e.g. Rkiouak et al. (2014) and Pope et al. (2012). To fully understand the outcome of the condensation, reproducing the system in the laboratory is essential. In the study described, silica beads from an aqueous solution were atomised to become airborne and were passed into the cell containing the counter-propagating laser beams. The silica particle was trapped and illuminated with the white LED; the backscattered white light was collected. The wavelength-dependent refractive index and radius of the silica particle was then calculated. Sulfuric acid droplets then entered the cell and collided with the silica aerosol to form a continuous film of acid around the aerosol. Again, the resultant aerosol was illuminated with white light and the backscattered light collected. The collected Mie spectra could then be compared to simulated Mie spectra of the same system to determine film thickness.

Papers 2 and 3 explore (1) the refractive index change of a reacting system in Paper 2 and (2) the refractive index of aerosol extracts sourced from the atmosphere in Paper 3. The atmosphere is a highly oxidising environment, and consequently aerosols change composition once in the atmosphere. Knowledge of the change in

Methodology

refractive index, and hence the change in an aerosols optical properties, would aid accurate understanding of global temperatures. Paper 2 followed the change in refractive index when the proxy atmospheric aerosol squalene was optically trapped and exposed to ozone. Continuous collection of Mie spectra of the optically trapped squalene droplet allowed the changes in the droplets refractive index to be followed.

The work conducted in Paper 3 involved the optical trapping of atmospheric aerosol extracts sourced from urban, remote and wood burning sources. Owing to the lack of sample, the optical trapping of aerosol was limited to a few aerosol droplets per sample. A large proportion of aerosol research involves the use of proxies, and therefore the work conducted in Paper 3 is extremely important as it provides refractive index values for atmospheric aerosol extracts.

2.1.5. Limitations of optical trapping

Optical trapping is an excellent technique for studying atmospheric aerosol as it provides a non-contact method to probe the physical and chemical properties of an aerosol levitated in a gaseous environment. A non-contact method for studying atmospheric aerosols provides a means to represent the natural environment for atmospheric aerosols.

One limitation of optical trapping is the possibility of the aerosol absorbing the laser beam, resulting in the aerosol temperature increasing, thereby becoming unstable in the trap. A temperature increase may also cause the chemical and physical properties of the aerosol to alter, and therefore the determined refractive index may not reflect the true aerosol. Hunt et al. (2013) investigated the heating power of a 514.5 nm Raman laser beam: laser powers in excess of 16 mW resulted in a concentrated droplet of sulfuric acid to increase in temperature by 5 to 10 °C, however maintaining a low laser power prevented significant laser heating effects. In the three optical trapping experiments presented, the laser powers were 10 mW for the lower laser beam pathway and 15 mW for the upper laser beam pathway. The

Methodology

1064 nm laser used is in the infrared region of the electromagnetic spectrum thereby minimising absorption.

In addition, use of lasers with a wavelength in the infrared region ensured that unwanted photochemical reactions did not occur. David et al. (2016) proved that UV photochemistry could be initiated by broadband radiation, further demonstrating the requirement of monochromatic lasers operating in the infrared region for successful optical trapping experiments.

Application of Mie theory added additional limitations. Mie theory can be easily solved for spherical aerosols, consequently only liquid or proxy-solid aerosols could be optically trapped. However, not all atmospheric aerosol is spherical as demonstrated by Takahama et al. (2010) who analysed 636 aerosols collected from over the western hemisphere. Takahama et al. (2010) classified the physical morphology of the aerosols into four categories: spherical, liquid, agglomeration (aggregation of smaller aerosols) and inclusion (aerosol with regional maxima): two of these categories are not spherical. To accurately replicate atmospheric aerosols, an experiment ought to include spherical, non-spherical and core-shell aerosols including alternative aerosol ensemble morphologies such as partial covering of the core aerosol. However, Mie theory for non-spherical aerosols is complex e.g. Liu et al. (2008) and therefore has not been attempted in the work presented here.

Paper 3 involved the optical trapping of atmospheric aerosol extracts. The wood burning atmospheric aerosol extracts contained an absorbing parameter and an absorption Ångstrom exponent and imaginary refractive index included in the Mie theory to accommodate the aerosols absorbance.

Additionally, the optical setup was sensitive to the size of aerosol trapped. An aerosol had to have a significant size parameter before a Mie spectrum of reasonable intensity was captured. The requirement was particularly important in Paper 3, the majority of aerosol that entered the sample cell was smaller than 1 μm in radius, and therefore once an aerosol was trapped further collisions with material in the cell

was required to progressively develop a larger optically trapped aerosol.

2.2. Neutron and x-ray scattering

Neutron and x-ray scattering experiments were conducted to study very thin films of atmospheric aerosol at the air-water or silica-water interface. Neutron and x-ray reflectivity techniques are two well-established methods often applied to study surfaces, interfaces and buried interfaces e.g. Lovell and Richardson (1999). A significant advantage of applying neutron or x-ray reflectivity to study an interface is the fact that neutrons and x-rays can probe the surface of a material with atomic resolution in space and time with a depth controlled sensitivity (approximately 0.2 nm for x-ray studies and slightly lower resolution for neutron based studies because of lower neutron flux). e.g. Dietrich and Haase (1995).

In the study presented, neutron and x-ray reflectivity were used as complimentary techniques to understand the thickness and structure of thin films extracted from atmospheric aerosol at the air-water interface, as well as following the oxidation of the films upon exposure to gas-phase oxidants. Additionally, neutron reflectivity was successfully employed to follow the oxidation of a proxy atmospheric aerosol film at the silica-water interface.

2.2.1. Neutron and x-ray scattering introduction

Fermi and Marshall (1947) and Fermi and Zinn (1946) published the first few reports on the total reflection of neutrons, and since then the phenomena has been applied to a range of scenarios such as the determination of scattering lengths and development of neutron scattering instruments e.g. Hayter et al. (1978) and Lynn et al. (1976).

In the study presented, neutron and x-ray reflection experiments were conducted on thin films at the air-water or silica-water interface using the instruments INTER and polREF at ISIS Neutron and Muon Source and I07 at Diamond Light Source. Figures 2.5 and 2.6 depict the instruments used.

Methodology

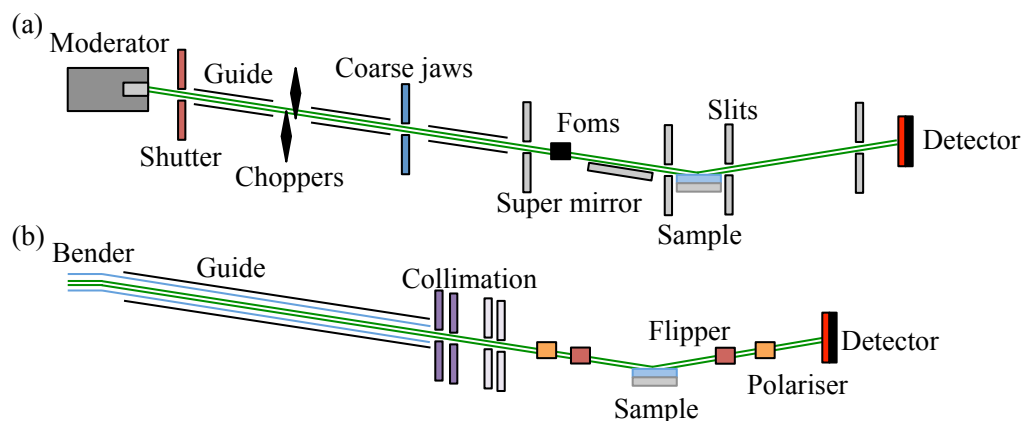


Figure 2.5. Depiction of the instruments used at ISIS: (a) INTER adapted from work conducted by Webster et al. (2006) and (b) polREF adapted from a document compiled by Goff et al.

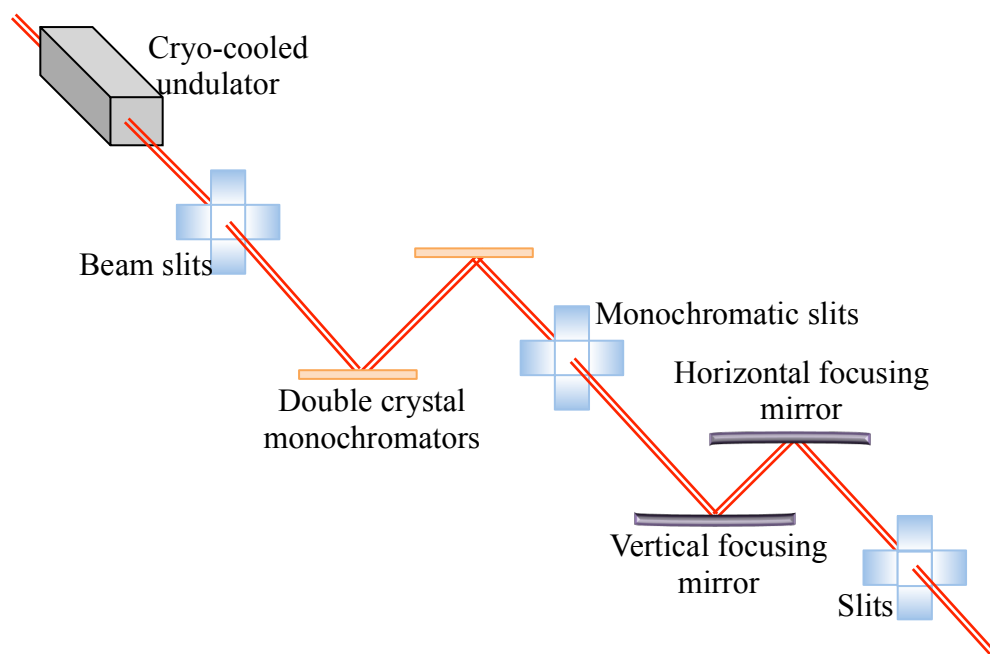


Figure 2.6. Depiction of the optic layout on the reflectometer, I07, used at Diamond Light Source. Schematic based on a diagram displayed on the Diamond Light Source website.

Both neutron and x-ray scattering techniques applied studied the change of the interface normal to the interface at small length scales. Incident neutron or x-ray beams grazed the surface and were specularly reflected from the film onto a detector. The specular reflection of neutrons or x-rays gave information on the neutron or x-ray refractive index profile of the material under study; the neutron or x-ray refractive index is related to the scattering length density of the

Methodology

sample, and thus from applying reflection studies to a material the composition and structure of the material was determined normal to the surface e.g. Penfold and Thomas (1990).

Neutron or x-ray specular reflection was recorded as a function of neutron or x-ray momentum to produce a reflectivity profile. Reflectivity, R , is defined as:

$$R = \frac{16\pi^2}{Q^4} (2\rho)^2 \sin\left(\frac{Q\delta}{2}\right)^2, \quad (\text{Eq.2.17})$$

where δ is film thickness, ρ is scattering length density and Q is momentum:

$$Q = \frac{4\pi \sin \theta}{\lambda}, \quad (\text{Eq.2.18})$$

where θ is the incident angle of the neutron or x-ray beam to the interface and λ is wavelength of the neutron or x-ray e.g. Lu et al.(2000). The distance from origin to detection and the time taken for the neutrons or x-rays to travel the distance was known, and therefore reflectivity was calculated in terms of momentum to produce a profile of reflectivity versus momentum transfer, which will be called a reflection profile henceforth in the thesis presented.

The scattering length density from Equation 2.17 can be defined as:

$$\rho = \sum n_i b_i, \quad (\text{Eq.2.19})$$

where n_i is the number density of the i^{th} element and b_i is the scattering length of the i^{th} element e.g. Lu et al. (2000). The scattering length is correlated to the interaction of either the neutrons with the nucleus of the material under study or x-rays with the electrons of the material under study. Neutrons interact with the nucleus of the material under study and are thus a complimentary technique to use consecutively with x-rays. Neutrons interact with the nucleus of different elements differently, for example the neutron scattering length for hydrogen (^1H) is $-3.74 \times 10^{-6} \text{ \AA}^2$, whilst for deuterium (^2H) the neutron scattering length is $6.6710^{-6} \text{ \AA}^2$. This property was used to mix aqueous subphases where the scattering length density matched the scattering length density of the other infinite thickness phase (either air or quartz). The technique is called contrast matching and allows chosen

Methodology

materials to be eliminated from the scattering profile. Contrast matching cannot be used in x-ray experiments.

Data was collected over more than one incident angle to determine neutron or x-ray reflection data. For example, the angles used in the experiments conducted on ISIS were 0.8° and 2.3° for INTER experiments and 0.6°, 1.2° and 2.4° for polREF experiments, data was collected at each angle for 15 and 30 minutes for the experiments conducted on INTER, whilst experiments conducted on polREF required 15, 60 and 60 minutes at each angle for data collection. Low angles required the least collection time to collect the data with reasonable resolution and consequently only the lowest angle was used to collect data when the film was exposed to oxidants. Owing to the film quickly changing during exposure to oxidants, it was important to collect a sufficient number of reflection profiles during the oxidation so as to enable accurate representation of the film change. The incident angles used in the experiments conducted on INTER and polREF gave a momentum transfer range of 0 to 0.35 Å⁻¹ and 0-0.1 Å⁻¹ respectively, whilst on I07 an x-ray momentum transfer range of 0 to 0.7 Å⁻¹ was achieved.

2.2.2. Neutron and x-ray scattering data analysis

The collected neutron or x-ray reflectivity profiles could be simulated by Abelès formalism e.g. Abelès (1950) where film thickness, δ , and scattering length density, ρ , were used in the following relationship :

$$\Gamma b = \delta \rho, \quad (\text{Eq.2.20})$$

where Γ is the surface coverage of a film composed entirely of molecules with the scattering length $\delta \rho$ e.g. Penfold (1997). The Abelès formalism was applied in the computer software Motofit e.g. Nelson (2006). The software created a model comprising of scattering length density, layer thickness and film roughness that could be adjusted to simulate the reflection profile.

The scattering length density and film thickness were initially estimated and then refined until a fit between the experimental and simulated profiles was determined by eye. Film roughness was typically

Methodology

held at 3 Å throughout the fitting process. Application of a χ^2 test on all fits ensured the final value of scattering length density and film thickness best described the experimental data. Figure 2.7 depicts the high quality of fit between simulated and experimental reflection profiles.

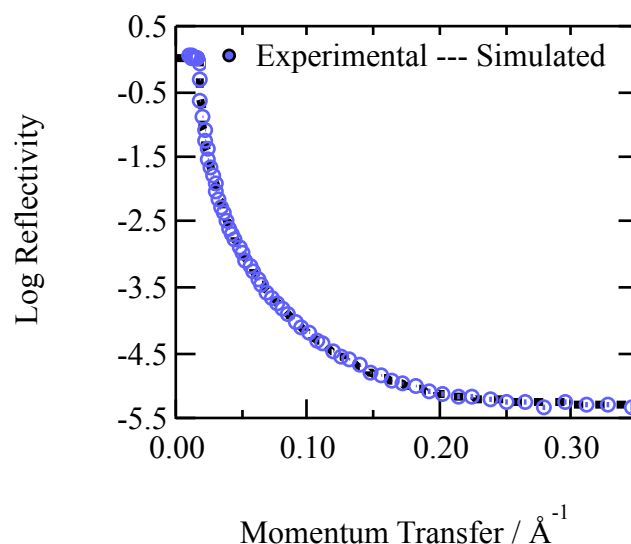


Figure 2.7. An experimental and simulated neutron reflection profile for a bare deuterium oxide air-water interface.

In addition, through applying Abelès formalism the number of layers in the system under study could be controlled. Figure 2.8 depicts the layers used in the two neutron studies and the neutron scattering length density and film thickness that best described the layer. Four layers best described the film used on I07 at Diamond Light Source, but as shown in Figure 2.8, six layers best described the film studied on polREF and three layers best described the film used on INTER.

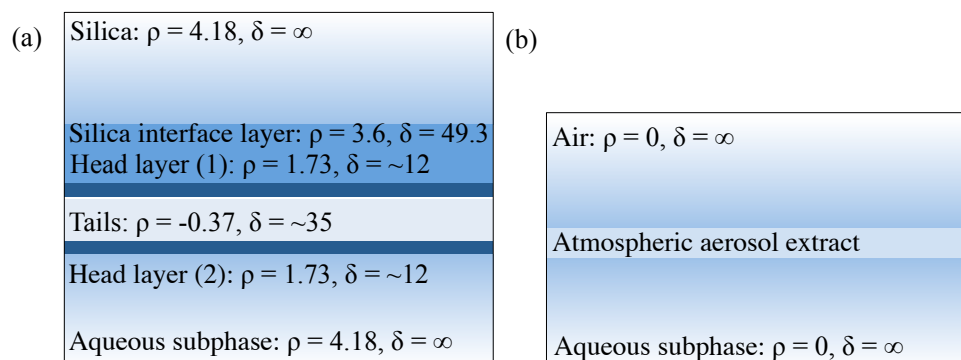


Figure 2.8. The layers simulated to reproduce the reflectivity profiles for experiments conducted on (a) polREF and (b) INTER.

Methodology

The composition of the atmospheric aerosol extracts before and during exposure to oxidants was not known, and hence the scattering length could not be determined. Therefore, $\delta\rho$ was instead calculated as the scattering length per unit area: $\left(\frac{\rho_t\delta_t}{\rho_{t=0}\delta_{t=0}}\right)$. For films exposed to atmospheric oxidant, $\frac{\rho_t\delta_t}{\rho_{t=0}\delta_{t=0}}$ was followed as a function of time. For systems where the number of layers required to describe the film was greater than one, the $\frac{\rho_t\delta_t}{\rho_{t=0}\delta_{t=0}}$ per layer was followed and then either combined as a weighted sum (e.g. the experiment conducted on Diamond Light Source) or left as $\frac{\rho_t\delta_t}{\rho_{t=0}\delta_{t=0}}$ (e.g. the study conducted on polREF).

2.2.3. Neutron and x-ray scattering experiments conducted

The objective behind the three studies conducted was to characterise thin films in terms of scattering length density and film thickness as well as understand the oxidative behaviour of the thin films in relation to atmospheric conditions. Two of the studies used material extracted from atmospheric aerosols as thin films at the air-water interface. The complimentary use of neutrons and x-rays to study similar interfaces was exploited.

Paper 4 presents the work conducted at INTER. Thin films extracted from urban, remote and wood smoke aerosol were successfully formed at the air-water interface and characterised in terms of neutron scattering length density and film thickness. Film thickness was found not to exceed 11 Å, whilst wood smoke aerosol films were much thicker at approximately 18.6 Å. The films were exposed to gas-phase OH and the decay of the film was discovered to be exponential in nature with a bimolecular rate constant on the magnitude of 1×10^{-10} molecule $\text{cm}^{-3}\text{s}^{-1}$ and a film lifetime on the scale of minutes.

Similarly, paper 5 presents work conducted on I07, where extracts sourced from urban and remote samples formed films at the air-water interface. The x-ray scattering length density and film thickness were determined. Owing to x-ray reflection being sensitive to

Methodology

electron density of the sample, the film was determined to consist of a two-layer system. Total film thickness was calculated to be 18 Å for urban aerosol extracts and 9 Å for remote aerosol extracts. Again, the films were exposed to OH and again the decay of the film was discovered to be exponential with a bimolecular rate constant on the magnitude of 1×10^{-10} molecule $\text{cm}^{-3} \text{s}^{-1}$ and film lifetime on the scale of minutes. The purpose of Papers 4 and 5 was to provide further data on thin films formed from atmospheric aerosol extracts, currently the number of studies is limited e.g. Zhou et al. (2014) and Jones et al. (2017).

Lastly, the sixth paper presented in the thesis studies the oxidation of a proxy atmospheric aerosol film at the silica-water interface. The study replicated film formation at an aqueous mineral dust interface by using silica (quartz) and water. The proxy aerosol used was deuterated 1,2-dipalmitoyl-sn-glycero-3-phosphocholine (DPPC) and the lipid formed bilayers upon the silica. The film was oxidised and the kinetics of the decay studied. The decay followed step-wise degradation decay with a bimolecular rate constant on the magnitude of 10^{-12} to 10^{-13} molecule $\text{cm}^{-3} \text{s}^{-1}$, with a film lifetime of approximately 6 days.

2.2.4. Comparison between neutron and x-ray scattering experiments

Neutron and x-ray reflectivity techniques were applied to study atmospheric aerosol thin films at the air-water interface; additionally neutron reflectivity was employed to study a film of proxy atmospheric aerosol at the silica-water interface.

A significant difference between neutron and x-ray reflection experiments is the intensity of the beam. X-ray beams are considerably more intense owing to a weaker background resulting from greater x-ray absorption by the material at the interface e.g. Lu et al. (2000). Neutron reflectivity experiments will produce greater background signal from incoherent scattering. A positive result from using a more intense x-ray beam is that a wider momentum range can be studied:

Methodology

typical x-ray studies cover the momentum range of 0 to 0.7 \AA^{-1} , whilst neutron experiments commonly only reach 0 to 0.35 \AA^{-1} .

A second positive impact from using more intense x-ray beams in comparison to neutron beams is that x-rays were more sensitive to electron rich material under study. The experiments outlined in Papers 4 and 6 demonstrate the differences that can be observed between a reflection profile collected by applying neutron or x-ray reflectivity: the work that uses x-rays depicts fringes in the reflection profile, whilst the neutron reflection profile is comparatively weak. The fringes visible from the x-ray profile depicted a multilayer system; such information was not available from applying neutron reflection techniques. Figure 2.9 depicts the difference in reflection profile between neutron and x-ray techniques.

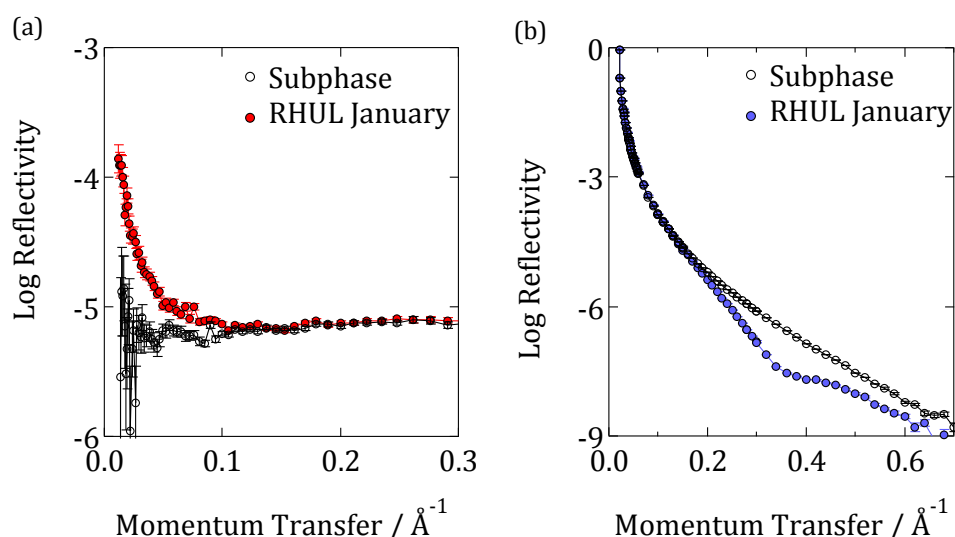


Figure 2.9. Comparison in (a) neutron and (b) x-ray reflectivity profiles for an urban atmospheric aerosol extract sourced during January 2016.

Additionally, the difference between neutron scattering length densities of hydrogen and deuterium can be applied to molecules under study. Hydrogen atoms in a molecule can be swapped with deuterium atoms to increase the neutron reflection signal of the molecule. The hydrogen atoms in the atmospheric aerosol extracts could not be substituted for deuterium atoms owing to the sample composition being unknown, however such a procedure was conducted in Paper 6. A deuterated phospholipid was used to ensure a strong signal was

Methodology

observed for the phospholipid dipalmitoylphosphatidylcholine (DPPC). Partial deuteration of a phospholipid would allow the head or tail region to be monitored individually. For example, Dabkowska et al. (2013) used deuterated distearoylphosphatidylcholine (DSPC) molecules to follow the interaction of calf thymus DNA with monolayers of the phospholipid. Use of deuterated DSPC allowed the head and tail regions to be studied individually.

The difference in neutron scattering length densities between hydrogen and deuterium can be further exploited to contrast match out certain materials of the system under study and thus eliminate their contribution to the neutron scatter. Contrast matching was used in both the neutron experiments to eliminate the scatter from the solvent used (the solvent was either contrast matched to air or quartz). Thus, the reflection profiles collected were of the film under study only.

2.2.5. Limitations of neutron and x-ray scattering

Two experiments required a thin film to be developed at the air-water interface of a Langmuir trough. The required geometry of the trough in relation to the direction of neutron or x-ray beam, prevented barriers or a tensiometer from being used during the oxidation of the thin film. The barriers and tensiometer would of provided an additional technique to monitor change in the film.

The experiments that used a Langmuir trough involved the formation of a thin film of material extracted from atmospheric aerosol. The composition of the thin film was not known, and hence for the neutron experiments the film could not be deuterated to enhance reflectivity signal. Consequently the signal was weak, which may have resulted in a loss in accuracy when determining film thickness and neutron scattering length density. Paradoxically, the sensitivity of x-rays resulted in fringes being recognised in the reflection signal, indicating a multilayer system.

The neutron reflectivity experiment conducted on polREF used the proxy atmospheric aerosol dipalmitoylphosphatidylcholine (DPPC) that could be partially or fully deuterated to provide a strong neutron

Methodology

reflection profile. Analysis of the film in Motofit demonstrated that the film could be analysed in terms of head or tail regions of the phospholipid. However, the head or tail region could not be followed individually from contrast matching the other region to the subphase. The resulting oxidation profiles were hence simulated by trial and error.

2.3. Sample collection

Atmospheric aerosol extracts sourced from urban, remote and wood burning aerosol were studied in Papers 3, 4 and 5 and Antarctic seawater extracts in Paper 5. The study of aerosol sourced directly from the atmosphere is paramount for accurate understanding of the physical and chemical properties of atmospheric aerosol.

The urban and remote atmospheric aerosol extracts were collected on a pre-combusted 47 mm quartz filter (SKC Ltd.) that was encased within a PFA Savillex commercial filter, whilst wood smoke samples were collected on equivalent filters encased in aluminium and steel filter holders. Metal filter holders were required for the collection of wood smoke aerosol as the aerosol was collected directly from the smoke plume and was hence very hot. Air was pulled through clean stainless steel pipelines into the filter holders at a flow of 30 L min⁻¹ at local ambient temperature and pressure. All instrumentation was cleaned with ultrapure water and chloroform (Sigma-Aldrich, 0.5 to 1 % ethanol as stabiliser) and were assembled and disassembled within a clean glove bag to minimise contamination risks. Chloroform was the solvent of choice owing to very few bacteria being able to survive within the solvent, minimising contamination.

Urban aerosol was collected from the campus of Royal Holloway, University of London. The aerosol collected from the campus represent urban aerosol owing to the proximity of central London, major motorways and Heathrow airport. The urban aerosol was collected in approximately monthly 30-day periods. For Paper 3, monthly samples were combined to allow for seasonal analysis.

Methodology

Remote aerosol was sourced from coastal Antarctica at the BAS Halley Clean Air Sector Laboratory during the 2015 and 2016 Antarctic summers. During each sample, aerosol was collected for approximately 60-day periods. Owing to the remoteness and lack of accessibility, sample collection time was twice as long as the time used to collect urban samples to ensure sufficient levels of sample was collected. As well as atmospheric aerosol, seawater samples from a depth of 10 m were collected during the Antarctic summer of 2015: Paper 4 analyses the seawater samples. The seawater sample was stored in a PTFE travel jar and frozen at -18 °C until use. Seawater samples have been studied previously e.g. Zhou et al. (2014).

The third aerosol sample was collected directly from the smoke plume of burning firewood. The smoke plume was produced from firewood that was burnt in a flaming fire contained within a domestic wood burner for six hours. Numerous studies have focused on the study of wood burning aerosol, for example Yamasoe et al. (2000) collected aerosol from smoke flumes from tropical fires and biomass burning fires in the Amazon basin and Chakrabarty et al. (2010) studied tar balls produced from the smouldering combustion of commonly occurring plant litter material.

For all atmospheric aerosol extracts, collection time varied from six hours to 60 days. An extract held on a filter paper in the atmosphere for any period of time would have been exposed to atmospheric oxidants and can be described as aged atmospheric extracts. Exposure to atmospheric oxidants may cause a reduction in unsaturated material, whereas extracts that were collected after six hours may not of aged so much and may consequently contain a higher content of unsaturated material. Unfortunately, owing to long timescales being required to collect sufficient amounts of material for the experiments conducted, shorter timescales would not of worked. Changing the filters on a daily basis may of allowed non-aged samples to be collected, however this would have required greater manpower and would have been impossible for the collection of remote aerosol extracts.

Methodology

For each aerosol extract collected, a corresponding filter blank was stored. The remote aerosol extracts travelled with an unused filter to create a travelling blank from which possible contamination from the journey could be identified. All aerosol extracts were stored at -18 °C until extraction. The aim of storing the extracts at -18 °C was to prevent the samples from changing (e.g. to prevent further oxidation reactions occurring) between extraction completion and use in an experiment.

Once the extracts were collected, they had to be subsequently removed from the filter. Each filter was cut in half. One half of the filter was stored at -18 °C for future reference, the other half was placed in a clean conical flask along with 10 ml of ultra pure water and 10 ml of chloroform. The conical flask and its contents was sonicated for 5 minutes, and then filtered to remove the filter paper. The filtrate was passed through a separating funnel and the organic layer kept. The chloroform from the filtrate was evaporated off under nitrogen. The resultant extract was an oily or waxy residue. 3 ml of chloroform was added to the extract, and the extract stored at -18 °C in amber vials. The purpose of using chloroform as the storage solvent was two-fold: (a) preventing the extracts from chemically ageing and (b) owing to chloroform being volatile, the solvent would readily evaporate to leave behind the extract ready for study. All glassware used in the extraction process was cleaned with ultra pure water and chloroform.

The Antarctic seawater extract was collected at a depth of 10 m, additional samples collected at the sea-surface microlayer were also collected but were unfortunately lost during the sample extraction process. The Antarctic seawater extract was extracted along similar lines to the atmospheric aerosol extracts. The water was filtered into a clean glass beaker and an equivalent amount of chloroform: passing the solution through a separating funnel separated off the organic layer. The chloroform was evaporated under nitrogen leaving the extract as a waxy residue at the bottom of the vial. 3 ml of chloroform was added to the extract, and the extract stored at -18 °C in amber vials.

Owing to limited sample, the same aerosol extracts were used for a number of experiments. Extracting the extracts from the vial in

Methodology

which they were stored by using a Hamilton syringe might be a cause of contamination, which might lead to the extract altering between time of extraction and experimental use; contamination was limited by thoroughly rinsing the syringe with chloroform between each use.

2.4 Formation of OH radicals

OH radicals were used in the two neutron reflectometry experiments as well as the x-ray reflectometry experiment. The OH radicals were created in either the gas-phase or aqueous-phase. The following section will outline the method of forming the OH radicals as well as the method applied to determine the concentration of the radicals formed.

2.4.1 Formation of gas-phase OH radicals

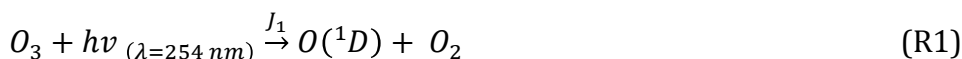
A gas-phase environment of OH radicals was formed through the photolysis of ozone. Hydrated oxygen was passed through an ozoniser at 1 L min^{-1} to form ozone; the ozoniser was arranged so as to keep the concentration of ozone low and therefore more consistent with atmospheric ozone levels. The gas was then hydrated by being bubbled through water; the concentration of water vapour was based on the vapour pressure of water (2.34 kPa at 20°C from Haynes, 2016). The gas then entered the Tedlar bag where it was exposed to UV lamps, with an output wavelength of 254 nm. Exposure of ozone to the UV lamps resulted in ozone photolysis. The UV lamps were suspended 9 cm above the reacting surface.

The concentration of the OH radicals was determined by conducting offline experiments. To estimate the concentration of ozone, the UV-VIS spectrum of ozone at varying concentrations was obtained in a 10 cm path length glass cell. The initial concentration of ozone was calculated to be 0.85 ppm. The photolysis rate of ozone, $J_1(O(^1D))$, was measured by a Metcon radiometer.

The rate constant value used for the photolysis of molecular oxygen was the value for ozone, scaled by the product of the absorption cross-sections and the quantum yields.

Methodology

To estimate the concentration of gas-phase OH radicals used in the experiment, kinetic modelling was based on a series of first-order differential equations using a Runge-Kutta algorithm. In the study presented, the basic HO_x and O_x reactions occurring in the photolysis of ozone in the presence of water vapour were based on work conducted by Atkinson et al. (2003). The modelling required 30 reaction steps to be modelled; however the key gas-phase reactions were:



A first-order wall loss with regard to OH radicals was added (R4) using the method outlined by Dilbeck and Finlayson-Pitts (2013). The wall loss was calculated to be 2 s⁻¹, assuming the reaction environment maintained a volume of 25 L and surface area of 0.612 m² (the measurements of the reaction chamber used in the neutron and x-ray reflectivity experiments). The reaction probability for OH radicals on the reaction chamber walls was assumed to be similar to halocarbon wax ($\gamma = 6 \times 10^4$) e.g. Bertram et al. (2001).

Overall, the concentration of OH radicals present in the Tedlar bag was estimated to be 7×10^6 molecule cm⁻³. A sensitivity analysis was conducted on the model used; the initial starting concentration or the rate constant for each reaction step was increased and decreased by a factor of 2 and the effect on the final OH radical concentration analysed. It was determined that the OH radical concentration was affected by the lamp intensity, initial ozone concentration and the water vapour concentration, each causing a relative percentage error of 0.5 percent, 2 percent and 1.7 percent respectively in the determined OH radical concentration.

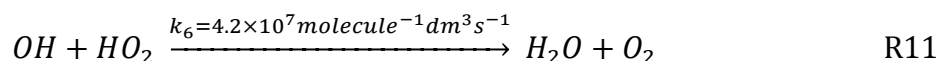
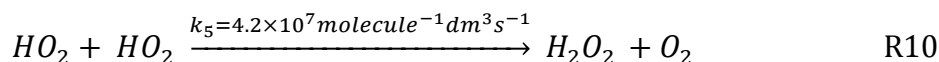
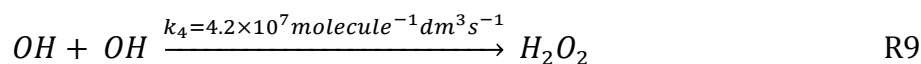
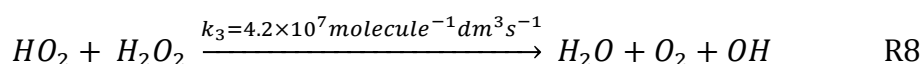
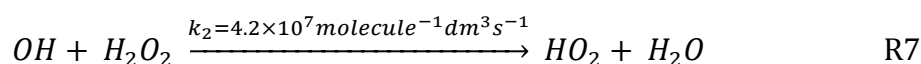
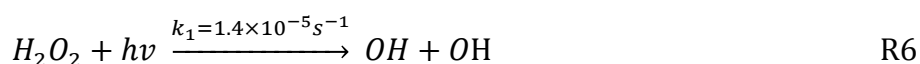
Once the OH radical concentration was known, the bimolecular

Methodology

rate constant for the oxidation reaction could be calculated, as well as the lifetime of the reaction starting material when exposed to an atmospheric level OH radical concentration.

2.4.2 Formation of aqueous-phase OH radicals

To create the hydrogen peroxide rich atmosphere, a solution comprising of a silica contrast matched solution formed from 69 percent D₂O and 31 percent H₂O volume/volume was used as the aqueous subphase with hydrogen peroxide present at 2.5 percent by volume. The subphase flowed at a rate of 1 L min⁻¹ through the experimental equipment. The hydrogen peroxide was subsequently photolysed by the presence of UV lamps to form OH radicals via the following Haber-Weiss chemistry:



Treating reactions R6 to R11 as a series of first-order differential equations and solving numerically with a Runge-Kutta method calculated the steady-state concentrations of the OH and HO₂ radicals.

The value of k_1 was dependent on the conditions of the reaction environment and was consequently determined by an offline experiment. The same apparatus setup as used on the beamline was created in the offline experiment. The offline experiment required four 0.003 mol dm⁻³ solutions of aqueous hydrogen peroxide solution to be photolysed for known time periods. The hydrogen peroxide would subsequently photolyse to form OH radicals, the concentration of which was determined by UV-VIS spectroscopy. The UV-VIS spectroscopy

Methodology

required an absorption cross section, in the study presented data from Anastasio et al. (2005) was used. It ought to be noted that to ensure any changes in the absorption signal was observed, a less concentrated solution of hydrogen peroxide had to be used. By plotting the concentration of hydrogen peroxide with photolysis time, the decay could be simulated by modeling R6 to R11 and varying k_1 until a line could be drawn through the plotted points. The best fit gave the k_1 used.

The presence of D₂O in the aqueous subphase was assumed to cause an increase in the steady-state concentration of hydroxyl radicals (OH and OD); a kinetic isotope effect will reduce the value of the rate constant by approximately a factor of five for the reactions involving the abstraction of a O-D bond. The steady-state concentrations of OH and HO₂ radicals in the neutron cell were calculated to be 6.9×10^{-10} molecule cm⁻³ and 2.2×10^{-3} molecule cm⁻³ respectively assuming no D₂O was present, whilst the steady-state concentrations of OD and DO₂ radicals in the neutron cell were calculated as 3.0×10^{-9} molecule cm⁻³ and 4.8×10^{-3} molecule cm⁻³ respectively during the bilayer oxidation assuming that H₂O was not present. The actual steady state concentrations of OH and HO₂ radicals were crudely estimated for the bilayer oxidation in a solution of 69 percent: 31 percent (volume/volume) D₂O: H₂O as 2.3×10^{-9} molecule cm⁻³ and 4.0×10^{-3} molecule cm⁻³ respectively.

2.5. Summary

In the thesis presented, optical trapping techniques were applied to study the wavelength-dependent refractive index and radius of atmospheric aerosol proxies and extracts collected from the atmosphere. Optical trapping allowed homogeneous aerosol to be characterised in terms of refractive index and radius, as well as core-shell aerosol, providing a means for understanding aerosol with and without a thin film in a non-invasive environment. Additionally, applying neutron and x-ray reflection methods to aerosol thin films at the air-water interface allowed the thickness and structure of the film to be determined.

Methodology

In addition, optical trapping and reflectometry techniques were all applied to monitor the changes in aerosol upon exposure to atmospheric oxidants. The application of neutron and x-ray reflection techniques to similar material at the air-water interface highlighted the differences between neutron and x-ray experimental methods in terms of sensitivity to the material under analysis.

The complimentary combination of using optical trapping and reflectometry methods allowed information such as the optical properties of the aerosol to be characterised as well as the oxidation decay profiles to be collected.

Methodology References

- Abelès F., *Le Journal de Physique et le Radium* **11**, 307–310 (1950).
- Aden, A. and M. Kerker, *Journal of Applied Physics* **22**(10), 1242–1246 (1951).
- Chu, L. and Anastasio, C., *Journal of Physical Chemistry A*, **2005**, 109, 6264–6271.
- Ashkin A. , *Physical Review Letters* **1**, 1–10 (1970).
- Ashkin A. and J. M. Dziedzic, *Applied Physics Letters* **19**(8), 283 (1971).
- Ashkin A. and J. M. Dziedzic, *Science* **187**(3), 1–3 (1975).
- Ashkin A. et al., *Optics Letters* **11**(5), 288 (1986).
- Atkinson R. et al. *Atmospheric Chemistry and Physics Discussions*, 3(6), pp. 6179–6699 (2003).
- Athanasiadis T. et al., *Physical Chemistry Chemical Physics* **18**(44), 30385–30393 (2016).
- Betram A. K. et al. *The Journal of Physical Chemistry A*, 105(41), 9415–9421 (2001).
- Bohren C. F. and D. R. Huffman, Wiley Scientific, (1983).
- Bowman R. W. and M. J. Padgett, *Reports on Progress in Physics* **76**(2), 1–28 (2013).
- Chakrabarty R. K. et al., *Atmospheric Chemistry and Physics* **10**(13), 6363–6370 (2010)
- Chu S., *Nobel Lectures Physics*, (1997).
- Dabkowska A. P. et al., *Soft Matter* **9**(29), 7095–7105 (2013).
- David G. et al., *Physical Chemistry Chemical Physics* **18**, 5477–5485 (2016).
- Dilbeck, C. W. and Finlayson-Pitts, B. J., *Physical Chemistry Chemical Physics*, 15, pp. 9833–9844 (2013).
- Dietrich S. and A. Haase, *Physics Reports* **260**, 1–138 (1995).
- Fällman E. and O. Axner, *Applied Optics* **36**(10), 2107–2113 (1997).
- Fermi E. and W. Marshall, *Physical Reviews* **71**(666), (1947).
- Fermi E. and W. Zinn, *Physical Reviews* **70**(103) (1946).
- Fontes A. et al., *Applied Physics Letters* **87**(22), 1–3 (2005).
- Goff, J. P. et al., *ISIS Second Target Station Project: Beamline Name*

polREF.

Haynes W. CRC Press (2016).

Hayter J. B., J. Penfold and W. G. Williams, *Journal of Physics E: Scientific Instruments* **11**(5), (1978).

Hergert, W. and T. Wriedt, Wolfram Hergert, (2012).

Hunt O. R., A. D. Ward and M. D. King, *RSC Advances* **3**, 19448-19454 (2013).

Hunt O. R., A. D. Ward and M. D. King., 2015. *Physical Chemistry Chemical Physics* **17**(4), 2734–2741.

Jauffred L. et al., *Nano Letters* **15**(7), 4713–4719 (2015).

Jones S. H. et al., *Atmospheric Environment* **161**, 274-287, (2017).

Jones, S. H., M. D. King and A. D. Ward, *Physical Chemistry Chemical Physics* **15**(47), 20735–20741 (2013).

Lebedev P. N. *Ann. der Physik* **6**, 433 (1901).

Liu L., M. I. Mishchenko and W. P. Arnott, *Journal of Quantitative Spectroscopy and Radiative Transfer* **109**(15), 2656–2663 (2008).

Lovell M. R. and R. M. Richardson, *Current Opinion in Colloid and Interface Science* **4**, 197–204 (1999)

Lu J. R., R. K. Thomas, and J. Penfold, *Advances in Colloid and Interface Science* **84**(1), 143–304 (2000).

Lynn J. W. et al., *Journal of Applied Crystallography* **9**, 454–459 (1976).

MacDonald M. P., G. C. Spalding, and K. Dholakia, *Nature* **426**, 421–424 (2003).

McGloin D., 2006. *Philosophical Transactions: Series A: Mathematical, Physical and Engineering Sciences* **364**, 3521–3537 (2006).

Mie G. *Ann. der Physik* **25**, 377–445 (1908).

Mitchem L. et al., *Journal of Physical Chemistry A* **110**(26), 8116–8125 (2006).

Moore L. J., M. D. Summers and G. A. D. Ritchie, *Physical Chemistry Chemical Physics* **15**(32), 13489–13498 (2013).

Nelson A., *Journal of Applied Crystallography* **39**(2), 273–276 (2006).

Neuman K. C. and S. M. Block, *Review of Scientific Instruments* **75**(9), 2787–2809 (2004).

Penfold, J. et al., 1997. *Journal of the Chemical Society, Faraday*

Methodology

- Transactions **93**(22), 3899–3917 (1997).
- Penfold, J. and R. K. Thomas, Journal of Physics: Condensed Matter **2**(6), 1369–1412 (1990).
- Pope F. D. et al., Nature Climate Change **2**(10), 713–719 (2012).
- Rkiouak L. et al., Physical Chemistry Chemical Physics **16**(23), 11426–11434 (2014).
- Takahama S., S. Liu and L. M. Russell, Journal of Geophysical Research Atmospheres **115**(1), 1–21 (2010).
- Tang M. et al., The Journal of Physical Chemistry **118**, 8817–8827 (2014).
- Toon O. B. and T. P. Ackerman, Optical Society of America **20**, 3657–3660 (1981).
- Vergucht E. et al., Scientific Reports **5**, 1–8 (2015).
- Webster J., S. Holt, and R. Dalgliesh, Physica B: Condensed Matter **385–386**, 1164–1166 (2006).
- Yamasoe M. A. et al., Atmospheric Environment **34**(10), 1641–1653 (2000).
- Zhou S. et al., Atmospheric Chemistry and Physics **14**(3), 1371–1384 (2014).

Paper 1: Mie scattering from optically levitated mixed sulfuric acid-silica core-shell aerosols: confirmation of core-shell morphology for atmospheric science

Rosalie H. Shepherd, Martin D. King, Nicholas Davidson, Francis Pope, Matt Watson, Roy G. Grainger and Andrew D. Ward

To be submitted to the Journal of Physical Chemistry Chemical Physics.

I declare I have made the following contributions to the piece of co-authored work:

- Conducted the experiments, and collected and analysed all data collected
- Contributed to the conclusions drawn from the experiments conducted
- Authored the paper

ARTICLE

Mie scattering from optically levitated mixed sulfuric acid-silica core-shell aerosols: confirmation of core-shell morphology for atmospheric science

Received 00th January 20xx,
Accepted 00th January 20xx

DOI: 10.1039/x0xx00000x

www.rsc.org/

Rosalie H. Shepherd,^{a,b} Martin D. King,^b Nicholas Davidson,^c Francis D. Pope,^c Matt Watson,^d Roy G. Grainger^e and Andrew D. Ward^{a*}

The study investigates the consequences of sulfuric acid colliding with a mineral aerosol through the application of optical trapping applied simultaneously with Mie spectroscopy. Micron-sized silica particles (silica particles were used as a proxy for atmospheric silica mineral aerosols) were levitated in a mist of sulfuric acid droplets; continuous collection of Mie spectra throughout the collision of sulfuric acid droplets with the optically trapped silica particle demonstrated that the resulting aerosol had a core-shell morphology. Contrastingly, the collision of aqueous sulfuric acid droplets with optically trapped polystyrene particles resulted in a partially coated system. The light scattering from the optically levitated aerosols was successfully modelled to determine the diameter of the core particle ($\pm 0.005 \mu\text{m}$), the shell thickness ($\pm 0.005 \mu\text{m}$) and the refractive index (± 0.001). The experiment demonstrated that the presence of a thin film rapidly changed the light scattering of the original aerosol. When a $1.930 \mu\text{m}$ diameter silica particle was covered with a film of sulfuric acid $0.190 \mu\text{m}$ thick, the wavelength dependent Mie peak positions resembled sulfuric acid.

1. Introduction

Stratospheric aerosols have a large impact on Earth's climate^{1–7}; the scattering of incoming solar radiation⁸ can depend on the shape, composition and refractive index of the aerosol^{9–11}. Quantification of the optical properties of stratospheric aerosol is needed to fully understand the influence of stratospheric aerosols upon the planet's radiative balance¹².

Sulfuric acid aerosols are relatively abundant in the stratosphere^{13–15}; the number density of sulfuric acid in the stratosphere has been determined from balloon-borne mass spectrometer experiments to be 10^4 to 10^5 molecules cm^{-3} below an altitude of 30 km and 10^6 to 10^7 molecules cm^{-3} between 30 to 35 km^{16,17}. Anthropogenic emissions, biogenic processes and volcanic emissions act as the major sources of stratospheric sulfuric acid^{18–20}. Owing to the abundance of sulfuric acid within the stratosphere, the condensation of sulfuric acid onto other stratospheric aerosol occurs readily^{21,22}. Saunders et al.²³ estimated an encounter occurring purely from Brownian motion between a mineral dust particle with a radii of $0.0015 \mu\text{m}$ and a sulfuric acid aerosol with radii

of $0.25 \mu\text{m}$ would take approximately 4 days.

Deshler et al.²⁴ demonstrated that volcanic eruptions have influenced stratospheric aerosol size distributions for twenty of the last thirty years. Glass fragments make up a large proportion (60 to 80 percent) of mineralogy from volcanic eruptions²⁵ and tend to become coated in sulfuric acid, as shown by U2 flights in Mount St Helen's ash cloud²⁵. The formation of a thin film of sulfuric acid on a stratospheric mineral aerosol would change the refractive index of the mineral aerosol and hence change the amount of incoming solar radiation that the aerosol scatters^{26,27}. Stratospheric mineral aerosol coated in a thin film of stratospheric sulfuric acid could display the optical properties of (a) the mineral aerosol, (b) the mineral aerosol slightly modified by thin film development or (c) sulfuric acid resulting from a core-shell aerosol resembling the sulfuric acid shell to a first approximation.

In the study presented, the light scattering from an optically trapped silica bead coated in a thin film of sulfuric acid has been studied. The study will (a) determine that aqueous sulfuric acid can wet and uniformly coat mineral aerosol to form an aerosol with core-shell morphology and (b) record the Mie scattering, backscattered, visible light to size the aerosol and determine the refractive index and shell thickness. Additionally, the Mie scattering as sulfuric acid collided with polystyrene particles was monitored: in the presented study it was observed that sulfuric acid did not wet on polystyrene particles, thus demonstrating the lack of core-shell geometry. Comparison between the two systems that used either silica or polystyrene as the core particle provided

^a Central Laser Facility, Research Complex, STFC Rutherford Appleton Laboratory, Oxford, OX11 0FA, UK

^b Department of Earth Sciences, Royal Holloway, University of London, Egham, Surrey, TW20 0EX, UK

^c School of Geography, Earth & Environmental Sciences, University of Birmingham, Birmingham, B15 2TT, UK

^d Department of Earth Science, University of Bristol, Wills Memorial Building, Bristol, BS8 1RJ, UK

^e National Centre for Earth Observation, Atmospheric, oceanic and Planetary Physics, University of Oxford, Parks Road, Oxford OX1 3PU, UK

additional evidence for the formation of core-shell aerosol when sulfuric acid collided with the silica particles.

Other studies have focused on the deliberate injection of particles into the stratosphere as a method of combating climate change^{11,22,28–30}. It is reported that the injection of particles with a large refractive index may greatly increase the amount of solar radiation reflected back to space²⁸. Sulfates released into the stratosphere (and which later convert into sulfuric acid³¹) have been suggested as a material to purposefully implant into the stratosphere³². However, very little attention has been given to the microphysical interactions between the perturbing material and the ambient stratospheric aerosol layer. Owing to the composition and size of the acid aerosols²⁸, sulfuric acid does not have the desirable characteristics of a highly reflective aerosol and therefore recent studies have begun to explore other, non-sulfate possibilities such as silica or titania^{28,33}. Understanding how a thin film of sulfuric acid alters the scattering properties of the mineral aerosol is crucial to estimate how effective mineral aerosols are at scattering solar radiation.

Atmospheric films on liquid or solid aerosols have been studied previously^{26,27,33–43}. Inorganic coatings on atmospheric aerosol has been investigated^{27,33,44–46}. For example, Rkiouak²⁷ et al. applied Raman spectroscopy to follow the development of sulfuric acid films on silica particles, whilst Tang et al.³³ studied the heterogeneous reaction of N₂O₅ on silica particles. Film development on atmospheric aerosols has previously been studied through application of optical trapping techniques^{26,27,33,47}, for example Jones et al.²⁶ determined the refractive index change as a film of oleic acid developed on a silica particle.

2. Experimental

To investigate the light scattering from a sulfuric acid film of varying thickness upon a mineral aerosol, single mineral particles were optically levitated using vertically aligned, counter propagating laser beams^{48–50}. The counter-propagating laser beams provided a contact free method of levitating aerosols, allowing a replication of airborne processes with the correct aerosol morphology. Mie theory was applied to the backscattered spectrum to determine aerosol radius and refractive index using the relationship between wavelength and refractive index expressed in the Cauchy equation⁵¹:

$$n = A + \frac{B}{\lambda^2} + \frac{C}{\lambda^4}, \quad (\text{Equation 1})$$

where the unknown parameters can be determined as a function of wavelength. Within the Cauchy equation, n is the refractive index, λ is wavelength and A , B and C are the Cauchy coefficients.

To study core-shell systems, it was important to study the core and shell material separately at the beginning of the

study. The application of Mie theory allowed the refractive index of sulfuric acid droplets and the refractive index and size of the core mineral particle to be determined prior to formation of a core-shell system. Afterwards, a film of sulfuric acid could be formed on the silica particle from a mist of sulfuric acid in air generated from a bulk aqueous sulfuric acid solution. The airborne aqueous sulfuric acid droplets wetted and spread on the core mineral particle. Mie spectra were continuously collected whilst sulfuric acid droplets collided with the silica particle; the experimental Mie spectra were then simulated allowing the refractive index, radius and film thickness of the core-shell system to be characterised. For the purpose of the study, silica was used as a proxy-mineral aerosol.

2.1. Sulfuric Acid and Silica Particles

VWR Chemicals supplied aqueous sulfuric acid as a 50 % w/w solution. Dilutions were made by weight using water with conductivity below 18 MΩ cm⁻¹.

Spherical silica particles were sourced from Bangs Laboratories Inc., product number SS04N, lot number 7920. The particles are reported as non-porous with a reported density of 2 g cm⁻³ and a radius of approximately 1.035 μm. To determine the refractive index and radius of a trapped aerosol Mie spectroscopy requires the shape of the aerosol to be accurately known, and thus use of mineral aerosol samples extracted from the atmosphere was not possible.

Additionally, Bangs Laboratories Inc. supplied polystyrene particles: product number PS04N, lot number 12487. The polystyrene particles had a density of 1.04 to 1.15 g cm⁻³ and a radius of approximately 1.04 μm.

2.2. Aerosol Generation

An ultrasonic nebuliser (aerosonic travel ultrasonic nebuliser) delivered sulfuric acid droplets to the sample cell. The radius of the trapped aqueous sulfuric acid droplets varied from 0.1 μm to over 5 μm. Droplets in the range 1.4 to 2.0 μm were used for Mie scattering studies.

An atomiser (Topas, ATM 220) with diffusion dryer (Topas, DDU 570/L) was used to deliver silica and polystyrene to the sample cell from aqueous suspensions. Prior to atomisation, the silica or polystyrene particles were dispersed in water at a concentration of 2 % w/w.

Table 1: The mass ratio of sulfuric acid droplets increased upon trapping, as determined through the application of Mie theory. A, B and C are the Cauchy coefficients from Equation 1.

Bulk Sulfuric Acid		Sulfuric Acid Aerosol				
Concentration (% w/w)	Radius μm	Concentration (% w/w)	Refractive Index	A	B (nm^2)	C (nm^4)
5	1.349	55	1.401	1.395	2425	1.0×10^7
10	1.733	55	1.401	1.393	2210	3.0×10^6
15	1.605	52	1.397	1.394	425	8.5×10^7
20	1.785	48	1.393	1.384	2750	8.0×10^7

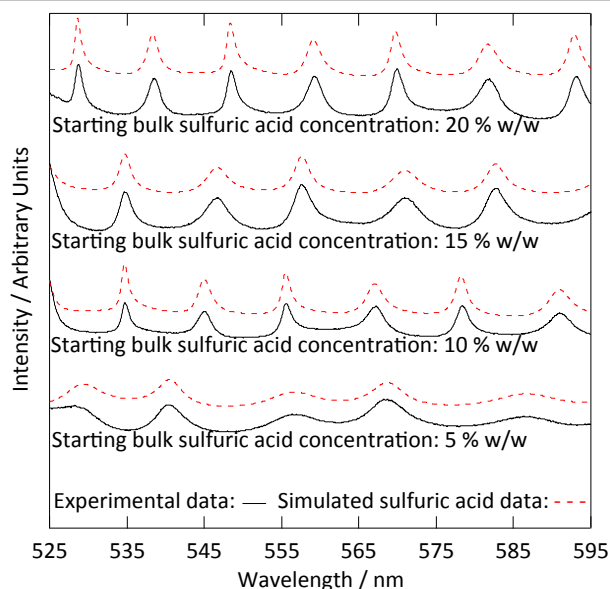


Figure 1: Measured and simulated Mie spectra for optically trapped sulfuric acid droplets, each of the four spectra represent a sulfuric acid droplet that originates from a different concentration bulk aqueous sulfuric acid solution. Simulated Mie spectra for each experimental Mie spectra are additionally shown. The displayed spectra are offset to provide a clear depiction of the spectra.

2.3. Optical Trapping

A 1064 nm, continuous wave Nd:YAG laser beam (Ventus, Laser Quantum) was split into two paths. The beams were delivered, via beam expansion optics, to two opposing microscope objective lenses (Mitutoyo NIR x50, NA 0.42) that focused the two beams to form an optical trap⁵². A piezo-stage (Physik-Instrumente) was used to control the x, y and z positions on the upper laser beam pathway allowing accurate alignment of the focused beams. The power of the laser beam at the point of focus was set to 10 mW for the upward propagating beam and 15 mW for the downwards propagating beam. A simplified schematic of the optical trapping equipment is depicted in Jones et al.⁴⁹.

A custom-made aluminium sample cell was used as a chamber to trap the aerosols. The cell had two-quarter inch fittings to allow entry of the aerosols and to provide an exhaust path. Windows at the top and bottom allowed the laser beam to enter the cell. Brightfield illumination was configured along the same axis using the lower microscope objective for imaging, with an optical filter to attenuate the laser wavelength. The radius of the trapped aerosol could be

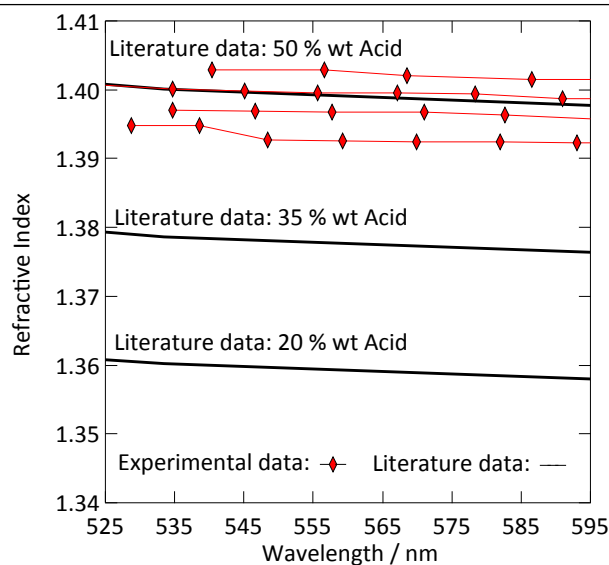


Figure 2: Experimental (red diamond) refractive index of trapped sulfuric acid droplets as a function of wavelength are compared to literature values for aqueous sulfuric acid solutions that have different mass ratios of sulfuric acid to water⁶³.

estimated from images with a resolution of 0.5 μm to provide a coarse starting value for aerosol size when modelling the Mie light scattering with wavelength. Brightfield sources were isolated whilst a spectrum was acquired.

Brightfield illumination additionally allowed imaging of aerosols deliberately placed on the coverslip. The phase of the aerosol could then be analysed; all optically levitated aerosols were subjected to the test to ensure the aerosol was the desired material under study.

2.4. Acquisitions and Modelling of Mie Spectra

A white-light LED was focussed on the trapped aerosol and the elastic, backscattered light collected using the microscope objective; the light was then dispersed by a spectrometer onto a charge-coupled device detector (Princeton Instrument Spec 10:400 BR), which recorded light intensity as a function of wavelength. Typically a 600 line mm^{-1} grating dispersed the collected light across a wavelength range of 520 to 600 nm with a resolution of 0.06 nm per pixel as shown in Figure 1. Henceforth in the study presented, the spectrum of the intensity of backscattered light versus wavelength will be called a Mie spectrum. An argon pen-ray lamp was used for the wavelength calibration of the spectrometer.

To determine the refractive index and radius of the trapped aerosol, the experimental Mie spectrum was compared to a calculated Mie spectrum produced through application of Mie theory based on Bohren and Huffman⁵³; the radius and refractive index were varied until a global minimum was determined with the least squares fitting residual between experimental and theoretical peak positions^{49,54}.

Additionally, core-shell Mie theory^{55,56} was applied to calculate the Mie spectra of the core-shell silica-sulfuric acid aerosol; the calculated spectra simulated a series of sulfuric acid films of known thickness on a silica particle of known radius and refractive index. The calculated Mie spectra were then compared to experimentally collected core-shell Mie spectra to determine the thickness of the acid film.

3. Results and Discussion

3.1. Sulfuric Acid

The optical properties of aqueous sulfuric acid has been characterised for a range of sulfuric acid concentrations: Remsburg et al.⁵⁷ studied aqueous sulfuric acid in the concentration range 75 to 90 % w/w, whilst Palmer and Williams⁵⁸ studied the concentration range 25 to 95.6 % w/w. In more recent years, studies have begun to determine the optical properties of sulfuric acid experiencing stratospheric-like conditions, for example Tisdale et al.⁵⁹, Niedziela et al.⁶⁰ and Lund Myhre et al.⁶¹ studied the effect of temperature upon the optical properties of sulfuric acid droplets, whilst Wagner et al.⁶² investigated the change in refractive index as a sulfuric acid system was supercooled.

In the study presented here, precursory experiments to determine the optical properties, and hence concentration of optically trapped aqueous sulfuric acid droplets were paramount for calculation of core-shell silica-sulfuric acid systems; the refractive index of optically trapped sulfuric acid was required to create accurate simulations of core-shell silica-sulfuric acid droplets.

Bulk aqueous solutions with the concentrations of 5, 10, 15 or 20 % w/w were prepared and nebulised separately to deliver droplets to the optical trap. The Mie spectrum for each droplet was obtained: Figure 1 depicts the experimental and calculated Mie spectra for the aqueous sulfuric acid droplets for each initial concentration. The refractive index and radius of the optically trapped droplets are summarised in Table 1. The refractive index can be determined with 0.001 precision, whilst the radius of the aerosol was determined to $\pm 0.005 \mu\text{m}$.

Figure 2 compares the refractive index dispersion for the optically trapped sulfuric acid droplets to literature refractive index dispersions for bulk aqueous sulfuric acid solutions of known mass ratio⁶³. The refractive index for experimental sulfuric acid droplets lie at a refractive index of approximately 1.395 ± 0.005 at 589 nm, which corresponds to a mass ratio of 50 ± 4 % w/w. The mass ratio of sulfuric acid to water of the

optically trapped aerosols has increased upon trapping; water has evaporated.

The relationship between sulfuric acid concentration and the surrounding environment was demonstrated by Mund and Zellner⁶⁴, in particular showing a dependence on the local relative humidity and temperature of the surrounding environment. The relative humidity of the laboratory was measured between 30 and 35 percent during these experiments, which is commensurate with an equilibrium of 50 to 53 % w/w sulfuric acid⁶⁵.

The sulfuric acid to water ratio is controlled by local relative humidity, and this is refined by the microenvironment of the aerosol.

For all experiments hereafter, it is assumed that nebulised sulfuric acid droplets will equilibrate with the surrounding environment to reach a concentration of 50 % w/w with a refractive index of 1.395 at 589 nm; the assumed refractive index will be used in calculations of core-shell silica-sulfuric acid aerosol.

3.2. Silica Aerosol

Simulation of Mie spectra for core-shell aerosols requires the size and refractive index of the core particle to be measured first. The silica Mie spectrum depicted in Figure 3 is typical of mineral aerosol. The Mie spectrum contains little structure and hence there might be slightly more combinations of *A*, *B*, *C* and radius that result in a good simulated fit of the experimental spectra - thereby increasing the uncertainty in the refractive index and radius of the particle. However, eighteen separate silica particles were individually optically trapped and gave an average and standard deviation radius of $0.957 \pm 0.005 \mu\text{m}$, whilst the refractive index was measured as 1.380 ± 0.018 at 589 nm. The variation in values of refractive index with wavelength were calculated to be 1.371 ± 0.018 , $2676 \pm 483 \text{ nm}^2$ and $1 \times 10^8 \text{ nm}^4$ for *A*, *B* and *C* respectively as defined in Equation 1.

The measured values of refractive index for silica is notably lower than published values, for example 1.458 at 589 nm was determined by Jarglarz et al.⁶⁶. Variation in refractive index for different silica samples could be attributed to the mass density of silica. The density determined by the manufacturers and our own densitometer measurements is also lower than bulk silica. Previously low refractive index values of silica particles has been attributed to particle porosity as demonstrated by Tisdale et al.⁶⁷ who measured the refractive index for silica particles to range from 1.38 to 1.42; increased porosity would reduce the density of the particle.

3.3. Sulfuric Acid Film Growth on Silica Particles

Mie spectra of the optically trapped particles were obtained throughout the collision of sulfuric acid with silica particles. Figure 3 depicts the Mie light scattering spectra during growth of a film of sulfuric acid upon the silica particles.

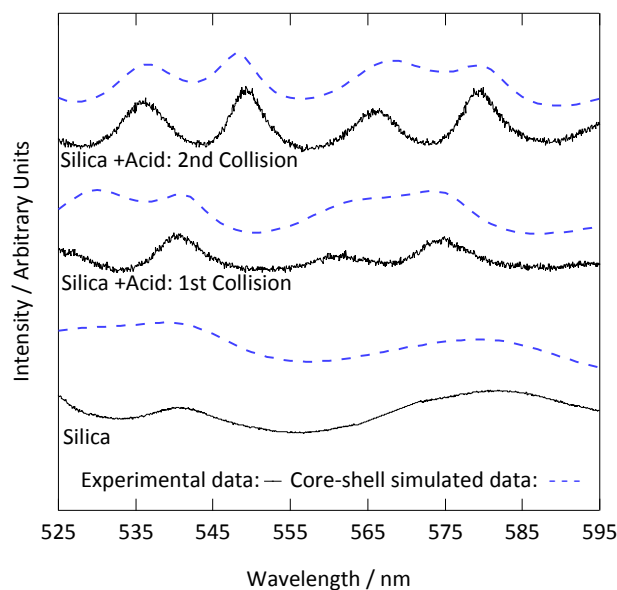


Figure 3: Mie spectra showing how the Mie scattering of silica particle alters upon growth of a film of sulfuric acid. Core-shell Mie theory was applied to determine thickness of the developing shell, the Mie theory simulations are depicted with blue, dashed lines. Two collisions are depicted: the first collision formed a film of sulfuric acid on the silica of thickness $0.190\ \mu\text{m}$, whilst the second collision thickened the film further to a total film thickness of $0.263\ \mu\text{m}$.

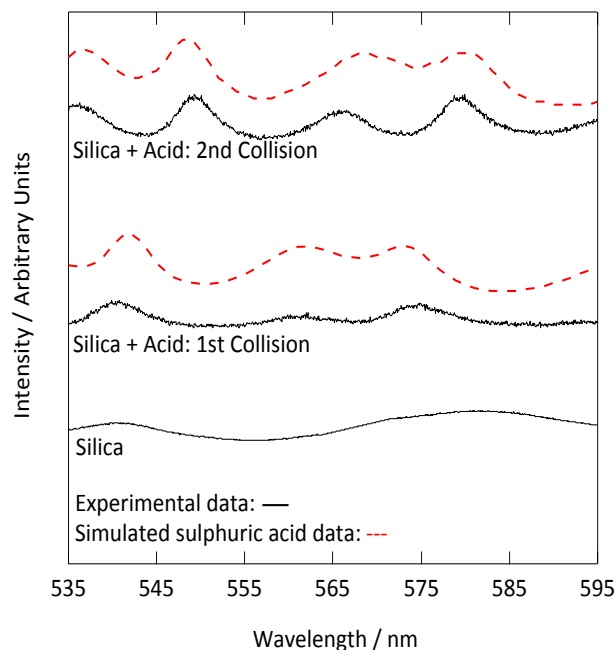


Figure 4: Experimentally collected Mie spectra from the collision of sulfuric acid on silica displayed with overlying theoretical simulations of sulfuric acid at similar diameters.

The film thickness of the sulfuric acid film was calculated by assuming a constant silica core surrounded by a shell of increasing thickness with the refractive index of a 50 % w/w aqueous sulfuric acid solution. After the first collision, the

thickness of the acid film was $0.190\pm0.005\ \mu\text{m}$, requiring a sulfuric acid droplet with a volume of $2.863\ \mu\text{m}^3$ to collide with the silica particle. After the second collision the film was $0.263\pm0.005\ \mu\text{m}$ thick; to develop the film a second sulfuric acid droplet with a volume of $1.494\ \mu\text{m}^3$ collided with the silica particle.

To determine whether the film of sulfuric acid alters the light scattering properties of the core silica particle, the Mie scattering properties of the core-shell aerosol were compared with those of pure sulfuric acid droplets as depicted in Figure 4. The modelled Mie spectra in Figure 4 are of pure sulfuric acid droplets. The product of the first collision had a radius of $1.155\pm0.003\ \mu\text{m}$, and has a similar spectrum to a sulfuric acid droplet with a radius of $1.225\ \mu\text{m}$. Additionally, the product of the second collision (which has a radius of $1.250\ \mu\text{m}$) has a similar spectrum to a sulfuric acid droplet with the radius of $1.228\ \mu\text{m}$.

Therefore, we infer that when a micron-sized sulfuric acid droplet collides with an optically trapped silica aerosol the resultant core-shell aerosol will begin to resemble a sulfuric acid aerosol of similar diameter as the shell becomes thicker.

3.4. Sulfuric Acid Film Growth on Polystyrene Particles

As further evidence for demonstrating the sensitivity of the technique to core-shell aerosol formation, a system unlikely to form a core-shell system was chosen. Hydrophobic polystyrene particles were trapped and the collision of aqueous sulfuric acid with the polystyrene followed with Mie spectroscopy.

Figure 5a depicts calculated core-shell Mie spectra as a film of sulfuric acid develops on a polystyrene particles; the simulation shows an increase in the number of resonances as the film thickens. Contrastingly, the experimental results depicted in Figure 5b demonstrate a loss of resonances as the sulfuric acid collided with the polystyrene particles. The contrast in Mie spectra shown in Figures 5a and 5b indicate that sulfuric acid and polystyrene do not form a core-shell geometry.

Owing to the contrast in hydrophobic and hydrophilic nature of polystyrene and aqueous sulfuric acid, the condensation product may represent a partially engulfed system. Phase separation between contrasting liquids in aerosols has been extensively studied^{68–71}. In particular, Reid et al.⁷² investigated the morphology of mixed phase systems through application of optical trapping techniques; concentrating on compounds containing hydrophobic and hydrophilic domains demonstrated that systems containing partitioning constituents do not always form core-shell morphology.

3.5 Stratospheric Implications

Owing to the relative abundance of sulfuric acid aerosols residing in the stratospheric aerosol layer^{13–15}, the consequences of the collision of sulfuric acid aerosols with solid aerosols is highly relevant to understanding the optical scattering efficiency (Q_{sca}) of the stratosphere. The optical scattering efficiency of a sphere is the fraction of the incident light scattered per unit cross-sectional area of the sphere.

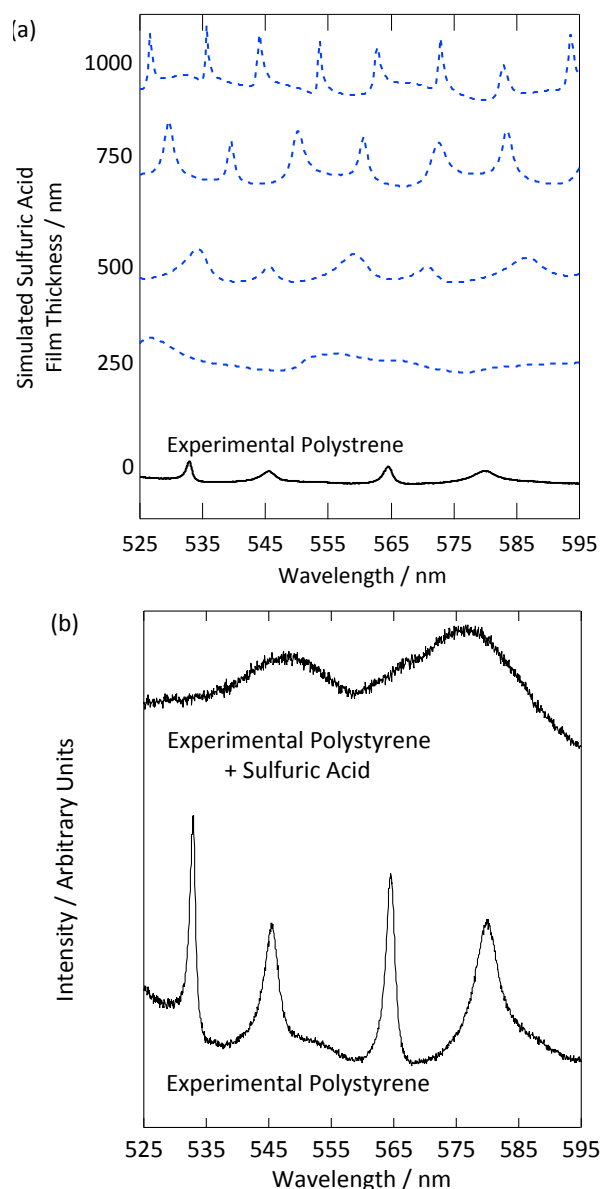


Figure 5: Graphs depicting (a) the Mie-theory simulated spectra for film development on the experimental obtained Mie spectrum for polystyrene and (b) the experimentally obtained Mie spectra for the growth of a film of sulfuric acid on polystyrene.

The difference in optical properties of a coated aerosol in comparison to an uncoated sphere has drawn significant attention in recent years^{26,73–76}; in particular Kahnert et al.⁷⁵ has modelled the encapsulation of aggregates by a sulfate film whilst Soewono and Rogak⁷⁴ and Wu et al.⁷⁶ have explored the effect of a sulfate film on a soot particle.

As demonstrated in the study presented, sulfuric acid collides with a silica particle, and then wets and spreads over the surface of the silica particle to form a symmetrical core-shell aerosol. Laboratory experiments demonstrated that the light scattering properties of the core-shell aerosol system moved rapidly away from the mineral particle, and began to represent the Mie spectra of a pure aqueous sulfuric acid droplet.

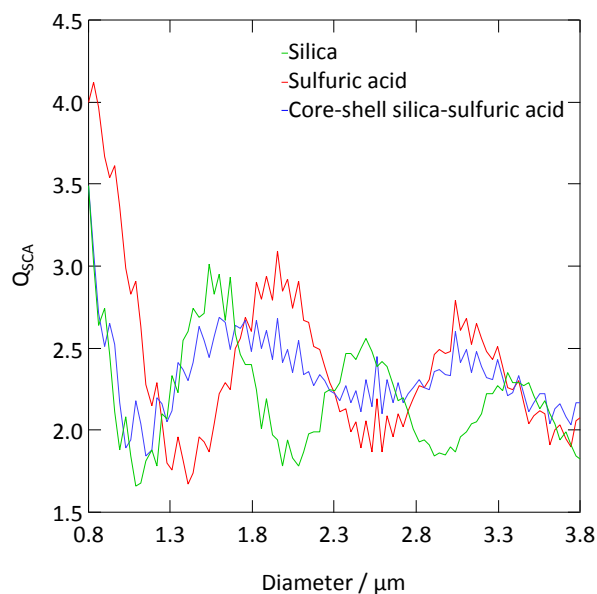


Figure 6: The scattering efficiency of atmospheric silica, sulfuric acid and core-shell silica-sulfuric acid aerosol as a function of aerosol diameter. When the shell upon a 0.8 μm core aerosol is 0.75 μm thick, the optical properties resemble the sulfuric acid shell.

The scattering efficiency of a typical stratospheric silica aerosol was calculated as a function of sulfuric acid film thickness using a refractive index of 1.55-0.002i to represent the silica aerosol²⁵, 1.44-0i to represent sulfuric acid^{58,63} and 0.80 μm for the core diameter^{24,25}. It ought to be noted, the values used were taken from atmospheric measurements. The shell thickness was increased in 0.03 increments until the total diameter of the core-shell system had reached 4.00 μm . The results are compared to the scattering efficiency of a pure sulfuric acid droplet with the refractive index of 1.44-0i and a silica particle with the refractive index of 1.55-0.002i in Figure 6. All refractive index values are taken at a wavelength of 532 nm.

Figure 6 demonstrates that the structure of the scattering efficiency of the core-shell aerosol begin to represent the shell sulfuric acid quickly; similar results were determined with the laboratory results. As explained in section 3.3, Mie spectra of laboratory optically trapped core-shell aerosol represented the Mie spectra of pure aqueous sulfuric acid when the film of the aqueous sulfuric acid was 0.190 μm thick. Comparatively, the film thickness required for a modelled atmospheric silica and sulfuric acid system required a thicker film thickness of 0.75 μm before the Mie peaks of the core-shell system and sulfuric acid aligned. Both laboratory and the modelled atmospheric system demonstrated a core-shell silica-sulfuric acid system resembled sulfuric acid only upon film formation and consequently the formation and resultant optical properties of core-shell aerosols ought to be carefully considered in future modelling of stratospheric aerosols.

4. Conclusions

The study presented here demonstrates that sulfuric acid successfully forms a core-shell geometry aerosol upon collision with silica. Through application of optical trapping techniques alongside Mie spectroscopy, it was observed that when a sulfuric acid droplet collides with a silica particle, the system would begin to resemble a sulfuric acid droplet of similar diameter to the combined aerosol.

Secondly, the study experimentally demonstrates that mineral particles emitted to the stratosphere will soon adopt the light scattering patterns associated with a pure sulfuric acid aerosol. The implication of the study to stratospheric science is that hydrophilic stratospheric mineral aerosol will rapidly take on the optical properties of sulfuric acid through natural collision processes and the formation of core-shell morphology.

Appendix A

The aim of the study was to study the changes in optical scattering of a mineral dust aerosol upon collision with sulfuric acid. Two other mineral dust particles (titania and alumina) were investigated.

Alumina and titania particles sourced from Corpuscular were optically trapped and the Mie spectrum collected. Figure 7 depicts typical Mie spectrum for the particles. Simulation of the Mie spectra for the alumina and titania particles allowed the wavelength dependent and radius of the particles to be determined. The average refractive index calculated from simulating Mie spectra for five alumina particles was determined to be 1.3644 ± 0.001 at 589 nm for alumina particles covering the radius range of 0.888 to 1.060 nm. The

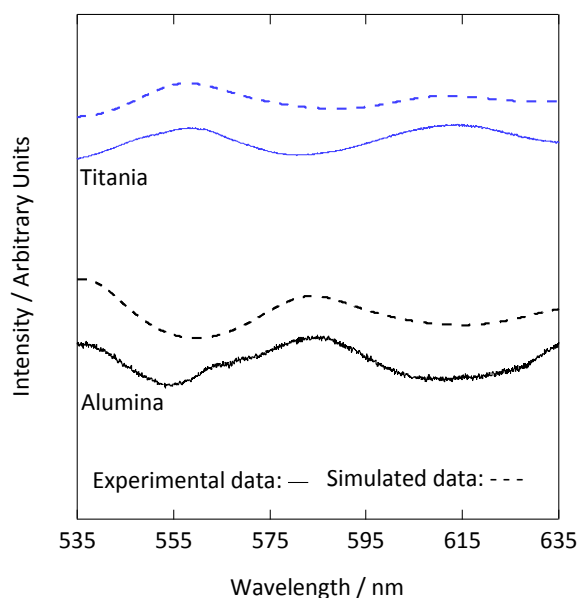


Figure 7: Typical Mie spectra for alumina and titania aerosols. The calculated Mie spectra are depicted above the experimentally collected data.

Cauchy coefficients determined for the alumina particles were 1.3546 ± 0.0044 , 3100 ± 575 and 1×10^8 for the Empirical

constants A , B and C respectively. The average wavelength dependent refractive index for titania particles (determined from five particles) was calculated to be 1.3605 ± 0.001 at 589 nm for titania particles covering the radius range of 0.852 to 1.055. The Cauchy coefficients were determined to be 1.3539 ± 0.0014 , 2000 ± 500 and 1×10^8 for the Empirical constants A , B and C respectively.

The calculated refractive index for alumina and titania particles lie much lower than literature values⁶⁵ (approximately 1.76 or 2.50 for alumina or titania at 589 nm respectively) and has been attributed to the alumina and titania particles having a much lower than expected density. Use of an Acton Parr densitometer allowed the density of a suspension of the particles in ultra pure water to be determined. The density of the particles was calculated upon plotting the inverse of the density versus the weight fraction of the particles in the ultrapure water. The density of alumina was determined to be $3.22 \text{ cm}^3 \text{ g}^{-1}$ and $2.26 \text{ cm}^3 \text{ g}^{-1}$ for titania. The measured density values lie considerably lower than the reported density for the two minerals⁶⁵ (approximately $3.95 \text{ cm}^3 \text{ g}^{-1}$ for alumina and $4 \text{ cm}^3 \text{ g}^{-1}$ for titania). Owing to the discrepancies in density values, the authors decided not to pursue studying the formation of sulfuric acid on the mineral particles.

Corresponding Author

Dr Andrew Ward: andy.ward@stfc.ac.uk

Conflicts of Interest

The authors declare that they do not have any conflict of interest.

Acknowledgements

The authors are grateful for STFC for allowing access to the optical trapping laboratory at the Central Laser Facility, Rutherford Appleton Laboratories under the access grant 14230020. Rosalie H. Shepherd would like to thank STFC for funding the student grant ST/L504279/1.

References

- 1 A. Lacis, J. Hansen and M. Sato, *Geophysical Research Letters*, 1992, **19**, 1607.
- 2 C. Bruhl, J. Lelieveld, H. Tost, M. Hopfner and N. Glatthor, *Journal of Geophysical Research*, 2015, **120**, 2103–2118.
- 3 S. M. Andersson, B. G. Martinsson, J. P. Vernier, J. Friberg, C. A. M. Brenninkmeijer, M. Hermann, P. F. J. van Velthoven and A. Zahn, *Nature Communications*, 2015, **6**, 1–8.
- 4 G. Pitari, G. Di Genova, E. Mancini, D. Visioni, I. Gandolfi and I. Cionni, *Atmosphere*, 2016, **7**, 1–21.
- 5 R. Auchmann, F. Arfeuille, M. Wegmann, J. Franke, M. Barriados, M. Prohom, A. Sanchez-Lorenzo, J. Bhend, M.

- Wild, D. Folini, P. Štěpánek and S. Brönnimann, *Journal of Geophysical Research Atmospheres*, 2013, **118**, 9064–9077.
- 6 D. Baumgardner, *Geophysical Research Letters*, 2004, **31**, 10–13.
- 7 G. Myhre, T. F. Berglen, C. E. L. Myhre and I. S. A. Isaksen, *Tellus B: Chemical and Physical Meteorology*, 2004, **56**, 294–299.
- 8 O. B. T. and J. B. Pollack, *American Science*, 1980.
- 9 A. Lacis, J. Hansen and M. Sato, *Geophysical Research Letters*, 1992, **19**, 1607–1610.
- 10 A. J. Durant, S. P. Harrison, I. M. Watson and Y. Balkanski, *Progress in Physical Geography*, 2009, **33**, 80–102.
- 11 A. C. Jones, J. M. Haywood and A. Jones, *Atmospheric Chemistry and Physics*, 2016, **16**, 2843–2862.
- 12 K. D. Beyer, A. R. Ravishankara and R. Lovejoy, *Journal of Geophysical Research*, 1996, **101**, 14519–14524.
- 13 G. K. Yue, L. R. Poole, P. H. Wang and E. W. Chiou, *Journal of Geophysical Research*, 1994, **99**, 3727–3738.
- 14 D. M. Murphy, K. D. Froyd, J. P. Schwarz and J. C. Wilson, *Quarterly Journal of the Royal Meteorological Society*, 2014, **140**, 1269–1278.
- 15 S. Kremser, L. W. Thomason, M. von Hobe, M. Hermann, T. Deshler, C. Timmreck, M. Toohey, A. Stenke, J. P. Schwarz, R. Weigel, S. Fueglistaler, F. J. Prata, J. P. Vernier, H. Schlager, J. E. Barnes, J. C. Antuña-Marrero, D. Fairlie, M. Palm, E. Mahieu, J. Notholt, M. Rex, C. Bingen, F. Vanhellemont, A. Bourassa, J. M. C. Plane, D. Klocke, S. A. Carn, L. Clarisse, T. Trickl, R. Neely, A. D. James, L. Rieger, J. C. Wilson and B. Meland, *Reviews of Geophysics*, 2016, **54**, 278–335.
- 16 F. Arnold, R. Fabian and W. Joos, *Geophysical Research Letters*, 1981, **8**, 293–296.
- 17 A. Viggiano and F. Arnold, *Geophysical Research Letters*, 1981, **8**, 583–586.
- 18 S. Solomon, J. S. Daniel, R. R. Neely, J. P. Vernier, E. G. Dutton and L. W. Thomason, *Science*, 2011, **333**, 866–870.
- 19 C. A. Brock, P. Hamill, J. C. Wilson, H. H. Jonsson and K. R. Chan, *Science*, 1995, **270**, 1650–1653.
- 20 R. G. Grainger and E. J. Highwood, *Geological Society*, 2003, **213**, 329–347.
- 21 S. E. Bauer and D. Koch, *Journal of Geophysical Research D: Atmospheres*, 2005, **110**, 91–105.
- 22 D. K. Weisenstein and D. W. Keith, *Atmospheric Chemistry and Physics*, 2015, **15**, 11835–11859.
- 23 R. W. Saunders, S. Dhomse, W. S. Tian, M. P. Chipperfield and J. M. C. Plane, *Atmospheric Chemistry and Physics*, 2012, **12**, 4387–4398.
- 24 T. Deshler, M. E. Hervig, D. J. Hofmann, J. M. Rosen and J. B. Liley, *Journal of Geophysical Research: Atmospheres* 2003, **108**, 1–13.
- 25 N. H. Farlow, V. R. Oberbeck, K. G. Snetsinger, G. V. Ferry, G. Polkowski and D. M. Hayes, *Science*, 1981, **211**, 832–834.
- 26 S. H. Jones, M. D. King and A. D. Ward, *Chemical Communications*, 2015, **51**, 4914–4917.
- 27 L. Rkiouak, M. J. Tang, J. C. J. Camp, J. McGregor, I. M. Watson, R. A. Cox, M. Kalberer, A. D. Ward and F. D. Pope, *Physical Chemistry Chemical Physics*, 2014, **16**, 11426–11434.
- F. D. Pope, P. Braesicke, R. G. Grainger, M. Kalberer, I. M. Watson, P. J. Davidson and R. A. Cox, *Nature: Climate Change*, 2012, **2**, 713–719.
- K. E. McCusker, D. S. Battisti and C. M. Bitz, *Geophysical Research Letters*, 2015, **42**, 4989–4997.
- A. Laakso, H. Kokkola, A. I. Partanen, U. Niemeier, C. Timmreck, K. E. J. Lehtinen, H. Hakkarainen and H. Korhonen, *Atmospheric Chemistry and Physics*, 2016, **16**, 305–323.
- R. J. Eatough, D. J. Caka and F. M. Farber, *Israel Journal of Chemistry*, 1994, **34**, 301–314.
- P. J. Rasch, S. Tilmes, R. P. Turco, A. Robock, L. Oman, C. C. Chen, G. L. Stenchikov and R. R. Garcia, *Philosophical Transactions: Series A*, 2008, **366**, 4007–4037.
- M. Tang, J. C. J. Camp, L. Rkiouak, J. McGregor, I. M. Watson, R. A. Cox, M. Kalberer, A. D. Ward and F. D. Pope, *Journal of Physical Chemistry*, 2014, **118**, 8817–8827.
- E. R. Garland, E. P. Rosen, L. I. Clarke and T. Baer, *Physical Chemistry Chemical Physics*, 2008, **10**, 3156–3161.
- Y. Li, M. J. Ezell and B. J. Finlayson-Pitts, *Atmospheric Environment*, 2011, **45**, 4123–4132.
- A. Ray, B. Devakottai, A. Souyri and J. Huckaby, *Langmuir*, 1991, **7**, 525–531.
- A. Riziq, M. Trainic, C. Erlick, E. Segre and Y. Rudich, *Atmospheric Chemistry and Physics Discussions*, 2007, **7**, 18113–18144.
- J. B. Gilman, T. L. Eliason, A. Fast and V. Vaida, *J. Colloid Interface Science*, 2004, **280**, 234–243.
- E. González-Labrada, R. Schmidt and C. E. DeWolf, *Physical Chemistry Chemical Physics*, 2007, **9**, 5814–5821.
- M. D. King, A. R. Rennie, K. C. Thompson, F. N. Fisher, C. C. Dong, R. K. Thomas, C. Pfrang and A. V. Hughes, *Physical Chemistry Chemical Physics*, 2009, **11**, 7699–7707.
- C. Pfrang, F. Sebastiani, C. O. M. Lucas, M. D. King, I. D. Hoare, D. Chang and R. A. Campbell, *Physical Chemistry Chemical Physics*, 2014, **16**, 13220–13228.
- L. F. Voss, M. F. Bazerbashi, C. P. Beekman, C. M. Hadad and H. C. Allen, *Journal of Geophysical Research: Atmospheres*, 2007, **112**, 1–9.
- L. F. Voss, C. M. Hadad and H. C. Allen, *Journal of Physics and Chemistry*, 2006, **110**, 19487–19490.
- M. N. Romanías, H. Ourrad, F. Thévenet and V. Riffault, *J. Physical Chemistry A*, 2016, **120**, 1197–1212.
- Y. Fang, M. Tang and V. H. Grassian, *J. Phys. Chem.*, 2016.
- M. J. Tang, P. J. Telford, F. D. Pope, L. Rkiouak, N. L. Abraham, A. T. Archibald, P. Braesicke, J. A. Pyle, J. McGregor, I. M. Watson, R. A. Cox and M. Kalberer, *Atmospheric Chemistry and Physics*, 2014, **14**, 6035–6048.
- M. D. King, O. R. Hunt, A. D. Ward and C. Pfrang, *Faraday Discussions*, 2008, **137**, 2007–2009.
- A. D. Ward, M. Zhang and O. Hunt, *Optical Express*, 2008, **16**, 16390–16403.
- S. H. Jones, M. D. King and A. D. Ward, *Physical Chemistry Chemical Physics*, 2013, **15**, 20735–20741.
- G. David, K. Esat, I. Ritsch and R. Signorell, *Physical*

- Chemistry Chemical Physics*, 2016, **18**, 5477–5485.
- 51 F. A. Jenkins and H. E. White, McGraw-Hill Science, 1976.
- 52 E. Fällman and O. Axner, *Applied Optics*, 1997, **36**, 2107–2113.
- 53 C. Bohren and D. R. Huffman, *Wiley Scientific*, 1998.
- 54 A. K. Ray and R. Nandakumar, *Applied Optics*, 1995, **34**, 7759–7770.
- 55 A. Aden and M. Kerker, *Journal of Applied Physics*, 1951, **22**, 1242–1246.
- 56 O. B. Toon and T. P. Ackerman, *Applied Optics*, 1981, **20**, 3657–3660.
- 57 E. E. Remsberg, D. Lavery and B. Crawford, *Journal of Chemical Engineering Data*, 1974, **19**, 263–265.
- 58 K. F. Palmer and D. Williams, *Applied Optics*, 1975, **14**, 208–219.
- 59 R. T. Tisdale, D. L. Glandorf, M. A. Tolbert and B. Toon, *Journal of Geophysical Research*, 1998, **103**, 25353–25370.
- 60 R. F. Niedziela, M. L. Norman, R. E. Miller and D. R. Worsnop, *Geophysical Research Letters*, 1998, **25**, 4477–4480.
- 61 C. E. Lund Myhre, D. H. Christensen, F. M. Nicolaisen and C. J. Nielsen, *Journal of Physical Chemistry A*, 2003, **107**, 1979–1991.
- 62 R. Wagner, S. Benz, H. Bunz, O. Mohler, H. Saathoff, M. Schnaiter, T. Leisner and V. Ebert, *Journal of Physical Chemistry A*, 2008, **112**, 11661–11676.
- 63 U. K. Krieger, J. C. Mössinger, B. Luo, U. Weers and T. Peter, *Applied Optics*, 2000, **39**, 3691–3703.
- 64 C. Mund and R. Zellner, *ChemPhysChem*, 2003, **4**, 638–645.
- 65 W. M. Haynes, CRC Press, 2016.
- 66 I. H. Malitson, *Journal of Optical Society America*, 1965, **55**, 1205–1209.
- 67 Z. Hu and D. C. Ripple, *Journal of Research of the National Institute of Standards and Technology*, 2014, **119**, 674–682.
- 68 Y. Qiu and V. Molinero, *Journal of the American Chemical Society*, 2015, **137**, 10642–10651.
- 69 R. E. O'Brien, B. Wang, S. T. Kelly, N. Lundt, Y. You, A. K. Bertram, S. R. Leone, A. Laskin and M. K. Gilles, *Environmental Scientific Technology*, 2015, **49**, 4995–5002.
- 70 D. J. Stewart, C. Cai, J. Nayler, T. C. Preston, J. P. Reid, U. K. Krieger, C. Marcolli and Y. H. Zhang, *Journal of Physical Chemistry A*, 2015, **119**, 4177–4190.
- 71 Y. You and A. K. Bertram, *Atmospheric Chemistry and Physics*, 2015, **15**, 1351–1365.
- 72 J. P. Reid, B. J. Dennis-Smith, N. O. A. Kwamena, R. E. H. Miles, K. L. Hanford and C. J. Homer, *Physical Chemistry Chemical Physics*, 2011, **13**, 15559–15572.
- 73 Y. Wu, T. Cheng, X. Gu, L. Zheng, H. Chen and H. Xu, *Journal of Quantitative Spectroscopy and Radiative Transfer*, 2014, **135**, 9–19.
- 74 A. Soewono and S. N. Rogak, *Aerosol Science and Technology*, 2013, **47**, 267–274.
- 75 M. Kahnert, T. Nousiainen and H. Lindqvist, *Optical*, 2013, **21**, 7974–7993.
- 76 Y. Wu, T. Cheng, L. Zheng and H. Chen, *Journal of Quantitative Spectroscopy and Radiative Transfer*, 2016, **182**, 1–11.

Paper 2: Following the refractive index of squalene droplets during oxidative ageing

Rosalie H. Shepherd, Martin D. King and Andrew D. Ward

To be submitted to the Journal of Atmospheric Chemistry and Physics.

I declare I have made the following contributions to the piece of co-authored work:

- Conducted the experiments, and collected and analysed all data collected
- Contributed to the conclusions drawn from the experiments conducted
- Authored the paper

Following the refractive index of squalene droplets during oxidative ageing

Rosalie H. Shepherd^{1, 2}, Martin D. King¹ and Andrew D. Ward²

¹Department of Earth Sciences, Royal Holloway, University of London, Egham, Surrey, TW20 0EX, UK

5 ²Central Laser Facility, Research Complex, Rutherford Appleton Laboratory, Oxford, OX11 0FA, UK

Correspondence to: Andrew D. Ward (andy.ward@stfc.ac.uk)

Organic aerosols are ubiquitous in the atmosphere. The behaviour of organic aerosols or organic coatings on aerosol are of interest when considering the physical properties, light scattering properties and albedo of atmospheric aerosols. In the study presented, the chemical ageing of squalene when in the form of an organic aerosol was investigated. Squalene was used as a proxy aerosol to provide an insight into the oxidation of an unsaturated organic aerosol. The study applied optical trapping techniques simultaneously with Mie spectroscopy to determine the refractive index of squalene droplets over a wide wavelength range with sub-nanometre resolution. The change in refractive index and diameter as a function of time was followed as the squalene droplets were exposed to the atmospheric oxidant, ozone. During the oxidative ageing process the diameter of optically trapped squalene droplets decreased from 2.736±0.002 µm to 2.570±0.002 µm and the refractive index increased by 0.169±0.0026. Such changes were accompanied by a density increase and a change in phase from a liquid to a solid. Interestingly, similar changes were observed when the squalene droplets were exposed to oxygen.

1. Introduction

20 Atmospheric aerosols have a prominent role in determining climate and global temperatures e.g. Alley et al. (2007). Aerosols directly affect climate through scattering or absorbing incoming solar radiation e.g. Toon and Pollack (1980), and additionally have an indirect effect on global temperatures through serving as cloud condensation nuclei and ice particle nuclei e.g. Andreaea and Rosenfeld (2008), Breon et al. (2002) and Rosenfeld et al. (2008). Understanding atmospheric aerosols is paramount for accurate predictions of current and future climate scenarios e.g. Stocker et al. (2013).

25 Organic aerosols are omnipresent in the atmosphere e.g. Eliason et al. (2004) and Slade and Knopf (2014). Substantial research has been conducted to understand organic aerosols contribution to the radiative forcing balance of the atmosphere through characterising the optical scattering and absorbing cross-sections of atmospheric aerosols. Organic aerosols that fall into the category of brown carbon are commonly known for their absorption properties e.g. Andreae and Ramanathan (2013), with the absorption properties of brown carbon having been reported to be 0.1 to 0.25 W m⁻² as determined by Bond et al. (2013) and Feng et al. (2013). On the other hand, the refractive index of atmospheric aerosols has been commonly used to quantify the optical scattering ability of the aerosol. Measurements of the refractive indices of organic aerosols have been predominantly determined at fixed monochromatic wavelengths e.g. Cai et al. (2016), Flowers et al. (2010), Guyon et al. (2003), Hoffer et al. (2005), Kim and Paulson (2013), Kim et al. (2014), Liu et al. (2013) and Yamasoe et al. (1998). Washenfelder et al. (2013) applied broadband cavity enhanced spectroscopy alongside cavity ring-down spectroscopy to determine the refractive index of the atmospheric proxy compounds nigrosin and fulvic acid at 360

and 420 nm, whilst Zhao et al. (2013) developed a blue light-emitting diode incoherent broad-band cavity-enhanced spectroscopy technique to determine the refractive index of polystyrene latex spheres and ammonium sulphate in the wavelength range of 445 to 484 nm.

The optical properties of atmospheric aerosol need to be quantified for the entire lifetime of the aerosol owing to the highly oxidising environment of the atmosphere e.g. Chapleski et al. (2016) and Ellison et al. (1999). Oxidative chemical ageing will change the refractive index of the aerosol owing to changes in chemical speciation, molecular weight, density and polarisability e.g. Cappa et al. (2011), Flores et al. (2014) and Lambe et al. (2013). Refractive indices are a critical parameter used to quantify the optical properties of aerosols. Flores et al. (2014) monitored the evolution of the complex refractive index of an organic aerosol comprising of α -pinene and limonene in the UV range of 360 to 420 nm, Lambe et al. (2013) studied the refractive index change of proxy anthropogenic aerosols at 405 nm and 532 nm, whilst Cappa et al. (2011) studied the change in refractive index at 532 nm of squalene and azelic acid upon exposure to OH radicals. Several studies have observed an increase in refractive index upon exposure to oxidants e.g. Cappa et al. (2011) who exposed biogenic aerosols to OH radicals, Nakayama et al. (2013) who photooxidised anthropogenic-like aerosols, and Flores (2014) who oxidised anthropogenic and biogenic aerosols. However, Lambe et al. (2013) observed a decrease in refractive index when secondary organic aerosol was exposed to oxidants. Cappa et al. (2011), Nakayama et al. (2013) and Lambe et al. (2013) studied the refractive index of aerosols at fixed wavelengths.

The study presented here has focused on the refractive index change of squalene upon exposure to atmospheric levels of ozone; the study presented extends previous work by studying the change in refractive index over a continuous wavelength range of 450 to 650 nm. A number of studies referenced in the paper used squalene as a model indoor-aerosol, however for the purpose of the study presented here squalene was used to provide an insight into an unsaturated proxy-aerosol

Previous studies have investigated the exposure of indoor squalene to ozone. Ozone has significant presence in buildings owing to ventilation bringing outdoor ozone indoors and machines such as photocopiers and electrostatic precipitators generating ozone e.g. Wisthaler and Weschler (2010). Subsequently, the oxidation of squalene with ozone has featured in a number of previous studies e.g. Athanasiadis et al. (2016), Fooshee et al. (2015), Fu et al. (2013), Petrick and Dubowski (2009), Wang and Waring (2014), Wells et al. (2008) and Wisthaler and Weschler (2010). Squalene is a triterpene containing six unconjugated double bonds (Fu et al., 2013), and hence squalene reacts rapidly with ozone (Fooshee et al., 2015). The oxidation of squalene with ozone in previous studies has demonstrated that the reaction pathway can be varied and the resulting products complex: early studies in the field demonstrated the production of diperoxides e.g. Bolland and Hughes (1949), whilst later studies conducted by Fooshee et al. (2015) identified peroxy containing products to be prominent, with many products also containing hydroxyl and ether groups. Naziri et al. (2014) additionally determined epoxides, aldehydes and ketones as possible products. To identify products from the reaction between ozone and squalene, Wells et al. (2008) applied experimental techniques such as gas chromatography and mass spectroscopy to identify reaction products such as 6-methyl-5-hepten-2-one, glyoxal and 4-oxopentanal.

Other studies have moved away from focusing on indoor squalene and investigated the oxidation of squalene with OH radicals e.g. Kolesar et al. (2014), Nah et al. (2014) and Nah et al. (2014), singlet oxygen e.g. Kohno et al. (1995) and by photooxidation e.g. Fujita et al. (1993).

In the study presented, squalene was exposed to ozone to replicate the oxidation of unsaturated organic atmospheric aerosols in the atmosphere. Optical trapping techniques applied simultaneously with Mie spectroscopy allowed levitated squalene droplets to be characterised in terms of refractive index and diameter before and after exposure to either ozone, oxygen or nitrogen by a contact free method e.g. Huckaby et al. (1994), Jones et al. (2013) and David et al. (2016). The refractive index as a function of wavelength was determined over the wavelength range 450 to 650 nm. The central aim of the study was to determine the refractive index of squalene droplets before and after oxidation, however through applying the optical trapping technique simultaneously with Mie spectroscopy the change in refractive index and diameter was

monitored as a function of time during the oxidative ageing of squalene droplets as well.

2. Experimental Methods

Squalene micron-sized droplets were optically trapped and the refractive index and diameter of the droplets determined by applying Mie spectroscopy.

5 2.1. Optical trapping and aerosol generation

Single squalene droplets were optically levitated by a 1064 nm continuous wave Nd:YAG laser beam (Ventus, Laser Quantum) that was split into two by a 50:50 beam splitter to form a vertically aligned, counter propagating optical trap e.g. Ashkin and Dziedzic (1975) and Fällman and Axner (1997). The optical trap provided a contact free method of studying atmospheric aerosols. The two laser beams passed through beam expansion optics before entering two vertically opposing
10 microscope objective lenses (Mitutoyo NIR $\times 50$ NA 0.42) that focused the laser beams to form an optical trap. The position of the upper optical pathway and objective lens was controlled by a piezo-stage (Physik-Instrumente) in the x, y and z planes. A simplified schematic of the optical trapping setup is shown by Jones et al. (2013).

An aluminium cell encased the trapping environment. The cell had two quarter-inch inlets and one quarter-inch outlet: the two inlets were used as a pathway for airborne aerosols or gases to enter the cell, whilst the outlet acted as an
15 exhaust. One inlet was for the passage of airborne squalene droplets, whilst the other allowed the gases to enter the cell. Borosilicate cover slips were mounted on the top and bottom of the aluminium cell to allow the two laser beams to enter the cell unattenuated. A MassView flow mass meter maintained the flow of all gases at 40 ml min⁻¹. Ozone was produced by flowing oxygen at 40 ml min⁻¹ through an ozoniser (Ultra Violet Products Ltd). The ozone-mixing ratio was kept at a concentration of 0.4 ppm, an ozone concentration higher than tropospheric conditions by approximately a factor of ten. . The
20 ozone concentration of the cell was calibrated with an electrochemical sensor (EcoSensors A-22 Portable Ozone Meter). Owing to the highly oxidative nature of ozone, oxidative ageing blank experiments where either nitrogen or oxygen flowed through the cell were also carried out with the ozoniser switched off.

Brightfield illumination was configured along the same axis as the laser pathway. Just before the imaging camera an optical filter was placed to remove the laser wavelength and allow imaging of the trapped droplet. Images of the droplet
25 could be acquired whilst the droplet was trapped and after the droplet was lowered onto the borosilicate cover slip.

A nebuliser (aerosonic travel ultrasonic nebuliser) delivered a mist of squalene droplet to the sample cell. Squalene was sourced from Sigma Aldrich, product number S3626. Owing to the viscosity of pure squalene, isopropanol (Sigma-Aldrich, product number 34965) was added in the ratio 14 to 1 (isopropanol to squalene) to enable squalene to form airborne droplets e.g. Athanasiadis et al. (2016). The isopropanol evaporated during transit or immediately upon the optical trapping
30 of the squalene droplet. The airborne droplets travelled through quarter-inch PTFE tubing to reach the cell. Once trapped, the diameter of the trapped squalene droplets varied from 1 μm to over 4 μm , however droplets with a diameter of approximately 2 μm were used in the study presented here.

2.2. Data collection and analysis

Upon trapping, a white light LED (Comar 0.1 LD 555, 6 V) illuminated the trapped droplet, and the elastic, backscattered
35 light was collected over the 25-degree cone angle of the microscope. The light then passed into a spectrometer (Acton SP2500i) and onto a charge coupled device (Princeton Instrument Spec 10:400 BR). The light was dispersed over a total wavelength range of 450 to 650 nm. The process produced a spectrum of light intensity versus wavelength, with a resolution

of 0.06 nm per pixel; for the purpose of the study the spectrum will be called a Mie spectrum henceforth in the paper. The spectrometer and charge-coupled device were calibrated for wavelength using the spectral lines from an Argon gas lamp.

Mie spectra collected at the start and end of the oxidative ageing process covered the wavelength range 450 to 650 nm. Spectra collected during the oxidation of the squalene droplets were collected without scanning the grating and over an integration time of 3 seconds, and thus the wavelength range was reduced to 520 to 600 nm. Mie spectra were continuously collected until the Mie spectra were observed not to change.

Mie spectroscopy, as explained by Bohren and Huffman (1998), was applied to the spectrum to determine the refractive index as a function of wavelength and diameter of the trapped droplet by using the relationship as outlined in the Cauchy equation (Jenkins and White, 1976):

$$n = A + \frac{B}{\lambda^2} + \frac{C}{\lambda^4}, \quad (1)$$

where n is the real component of the refractive index, λ is wavelength and A , B and C are the Cauchy coefficients. To determine the refractive index and diameter of the squalene droplets, Mie spectra collected at the start and end of the oxidative process, as well as a selection of spectra picked during the oxidative process, were simulated. The diameter and refractive index values of the squalene droplets were iterated until the calculated spectrum matched the experimental data.

To determine the change in refractive index and diameter throughout the oxidative ageing, every fifth to eighth spectra were fitted by the method outlined above. The refractive index and diameter of the remaining spectra were interpolated between these points. A differential refractometer (Brookhaven Differential) was applied to determine the refractive index of bulk-unoxidized squalene to provide a reference for the refractive index of newly trapped squalene droplets at a fixed wavelength.

3. Results & Discussion

Optical trapping and Mie spectroscopy techniques were applied to determine the continuous change in refractive index as a function of wavelength and diameter of a squalene droplet upon exposure to either 0.4 ppm ozone in oxygen, oxygen only or nitrogen only. All gases were dry. Each different gaseous condition was repeated three times. Between each experimental run, the cell was cleaned with methanol, flushing with nitrogen and a new squalene droplet optically trapped.

3.1. Refractive index of freshly trapped squalene droplets

Mie spectra of optically levitated squalene droplets were obtained upon trapping and simulated to determine the refractive index and diameter of the squalene droplet before oxidation. Figure 1 compares a typical experimental Mie spectrum for a freshly trapped squalene droplet with the simulated Mie spectrum. From the Mie spectra of four freshly trapped different squalene droplets the average and standard deviation for the Cauchy coefficients A , B and C were determined to be 1.4730 ± 0.0008 , $7500 \pm 750 \text{ nm}^2$, $8.4\text{E}+7 \pm 7.0\text{E}+7 \text{ nm}^4$ respectively, which gives a refractive index of 1.4953 ± 0.0026 at 589 nm. Figure 2 depicts the refractive index dispersion of the trapped squalene droplets before and after exposure to gas. The decrease in refractive index as the wavelength increases is a pattern also demonstrated by Nakayama et al. (2015), who photooxidised the proxy secondary organic aerosol isoprene in the presence of NO_x , as well as Liu (2015) and Liu (2013) who studied the oxidation of proxy secondary organic aerosols over the wavelength range 220 to 1200 nm in both studies. The diameter of the initially trapped squalene droplets ranged from 2.544 to 2.910 μm .

A small variation in the refractive index of squalene upon optical trapping can be observed in Fig. 2, and has been attributed to a slow oxidation in air e.g. Archer et al. (2005) and Mountfort et al. (2007). Application of a differential refractometer to bulk samples of squalene determined the typical refractive index range for squalene under room conditions

to be 1.5058 ± 0.0154 at 470 nm and is displayed by the error bars in Fig. 2. Additionally, close similarities between literature refractive index values (1.494 at 589 nm e.g. Haynes, 2016) and the experimental refractive index values demonstrates how little the optically trapping process altered the physical and chemical properties of the squalene droplets.

3.2. Oxidation of squalene droplets

In the study presented, squalene was exposed to 0.4 ppm ozone to replicate atmospheric oxidative ageing. Through applying optical trapping techniques simultaneously with Mie spectroscopy, the refractive index and diameter of the droplets could be determined. Interestingly, previous studies in similar fields reported either an increase or decrease in refractive index as an aerosol was exposed to atmospheric oxidants e.g. Cappa et al. (2011), Flores et al. (2014), Lambe et al. (2013) and Nakayama et al. (2013). Cappa et al. (2011) observed the complex refractive index of the saturated version of squalene, squalane, to increase by 20 percent upon exposure to OH radicals, but contrastingly Lambe et al. (2013) studied the OH oxidation of secondary organic aerosol precursors such as α -pinene and naphthalene and observed the complex refractive index to decrease with an increasing oxygen to carbon ratio.

Figure 3 depicts a profile of the measured refractive index and diameter change of an optically trapped squalene droplets upon exposure to ozone. Figure 3 shows an overall increase in refractive index of 0.0169 ± 0.0026 ; the increase in refractive index upon exposure to atmospheric oxidants is in line with results reported by Flores et al. (2014), Cappa et al. (2011) and Nakayama et al. (2013). Interestingly, a decrease in refractive index was observed after the diameter of the trapped droplet had stabilised.

The diameter of the optically trapped squalene showed an initial increase followed by a decrease: the diameter of the squalene droplets overall decreased by $0.166 \mu\text{m}$. The initial increase in diameter of the droplet was attributed to ozone dissolving into the droplet, whilst the departure of volatile by-products and potential formation of polymer products would result in a decrease in diameter. In addition, the departure of volatile by-products and potential formation of polymer products may result in the formation of a more viscous droplet e.g. Athanasiadis et al. (2016). To test if the squalene droplet was becoming more viscous, the optical trap could be lowered so as to place the optically trapped droplet onto the borosilicate cover slip. The initial pure squalene droplet would wet the surface and lose its spherical shape, whilst the squalene droplets that were exposed to ozone did not. Figure 4 depicts images for (a) an oxidised squalene droplet and (b) an unoxidized droplet. In Fig. 4a, the droplet held its spherical shape upon deposition onto the borosilicate cover slip. The spherical shape and size did not change on inspecting the droplet at later times after deposition and it was assumed that the droplet was in fact a solid. In accordance to the results reported in the study presented here, Athanasiadis et al. (2016) reported partial solidification of squalene droplets upon complete ozonolysis. For a droplet exposed to 0.4 ppm ozone, and assuming there is no evaporation of products, the reduction in droplet size would result in the density of squalene increasing from 0.858 g cm^{-3} e.g. Haynes (2016) to 1.021 g cm^{-3} , indicating the potential for an oligomerisation or polymerisation process to be occurring.

Owing to the likely solidification of the squalene droplet during oxidative chemical ageing, it was of interest to determine whether the droplet had become partially solid or solid throughout. A partially solid aerosol could resemble a solid shell surrounding a liquid core; a morphology often called core-shell. To elucidate the potential morphology of the aerosol, several steps need to be considered. Firstly, the diffusion of ozone through the sample cell to the optically trapped droplet is considered. Ozone will likely move quickly through the cell to the trapped droplet by turbulence in the cell, however the last few μm surrounding the trapped droplet may be diffusion controlled. From Table 1, it can be noted that the diffusion of ozone through air is quick and therefore ozone will quickly reach the optically trapped aerosol. Secondly, the travel of ozone through a viscous liquid is considered. From Table 1, it can be observed that the condensed phase diffusion of ozone in a viscous liquid is slow (0.1 ms), whilst the condensed phase reaction is fast (0.0006 ms). However, the diffusion reactive length of ozone in a viscous liquid is $2.9 \mu\text{m}$, which is similar to the size of the optically trapped squalene droplet. Therefore, it is

unlikely that there will be an ozone concentration profile throughout the optically trapped droplet as the ozone will be able to penetrate the entire droplet before reacting. Hence, it is unlikely that the aerosol will form a core-shell morphology upon exposure to ozone. The movement of ozone through a viscous liquid is fast enough to reach the core of the aerosol over very short timescales. However, as the aerosol reacts and becomes more viscous these parameters may change.

5 3.4. Oxidation control experiments

Owing to the highly oxidative nature of ozone, oxidative ageing blanks were run. The experiments involved exposing a freshly trapped squalene droplet to either nitrogen flowing at 40 ml min⁻¹ or oxygen flowing at 40 ml min⁻¹. The oxidative ageing blank involving nitrogen gas demonstrated that the optically trapped squalene is, in essence, inert to nitrogen gas and hence very little change in refractive index and diameter is observed over the 100-minute timescale. Figure 2 demonstrates that there is very little change in the refractive index dispersion of a squalene droplet before and after exposure to nitrogen.

The second oxidative ageing blank was the exposure of optically trapped squalene droplet to gas-phase oxygen only. Naziri et al. (2014) described squalene as stable in the presence of oxygen, however, work conducted by Archer et al. (2005) and Mountford et al. (2007) demonstrated that squalene does alter upon exposure to room-level oxygen; squalene is a known compound in fingerprints and has been a chemical studied to determine the ageing of fingerprints. Archer et al. (2005) determined the proportion of squalene present in a fingerprint decreases when stored in air in either light or dark conditions, whilst Mountford et al. (2007) discovered that squalene decreased to 1 percent of its original amount after 15 days exposure to room light. In the study presented it was observed that oxygen caused a significant change in an optically trapped squalene droplet, as displayed in Fig. 5.

From Fig. 5, it can be observed that over 100 minutes the refractive index increases by 0.0169±0.0026 or 0.0173±0.0026 for squalene droplets exposed to ozone or oxygen respectively, whilst the diameter of the trapped droplet decreases by 0.166±0.002 when exposed to ozone, or increases by 0.020±0.002 µm when exposed to oxygen. The increase in diameter could be attributed to an additional 40 minutes being required until the Mie spectrum was observed to have stopped changing. Over the extended time period the change in refractive index and diameter began to show similarities to the squalene droplet that was exposed to ozone: the refractive index increased and the diameter began to decrease. However, owing to an additional 40 being required for the similarities to be observed, it can be concluded that the reaction between ozone and squalene is much faster relative to the reaction between oxygen and squalene. Hence, when considering the reaction between ozone and squalene any effects from oxygen can be ignored.

Interestingly, the reaction between squalene and oxygen shows a sudden increase in refractive index at approximately 80 minutes whilst the reaction between squalene and ozone does not. The sudden increase indicates that squalene is reacting with oxygen; the initially slow alteration in refractive index indicates that a slow initial reaction is occurring, resulting in the formation of a species that may lead to the catalysis of a further quick reaction.

4. Conclusion

The results presented in the paper demonstrate the application of a technique that successfully determined the wavelength-dependent refractive index and diameter of a trapped squalene droplet with a high level of accuracy for a continuously changing system.

Initial refractive index measurements of freshly trapped squalene droplet showed slight variation, demonstrating the susceptibility of squalene to alter upon exposure to laboratory room air. Upon trapping, the squalene droplets were exposed to the atmospheric oxidant ozone at a concentration of 0.4 ppm. The oxidative ageing profile was collected in terms of refractive index and diameter; the refractive index increased by 0.0169±0.0026, whilst the diameter decreased by 0.166±0.002 µm. From analysis of the profile gaseous uptake, density change as well as phase change could be identified.

Squalene is an atmospheric chemical owing to plants and animals producing squalene as a biochemical intermediate. Understanding the behaviour of atmospheric squalene, in particular focusing on the change in refractive index and droplet diameter, is important to quantify how organic aerosol affects the radiative balance of our planet. In the absence of other data sources, the change in squalene could be applied for other chemical systems with similar properties to squalene.

5 Author Contributions

Rosalie H. Shepherd conducted all experiments, analysed and interpreted the data collected and wrote the paper. Martin D. King and Andrew D. Ward conceived the experimental idea and assisted during the experiment.

Data Availability

Data can be found at 10.5281/zenodo.845408.

10 Competing Interests

The authors declare that they have no conflict of interest.

Acknowledgments

The authors would like to thank the Central Laser Facility for granting access time on the optical trapping equipment based at Rutherford Appleton Laboratories. In addition, Rosalie H. Shepherd would like to thank STFC for funding the student grant ST/L504279/1.

References

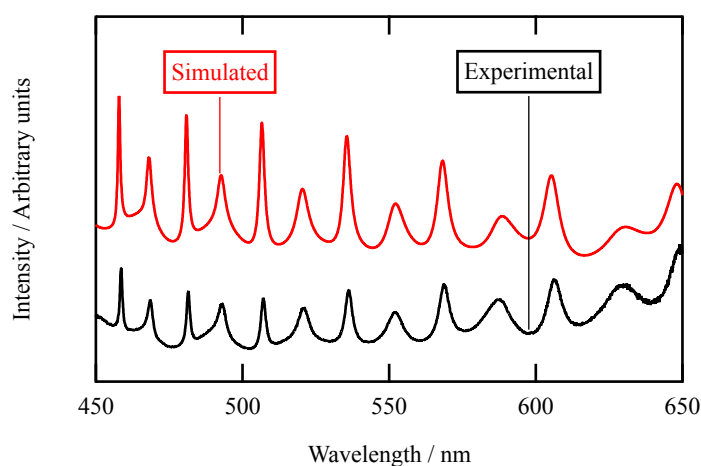
- Alley, R., Berntsen, T., Bindoff, N. L., Chen, Z., Chidthaisong, A., Friedlingstein, P., Gregory, J., Hegerl, G., Heimann, M., Hewitson, B., Hoskins, B., Joos, F., Jouzel, J., Kattsov, V., Lohmann, U., Manning, M., Matsuno, T., Molina, M., Nicholls, N., Overpeck, J., Qin, D., Raga, G., Ramaswamy, V., Ren, J., Rusticucci, M., Solomon, S., Somerville, R., Stocker, T. F., Stott, P., Stouffer, R. J., Whetton, P., Wood, R. A. and Wratt D R., T..Berntsen, N. I. Bindoff, Z. Chen, A. Chidthaisong, P. Friedlingstein, J. Gregory and G. Hegerl. 2007. "Climate Change 2007: The Physical Science Basis." Intergovernmental Panel on Climate Change.
- Andreae, M. O., and V Ramanathan. 2013. "Climate's Dark Forcings." *Science*. **340**(April): 280–81. doi: 10.1126/science.1235731.
- Andreaea, M. O. and D. Rosenfeld. 2008. "Aerosol–cloud–precipitation Interactions. Part 1. The Nature and Sources of Cloud-Active Aerosols." *Earth Science Reviews*. **89**(1–2): 13–41. doi: 10.1016/j.earscirev.2008.03.001..
- Archer, N. E., Y. Charles, J. A. Elliott and S. Jickells. 2005. "Changes in the Lipid Composition of Latent Fingerprint

- Residue with Time after Deposition on a Surface.” *Forensic Science International*. **154**(2–3): 224–39. doi: 10.1016/j.forsciint.2004.09.120.
- Ashkin, A. and J. M. Dziedzic. 1975. “Optical Levitation of Liquid Droplets By Radiation Pressure.” *Science*. **187**(March): 1–3. doi: 10.1126/science.187.4181.1073.
- 5 Athanasios, A., C. Fitzgerald, N. M. Davidson, C. Giorio, S. W. Botchway, A. D. Ward, M. Kalberer, F. D. Pope and M. Kuimiva. 2016. “Dynamic Viscosity Mapping of the Oxidation of Squalene Aerosol Particles.” *Physical Chemistry Chemical Physics*. **18**(44): 30385–30393. doi: 10.1039/c6cp05674a.
- Bohren, C. F. and Donald. R Huffman. 1983. “Absorption and Scattering of Light by Small Particles.” Wiley Scientific.
- Bolland, J. L. and H. Hughes. 1949. “The Primary Thermal Oxidation Product of Squalene.” *Journal of the Chemical*
 10 *Society*. **0**: 492–497. doi: 10.1039/JR9490000492/
- Bond, T. C., S. J. Doherty, D. W. Fahey, P. M. Forster, T. Berntsen, B. J. DeAngelo, M. G. Flanner, S. Ghan, B. Kärcher, D. Koch, S. Kinne, Y. Kondo, P. K. Quinn, M. C. Sarofim, M. G. Schultz, M. Schulz, C. Venkataraman, H. Zhang, S. Zhang, N. Bellouin, S. K. Guttikunda, P. K. Hopke, M. Z. Jacobson, J. W. Kaiser, Z. Klimont, U. Lohmann, J. P. Schwarz, D. Shindell, T. Storelvmo, S. G. Warren and C. S. Zender 2013. “Bounding the Role of Black Carbon in the Climate System: A
 15 Scientific Assessment.” *Journal of Geophysical Research Atmospheres* **118**(11): 5380–5552. doi: 10.1002/jgrd.50171.
- Breon, F. M., D. Tanre and S. Generoso. 2002. “Aerosol Effect on Cloud Droplet Size Monitored from Satellite.” *Science* **295**: 834–39. doi: 10.1029/2009GL038451.
- Chen, C., R. E. H. Miles, M. I. Cotterell, A. Marsh, G. Rovelli, A. M. J. Rickards, Y. Zhang and J. P. Reid. 2016. “Comparison of Methods for Predicting the Compositional Dependence of the Density and Refractive Index of Organic-
 20 Aqueous Aerosols.” *Journal of Physical Chemistry A*. **120**(33): 6604–17. doi: 10.1021/acs.jpca.6b05986.
- Cappa, C. D., D. L. Che, S. H. Kessler, J. H. Kroll, and K. R. Wilson. 2011. “Variations in Organic Aerosol Optical and Hygroscopic Properties upon Heterogeneous OH Oxidation.” *Journal of Geophysical Research: Atmospheres*. **116**(15): 1–12. doi: 10.1029/2011JD015918.
- Chapleski, R. C., Y. Zhang, D. Troya and J. R. Morris. 2016. “Heterogeneous Chemistry and Reaction Dynamics of the
 25 Atmospheric Oxidants, O₃, NO₃ and OH on Organic Surfaces.” *Chemical Society Reviews*. **45**(3): 3731–46.
- David, G., K. Esat, I. Ritsch and R. Signorell. 2016. “Ultraviolet Broadband Light Scattering for Optically-Trapped Submicron-Sized Aerosol Particles.” *Physical Chemistry Chemical Physics*. **18**: 5477–85. doi: 10.1039/c5cp06940h.
- Eliason, T. L., J. B. Gilman and V. Vaida. 2004. “Oxidation of Organic Films Relevant to Atmospheric Aerosols.” *Atmospheric Environment*. **38**(9): 1367–78. doi: 10.1016/j.atmosenv.2003.11.025.
- 30 Ellison, G. B., A. F. Tuck and V. Vaida. 1999. “Atmospheric Processing of Organic Aerosols.” *Journal of Geophysical Research*. **104**(D9): 11633–11641. doi: 10.1029/1999JD900073.
- Fällman, E. and O. Axner. 1997. “Design for Fully Steerable Dual-Trap Optical Tweezers.” *Applied optics*. **36**(10): 2107–2113. doi: 10.1364/AO.36.002107.
- Feng, Y., V. Ramanathan and V. R. Kotamarthi. 2013. “Brown Carbon: A Significant Atmospheric Absorber of

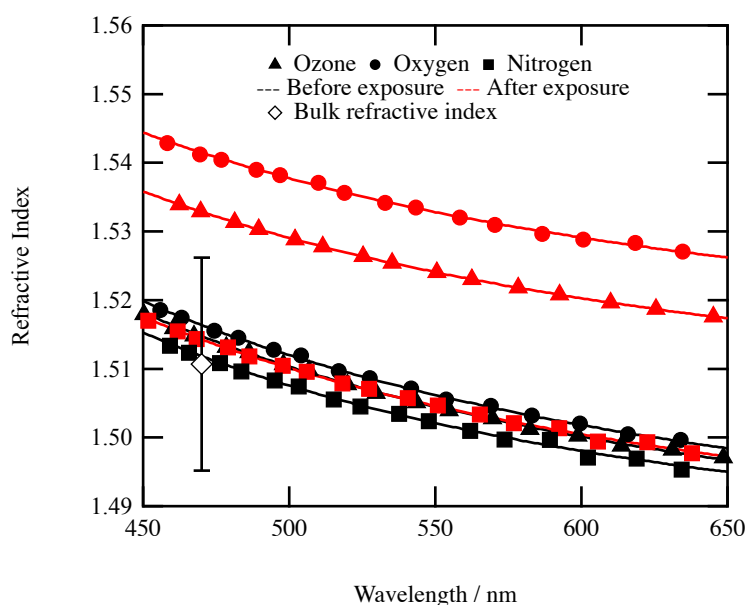
- Solar Radiation.” *Atmospheric Chemistry and Physics*. **13**(17): 8607–8621. doi: 10.5194/acp-13-8607-2013.
- Flores, J. M., D. F. Zhao, L. Segev, P. Schlag, A. Kiendler-Scharr, H. Fuchs, Å. K. Watne, N. Bluvshstein, T. F. Mentel, M. Hallquist and Y. Rudich. 2014. “Evolution of the Complex Refractive Index in the UV Spectral Region in Ageing Secondary Organic Aerosol.” *Atmospheric Chemistry and Physics*. **14**(11): 5793–5806. doi: 10.5194/acp-14-5793-2014.
- 5 Flowers, B. A., M. K. Dubey, C. Mazzoleni, E. A. Stone, J. J. Schauer, S. W. Kim and S. C. Yoon. 2010. “Optical-Chemical-Microphysical Relationships and Closure Studies for Mixed Carbonaceous Aerosols Observed at Jeju Island; 3-Laser Photoacoustic Spectrometer, Particle Sizing, and Filter Analysis.” *Atmospheric Chemistry and Physics*. **10**(21): 10387–10398. doi: 10.5194/acp-10-10387-2010.
- Fooshee, D. R., P. K. Aiona, A. Laskin, J. Laskin and S. A. Nizkorodov and P. F. Baldi. 2015. “Atmospheric Oxidation of Squalene: Molecular Study Using COBRA Modeling and High-Resolution Mass Spectrometry.” *Environmental Science & Technology*. **49**: 13304–13313. doi: 10.1021/acs.est.5b03552.
- 10 Grosjean, E. and D. Grosjean. 1995. “Rate Constants for the Gas-Phase Reaction of C5-C10 Alkenes with Ozone.” *International Journal of Chemical Kinetics*. **27**: 1045–1054. doi: 10.1002/kin.550271102.
- Guyon, P., O. Boucher, B. Grahama, J. Becka, O. L. Mayol-Bracero, G. C. Roberts, W. Maenhaut, P. Artaxoe and M. O. Andreae. 2003. “Refractive Index of Aerosol Particles over the Amazon Tropical Forest during LBA-EUSTACH 1999.” *Journal of Aerosol Science*. **34**(7): 883–907. doi: 10.1016/S0021-8502(03)00052-1.
- 15 Fujita, H., K. Tokiwa, K. Sayama, H. Mori and M. Sasaki. 1993. “Mechanistic Study of the Photooxidation of Squalene Sensitized with Terthiophene and Bithiophene.” *The Chemical Society of Japan*. **66**(10): 2960–2964. doi: 10.1246/bcsj.66.2960.
- 20 Haynes, W. 2016. *Handbook of Chemistry and Physics*. CRC Press.
- Hoffer, A., A. Gelencsér, P. Guyon, G. Kiss, O. Schmid, G. P. Frank, P. Artaxo and M. O. Andreae. 2005. “Optical Properties of Humic-like Substances (HULIS) in Biomass-Burning Aerosols.” *Atmospheric Chemistry and Physics*. **5**(4): 7341–7360. doi: 10.5194/acp-5-7341-2005.
- Huckaby, J. L., A. K. Ray and B. Das. 1994. “Determination of Size, Refractive Index, and Dispersion of Single Droplets from Wavelength-Dependent Scattering Spectra.” *Applied Optics*. **33**(30): 7112–7125. doi: 10.1364/AO.33.007112.
- 25 Jenkins, F. A. and H. E. White. 1976. *Fundamentals of Optics*. McGraw-Hill Science.
- Jones, S. H., M. D. King and A. D. Ward. 2013. “Determining the Unique Refractive Index Properties of Solid Polystyrene Aerosol Using Broadband Mie Scattering from Optically Trapped Beads.” *Physical Chemistry Chemical Physics*. **15**(47): 20735–20741. doi: 10.1039/c3cp53498g.
- 30 Kim, H. and S. E. Paulson. 2013. “Real Refractive Indices and Volatility of Secondary Organic Aerosol Generated from Photooxidation and Ozonolysis of Limonene, α -Pinene and Toluene.” *Atmospheric Chemistry and Physics*. **13**(15): 7711–7723. doi: 10.5194/acp-13-7711-2013.
- Kim, H., S. Liu, L. M. Russell and S. E. Paulson. 2014. “Dependence of Real Refractive Indices on O:C, H:C and Mass Fragments of Secondary Organic Aerosol Generated from Ozonolysis and Photooxidation of Limonene and α -Pinene.”

- Aerosol Science and Technology. **48**(5): 498–507. doi: 10.1080/02786826.2014.893278.
- Kohno, Y., Y. Egawa, S. Itoh, S. Nagaoka, M. Takahashi and K. Mukai. 1995. “Kinetic Study of Quenching Reaction of Singlet Oxygen and Scavenging Reaction of Free Radical by Squalene in N-Butanol.” *Biochimica et Biophysica Acta*. **1256**: 52–56. doi: 10.1016/0005-2760(95)00005-W.
- 5 Kolesar, K. R., G. Buffaloe, K. R. Wilson and C. D. Cappa. 2014. “OH-Initiated Heterogeneous Oxidation of Internally-Mixed Squalene and Secondary Organic Aerosol.” *Environmental Science and Technology*. **48**(6): 3196–3202. doi: 10.1021/es405177d.
- Kowert, B. A., M. B. Watson and N. C. Dang. 2014. “Diffusion of Squalene in N-Alkanes and Squalene.” *Journal of Physical Chemistry B*. **118**(8): 2157–2163. doi: 10.1021/jp411471r.
- 10 Laisk, A., O. Kull and H. Moldau. 1989. “Ozone Concentration in Leaf Intercellular Air Spaces Is close to Zero.” *Plant Physiology*. **90**(3): 1163–1167.
- Lambe, A. T., C. D. Cappa, P. Massoli, Timothy B. Onasch, S. D. Forestieri, A. T. Martin, M. J. Cummings, D. R. Croasdale, W. H. Brune, D. R. Worsnop and P. Davidovits. 2013. “Relationship between Oxidation Level and Optical Properties of Secondary Organic Aerosol.” *Environmental Science and Technology*. **47**(12): 6349–57. doi: 15 /10.1021/es401043j.
- Liu, P. F., N. Abdelmalki, H. M. Hung, Y. Wang, W. H. Brune and S. T. Martin. 2015. “Ultraviolet and Visible Complex Refractive Indices of Secondary Organic Material Produced by Photooxidation of the Aromatic Compounds Toluene and M-Xylene.” *Atmospheric Chemistry and Physics*. **15**(3): 1435–1446. doi: 10.5194/acp-15-1435-2015.
- Liu, P., Y. Zhang and S. T. Martin. 2013. “Complex Refractive Indices of Thin Films of Secondary Organic Materials by Spectroscopic Ellipsometry from 220 to 1200 nm.” *Environmental Science and Technology*. **47**(23): 13594–13601. doi: 20 10.1021/es403411e.
- Mountfort, K. A., H. Bronstein, N. Archer and S. M. Jickells. 2007. “Identification of Oxidation Products of Squalene in Solution and in Latent Fingerprints by ESI-MS and LC/APCI-MS.” *Analytical Chemistry*. **79**(7): 2650–2657. doi: 10.1021/ac0623944.
- 25 Nah, T., S. H. Kessler, K. E. Daumit, J. H. Kroll, S. R. Leoneabe and K. R. Wilson. 2014. “Influence of Molecular Structure and Chemical Functionality on the Heterogeneous OH-Initiated Oxidation of Unsaturated Organic Particles.” *Journal of Physical Chemistry A*. **118**(23): 4106–4119. doi: 10.1039/c3cp52655k.
- Nah, T., H. Zhang, D. R. Worton, C. R. Ruehl, B. B. Kirk, A. H. Goldstein, S. R. Leone and K. R. Wilson. 2014. “Isomeric Product Detection in the Heterogeneous Reaction of Hydroxyl Radicals with Aerosol Composed of Branched and Linear Unsaturated Organic Molecules.” *The Journal of Physical Chemistry A*. **118**: 11555–11571. doi: 10.1021/jp508378z.
- 30 Nakayama, T., Y. Matsumi, T. Imamura, A. Yamazaki and A. Uchiyama. 2013. “Wavelength and NO_x Dependent Complex Refractive Index of SOAs Generated from the Photooxidation of Toluene.” *Atmospheric Chemistry and Physics*. **13**(2): 531–545. doi: 10.5194/acp-13-531-2013.
- Nakayama, T., K. Sato, M. Tsuge, T. Imamura and Y. Matsumi. 2015. “Complex Refractive Index of Secondary Organic

- Aerosol Generated from isoprene/NO_x Photooxidation in the Presence and Absence of SO₂.” *Journal of Geophysical Research: Atmospheres*. **120**: 1–19. doi: 10.1002/2015JD023522.
- Naziri, E., R. Consonni and M. Z. Tsimidou. 2014. “Squalene Oxidation Products: Monitoring the Formation, Characterisation and pro-Oxidant Activity.” *European Journal of Lipid Science and Technology*. **116**(10): 1400–1411. doi: 10.1002/ejlt.201300506.
- Petrick, L. and Y. Dubowski. 2009. “Heterogeneous Oxidation of Squalene Film by Ozone under Various Indoor Conditions.” *Indoor Air*. **19**(5): 381–391. doi: 10.1111/j.1600-0668.2009.00599.x.
- Ramanathan, V. and G. Carmichael. 2008. “Global and Regional Climate Changes due to Black Carbon.” *Nature Geoscience*. **1**: 221–227. doi: 10.1038/ngeo156.
- Rosenfeld, D., U. Lohmann, G. B. Raga, C. D. O’Dowd, M. Kulmala, S. Fuzzi, A. Reissell and M. O. Andreae. 2008. “Flood or Drought: How Do Aerosols Affect Precipitation?” *Science*. **321**(5894): 1309–1313. doi: 10.1126/science.1160606.
- Slade, J. H. and D. A. Knopf. 2014. “Multiphase OH Oxidation Kinetics of Organic Aerosol: The Role of Particle Phase State and Relative Humidity.” *Geophysical Research Letters*. **41**(14): 5297–5306. doi: 10.1002/2014GL060582.
- Smith, G., D. E. Woods, C. L. DeForest, T. Baer and R. E. Miller. 2002. “Reactive Uptake of Ozone by Oleic Acid Aerosol Particles: Application of Single-Particle Mass Spectrometry to Heterogeneous Reaction Kinetics.” *Journal of Physical Chemistry A*. **106**(35): 8085–8095. doi: 10.1021/jp020527t.
- Stocker, T. F., D. Qin and G. K. Plattner. 2013. “Climate Change 2013: The Physical Science Basis (Technical Summary).” *International Panel on Climate Change*. 33–115.
- Toon, O. B. and J. B. Pollack. 1980. “Atmospheric Aerosols and Climate: Small Particles in the Earth’s Atmosphere Interact with Visible and Infrared Light, Altering the Radiation Balance and the Climate.” *American Scientist*. **66**(3): 268–278. doi: 10.1016/j.atmosenv.2013.11.009.
- Wang, C. and M. S. Waring. 2014. “Secondary Organic Aerosol Formation Initiated from Reactions between Ozone and Surface-Sorbed Squalene.” *Atmospheric Environment*. **84**: 222–29. doi: 10.1016/j.atmosenv.2013.11.009.
- Washenfeller, R. A., J. M. Flores, C. A. Brock, S. S. Brown and Y. Rudich. 2013. “Broadband Measurements of Aerosol Extinction in the Ultraviolet Spectral Region.” *Atmospheric Measurement Techniques*. **6**(4): 861–877. doi: 10.5194/amt-6-861-2013.
- Wells, J. R., G. C. Morrison and B. K. Coleman 2008. “Kinetics and Reaction Products of Ozone and Surface-Bound Squalene.” *Journal of ASTM International*. **5**(JULY): 1-12. doi: 10.1520/JAI101629.
- Wisthaler, A. and C. J. Weschler. 2010. “Reactions of Ozone with Human Skin Lipids: Sources of Carbonyls, Dicarboxylic Acids, and Hydroxycarbonyls in Indoor Air.” *Proceedings of the National Academy of Sciences*. **107**(15): 6568–6575. doi: 10.1073/pnas.0904498106.
- Yamasoe, M. A., Y. J. Kaufman, O. Dubovik, L. A. Remer, B. N. Holben and P. Artaxo 1998. “Retrieval of the Real Part of the Refractive Index of Smoke Particles from Sun/sky Measurements during SCAR-B.” *Journal of Geophysical Research*. **103**(98): 31893-31902. doi: 10.1029/98JD01211.
- Zhao, W., M. Dong, W. Chen, X. Gu, C. Hu, X. Gao, W. Huang and W. Zhang. 2013. “Wavelength-Resolved Optical



5 **Figure 1: An experimentally collected Mie spectrum of a freshly trapped squalene droplet with the simulated Mie spectrum purposefully offset.**



10 **Figure 2: Refractive index dispersion for optically trapped squalene droplets before (black markers) and after (red markers) oxidative ageing. Squalene aerosols were exposed to ozone, oxygen and nitrogen. The error bar represents the maximum refractive index change as determined by differential refractometer experiments; the error bar is at the wavelength the refractometer worked at (470 nm).**

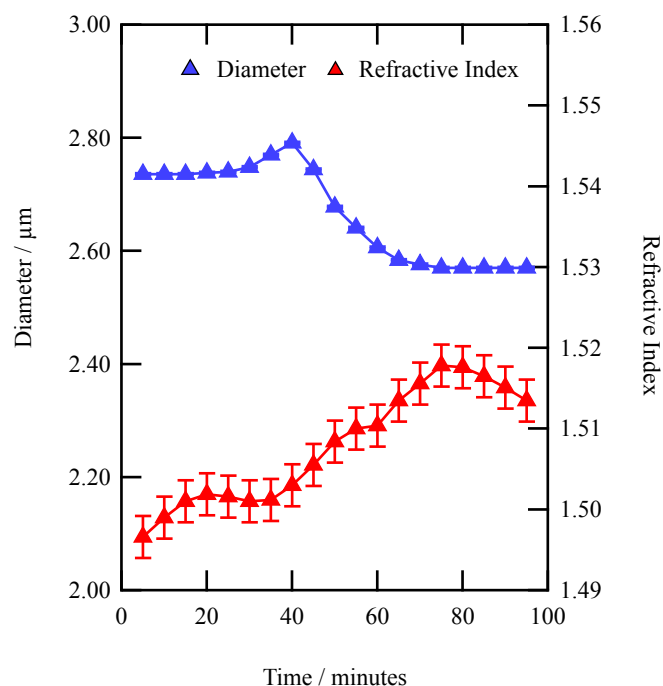


Figure 3: Continuous collection of Mie spectra whilst a squalene droplet was exposed to 0.4 ppm ozone facilitated the refractive index and diameter change during the oxidative ageing to be followed. The uncertainty in diameter is $\pm 0.002 \mu\text{m}$, however the error bars representing the uncertainty is smaller than the points used in the figure.

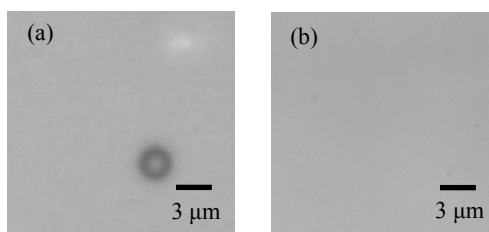


Figure 4: Brightfield illumination images of squalene droplets post exposure to oxidative gases. Squalene droplets were either found to be solid or liquid in phase. When squalene droplets were exposed to ozone or oxygen they were solid after the exposure (a), whilst freshly trapped aerosols were liquid (b). Squalene droplets exposed to nitrogen were also liquid after exposure. The white illumination in (a) is the laser reflection from the borosilicate cover slip.

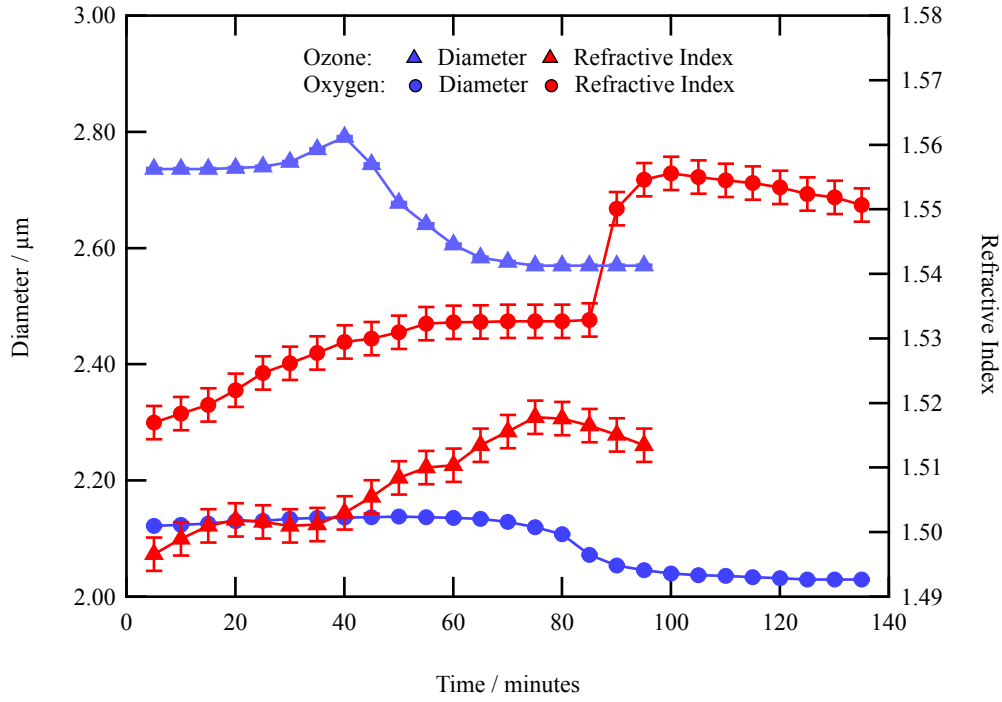


Figure 5: The refractive index and diameter change of an optically trapped squalene droplet upon exposure to gas-phase oxygen flowing at 40 ml min⁻¹ into the sample cell. The uncertainty in diameter is $\pm 0.002 \mu\text{m}$ and the error bars representing the uncertainty is smaller than the points used in the figure.

- 5 Table 1: Diffusion constants and reaction timescales were calculated for squalene droplets exposed to ozone. Owing to the lack of kinetic studies involving squalene, values for similar organic compounds were occasionally used. The radius of the trapped droplet was assumed to be 1.1 μm (the average radius of the optically trapped squalene droplets). The diffusion constants were taken from literature to be $D_g(O_3) = 1.37 \times 10^{-5} \text{ m}^2 \text{ s}^{-1}$ as measured by Laisk et al. (1989) and $1 \times 10^{-9} \text{ m}^2 \text{ s}^{-1}$ as measured by Smith et al. (2002) for ozone diffusion in oleic acid. For squalene [organic] was taken as $2.088 \text{ mol dm}^{-3}$ taken from Haynes (2016) and $k = 7.5 \times 10^5 \text{ dm}^3 \text{ mol}^{-1} \text{ s}^{-1}$ taken from the NIST kinetics database.
- 10

Process	Calculation	Value
Gas phase diffusion	$\frac{r^2}{\pi^2 D_g(O_3)}$	$9 \times 10^{-9} \text{ s} = 1 \text{ ns}$
Condensed phase diffusion of ozone in oleic acid	$\frac{r^2}{\pi^2 D_l(O_3)}$	$1.23 \times 10^{-4} \text{ s} = 0.1 \text{ ms}$
Condensed phase reaction	$\frac{1}{k[\text{organic}]}$	$6.3 \times 10^{-7} \text{ s} = 0.00063 \text{ ms}$
Diffuso reactive length	$\sqrt{\frac{D_l(O_3)}{k[\text{organic}]}}$	$2.9 \times 10^{-6} \text{ m} = 2.9 \mu\text{m}$

Paper 3: Determination of the refractive index of insoluble organic material from atmospheric aerosol over the visible wavelength range using optical tweezers

Rosalie H. Shepherd, Martin D. King, Amelia Marks, Neil Brough and Andrew D. Ward

A paper in the Journal of Atmospheric Chemistry and Physics Discussions: currently resubmitted after completing reviewer comments.

I declare I have made the following contributions to the piece of co-authored work:

- Collected wood smoke aerosol extracts and helped with the collection of urban aerosol extracts
- Extracted atmospheric aerosol from the collection filters
- Conducted the experiments, and collected and analysed all data collected
- Contributed to the conclusions drawn from the experiments conducted
- Authored the paper

Determination of the refractive index of insoluble organic extracts from atmospheric aerosol over the visible wavelength range using optical tweezers

Rosalie H. Shepherd^{1,2}, Martin D. King², Amelia Marks², Neil Brough³ and Andrew D. Ward¹

5 ¹Central Laser Facility, Research Complex, STFC Rutherford Appleton Laboratory, Oxford, OX11 0FA, UK

²Department of Earth Sciences, Royal Holloway University of London, Egham, Surrey, TW20 0EX, UK

³British Antarctic Survey, High Cross, Madingley Road, Cambridge, CB3 0ET, UK

Correspondence to: Martin King (m.king@rhul.ac.uk)

Optical trapping combined with Mie spectroscopy is a new technique used to record the refractive index of insoluble organic material extracted from atmospheric aerosol samples over a wide wavelength range with sub nanometer resolutions. The refractive index of the insoluble organic extracts was shown to follow a Cauchy equation between 460 to 700 nm for organic aerosol extracts collected from urban (London) and remote (Antarctica) locations. Cauchy coefficients for the remote sample were for the Austral summer and gave the Cauchy coefficients to be $A = 1.467$ and $B = 1000 \text{ nm}^2$ with a real refractive index of 1.489 at a wavelength of 589 nm. Cauchy coefficients for the urban samples varied with season, with extracts collected during summer having Cauchy coefficients of $A = 1.465 \pm 0.005$ and $B = 4625 \pm 1200 \text{ nm}^2$ with a representative real refractive index of 1.478 at a wavelength of 589 nm, whilst samples extracted during autumn had larger Cauchy coefficients of $A = 1.505$ and $B = 600 \text{ nm}^2$ with a representative real refractive index of 1.522 at a wavelength of 589 nm. The refractive index of absorbing aerosol was also recorded. The technique applied in the presented study allowed the absorption Ångström exponent to be determined for wood smoke and humic acid aerosol extract. Typical values of the Cauchy coefficient for the wood smoke aerosol extract were $A = 1.541 \pm 0.03$ and $B = 14800 \pm 2900 \text{ nm}^2$ resulting in a real refractive index of 1.584 ± 0.007 at a wavelength of 589 nm and an absorption Ångström exponent of 8.0. The measured values of refractive index compare well with previous monochromatic or very small wavelength range measurements of refractive index. In general, the real component of the refractive index increases from remote to urban to wood smoke. A one-dimensional radiative-transfer calculation of the top of the atmosphere albedo was applied to model an atmosphere containing a 3 km thick layer of aerosol comprising of pure water, insoluble organic aerosol or an aerosol consisting of an aqueous core-with an insoluble organic shell. The calculation demonstrated that the top of the atmosphere albedo increases by 0.01 to 0.04 for pure organic particles relative to water particles of the same size and the top of the atmosphere albedo increases by 0.03 for aqueous core-shell particles as volume fraction of the shell material increases by 25 percent.

1. Introduction

Atmospheric aerosols affect the radiative balance of our planet e.g. Pöschl (2005), Ramanathan et al. (2001), Stocker et al. (2013) and Wild et al. (2009). Aerosols directly affect the radiative balance by absorbing or scattering incoming solar radiation e.g. Moise et al. (2015), and indirectly through their role as cloud condensation nuclei e.g. Breon et al. (2002), Lohmann and Feichter (2005), Rosenfeld et al. (2008) and Charlson et al. (2001). However, current understanding of the atmospheric aerosol radiative balance and the cloud albedo effect is currently regarded as low e.g. Stocker (2013) and Fuzzi (2005).

Owing to the complexity of material in the atmosphere, atmospheric aerosols often contain a mixture of different compounds e.g. Cappa et al. (2011), Cai et al. (2016) and Cochran et al. (2016). The contrasting properties of the different compounds can result in atmospheric aerosols being coated in a film of organic material e.g. Gill et al. (1983) and Donaldson and Vaida (2006). The presence of a film may alter the physical, chemical and optical properties of the cloud droplet or aerosol particle by (a) reducing the rate of evaporation from the droplets or particles e.g. Davies et al. (2013), Eliason et al. (2003), Gill et al. (1983), Kaiser et al. (1996) and McFiggans et al. (2005), (b) altering the transport of chemicals between gas and liquid phase e.g. Donaldson and Anderson (1999) and Donaldson and Valsaraj (2010), (c) affecting gaseous uptake e.g. Enami et al. (2010), (d) reducing the scavenging by larger cloud droplets e.g. Andreaea and Rosenfeld (2008) and Feingold and Chuang (2002) and (e) altering the optical properties of the droplet e.g. Donaldson and Vaida (2006) and Li et al. (2011). To quantify the consequences of film formation on atmospheric aerosol particles and cloud droplets, further understanding of aerosol films is urgently required. However, obstacles such as accurately quantifying anthropogenic and natural aerosol emissions (Kanakidou et al. (2005)) or understanding the hugely varying chemistry of atmospheric aerosols (Jacobson and Hansson (2000)) means the current understanding of atmospheric aerosol remains low e.g. Stocker et al. (2013) and Flores et al. (2014).

Furthering the current understanding of film formation on cloud droplets or aerosol particles has largely been addressed by replicating the film with atmospheric proxy compounds such as oleic acid e.g. King et al. (2004, 2009) and Jones et al. (2015), methyl oleate e.g. Pfrang et al. (2014) and Sebastiani et al. (2015), pinonic acid e.g. Enami and Sakamoto (2016), DPPC (Thompson et al. 2010), or nonanoic acid e.g. Tinel et al. (2016). However organic material extracted from the environment has only featured in a limited number of studies, e.g. Jones et al. (2017) investigated the consequences of exposing organic films extracted from atmospheric aerosol and sea-water to ozone, whilst Zhou et al. (2014) studied the heterogeneous chemistry of material collected from the surface of the sea. Research that focus on the sea-surface layer is highly relevant to atmospheric studies owing to sea-surface material often becoming aerosols (Blanchard (1964)).

The work presented describes the application of the optical trapping technique to measure the refractive index of organic material that may form an organic film on atmospheric aerosol. The organic material was extracted from atmospheric aerosol (using the techniques of Folch and Lee, 1957 and Bligh and Dyer, 1959) and the refractive index of the aerosol measured through the application of white light scattering in conjunction with Mie spectroscopy e.g. Bohren and

Huffman (1983). The values of the refractive index were subsequently used to estimate the change in the top of the atmosphere albedo from radiative transfer calculations that modelled an aqueous aerosol with a thin film of the atmospheric aerosol film material.

Determining the refractive index of atmospheric aerosol is paramount to understanding the light scattering and absorption properties of atmospheric aerosol, and hence its contribution to global temperatures. Considerable work has focused on determining the real and imaginary component of the refractive indices of atmospheric aerosols as demonstrated by the work carried out by Liu et al. (2013), Wex et al. (2009), Barkey et al. (2007), Meskhidze et al. (2013), Nakayama et al. (2010) and Lang-Yona et al. (2010) to list a few. The use of morphological dependent resonances in Raman Spectra to determine refractive index at a fixed wavelength has been reported by Lin et al. (1990) and references therein and Miles et al. (2012). The absorbing properties of atmospheric aerosols have been extensively studied e.g. Zhao et al. (2013) studied the optical extinction properties of aerosols, Washenfeller et al. (2013) studied aerosol extinction in the ultra-violet region and Liu et al. (2016) investigated the absorbing properties of brown carbon. In the study presented, wavelength dependent real refractive indices were determined for common aerosol types such as organic atmospheric aerosol sourced from urban and remote locations and from wood smoke aerosol. In addition, the wavelength-dependent refractive index of the proxy atmospheric aerosol humic acid was determined.

Application of the optical trapping technique was successfully employed to determine the refractive index of aerosol over a wide wavelength range. The technique allowed the refractive index to be resolved to within 0.015 over a large wavelength range of 460 to 700 nm e.g. David et al. (2016), Jones et al. (2013) and Jones et al. (2015). Previous studies have determined the refractive index of atmospheric aerosols either over a narrower or monochromatic wavelength range. Flores et al. (2014) determined the refractive index for secondary organic aerosol over the wavelength range of 360 to 420 nm, whilst Lambe et al. (2013), Guyon et al. (2003) and Nakayama et al. (2015) studied the refractive index of aerosols at individual wavelengths.

The technique also allowed the imaginary component of the refractive index and absorption Ångström exponent to be calculated for the wood smoke aerosol extracts and aqueous humic acid droplets owing to the samples absorbing at smaller wavelengths. The absorption Ångström exponent describes the wavelength dependence of the absorption of light by aerosols e.g. Moosmüller (2011). The absorption Ångström exponent of atmospheric aerosols has been shown to be sensitive to wavelength e.g. Chakrabarty et al. (2010) and Lewis et al. (2008), chemical composition e.g. Ajtai et al. (2011), Chakrabarty et al. (2010), Flowers et al. (2010), Park and Yu (2016), Russell et al. (2009) and Sandradewi et al. (2008), morphology e.g. Liu et al. (2008) and Utry et al. (2014) and size e.g. Utry et al. (2014) and Gyawali et al. (2009).

2. Materials and Methods

To optically trap aerosol extracts, aerosol was collected from the atmosphere by pulling air through a pre-combusted quartz filter using an air pump. The aerosol material was then extracted from the filter and transferred to isopropanol from which

airborne aerosols could be generated by ultrasonic nebulization. Additionally, a commercial sample of humic acid in an aqueous solution was studied as an aerosol. The airborne aerosols were optically trapped and illuminated with white light, the backscattered white light was collected to generate a Mie spectrum of scattered light intensity as a function of wavelength. From the Mie spectrum the wavelength dependent refractive index and radius could be determined by replication with Mie calculations.

2.1. Collection of aerosol extracts

Three types of atmospheric aerosol were sampled to demonstrate the technique. Three samples were chosen to represent (a) a “dirty” sample from an urban environment, (b) a “clean” sample from a remote location and (c) samples with strong light absorbing properties. Wood smoke aerosol extract and aqueous humic acid droplets were chosen for this purpose.

10 The urban sample was collected from the campus of Royal Holloway, University of London. The proximity of Central London (30 km), major motorways (M25, M40 and M4) and the large international airport Heathrow (8 km) mean the sample has been categorized as urban for the purposes of the study. The urban atmospheric aerosol extracts were collected over 30-day periods and combined in the extraction process to allow seasonal (spring, summer, autumn and winter) analysis. Combining the urban aerosol extracts into seasons ensured enough material was present to create airborne aerosols
15 and to optically trap in a relatively inefficient process as described in Sect. 2.2.

The remote atmospheric aerosol extract was collected at the Halley Clean Air Sector Laboratory operated by the British Antarctic Survey (Jones (2008)). The sample was collected over the Antarctic summer of 2015 for 60 consecutive days. Antarctica is situated far from human populated areas, and therefore the sample has been called remote aerosol for the purpose of the study.

20 The wood smoke was collected over a six-hour time period from the smoke plume of a flaming log fire burning in a domestic wood burner. The firewood used in the wood burner was sourced from wild cherry trees. Two wood smoke samples were collected from two separate fires, and were labelled extract A and extract B.

To determine the contamination for each sample, corresponding analytical filter blanks were collected. To ensure all possible contamination sources were accounted for, the remote and wood smoke analytical blanks travelled to the field sites
25 and back with the collected sample.

The urban and wood smoke aerosols were sampled by using an air pump with a flow of 30 L min^{-1} through clean stainless steel pipelines into a PFA (perfluoroalkoxy) Savillex filter holder, whilst remote aerosols were sampled from Antarctic ambient air by using a short length of quarter inch O.D. PFA tubing at a flow rate of 20 L min^{-1} onto a filter holder using a Staplex low volume air sampler (Model VM-4). All filter holders contained pre-combusted quartz filters (SKC Ltd.)
30 with a diameter of 47 mm. The air was pulled through the filter for a known time period, after which the sample and filter were frozen in the dark at -18°C until the sample could be extracted from the filter (typically days).

After sample collection, the filter holder was disassembled in a clean glove box to prevent contamination. The filter encased in the filter holder was cut into two on clean PFA blocks with a stainless steel blade: one half was for analysis, the

other for reference. The filter was placed in a glass conical flask with 10 ml of chloroform (Sigma-Aldrich, 0.5 to 1 % EtOH as stabilizer) and 10 ml of ultrapure water ($> 18 \text{ M}\Omega\text{m}^{-1}$), and the mixture sonicated for 10 minutes. After sonication, the mixture was filtered through pre-combusted quartz filters to remove filter debris. The filter debris with un-extracted material was discarded. Sequentially, the filtrate was poured into a glass separating funnel and the chloroform layer drawn off. The atmospheric aerosol extract studied was soluble in chloroform. The chloroform was removed from the atmospheric aerosol extract by evaporation under dry nitrogen. Once all the chloroform had been removed, 2 ml of isopropanol (Sigma-Aldrich, purity $\geq 99.8 \%$) was added to the sample and the sample was stored in the dark at $-18 \text{ }^{\circ}\text{C}$ until use. All instrumentation used in the collection and extraction of the atmospheric aerosol extract was cleaned with ultrapure water and chloroform before use. The sonication in the extraction process was not found to change the Langmuir-Isotherm of atmospheric material at the air-water interface.

Every sample extracted from the atmosphere had a corresponding analytical blank to check for potential contamination of the filters. The analytical blanks for each sample were extracted following the same procedure above.

In addition to atmospheric aerosol extracts, aqueous humic acid aerosol (humic acid sodium salts, STBD5313V Sigma-Aldrich) was studied. the nebulised aqueous humic acid aerosol droplets were prepared at a concentration of 0.0005 g cm^{-3} .

2.2. Optical trapping of the aerosols

A vertically aligned, counter propagating optical trap was used to optically catch and levitate the aerosol extracts. The optical trapping description is described in full by Jones (2013), however a brief description will be given here. The optical trap consisted of two laser beams that were fibre coupled from a 1064 nm continuous wave Nd:YAG laser (Laser Quantum). The laser beams passed through beam expansion optics to two vertically opposed microscope objectives (Mitutoyo M Plan Apo $50 \times \text{NA } 0.42$). An aluminium sample cell (volume 38.4 cm^3) was placed between the two microscope objectives and used to contain the aerosol extracts. Borosilicate coverslip windows allowed the focused laser beams to pass into the sample cell and form the optical trap. The aerosol extracts could be held for more than 24 hours once trapped e.g. Rkiouak (2014). The relative humidity and the temperature of the trapping environment were held at ambient conditions (30 percent relative humidity and $20 \text{ }^{\circ}\text{C}$).

A nebulizer (ultrasonic nebulizer, Omron) was used to create aerosols from either the atmospheric aerosol extract in isopropanol or aqueous humic acid droplets. Inlet and exhaust ports allowed aerosol delivery into the sample cell. The solvent for the atmospheric aerosol extracts was exchanged from chloroform (removed by blowing down with nitrogen) to isopropanol prior to optically trapping as chloroform was found to be unsuitable for ultrasonic nebulisation. Isopropanol was added in the volume ratio 5:1 isopropanol to atmospheric extract, and this mixture was nebulised to deliver airborne droplets of the extract. Isopropanol evaporated from the aerosol both during transit and immediately upon capture in the optical trap.

2.3. Data analysis

The optically trapped aerosol extracts were illuminated with white light and the elastically backscattered light was collected over a 25 degree cone angle as a function of wavelength by an objective lens. Further optics described in Jones et al.(2013) focussed the light onto a spectrometer (Acton SP2500i). The resulting spectrum was a function of light intensity versus wavelength and will be called a Mie spectrum henceforth in the paper. The Mie spectrum covered the wavelength range 460- to 700 nm, with a resolution of 0.06 nm per pixel. The measured Mie spectrum was simulated through application of Bohren and Huffman(1983) formalism of Mie theory, integrating over a 25 degree cone angle of backscattered light. in conjunction with the Cauchy equation e.g. Bohren and Huffman (1983):

$$n = A + \frac{B}{\lambda^2} + \frac{C}{\lambda^4}, \quad (1)$$

to determine both size and a precise estimation of refractive index as a function of wavelength. The values in Eq. (1) represent the refractive index (n), Cauchy empirical constants (A , B and C) and wavelength (λ). The values of the three empirical constants and the radius of the trapped aerosol extracts were iterated until a good comparison was achieved between the simulated and the experimentally obtained Mie spectrum. Typically, the radius of the droplet was fixed and the values of A , B , and C varied until a good fit between the measured and simulated Mie spectra was achieved by simple comparison (inspection) of peak, trough and inflection point positions. The value of the radius was then iterated through a series of radii with optimization of the values of A , B . and C as a function of wavelength repeated at each radius. Thus, a qualitative grid search was performed over parameter space. Parameter space was A varying from 1.3 to 1.7, B from 0 to 20,000 nm⁻² and C from 0 to 1×10⁹ nm⁴. When simulating the Mie spectra of atmospheric aerosol extracts, small adjustment of the empirical constant, C , did not alter the simulated Mie spectrum noticeably and this value was therefore held at zero. An estimation of the uncertainty in the derived values of the refractive index and radius of the aerosol could be determined by variation of radius, A and B in turn and comparing the experimental and simulated spectra. The value of the radius was between 0 to 3 microns typically. The imaginary component of the refractive index was varied only after the grid search for the wood smoke and humic acid samples.

2.4. Ångström absorption coefficient

Samples including humic acid and those obtained from atmospheric sampling may have a measurable wavelength dependent absorption that can be defined by an Ångström exponent. In the context of Mie scattering, absorption is observed as a decrease in spectral intensity of the Mie spectrum. Inclusion of a wavelength dependent imaginary refractive index term in the Bohren and Huffman formalism can simulate the attenuation of intensity observed in the Mie spectra owing to absorption.

The absorption Ångström exponent was also determined by fitting an Ångström equation (Moosmüller et al., 2011) to the absorbance spectra of the atmospheric aerosol extract in isopropanol or humic acid in water obtained by using UV-VIS spectroscopy:

$$\frac{Abs}{Abs_0} = \left(\frac{\lambda}{\lambda_0}\right)^{-\alpha}, \quad (2)$$

where Abs is the absorbance measured by a UV-VIS spectrometer (Perkin Elmer Lambda 950), λ is the wavelength and α is the absorption Ångström exponent. It should be noted that Abs_0 is the value of absorbance at the reference wavelength $\lambda_0=460\text{nm}$. The absorbance spectra of the bulk atmospheric aerosol extracts dissolved in isopropanol or the humic acid dissolved in water were recorded with a spectrometer covering the wavelength range 460 to 640 nm. Wood smoke aerosol extract and aqueous humic acid both demonstrated measureable absorption at low wavelengths, however the spectra from the other samples were below the instrument detection limits. The quoted photometric noise for the UV-Vis spectrometer was $\sim 0.0002A$. However, the urban and remote aerosol extracts were diluted in isopropanol to fill the UV-Vis spectrometer cuvette and thus a value three orders of magnitude larger than $\sim 0.0002A$ may provide an upper bound for the absorbance of the samples reported below the detection limit.

In a UV-Vis spectrometer the absorption coefficient, β , can be related to the Absorbance, Abs , by,

$$Abs = -\beta l \quad (3)$$

where l is the pathlength (1 cm for the work described here) and absorbance, Abs has been corrected from base 10 to base e (Petty et al., 2006). The absorption coefficient can be related to the imaginary refractive index, $k(\lambda)$, by

$$k(\lambda) = \frac{\lambda \beta}{4\pi} \quad (4)$$

as described by Petty et al. (2006). Substitution of equation (4) into equation (3) and subsequently equation (2) demonstrates that the Ångström relationship for absorbance (equation 2) is modified to

$$\frac{k}{k_0} = \left(\frac{\lambda}{\lambda_0}\right)^{-(\alpha-1)} \quad (5)$$

for describing the imaginary refractive index (see appendix). In essence the value of Ångström exponent, α , measured by the UV-Vis spectrometer is larger than the corresponding value for the imaginary refractive index. Note for the work described here $\lambda_0=460\text{nm}$. The values of k_0 and α were measured for dilute solutions of the wood smoke extract in isopropanol and humic acid in water. In the optical trap the trapped droplet of wood smoke extract in isopropanol lost all of the isopropanol solvent to evaporation, as expected, leaving pure wood smoke extract. The aqueous humic acid solution lost some water to evaporation, but remained an aqueous and more concentrated solution. As will be described below the mass density of the wood smoke extract was measured independently. Thus, for the wood smoke droplet the values of k_0 and Abs_0 were corrected for the mass density of wood smoke extract in the optical trap and the attenuation of the resulting Mie spectrum will be shown to be consistent. For the aqueous humic acid solution, the value of k_0 was determined by fitting the attenuation of the Mie spectrum by inspection, i.e. by changing the value of k_0 until the intensity attenuation of the simulated and

experimental Mie spectra matched, thereby calculating the value of the mass density in the trapped humic acid droplet. For the wood smoke aerosol extract, the mass density of the wood smoke aerosol extract in isopropanol was determined from a measurement on an Anton Parr densitometer, whilst the mass density of the pure material was calculated gravimetrically by evaporating isopropanol from a pre-weighed sample of the wood smoke aerosol extract. For the measurement of mass density obtained by the densitometer, a plot of the inverse of the density versus its corresponding weight fraction allowed the mass density to be determined. The Ångström coefficient determined for the Absorbance in isopropanol or water was adjusted for use with the imaginary refractive index Ångström relationship (see Appendix). Simulated Mie spectra of wood smoke aerosol and humic acid aerosol were then calculated with and without an Ångström exponent absorption to demonstrate that the attenuation in Mie resonance intensity was consistent with absorption.

10 3. Results

Aqueous humic acid droplets and extracts of atmospheric aerosols were optically trapped and the real component of the refractive index determined through comparison of experimentally obtained Mie spectra to simulated Mie spectra by varying the radius and the Cauchy coefficients A and B . The correct simulation of the Mie spectra requires the variation of absorption with wavelength to be described in terms of the imaginary refractive index:

$$15 \quad \left(\frac{k}{k_0}\right) = \left(\frac{\lambda}{\lambda_0}\right)^{-(\alpha-1)}, \quad (4)$$

where k represents the imaginary refractive index, λ is the wavelength and α is the absorption Ångström exponent. The Mie spectra for urban and remote atmospheric aerosol extracts are shown in Fig. 1, and the Mie spectra for the wood smoke aerosol extract and aqueous humic acid droplets are shown in Fig. 2. Typically, small aerosols (with a radius of approximately 0.600 μm) were trapped when studying the atmospheric aerosol extracts and consequently only a few resonances were observed in the Mie spectra depicted in Figs. 1 and 2. Table 1 displays the Cauchy coefficients, refractive index and radius of the aerosols studied. In general the real component of the refractive index increases from remote to urban to wood smoke.

The mass density of the two pure wood smoke aerosol extracts was determined to be 1.47 g cm^{-3} for extract A and 1.64 g cm^{-3} for extract B. The values are similar to the values Hoffer et al.(2005) reported for humic like substances (HULIS) sourced from a biomass burning plume: 1.502 to 1.569 g cm^{-3} and Dinar et al.(2008) reported 1.42-151 gcm^{-3} . The mass density of the aqueous humic acid droplets in the nebuliser was 0.0005 g cm^{-3} , the mass density of the pure humic acid was reported from the supplier Sigma-Aldrich to be 1.52 g cm^{-3} . The absorption spectrum and imaginary component of the refractive index over the wavelength range of 460 to 640 nm for the wood smoke and humic acid samples are shown in Fig. 3. Table 2 contains the values of the k_0 , Abs_0 , and α determined in the study presented here. The dependence of the Mie spectral intensity with and without contribution from the absorption are shown for the two absorbing samples in Fig. 2.

Absorption attenuates the intensity of the Mie spectra and is most notable at shorter wavelengths where the mass absorption coefficient is largest.

Figure 2 demonstrates that it may be possible to determine the absorption spectra from Mie spectra recorded upon optically trapped aerosol extracts. The solvent (isopropanol) was lost from the trapped aerosol extracts by experimental design to ensure the pure extract was studied. In contrast the aqueous humic acid droplet retained some of its water in equilibrium with the local humidity of the optical trapping cell. The trapped droplet was observed to lose water and consequently shrink in size. The simulated Mie spectra in Fig 2. were calculated with and without absorption described by an Ångström exponent to demonstrate that the attenuation of Mie resonances (especially at shorter wavelengths) was consistent with measured Mie spectra. The mass density of humic acid in an aqueous droplet is proportional to the imaginary refractive index, allowing the mass density of the optically trapped humic acid droplet to be calculated. The concentration of the trapped humic acid was determined to be 0.016 g cm^{-3} . The concentration of the aqueous humic acid droplet had increased by a factor of ~ 32 upon trapping, thus demonstrating that water had evaporated from the droplet during the trapping and aerosol equilibration process.

4. Discussion

Studies reporting the refractive index of atmospheric aerosol extracts are predominantly conducted at individual wavelengths e.g. Guyon et al. (2003), Hoffer et al. (2005), Kim and Paulson (2013), Lambe et al. (2013), Lang-Yona et al. (2010), Nakayama et al. (2013), Redemann et al. (2000) and Stelson et al. (1990). Yamasoe et al. (1998) determined the real component of the refractive index of smoke aerosol extracts to be 1.53, 1.55, 1.59, and 1.58, for wavelengths of 438, 670, 870, and 1020 nm respectively, whilst Shingler et al. (2016) conducted in situ aerosol particle measurements of wildfire, biogenic, marine and urban air masses and discovered a refractive index of 1.52 to 1.54 at a wavelength of 532 nm. Contrastingly, the refractive index in the study presented here was not calculated at a single wavelength but over a large continuous wavelength range (460 to 700 nm).

4.1. Refractive index of atmospheric aerosol extracts

The variation in refractive index between the extracts investigated in the study indicates a distinctive difference between each sample from each location source. Figure 4 graphically compares the refractive index dispersion with wavelength obtained for the atmospheric aerosol extracts analysed in the study presented to selected values from literature. Large differences between the values of refractive index for remote, urban and wood smoke aerosol extracts can be easily observed in Fig. 4. Wood smoke aerosol extracts have the largest values of refractive index, followed by urban and then remote aerosol extracts. Antarctica is considered a clean environment owing to the physical remoteness of the continent and air that reaches Antarctica is considered relatively cleansed of anthropogenic particles (Wolff et al., 1990). However, some particles do reach Antarctica, examples of such aerosol sources include sea spray, the transport of industrial emissions (McConnell et

al., 2014) and particulate material from biomass burning and tropical forest fires (Tomasi et al., 2007). Aerosols from such sources have travelled far and have likely undergone chemical ageing, and are thus likely to be very different in chemical composition than their initial composition. The review authored by Moise, Flores and Rudich (2015) demonstrates the importance of chemical reactions in the alteration of the optical properties of atmospheric aerosols during atmospheric transport.

The urban aerosol extract samples have a wide distribution of the values of refractive index with values ranging from 1.478 to 1.522 at 589 nm. From the small sample analysed in the study presented, the autumn and winter samples are at the larger end of the refractive index range, with spring and summer at the mid to low end. The wavelength dependent refractive index values determined for atmospheric aerosol extracts lie in good agreement with previous monochromatic literature results. Studies focusing on anthropogenic aerosols determined values of refractive index varying from 1.498 to 1.653 nm at 532 nm; the refractive index range found in literature encompasses the urban and wood smoke aerosol extract wavelength dependent refractive indices determined in the study e.g. Adler et al. (2011), Yamasoe et al. (1998), Hoffer et al. (2005) and Shingler et al. (2016). Similarly, studies focused on aerosols sourced from the Antarctica demonstrate refractive index values similar to the refractive index values determined for the aerosol extract sourced from Antarctica e.g. Virkkula et al. (2006) measured a refractive index that generally lay between 1.4 and 1.5, but also reached as low as 1.3 for Antarctic aerosol extracts (these values are an average of measurements from the wavelengths 450, 550 and 700 nm).

Contrastingly, Guyon et al. (2003) studied the refractive index of biomass burning aerosols collected from the Amazon tropical forest and determined a refractive index of 1.41 at 545 nm (0.1812 lower than the wavelength dependent refractive index determined in the study presented here at the same wavelength). A likely reason for the variation is that Guyon collected samples from a station suspended 54 m above ground level (and 22 m above the forest canopy), whereas in the study presented here samples were drawn directly from the smoke plume from a burning fire and consequently samples did not have the opportunity to chemically age or to mix with other material present in the atmosphere. Refractive index values from literature for secondary organic aerosols demonstrate a wide range of refractive index values, for example the work carried out by Kim et al. (2010), Kim et al. (2013), Lambe et al. (2013), Lang-Yona et al. (2010), Spindler et al. (2007) and Yu et al. (2008). The work indicates that a single refractive index value cannot be used to describe secondary organic aerosol, perhaps owing to the wide range of organics present in the aerosol e.g. Yu et al. (2008).

4.2. Refractive index of aqueous humic acid droplets

Aqueous humic acid droplets were studied to demonstrate the ability of using optical trapping and Mie spectroscopy to study a known absorbing aerosol. Humic acid was dissolved in water to form a solution prior to nebulisation. The measured refractive index of the aqueous droplet had different refractive index than a pure sample of humic acid owing to the water content of the aerosol. The refractive index of humic-like substances has been reported to be quite large, for example Hoffer (2005) reported a refractive index of 1.653 for HULIS samples. However in the study presented, the aqueous humic acid droplets had a refractive index lower than any of the atmospheric aerosol extracts because the atmospheric aerosol extracts

were trapped as concentrated aerosol extracts (the solvent, isopropanol, used to allow the aerosol extracts to become airborne evaporated during nebulisation and trapping).

4.3. Calculation of the absorption Ångström exponent

Unlike the urban and remote atmospheric aerosol extracts, the wood smoke aerosol extract and aqueous humic acid droplets had strong absorption properties as shown by UV-VIS experiments on samples dissolved in isopropanol and water respectively. The imaginary component of the refractive index and absorption Ångström exponent could then be determined for the two samples.

Previous studies in the field have determined values for the absorption Ångström exponents to range from 2 to 16 for carbonaceous aerosol over the visible wavelength range e.g. Hoffer et al. (2005), Lewis et al. (2008); Chakrabarty et al. (2010), Flowers et al. (2010), Moosmüller et al. (2011), Utry et al. (2013), Zhang et al. (2013), He et al. (2015), Garg et al. (2016), Pokhrel et al. (2016), Rathod et al. (2016) and Shen et al. (2017). More specifically, values in the range of 3.5 to 8.3 have been calculated for studies focusing on the absorption Ångström exponent for smoke aerosols. Lewis (2008) studied the combustion of a variety of fuels with a dual wavelength photo-acoustic instrument to determine an absorption Ångström exponent of 3.5. Contrastingly, Hoffer et al. (2005) and Park and Yu (2016) obtained a much higher absorption Ångström exponents of 6 to 7 and 7.4 to 8.3 respectively for biomass burning aerosols.

The calculated absorption Ångström exponent for the wood smoke aerosol extract correlates with the absorption Ångström exponent measured in previous studies for biomass burning aerosols. Interestingly, it has been suggested that fire type plays a role in the amount of black carbon produced. A flaming fire has been shown to produce more particles e.g. Reid (2005), and in particular produce more black carbon than smouldering fires e.g. Hoffer et al. (2005) and Yamasoe et al. (2000). The fire from which the wood smoke aerosol extracts were collected from was flaming and hence a high absorption Ångström exponent is more likely. It ought to be noted that the wood smoke extract was included in this work as an exploratory sample with a strong absorption and future work will explore smoke aerosol where the fuel and fire temperature are carefully controlled.

Considering the absorption Ångström exponent for the aqueous humic acid droplets, it can be observed that the exponent correlates with studies that determined the absorption Ångström exponent for biomass fuels. For example, Schnaiter et al. (2006) deduced an absorption Ångström exponent between 2.2 and 3.5 for aerosols produced from the combustion of propane and Schnaiter et al. (2003) determined an absorption Ångström exponent of 1 for emissions produced from the combustion of diesel.

4.4. Uncertainty in Mie spectra fitting

The collection technique applied to extract remote and urban aerosols from the atmosphere was limited by airflow and filter size and therefore sample was very limited. An air pump with a significantly larger flow rate was used, however the aerosol

extracts that were collected contained contamination in their analytical blanks warranting the samples to not be used. The contamination was attributed to the quality of the filters used, demonstrating that pre-combusted filters are critical.

Owing to limited sample, only small aerosols were optically trapped causing the collected Mie spectra to have little structure. A less structured Mie spectrum reduces the accuracy of the determined wavelength dependent refractive index, radius and absorption Ångström exponent. The Mie spectrum in Fig. 1 of the summer urban aerosol extract is structured with pronounced peak shapes that allow the facile fitting between simulated and measured Mie Spectra. Such spectra allow a relatively small range of values of radius, Cauchy coefficients A, B and C to provide a good fit between measured and simulated Mie Spectra. The rest of the Mie spectra in Fig. 1 have significantly fewer Mie resonances and their peak shapes are less pronounced. The uncertainties become larger as the spectra become less structured. Despite the limitations in Mie spectra simulation, the typical uncertainty in radius and refractive index for a Mie spectra was typically ± 6 nm and ± 0.015 respectively, whilst the uncertainty for the absorption Ångström exponent was 7 percent for the wood smoke aerosol extract and 5 percent for the aqueous humic acid aerosol.

The liquid droplets are assumed to be perfectly spherical. Mie scattering from droplets experiencing small deformation has been shown by Arnold et al. (1990) and Schweiger (1990) to result in resonances that shift, broaden and split as the droplet asymmetry increases.

The sensitivity of the simulated Mie spectra to the refractive index (± 0.015) and radius (± 6 nm) of the droplet are shown in figure 5. The simulated spectra, with the stated variations and the experimental Mie spectra for the Spring Urban aerosol extract are plotted. Figure 5 also contains a third simulated set of Mie spectra calculated by re-optimizing the values of A, B, and C in Cauchy equation to achieve a fit between simulated and experimental Mie spectra for particles with a radius ± 12 nm from the optimum fit to the experimental data. Figure 5 demonstrates that the quoted uncertainties in radius (± 6 nm) and refractive index (± 0.015) are realistic.

4.5. Atmospheric Implications

Atmospheric aerosol can increase the top of the atmosphere albedo by scattering incoming solar radiation and decrease the top of the atmosphere albedo by absorbing solar radiation. Using the refractive index data collected in the study presented, a radiative transfer model was applied to consider the change in top of the atmosphere albedo owing to an aerosol film forming with the same optical properties as the extracts studied in the presented study. The material extracted from the atmospheric samples described in the study may form an organic shell at the air-water interface of an aqueous aerosol e.g. Gill et al. (1983). An atmospheric radiative-transfer model (Stamnes et al., 1988) was applied to study an atmospheric aerosol layer consisting of core aqueous aerosol coated in an organic shell with the optical properties of the atmospheric aerosol extract measured within the work presented here. The change in the top of the atmospheric albedo was calculated as the proportions of water and organic material were varied for different size aerosols.

The top of the atmosphere albedo was calculated for an aerosol layer with the composition of an aqueous core aerosol surrounded by a shell of either urban, wood smoke or remote atmospheric aerosol extract with the volume fraction varying from 0 to 1 (i.e. pure water to pure organic). The calculations represent only a small-scale study to simply identify potential effects on the top of the atmosphere albedo owing to the presence of pure core-shell particles in the atmosphere versus no aerosol present. The change in the top of the atmosphere albedo is reported as an aerosol relative effect, following the approach of Mishra et al. (2015).

The atmospheric radiative-transfer model uses the DISORT code (Stamnes et al., 1988). The model uses values of the scattering, absorption and the asymmetry parameter of aerosols to calculate the change in solar radiation through the atmosphere. To calculate the scattering and absorption parameters for coated spheres Mie calculations were performed for the core-shell particles using BHCOAT, a code developed by Bohren and Huffman (1983), which was later modified to also include a calculation of the asymmetry parameter. Scattering, absorption and asymmetry parameter for the particle are calculated from the refractive index of the core and shell. For all aerosols the refractive index of the core is a wavelength dependent value for water (IAPWS, 1997) and the refractive index of the surrounding medium a wavelength independent value for air of 1.00-0.0i. The shell of the aerosol has a wavelength dependent refractive index of the urban, remote or wood smoke aerosol extracts, as displayed in Table 1. In addition, the absorption properties of the wood smoke aerosol extract were included in the calculation.

The core-shell Mie calculation was used to obtain scattering and absorption cross-sections and asymmetry parameters for particles with a radius of 100 to 10,000 nm (in 100 nm intervals from 100 to 1000 nm, and 1000 nm intervals from 1000 to 10,000 nm), and with the shell volume making up 0.01 to 0.99 of the whole particle volume. Calculations were performed over wavelengths covering 350 to 750 nm. The ground albedo was set to 0.1. Aerosol of one size was placed in three consecutive 1 km thick layers at the surface, forming a 3 km thick aerosol layer. The aerosol optical depth for each of these layers was set to 0.126, the global average set by Mao et al. (2014), and no aerosol or cloud was placed in any subsequent layers. The solar zenith angle was set at 60°. The albedo of the top of the atmosphere was calculated as the ratio of incoming to outgoing irradiance at 100km altitude and averaged over wavelengths from 350 to 750 nm for each particle size. Calculations were also performed for no aerosol present in the atmosphere. The aerosol radiative effect was then calculated using Eq. (5).

$$ARE_{TOT} = TOA\ albedo_{aerosol} - TOA\ albedo_{no\ aerosol} , \quad (5)$$

where ARE_{TOT} stands for total aerosol radiative effect, $TOA\ albedo_{aerosol}$ stands for the top of the atmosphere albedo with aerosol present and $TOA\ albedo_{no\ aerosol}$ stands for the top of atmosphere albedo without aerosol present.

The results of these calculations are presented in Fig. 6. The overall trend for each different atmospheric aerosol film is similar: smaller aerosols have an almost positive linear relationship with the aerosol radiative effect, whilst larger aerosols (e.g. those with a radius of 5000 or 10000 nm) have a much more complex relationship between aerosol radius and the total aerosol radiative effect, with the relationship becoming more complex as the aerosol becomes larger. Interestingly,

larger aerosols demonstrate a negative and then positive relationship between aerosol radius and the total aerosol radiative effect; with larger aerosols having a stronger negative relationship.

Particles with a radius of 200 nm do not show a particularly strong relationship between size and total aerosol radiative effect: an effect that can be attributed to the aerosols being incredibly small and consequently much closer to the Rayleigh scattering regime. Contrastingly, composition can cause an increase in the pronunciation of the relationship between aerosol size and the aerosol radiative effect; the wood smoke containing aerosols depict the greatest range in total aerosol radiative effect. An effect that the strong absorption properties of the wood smoke containing aerosols may cause.

From Fig. 6, it can be observed that all aerosols have a positive overall effect on the total aerosol radiative effect, with the most positive effect observed for particle sizes of 600 and 800 nm for the urban and remote atmospheric aerosol extracts and 400 and 600 nm for the wood smoke aerosol extract. Note the change in top of the atmosphere albedo is most pronounced when the volume of shell increases from 0 to 25 percent of the total volume.

5. Conclusions

A new technique employing optical trapping techniques applied alongside Mie spectroscopy was employed to determine the real and imaginary components of the refractive index of insoluble organic material from atmospheric aerosol extracts over a wide wavelength range. The atmospheric aerosol extract was successfully trapped, demonstrating that the material forms spherical liquid droplets onto which Mie theory could be applied. From application of Mie theory, the refractive indices of the atmospheric aerosol extract were determined to vary from 1.470 for aerosol extracted from Antarctica to 1.588 for wood smoke aerosol extracts at the wavelength 589 nm, whilst seasonal refractive index dependence was observed for atmospheric aerosol extracted from an urban environment.

Additionally, owing to the efficient light absorbing nature of the wood smoke aerosol extract and aqueous humic acid extract, the absorption Ångström exponent could be determined with a high level of certainty for the extract; through applying optical trapping and Mie spectroscopy alongside UV-VIS spectroscopy it was possible to determine the real and imaginary component of the refractive index simultaneously.

The aerosol collected may exist as an aerosol in the atmosphere or may coagulate with other atmospheric aerosols to form a film. Use of a simple one dimensional radiative-transfer model to study a shell of atmospheric aerosol extracts on an aqueous aerosol indicates that the albedo of the top of the atmosphere albedo may change by 0.03 relative to a pure aqueous droplet.

Data Availability

Data can be found at [10.5281/zenodo.834450](https://zenodo.org/record/834450).

Appendix A

The absorption Ångström exponent and imaginary refractive index were determined by using experimentally determined absorption in a series of equations. Equation (2) from Sect. 2.4. is

$$\frac{Abs}{Abs_0} = \left(\frac{\lambda}{\lambda_0} \right)^{-\alpha}, \quad (A1)$$

- 5 where Abs is the absorbance, λ is the wavelength and α is the absorption Ångström exponent. It ought to be noted that Abs_0 is the value of absorbance at the reference wavelength λ_0 . By substituting Eq. (4) into Eq. (3) and then equation (A1) the relationship between the two variables was determined:

$$\left(\frac{\frac{4\pi k}{\lambda}}{\frac{4\pi k_0}{\lambda_0}} \right) = \left(\frac{\lambda}{\lambda_0} \right)^{-\alpha}, \quad (A2)$$

$$\left(\frac{k}{k_0} \right) \left(\frac{\lambda_0}{\lambda} \right) = \left(\frac{\lambda}{\lambda_0} \right)^{-\alpha}, \quad (A3)$$

10 $\left(\frac{k}{k_0} \right) = \left(\frac{\lambda}{\lambda_0} \right)^1 \left(\frac{\lambda}{\lambda_0} \right)^{-\alpha}, \quad (A4)$

$$\left(\frac{k}{k_0} \right) = \left(\frac{\lambda}{\lambda_0} \right)^{-(\alpha-1)}, \quad (A5)$$

- where σ is the mass absorption coefficient for absorbance, λ is the wavelength, α is the absorption Ångström exponent and k is the imaginary refractive index. Note that k_0 is the imaginary refractive index at λ_0 . λ_0 was taken to be 460 nm. Equation (A5) demonstrates that the relationship between the Ångström exponent of absorbance and Ångström exponent of imaginary refractive index occurs when the Ångström exponent of the imaginary refractive index is $\alpha-1$. Hence, throughout the paper the Ångström exponent is of the imaginary refractive index is $\alpha-1$.
- 15

Author Contributions

- Rosalie H. Shepherd conducted all experiments, extracted all atmospheric aerosol, analysed and interpreted the data collected and wrote the paper. Martin D. King and Andrew D. Ward conceived the experiment idea and assisted during the experiment. Additionally, Martin D. King collected the urban atmospheric aerosol extracts. Amelia Marks with the assistance of Martin D. King modelled a film of atmospheric aerosol extract on an aqueous aerosol. Neil Brough collected aerosol samples from Antarctica.
- 20

Competing Interests

The authors declare that they have no conflict of interest.

Acknowledgments

The authors would like to thank the Central Laser Facility for granting access time on the optical trapping equipment at Rutherford Appleton Laboratories, Oxfordshire under the grant number ISI002. Rosalie H. Shepherd would like to thank STFC for funding the student grant ST/L504279/1.

5 References

- Adler, G., Flores, J. M., Riziq, A. A., Borrmann, S. and Rudich, Y. (2011) 'Chemical, physical, and optical evolution of biomass burning aerosols: a case study', *Atmospheric Chemistry and Physics*, 11, pp. 1491–1503. doi: 10.5194/acp-11-1491-2011.
- Ajtai, T., Filep, A., Utry, N., Schnaiter, M., Linke, C., Bozoki, Z., Szabo, G. and Leisner, T. (2011) 'Inter-comparison of optical absorption coefficients of atmospheric aerosols determined by a multi-wavelength photoacoustic spectrometer and an Aethalometer under sub-urban wintry conditions', *Journal of Aerosol Science*, 42(12), pp. 859–866. doi: 10.1016/j.jaerosci.2011.07.008.
- Andreaea, M. O. and Rosenfeld, D. (2008) 'Aerosol–cloud–precipitation interactions. Part 1. The nature and sources of cloud-active aerosols', *Earth Science Reviews*, 89(1–2), pp. 13–41. doi: 10.1016/j.earscirev.2008.03.001.
- Arnold, A., Spock, D.E., Folan, L.M., (1990) 'Electric-field-modulated light scattering near a morphological resonance of a trapped aerosol particle', *Optics Letters*, 15(20) pp: 1111–1113 doi: 10.1364/OL.15.001111
- Barkey, B., Paulson, S. E. and Chung, A. (2007) 'Genetic Algorithm Inversion of Dual Polarization Polar Nephelometer Data to Determine Aerosol Refractive Index', *Aerosol Science and Technology*, 41(8), pp. 751–760. doi: 10.1080/02786820701432640.
- Blanchard, D. C. (1964) 'Material, Sea-to-Air Transport of Surface Active', *Science*, 146, pp. 396–397. doi: 10.1126/science.146.3642.396.
- Bligh, E.G. and Dyer, W.J. (1959) 'A rapid method of total lipid extraction and purification' *Canadian Journal of Biochemistry and Physiology*, 37, pp497–509
- Bohren, C. F. and Huffman, D. R. (1983) 'Absorption and Scattering of Light by Small Particles', Wiley Scientific.
- Breon, F. M., Tanré, D. and Generoso, S. (2002) 'Aerosol Effect on Cloud Droplet Size Monitored from Satellite', *Science*, 295, pp. 834–839. doi: 10.1126/science.1066434.
- Cai, C., Miles, R. E. H., Cotterell, M. I., Marsh, A., Rovelli, G., Rickards, A. M. J., Zhang, Y. H. and Reid, J. P. (2016) 'Comparison of methods for predicting the compositional dependence of the density and refractive index of organic-aqueous aerosols', *Journal of Physical Chemistry A*, 120(33), pp. 6604–6617. doi: 10.1021/acs.jpca.6b05986.
- Cappa, C. D., Che, D. L., Kessler, S. H., Kroll, J. H. and Wilson, K. R. (2011) 'Variations in organic aerosol optical and hygroscopic properties upon heterogeneous OH oxidation', *Journal of Geophysical Research: Atmospheres*, 116(15), pp. 1–12. doi: 10.1029/2011JD015918.

- Chakrabarty, R. K., Moosmüller, H., Chen, L. W. A., Lewis, K., Arnott, W. P., Mazzoleni, C., Dubey, M. K., Wold, C. E., Hao, W. M. and Kreidenweis, S. M. (2010) 'Brown carbon in tar balls from smoldering biomass combustion', *Atmospheric Chemistry and Physics*, 10(13), pp. 6363–6370. doi: 10.5194/acp-10-6363-2010.
- Charlson, R. J., Seinfeld, J. H., Nenes, A., Kulmala, M., Laaksonen, A. and Facchini, M. C. (2001) 'Reshaping the theory of cloud formation', *Science*, pp. 2025–2026. doi: 10.1126/science.1060096.
- Cochran, R. E., Laskina, O., Jayarathne, T., Laskin, A., Laskin, J., Lin, P., Sultana, C., Lee, C., Moore, K. A., Cappa, C. D., Bertram, T. H., Prather, K. A., Grassian, V. H. and Stone, E. A. (2016) 'Analysis of Organic Anionic Surfactants in Fine and Coarse Fractions of Freshly Emitted Sea Spray Aerosol', *Environmental Science and Technology*, 50(5), pp. 2477–2486. doi: 10.1021/acs.est.5b04053.
- David, G., Esat, K., Ritsch, I. and Signorell, R. (2016) 'Ultraviolet broadband light scattering for optically-trapped submicron-sized aerosol particles', *Physical chemistry chemical physics*, pp. 5477–5485. doi: 10.1039/C5CP06940H.
- Davies, J. F., Miles, R. E. H., Haddrell, A. E. and Reid, J. P. (2013) 'Influence of organic films on the evaporation and condensation of water in aerosol.', *Proceedings of the National Academy of Sciences of the United States of America*, 110(22), pp. 8807–12. doi: 10.1073/pnas.1305277110.
- Dinar, E., Riziq, A. A., Spindler, C., Erlick, C., Kiss, G. and Rudich, Y. (2008) 'The complex refractive index of atmospheric and model humic-like substances (HULIS) retrieved by a cavity ring down aerosol spectrometer (CRD-AS)', *Faraday Discussions*, 137, pp 137, doi: 10.1039/B703111D.
- Donaldson, D. J. and Anderson, D. (1999) 'Adsorption of atmospheric gases at the air-water interface. 2. C₁-C₄ alcohols, acids, and acetone', *J. Phys. Chem. A*, 103(7), pp. 871–876. doi: 10.1021/jp983963h.
- Donaldson, D. J. and Vaida, V. (2006) 'The influence of organic films at the air-aqueous boundary on atmospheric processes', *Chemical Reviews*, 106(4), pp. 1445–1461. doi: 10.1021/cr040367c.
- Donaldson, D. J. and Valsaraj, K. T. (2010) 'Adsorption and reaction of trace gas-phase organic compounds on atmospheric water film surfaces: A critical review', *Environmental Science and Technology*, 44(3), pp. 865–873. doi: 10.1021/es902720s.
- Eliason, T. L., Aloisio, S., Donaldson, D. J., Cziczo, D. J. and Vaida, V. (2003) 'Processing of unsaturated organic acid films and aerosols by ozone', *Atmospheric Environment*, 37(16), pp. 2207–2219. doi: 10.1016/S1352-2310(03)00149-3.
- Enami, S., Hoffmann, M. R. and Colussi, A. J. (2010) 'Molecular control of reactive gas uptake "on Water"', *Journal of Physical Chemistry A*, 114(18), pp. 5817–5822. doi: 10.1021/jp1019729.
- Enami, S. and Sakamoto, Y. (2016) 'OH-Radical Oxidation of Surface-Active cis-Pinonic Acid at the Air-Water Interface', *Journal of Physical Chemistry A*, 120(20), pp. 3578–3587. doi: 10.1021/acs.jpca.6b01261.
- Feingold, G. and Chuang, P. Y. (2002) 'Analysis of the Influence of Film-Forming Compounds on Droplet Growth: Implications for Cloud Microphysical Processes and Climate', *Journal of the Atmospheric Sciences*, 59(12), pp. 2006–2018. doi: 10.1175/1520-0469.
- Flores, J. M., Washenfelder, R. A., Adler, G., Lee, H. J., Segev, L., Laskin, J., Laskin, A., Nizkorodov, S. A., Brown, S. S.

- and Rudich, Y. (2014) ‘Complex refractive indices in the near-ultraviolet spectral region of biogenic secondary organic aerosol aged with ammonia.’, *Physical chemistry chemical physics*, 16(22), pp. 10629–42. doi: 10.1039/c4cp01009d.
- Flores, J. M., Zhao, D. F., Segev, L., Schlag, P., Kiendler-Scharr, A., Fuchs, H., Watne, A. K., Bluvshstein, N., Mentel, T. F., Hallquist, M. and Rudich, Y. (2014) ‘Evolution of the complex refractive index in the UV spectral region in ageing secondary organic aerosol’, *Atmospheric Chemistry and Physics*, 14(11), pp. 5793–5806. doi: 10.5194/acp-14-5793-2014.
- Flowers, B. A., Dubey, M. K., Mazzoleni, C., Stone, E. A., Schauer, J. J., Kim, S. W. and Yoon, S. C. (2010) ‘Optical-chemical-microphysical relationships and closure studies for mixed carbonaceous aerosols observed at Jeju Island; 3-laser photoacoustic spectrometer, particle sizing, and filter analysis’, *Atmospheric Chemistry and Physics*, 10(21), pp. 10387–10398. doi: 10.5194/acp-10-10387-2010.
- Folch, J., Lees, M., Sloane Stanley, G.H., (1957) ‘A simple method for the isolation and purification of total lipides from animal tissues’ *Journal of Biological Chemistry*, 226, pp 497-509.
- Fuzzi, S., Andreae, M. O., Huebert, B. J., Kulmala, M., Bond, T. C., Boy, M., Doherty, S. J., Guenther, A., Kanakidou, M., Kawamura, K., Kerminen, V. M., Lohmann, U., Russell, L. M. and Pöschl, U. (2005) ‘Critical assessment of the current state of scientific knowledge, terminology, and research needs concerning the role of organic aerosols in the atmosphere, climate, and global change’, *Atmospheric Chemistry and Physics Discussions*, 5(6), pp. 11729–11780. doi: 10.5194/acpd-5-11729-2005.
- Garg, S., Chandra, B. P., Sinha, V., Sarda-Estève, R., Gros, V. and Sinha, B. (2016) ‘Limitation of the Use of the Absorption Ångström Exponent for Source Apportionment of Equivalent Black Carbon: A Case Study from the North West Indo-Gangetic Plain’, *Environmental Science and Technology*, 50(2), pp. 814–824. doi: 10.1021/acs.est.5b03868.
- Gill, P. S., Graedel, T. E. and Weschler, C. J. (1983) ‘Organic films on atmospheric aerosol particles, fog droplets, cloud droplets, raindrops, and snowflakes’, *Reviews of Geophysics*, 21(4), p. 903. doi: 10.1029/RG021i004p00903.
- Guyon, P., Boucher, O., Graham, B., Beck, J., Mayol-Bracero, O. L., Roberts, G. C., Maenhaut, W., Artaxo, P. and Andreae, M. O. (2003) ‘Refractive index of aerosol particles over the Amazon tropical forest during LBA-EUSTACH 1999’, *Journal of Aerosol Science*, 34(7), pp. 883–907. doi: 10.1016/S0021-8502(03)00052-1.
- Gyawali, M., Arnott, W. P., Lewis, K. and Moosmüller, H. (2009) ‘In situ aerosol optics in Reno, NV, USA during and after the summer 2008 California wildfires and the influence of aerosol coatings’, *Atmospheric Chemistry and Physics Discussions*, 9, pp. 8007–8015. doi: 10.5194/acp-9-8007-2009.
- He, Q., Zhao, X., Lu, J., Zhou, G., Yang, H., Gao, W., Yu, W. and Cheng, T. (2015) ‘Impacts of biomass-burning on aerosol properties of a severe haze event over Shanghai’, *Particuology*. Chinese Society of Particuology, 20, pp. 52–60. doi: 10.1016/j.partic.2014.11.004.
- Hoffer, A., Gelencsér, A., Guyon, P., Kiss, G., Schmid, O., Frank, G. P., Artaxo, P. and Andreae, M. O. (2005) ‘Optical properties of humic-like substances (HULIS) in biomass-burning aerosols’, *Atmospheric Chemistry and Physics Discussions*, 5(4), pp. 7341–7360. doi: 10.5194/acpd-5-7341-2005.
- Hoffer, A., Tóth, A., Nyirő-Kósa, I., Pósfai, M. and Gelencsér, A. (2016) ‘Light absorption properties of laboratory-

- generated tar ball particles', *Atmospheric Chemistry and Physics*, 16(1), pp. 239–246. doi: 10.5194/acp-16-239-2016.
- IAPWS (1997) 'Release on the Refractive Index of Ordinary Water Substance as a Function of Wavelength, Temperature and Pressure'.
- Jacobson, M. C. and Hansson, H. (2000) 'Organic atmospheric aerosols: Review and state of the science', *Reviews of Geophysics*, (38), pp. 267–294. doi: 10.1029/1998RG000045.
- Jauffred, L., Taheri, S. M. R., Schmitt, R., Linke, H. and Oddershede, L. B. (2015) 'Optical Trapping of Gold Nanoparticles in Air', *Nano Letters*, 15(7), pp. 4713–4719. doi: 10.1021/acs.nanolett.5b01562.
- Jones, A. E., Wolff, E. W., Salmon, R. A., Bauguutte, S. J. B., Roscoe, H. K., Anderson, P. S., Ames, D., Clemitshaw, K. C., Fleming, Z. L., Bloss, W. J., Heard, D. E., Lee, J. D., Read, K. A., Hamer, P., Shallcross, D. E., Jackson, A. V., Walker, S. L., Lewis, A. C., Mills, G. P., Plane, J. M. C., Saiz-Lopez, A., Sturges, W. T. and Worton, D. R. (2008) 'Chemistry of the Antarctic Boundary Layer and the Interface with Snow: an overview of the CHABLIS campaign', *Atmospheric Chemistry and Physics*, 8(14), pp. 3789–3803. doi: 10.5194/acp-8-3789-2008.
- Jones, S. H., King, M. D. and Ward, A. D. (2013) 'Determining the unique refractive index properties of solid polystyrene aerosol using broadband Mie scattering from optically trapped beads.', *Physical chemistry chemical physics*, 15(47), pp. 20735–41. doi: 10.1039/c3cp53498g.
- Jones, S. H., King, M. D. and Ward, A. D. (2015) 'Atmospherically relevant core-shell aerosol studied using optical trapping and Mie scattering', *Chem. Commun., Royal Society of Chemistry*, 51(23), pp. 4914–4917. doi: 10.1039/C4CC09835H.
- Jones, S. H., King, M. D., Ward, A. D., Rennie, A. R., Jones, A. C. and Arnold, T. (2017) 'Are organic films from atmospheric aerosol and sea water inert to oxidation by ozone at the air-water interface', *Atmospheric Environment*, 161, pp. 274–287, doi: 10.1016/j.atmosenv.2017.04.025.
- Kaiser, T., Roll, G. and Schweiger, G. (1996) 'Investigation of coated droplets in an optical trap: Raman-scattering, elastic-light-scattering, and evaporation characteristics.', *Applied optics*, 35(30), pp. 5918–5924. doi: 10.1364/AO.35.005918.
- Kanakidou, M., Seinfeld, J. H., Pandis, S. N., Barnes, I., Dentener, F. J., Facchini, M. C., Van Dingenen, R., Ervens, B., Nenes, A., Nielsen, C. J., Swietlicki, E., Putaud, J. P., Balkanski, Y., Fuzzi, S., Horth, J., Moortgat, G. K., Winterhalter, R., Myhre, C. E. L., Tsigaridis, K., Vignati, E., Stephanou, E. G. and Wilson, J. (2005) 'Organic aerosol and global climate modelling: a review', *Atmospheric Chemistry and Physics*, 5, pp. 1053–1123. doi: 10.5194/acp-5-1053-2005.
- Kim, H., Barkey, B. and Paulson, S. E. (2010) 'Real refractive indices of alpha and beta pinene and toluene secondary organic aerosols generated from ozonolysis and photo-oxidation', *Journal of Geophysical Research Atmospheres*, 115(23). doi: 10.1029/2010JD014549.
- Kim, H. and Paulson, S. E. (2013) 'Real refractive indices and volatility of secondary organic aerosol generated from photooxidation and ozonolysis of limonene, α -pinene and toluene', *Atmospheric Chemistry and Physics*, 13(15), pp. 7711–7723. doi: 10.5194/acp-13-7711-2013.
- King, M.D., Thompson, K.C. and Ward, A.D., (2004) 'Laser Tweezers Raman Study of Optically Trapped Aerosol Droplets

- of Seawater and Oleic Acid Reacting with Ozone: Implications for Cloud-Droplet Properties' *Journal of the American Chemical Society*, 126 (51), 16710–16711. doi: 10.1021/ja044717o
- King, M. D., Rennie, A. R., Thompson, K. C., Fisher, F. N., Dong, C. C., Thomas, R. K., Pfrang, C. and Hughes, A. V (2009) 'Oxidation of oleic acid at the air-water interface and its potential effects on cloud critical supersaturations.', *Physical chemistry chemical physics*. 11(35), pp. 7699–7707. doi: 10.1039/b906517b.
- Lambe, A. T., Cappa, C. D., Massoli, P., Onasch, T. B., Forestieri, S. D., Martin, A. T., Cummings, M. J., Croasdale, D. R., Brune, W. H., Worsnop, D. R. and Davidovits, P. (2013) 'Relationship between oxidation level and optical properties of secondary organic aerosol', *Environmental Science and Technology*, 47(12), pp. 6349–6357. doi: 10.1021/es401043j.
- Lang-Yona, N., Abo-Riziq, A., Erlick, C., Segre, E., Trainic, M. and Rudich, Y. (2010) 'Interaction of internally mixed aerosols with light.', *Physical chemistry chemical physics*. 12(1), pp. 21–31. doi: 10.1039/b913176k.
- Lang-Yona, N., Rudich, Y., Mentel, T. F., Bohne, A., Buchholz, A., Kiendler-Scharr, A., Kleist, E., Spindler, C., Tillmann, R. and Wildt, J. (2010) 'The chemical and microphysical properties of secondary organic aerosols from Holm Oak emissions', *Atmospheric Chemistry and Physics*, 10(15), pp. 7253–7265. doi: 10.5194/acp-10-7253-2010.
- Lewis, K., Arnott, W. P., Moosmuller, H. and Wold, C. E. (2008) 'Strong spectral variation of biomass smoke light absorption and single scattering albedo observed with a novel dual-wavelength photoacoustic instrument', *Journal of Geophysical Research Atmospheres*, 113(16), pp. 1–14. doi: 10.1029/2007JD009699.
- Li, Y., Ezell, M. J. and Finlayson-Pitts, B. J. (2011) 'The impact of organic coatings on light scattering by sodium chloride particles', *Atmospheric Environment*, 45(25), pp. 4123–4132. doi: 10.1016/j.atmosenv.2011.05.031.
- Lin, H.-B., Eversole, J.D., Campillo, A.J. (1990) 'Identification of morphology dependent resonances in stimulated Raman scattering from microdroplets', *Optics communications*, 77(5,6), pp.407–410
- Liu, J., Lin, P., Laskin, A., Laskin, J., Kathmann, S. M., Wise, M., Caylor, R., Imholt, F., Selimovic, V. and Shilling, J. E. (2016) 'Optical properties and aging of light-absorbing secondary organic aerosol', *Atmospheric Chemistry and Physics*, 16(19), pp. 12815–12827. doi: 10.5194/acp-16-12815-2016.
- Liu, L., Mishchenko, M. I. and Patrick Arnott, W. (2008) 'A study of radiative properties of fractal soot aggregates using the superposition T-matrix method', *Journal of Quantitative Spectroscopy and Radiative Transfer*, 109(15), pp. 2656–2663. doi: 10.1016/j.jqsrt.2008.05.001.
- Liu, P., Zhang, Y. and Martin, S. T. (2013) 'Complex refractive indices of thin films of secondary organic materials by spectroscopic ellipsometry from 220 to 1200 nm', *Environmental Science and Technology*, 47(23), pp. 13594–13601. doi: 10.1021/es403411e.
- Lohmann, U. and Feichter, J. (2005) 'Global indirect aerosol effects : a review', *Atmospheric Chemistry and Physics*, 5, pp. 715–737. doi: 1680-7324/acp/2005-5-715.
- Mao, K., Ma, Y., Xia, L., Chen, W., Shen, X., He, T. and Xu, T. (2014) 'Global aerosol change in the last decade: An analysis based on MODIS data', *Atmospheric Environment*, 94, pp. 680–686. doi: 10.1016/j.atmosenv.2014.04.053.
- McConnell, J. R., Maselli, O. J., Sigl, M., Vallelonga, P., Neumann, T., Anschütz, H., Bales, R. C., Curran, M. A. J., Das, S.

- B., Edwards, R., Kipfstuhl, S., Layman, L. and Thomas, E. R. (2014) 'Antarctic-wide array of high-resolution ice core records reveals pervasive lead pollution began in 1889 and persists today.', *Scientific reports*, 4, p. 5848. doi: 10.1038/srep05848.
- McFiggans, G., Artaxo, P., Baltensperger, U., Coe, H., Facchini, M. C., Feingold, G., Fuzzi, S., Gysel, M., Laaksonen, A., Lohmann, U., Mentel, T. F., Murphy, D. M., O'Dowd, C. D., Snider, J. R. and Weingartner, E. (2005) 'The effect of physical and chemical aerosol properties on warm cloud droplet activation', *Atmospheric Chemistry and Physics Discussions*, 5(5), pp. 8507–8646. doi: 10.5194/acpd-5-8507-2005.
- Meskhidze, N., Petters, M. D., Tsigaridis, K., Bates, T., O'Dowd, C., Reid, J., Lewis, E. R., Gantt, B., Anguelova, M. D., Bhawe, P. V., Bird, J., Callaghan, A. H., Ceburnis, D., Chang, R., Clarke, A., de Leeuw, G., Deane, G., Demott, P. J., Elliot, S., Facchini, M. C., Fairall, C. W., Hawkins, L., Hu, Y., Hudson, J. G., Johnson, M. S., Kaku, K. C., Keene, W. C., Kieber, D. J., Long, M. S., Mårtensson, M., Modini, R. L., Osburn, C. L., Prather, K. A., Pszenny, A., Rinaldi, M., Russell, L. M., Salter, M., Sayer, A. M., Smirnov, A., Suda, S. R., Toth, T. D., Worsnop, D. R., Wozniak, A. and Zorn, S. R. (2013) 'Production mechanisms, number concentration, size distribution, chemical composition, and optical properties of sea spray aerosols', *Atmospheric Science Letters*, 14(4), pp. 207–213. doi: 10.1002/asl2.441.
- Miles, R.E.H., Walker, J.S., Burham, D.R. and Reid, J.P. (2012) 'Retrieval of the complex refractive index of aerosol droplets from optical tweezers measurements', *Physical Chemistry Chemical Physics*, 14, pp.3037-3037
- Mishra, A., Koren, I. and Ruddich, Y. (2015) 'Effect of aerosol vertical distribution on aerosol-radiation interaction: A theoretical prospect', *Atmospheric Environment*, 2, doi: 10.1016/j.heliyon.2015.e00036.
- Moise, T., Flores, J. M. and Rudich, Y. (2015) 'Optical Properties of Secondary Organic Aerosols and Their Changes by Chemical Processes', *Chemical Reviews*, 115(10), pp. 4400–4439. doi: 10.1021/cr5005259.
- Moosmüller, H., Chakrabarty, R. K., Ehlers, K. M. and Arnott, W. P. (2011) 'Absorption Ångström coefficient, brown carbon, and aerosols: Basic concepts, bulk matter, and spherical particles', *Atmospheric Chemistry and Physics*, 11(3), pp. 1217–1225. doi: 10.5194/acp-11-1217-2011.
- Nakayama, T., Matsumi, Y., Sato, K., Imamura, T., Yamazaki, A. and Uchiyama, A. (2010) 'Laboratory studies on optical properties of secondary organic aerosols generated during the photooxidation of toluene and the ozonolysis of α -pinene', *Journal of Geophysical Research: Atmospheres*, 115(24), pp. 1–11. doi: 10.1029/2010JD014387.
- Nakayama, T., Sato, K., Matsumi, Y., Imamura, T., Yamazaki, A. and Uchiyama, A. (2013) 'Wavelength and NO_x dependent complex refractive index of SOAs generated from the photooxidation of toluene', *Atmospheric Chemistry and Physics*, 13(2), pp. 531–545. doi: 10.5194/acp-13-531-2013.
- Nakayama, T., Sato, K., Tsuge, M., Imamura, T. and Matsumi, Y. (2015) 'Complex refractive index of secondary organic aerosol generated from isoprene/NO_x photooxidation in the presence and absence of SO₂', *Journal of Geophysical Research: Atmospheres*, pp. 1–19. doi: 10.1002/2014JD022121. Received.
- Park, S. S. and Yu, J. (2016) 'Chemical and light absorption properties of humic-like substances from biomass burning emissions under controlled combustion experiments', *Atmospheric Environment*, 136, pp. 114–122. doi:

- Petty, G. W. (2006) *A First Course in Atmospheric Radiation*. Sundog Publishing, Madison, Wisconsin.
- Pfrang, C., Sebastiani, F., Lucas, C. O. M., King, M. D., Hoare, I. D., Chang, D. and Campbell, R. A. (2014) ‘Ozonolysis of methyl oleate monolayers at the air-water interface: oxidation kinetics, reaction products and atmospheric implications.’, *Physical chemistry chemical physics*, 16(26), pp. 13220–8. doi: 10.1039/c4cp00775a.
- 5 Pokhrel, R. P., Wagner, N. L., Langridge, J. M., Lack, D. A., Jayarathne, T., Stone, E. A., Stockwell, C. E., Yokelson, R. J. and Murphy, S. M. (2016) ‘Parameterization of Single Scattering Albedo (SSA) and Absorption Ångström Exponent (AAE) with EC/OC for Aerosol Emissions from Biomass Burning’, *Atmospheric Chemistry and Physics Discussions*, (March), pp. 1–27. doi: 10.5194/acp-2016-184.
- 10 Pöschl, U. (2005) ‘Atmospheric aerosols: Composition, transformation, climate and health effects’, *Angewandte Chemie - International Edition*, 44(46), pp. 7520–7540. doi: 10.1002/anie.200501122.
- Ramanathan, V., Crutzen, P. J., Kiehl, J. T. and Rosenfeld, D. (2001) ‘Aerosols, Climate and the Hydrological Cycle’, *Science*, 294(December), pp. 2119–2125. doi: 10.1126/science.1064034.
- Rathod, T., Sahu, S. K., Tiwari, M., Yousaf, A., Bhangare, R. C. and Pandit, G. G. (2016) ‘Light Absorbing Properties of Brown Carbon Generated from Pyrolytic Combustion of Household Biofuels’, *Aerosol and Air Quality Research*, 1, pp. 108–116. doi: 10.4209/aaqr.2015.11.0639.
- 15 Redemann, J., Turco, R. P., Liou, K. N., Russell, P. B., Bergstrom, R. W., Schmid, B., Livingston, J. M., Hobbs, P. V., Hartley, W. S., Ismail, S., Ferrare, R. A. and Browell, E. V. (2000) ‘Retrieving the vertical structure of the effective aerosol complex index of refraction from a combination of aerosol in situ and remote sensing measurements during TARFOX’, *Journal of Geophysical Research: Atmospheres*, 105(D8), pp. 9949–9970. doi: 10.1029/1999JD901044.
- 20 Reid, J. S., Koppmann, R., Eck, T. F. and Eleuterio, D. P. (2005) ‘A review of biomass burning emissions part II: intensive physical properties of biomass burning particles’, *Atmospheric Chemistry and Physics Discussions*, 4(5), pp. 799–825. doi: 10.5194/acpd-4-5135-2004.
- Rkiouak, L., Tang, M. J., Camp, J. C. J., McGregor, J., Watson, I. M., Cox, R. A., Kalberer, M., Ward, A. D. and Pope, F. D. (2014) ‘Optical trapping and Raman spectroscopy of solid particles.’, *Physical chemistry chemical physics*, 16(23), pp. 11426–34. doi: 10.1039/c4cp00994k.
- 25 Rosenfeld, D., Lohmann, U., Raga, G. B., O’Dowd, C. D., Kulmala, M., Fuzzi, S., Reissell, A. and Andreae, M. O. (2008) ‘Flood or drought: how do aerosols affect precipitation?’, *Science*, 321(5894), pp. 1309–1313. doi: 10.1126/science.1160606.
- 30 Russell, P. B., Bergstrom, R. W., Shinozuka, Y., Clarke, A. D., DeCarlo, P. F., Jimenez, J. L., Livingston, J. M., Redemann, J., Holben, B., Dubovik, O. and Strawa, A. (2009) ‘Absorption Ångström Exponent in AERONET and related data as an indicator of aerosol composition’, *Atmospheric Chemistry and Physics Discussions*, 9(5), pp. 21785–21817. doi: 10.5194/acpd-9-21785-2009.
- Sandradewi, J., Prévôt, A. S. H., Weingartner, E., Schmidhauser, R., Gysel, M. and Baltensperger, U. (2008) ‘A study of

- wood burning and traffic aerosols in an Alpine valley using a multi-wavelength Aethalometer', *Atmospheric Environment*, pp. 101–112. doi: 10.1016/j.atmosenv.2007.09.034.
- Schnaiter, M., Gimmler, M., Llamas, I., Linke, C., Jäger, C. and Mutschke, H. (2006) 'Strong spectral dependence of light absorption by organic carbon particles formed by propane combustion', *Atmospheric Chemistry and Physics Discussions*, 6(2), pp. 1841–1866. doi: 10.5194/acpd-6-1841-2006.
- Schnaiter, M., Horvath, H., Möhler, O., Naumann, K. H., Saathoff, H. and Schöck, O. W. (2003) 'UV-VIS-NIR spectral optical properties of soot and soot-containing aerosols', *Journal of Aerosol Science*, 34(10), pp. 1421–1444. doi: 10.1016/S0021-8502(03)00361-6.
- Schweiger, S., (1990) 'Observation of input and output structural resonances in the Raman spectrum of a single spheroidal dielectric microparticle' *Optics Letters*, 15(3), pp. 156–158, doi: 10.1364/OL.15.000156
- Sebastiani, F., Campbell, R. A. and Pfrang, C. (2015) 'Complementarity of neutron reflectometry and ellipsometry for the study of atmospheric reactions at the air–water interface', *RSC Adv.*, 5(129), pp. 107105–107111. doi: 10.1039/C5RA22725A.
- Shen, Z., Zhang, Q., Cao, J., Zhang, L., Lei, Y., Huang, Y., Huang, R. J., Gao, J., Zhao, Z., Zhu, C., Yin, X., Zheng, C., Xu, H. and Liu, S. (2017) 'Optical properties and possible sources of brown carbon in PM_{2.5} over Xi'an, China', *Atmospheric Environment*, 150, pp. 322–330. doi: 10.1016/j.atmosenv.2016.11.024.
- Shingler, T., Crosbie, E., Ortega, A., Shiraiwa, M., Zuend, A., Beyersdorf, A., Ziemba, L., Anderson, B., Thornhill, L., Perring, A. E., Schwarz, J. P., Campazano-Jost, P., Day, D. A., Jimenez, J. L., Hair, J. W., Mikoviny, T., Wisthaler, A. and Sorooshian, A. (2016) 'Airborne characterization of subsaturated aerosol hygroscopicity and dry refractive index from the surface to 6.5km during the SEAC4RS campaign', *Journal of Geophysical Research*, pp. 4282–4303. doi: 10.1002/2014JD022963.
- Spindler, C., Abo Riziq, A. and Rudich, Y. (2007) 'Retrieval of Aerosol Complex Refractive Index by Combining Cavity Ring Down Aerosol Spectrometer Measurements with Full Size Distribution Information', *Aerosol Science and Technology*, 41(11), pp. 1011–1017. doi: 10.1080/02786820701682087.
- Stamnes, K., C. T. S., Wiscombe, W. J. and Jayaweera, K. (1988) 'Numerically stable algorithm for discrete-ordinate-method radiative transfer in multiple scattering and emitting layered media', *Applied optics*, 27, pp. 2502–2509. doi: 10.1364/AO.27.002502.
- Stocker, T. F., Qin, D. and Plattner, G. K. (2013) 'Climate Change 2013: The Physical Science Basis (Technical Summary)', *Climate Change 2013: The Physical Science Basis.*, pp. 33–115. doi: 10.1017/CBO9781107415324.005.
- Tinel, L., Rossignol, S., Bianco, A., Passananti, M., Perrier, S., Wang, X., Brigante, M., Donaldson, D. J. and George, C. (2016) 'Mechanistic Insights on the Photosensitized Chemistry of a Fatty Acid at the Air/Water Interface', *Environmental Science and Technology*, 50(20), pp. 11041–11048. doi: 10.1021/acs.est.6b03165.
- Tomasi, C., Vitale, V., Lupi, A., Di Carmine, C., Campanelli, M., Herber, A., Treffeisen, R., Stone, R. S., Andrews, E., Sharma, S., Radionov, V., von Hoyningen-Huene, W., Stebel, K., Hansen, G. H., Myhre, C. L., Wehrli, C., Aaltonen, V.,

- Lihavainen, H., Virkkula, A., Hillamo, R., Ström, J., Toledano, C., Cachorro, V. E., Ortiz, P., de Frutos, A. M., Blindheim, S., Frioud, M., Gausa, M., Zielinski, T., Petelski, T. and Yamanouchi, T. (2007) 'Aerosols in polar regions: A historical overview based on optical depth and in situ observations', *Journal of Geophysical Research Atmospheres*, 112(16). doi: 10.1029/2007JD008432.
- 5 Thompson, K.C., Rennie, A.R., King, M.D., Hardman, S.J.O., Lucas, C.O.M., Pfrang, C., Hughes, B.R. and Hughes, A.V., (2010) 'Reaction of a Phospholipid Monolayer with Gas-Phase Ozone at the Air–Water Interface: Measurement of Surface Excess and Surface Pressure in Real Time', *Langmuir*, 26 (22), 17295–17303. doi: 10.1021/la1022714
- Trainic, M., Riziq, A. A., Lavi, A., Flores, J. M. and Rudich, Y. (2011) 'and Physics The optical , physical and chemical properties of the products of glyoxal uptake on ammonium sulfate seed aerosols', pp. 9697–9707. doi: 10.5194/acp-11-9697-10 2011.
- Utry, N., Ajtai, T., Filep, A., Pinter, M., Torok, Z., Bozoki, Z. and Szabo, G. (2014) 'Correlations between absorption Ångström exponent (AAE) of wintertime ambient urban aerosol and its physical and chemical properties', *Atmospheric Environment*. Elsevier Ltd, 91, pp. 52–59. doi: 10.1016/j.atmosenv.2014.03.047.
- Utry, N., Tibor, A., Filep, A., Daniel Pinter, M., Hoffer, A., Bozoki, Z. and Szabo, G. (2013) 'Mass specific optical 15 absorption coefficient of HULIS aerosol measured by a four-wavelength photoacoustic spectrometer at NIR, VIS and UV wavelengths', *Atmospheric Environment*, 69, pp. 321–324. doi: 10.1016/j.atmosenv.2013.01.003.
- Virkkula, A., Koponen, I. K., Teinilä, K., Hillamo, R., Kerminen, V. M. and Kulmala, M. (2006) 'Effective real refractive index of dry aerosols in the Antarctic boundary layer', *Geophysical Research Letters*, 33(6), pp. 10–13. doi: 10.1029/2005GL024602.
- 20 Washenfelder, R. A., Flores, J. M., Brock, C. A., Brown, S. S. and Rudich, Y. (2013) 'Broadband measurements of aerosol extinction in the ultraviolet spectral region', *Atmospheric Measurement Techniques*, 6(4), pp. 861–877. doi: 10.5194/amt-6-861-2013.
- Wex, H., Petters, M. D., Carrico, C. M., Hallbauer, E., Massling, A., McMeeking, G. R., Poulain, L., Wu, Z., Kreidenweis, S. M. and Stratmann, F. (2009) 'Towards closing the gap between hygroscopic growth and activation for secondary organic 25 aerosol: Part 1 – Evidence from measurements', *Atmospheric Chemistry and Physics Discussions*, 9(1), pp. 955–989. doi: 10.5194/acpd-9-955-2009.
- Wild, M. (2009) 'Global dimming and brightening: A review', *Journal of Geophysical Research*, 114. doi: 10.1029/2008JD011470.
- Wolff, E. W. (1990) 'Signals of atmospheric pollution in polar snow and ice', *Antarctic Science*, 2(3), pp. 189–205. doi: 30 10.1017/S095410209000027X.
- Yamasoe, M. A., Artaxo, P., Miguel, A. H. and Allen, A. G. (2000) 'Chemical composition of aerosol particles from direct emissions of vegetation fires in the Amazon Basin: Water-soluble species and trace elements', *Atmospheric Environment*, 34(10), pp. 1641–1653. doi: 10.1016/S1352-2310(99)00329-5.
- Yamasoe, M. A., Kaufman, Y. J., Dubovik, O., Remer, L. A., Holben, B. N. and Artaxo, P. (1998) 'Retrieval of the real part

of the refractive index of smoke particles from Sun/sky measurements during SCAR-B', *Journal of Geophysical Research*, 103(98), p. 31893. doi: 10.1029/98JD01211.

Yu, Y., Ezell, M. J., Zelenyuk, A., Imre, D., Alexander, L., Ortega, J., D'Anna, B., Harmon, C. W., Johnson, S. N. and Finlayson-Pitts, B. J. (2008) 'Photooxidation of alpha-pinene at high relative humidity in the presence of increasing concentrations of NO_x', *Atmospheric Environment*, 42(20), pp. 5044–5060. doi: 10.1016/j.atmosenv.2008.02.026.

Zhang, X., Lin, Y. H., Surratt, J. D. and Weber, R. J. (2013) 'Sources, composition and absorption Ångström exponent of light-absorbing organic components in aerosol extracts from the los angeles basin', *Environmental Science and Technology*, 47(8), pp. 3685–3693. doi: 10.1021/es305047b.

Zhao, W., Dong, M., Chen, W., Gu, X., Hu, C., Gao, X., Huang, W. and Zhang, W. (2013) 'Wavelength-resolved optical extinction measurements of aerosols using broad-band cavity-enhanced absorption spectroscopy over the spectral range of 445-480 nm', *Analytical Chemistry*, 85(4), pp. 2260–2268. doi: 10.1021/ac303174n.

Zhou, S., Gonzalez, L., Leithead, A., Finewax, Z., Thalman, R., Vlasenko, A., Vagle, S., Miller, L. A., Li, S. M., Bureekul, S., Furutani, H., Uematsu, M., Volkamer, R. and Abbatt, J. (2014) 'Formation of gas-phase carbonyls from heterogeneous oxidation of polyunsaturated fatty acids at the air-water interface and of the sea surface microlayer', *Atmospheric Chemistry and Physics*, 14(3), pp. 1371–1384. doi: 10.5194/acp-14-1371-2014.

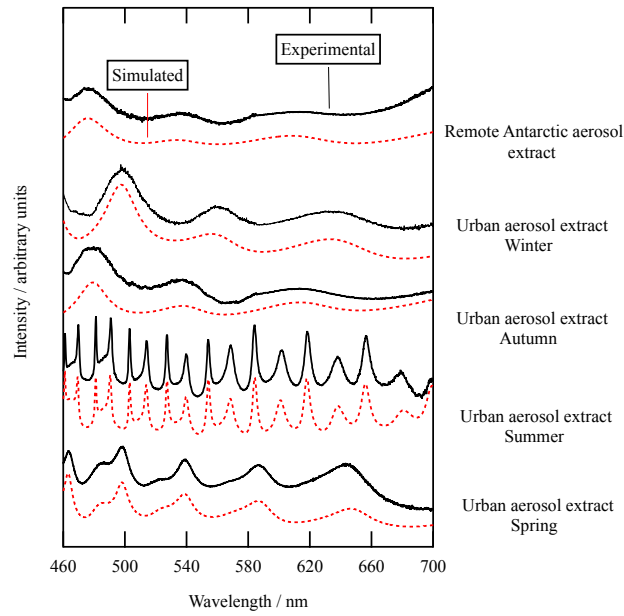


Figure 1: The typical Mie spectra as a function of wavelength obtained for the urban atmospheric aerosol extract collected over the four seasons and the remote atmospheric aerosol extract. From the Mie spectra, the refractive index and radius of the trapped droplet could be determined. Simulated and measured Mie spectra are compared. It ought to be noted that the Summer urban aerosol extract depicts a greater number of peaks owing to the size of the trapped droplet being considerably greater than the size of the other optically trapped droplets.

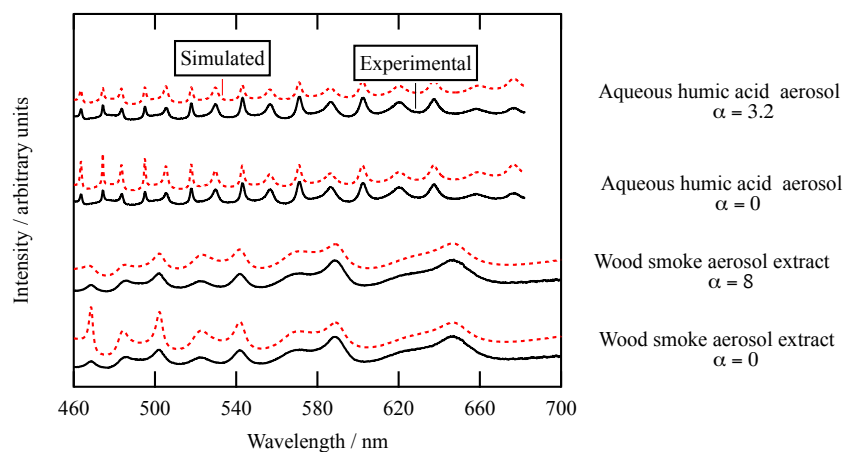


Figure 2: Typical Mie spectra for (a) the wood smoke aerosol extract B and (b) the humic acid droplet with simulated Mie spectra with and without absorption. The simulated Mie spectra when the measured absorption Ångström exponent, α , was included or when the absorption Ångström exponent was held at zero are shown for wood smoke aerosol extract and humic acid droplets. Note the absorption measured in Fig. 2 is required to provide a good fit to the intensity of the data, especially at short wavelength.

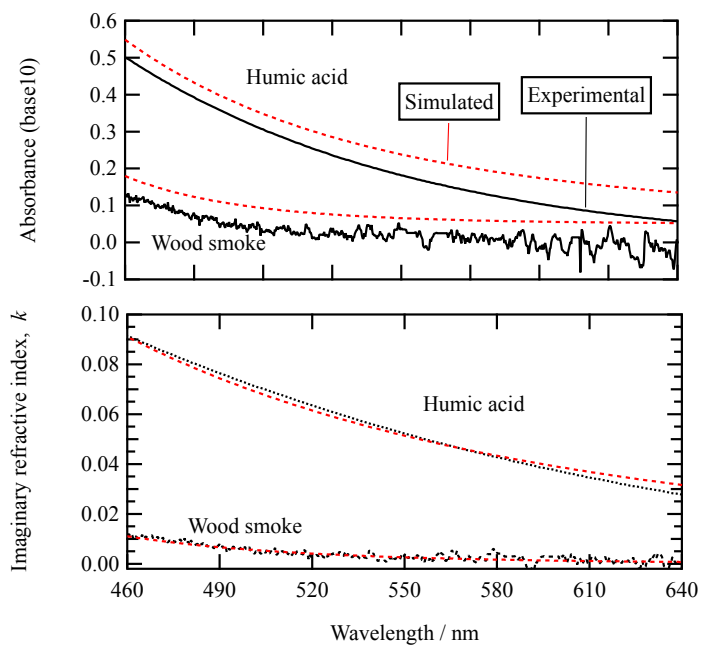


Figure 3: The absorbance (base 10) of the aqueous humic acid solution and wood smoke aerosol in isopropanol. The mass density of humic acid in water is $7.00 \times 10^{-5} \text{ g cm}^{-3}$ and the mass density of the wood smoke extract in isopropanol is $6.60 \times 10^{-5} \text{ g cm}^{-3}$. Using mass densities of pure humic acid (1.52 g cm^{-3}) and wood smoke extract B (1.64 g cm^{-3}) allows calculation of the imaginary refractive index of the pure components as displayed in the second, lower panel. Parameters for equation (2) displayed in the figure are contained in table 2. The simulated absorbance curves in the upper panel have been displaced upwards for clarity.

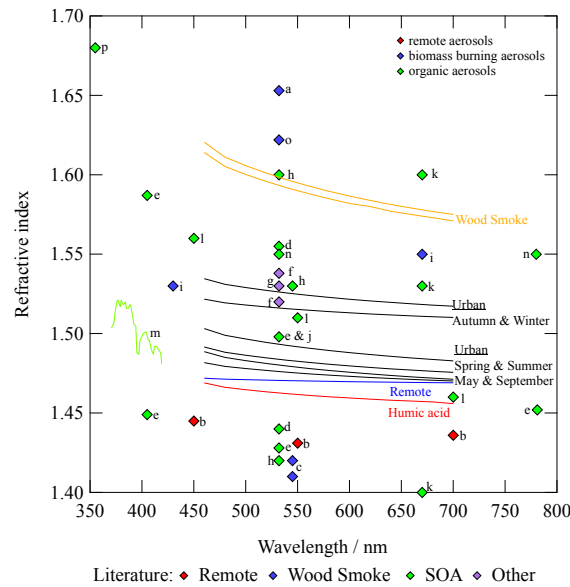


Figure 4: Refractive index dispersions for urban, remote and wood smoke atmospheric aerosol extracts and humic acid droplets, compared to refractive index values from literature. A sample of literature studies investigated aerosols from (1) remote locations e.g. b Virkkula (2006), (2) biomass burning e.g. a: Hoffer et al. (2005), c: Guyon et al. (2003) i: Yamasoe et al. (1998), n: Chakrabarty et al. (2010) and (o) Dinar et al. (2008) and (3) organic aerosols e.g. d: Kim and Paulson (2013), e: Nakayama et al. (2013), h: Lambe et al. (2013), j: Spindler et al. (2007), k: Kim et al. (2010), l: Yu et al. (2008), m: Flores et al. (2014), n: Chakrabarty et al. (2010) and p: Trainic et al. (2011).

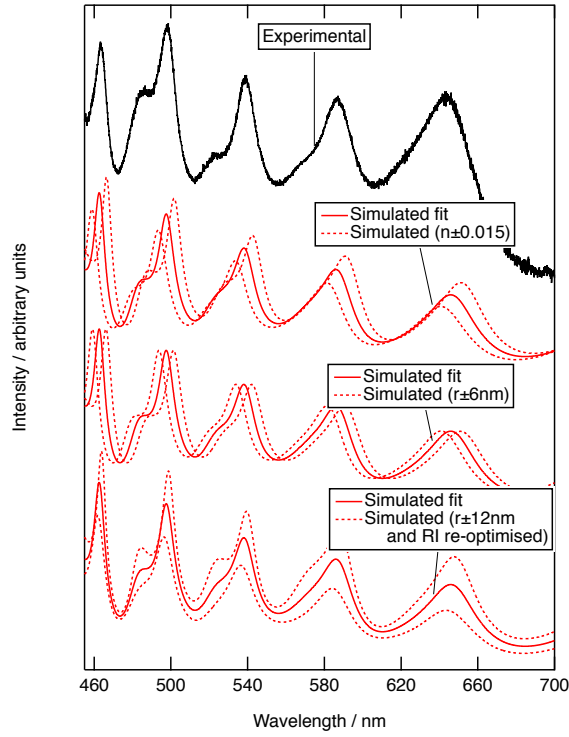


Figure 5: The experimental Mie spectra for the urban spring aerosol extract with the simulated best fit perturbed in three different scenarios to demonstrate the sensitivity of fitting simulated Mie spectra to experimental Mie spectra. Initially the simulated fit (red solid line) is recalculated with a refractive index increased and decreased by 0.015 ($n \pm 0.015$), followed by the simulated fit (red solid line) recalculated with a radius increased and decreased by 6nm ($r \pm 6\text{nm}$). The final set of simulated Mie spectra consider the simulated fit (red solid line) is recalculated with a droplet radius increased and decreased by 12nm, but the refractive index re-optimized to get the best fit to the experimental fit ($r \pm 12\text{nm}$ and RI re-optimised). A clear demonstration that the quoted uncertainties in radius ($\pm 6\text{nm}$) and refractive index (± 0.015) are conservative and more than adequate.

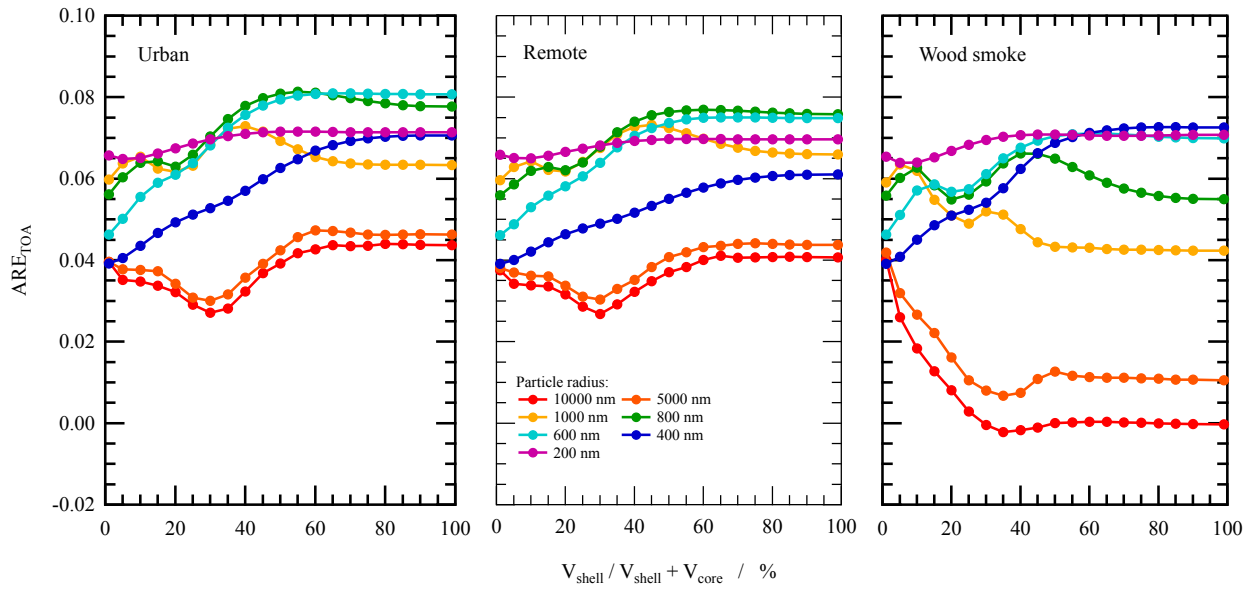


Figure 6: The aerosol radiative effect for the change in top of the atmosphere albedo upon core-shell morphology formation in atmospheric aerosols. The shell material consists of the urban atmospheric aerosol extract (left), remote atmospheric aerosol extract (middle) or wood smoke atmospheric aerosol extract (right), whilst the core for all calculations was water. The radius of the core was varied 7 times. The left-hand side of the graph corresponds to pure aqueous droplets, the right hand side to pure organic droplets.

5 Table 1: The number of aerosols studied, their determined Cauchy coefficients and the particle sizes. Many more particles were studied but were too small to produce Mie spectra that could be fitted with confidence (i.e. the Mie spectra lacked structure). A very limited amount of sample prevented a larger aerosol becoming optically trapped. Where more than one particle was analyzed for a single type of sample, e.g. urban spring, the average and standard deviation of the Cauchy coefficients and real refractive index were reported for the particle studied. The standard deviation does not reflect the uncertainty estimated from the fitting process (which is ± 0.015 for the real refractive index) but a spread of values obtained for the few particles studied. The range in particle sizes studied is also reported. Note the wood smoke aerosol extract was plentiful and repeated experiments could be performed.

		Droplets & Particles Analysed	A	B (nm ²)	C (nm ⁴)	Real Refractive Index (589 nm)	Radius Range (μm)
Urban	Spring	3	1.478±0.010	3750±3250	0	1.489	0.49-0.762
	Summer	4	1.465±0.005	4625±1200	0	1.478	0.474-1.252
	Autumn	1	1.505	6000	0	1.522	0.492
	Winter	2	1.495±0.007	4000	0	1.507	0.515
Wood Smoke	Extract A	6	1.543	15700± 750	0	1.588± 0.002	0.500-0.723
	Extract B	6	1.541± 0.003	14800± 2900	0	1.584± 0.007	0.475-0.593

Table 1: The mass densities and absorption properties of the wood smoke and Humic acid samples used in the work described here.

Sample	Mass density / g cm ⁻³	Absorption coefficient, β , at $\lambda_0 = 460$ nm / cm ⁻¹	k_0 ($\lambda_0 = 460$ nm)	Abs ₀ ($\lambda_0 = 460$ nm)	α
Pure Wood smoke extract B	1.64	3033	0.0111±0.0010	-	9.0±0.1
Wood smoke extract B in isopropanol (Fig. 3 – top pane)	6.60×10 ⁻⁵	0.122	(4.47±0.40)×10 ⁻⁷	0.122	9.0±0.1
Aqueous Humic acid (Fig. 3 – top pane)	7.00×10 ⁻⁵	1.513	(4.214±0.38)×10 ⁻⁶	0.499	4.2±0.1
Pure Humic acid	1.52	25,000	0.092±0.046	-	4.2±0.1
Optically trapped aqueous Humic acid droplet	0.016	273.2	(1.00±0.50)×10 ⁻³	-	4.2±0.1

Paper 4: Gas-phase OH radical oxidation of an organic film at the air-water interface using material extracted from urban, remote and wood smoke aerosol

Rosalie H. Shepherd, Martin D. King, Adrian R. Rennie, Andrew D. Ward, Markus M. Frey, Neil Brough and Max Skoda

To be submitted to the Journal of Atmospheric Chemistry and Physics.

I declare I have made the following contributions to the piece of co-authored work:

- Collected wood smoke aerosol extracts and helped with the collection of urban aerosol extracts
- Extracted atmospheric aerosol from the collection filters
- Conducted the experiments, and collected and analysed all data collected
- Contributed to the conclusions drawn from the experiments conducted
- Authored the paper

Gas-Phase OH Radical Oxidation of an Organic Film at the Air-Water Interface using Material Extracted from Urban, Remote & Wood Smoke Aerosol

Rosalie H. Shepherd^{1,2}, Martin D. King², Adrian R. Rennie³, Andrew D. Ward¹,
5 Markus M. Frey⁴, Neil Brough⁴ and Max Skoda⁵

¹Central Laser Facility, Research Complex, STFC Rutherford Appleton Laboratory, Oxford, OX11 0FA, UK

²Department of Earth Sciences, Royal Holloway, University of London, Egham, Surrey, TW20 0EX, UK

³Department of Physics and Astronomy, Uppsala University, 75120 Uppsala, Sweden

⁴British Antarctic Survey, Natural Environment Research Council, High Cross, Madingley Road, Cambridge, CB3 0ET, UK

10 ⁵ISIS Pulsed Neutron and Muon Source, Rutherford Appleton Laboratory, Oxford, OX11 0FA, UK

Correspondence to: Martin King (m.king@es.rhul.ac.uk)

Abstract. The presence of an organic film on a cloud droplet or aqueous aerosol has the potential to alter the chemical and physical properties of the droplet or particle. In the study presented, atmospheric aerosol extracts sourced from urban, remote and wood-burning aerosol demonstrated successful formation of a film at the air-water interface. The atmospheric aerosol
15 extract films were analysed by using neutron reflection to determine the neutron scattering length density and film thickness. Knowledge of film thickness is paramount for correct modelling of the atmosphere. Neutron reflectometry was subsequently applied to monitor the change in the films upon exposure to OH radicals, an abundant atmospheric oxidant. Analysing the kinetics of the oxidation data demonstrated that all films, regardless of source, decayed exponentially in terms of neutron scattering length density and film thickness. Determining a rate constant for the decay allowed the film lifetime under
20 atmospheric conditions to be calculated. The lifetime of the film was short in comparison to the typical lifetime of an aerosol in the troposphere (days), and hence determining the presence of atmospheric aerosol thin films in the atmosphere might be difficult. Additionally, the oxidation kinetics of the atmospheric aerosol proxy, 1,2-distearoyl-*sn*-glycero-3-phosphocholine, was studied. It demonstrated a significantly different decay profile, therefore it was concluded that it was not a good proxy for aerosol.

25 1. Introduction

Atmospheric aerosols have a crucial role in global climate e.g. Alley et al. (2007) and Toon et al. (1980); they contribute directly to global climate by either warming or cooling the planet by absorption or scattering incoming solar radiation, and indirectly affect global climate via cloud condensation effects e.g. Alley et al. (2007) and Andreaea and Rosenfeld (2008). However, current knowledge of atmospheric aerosols is far from complete e.g. Burkholder et al. (2017) and Stocker et
30 al.(2013).

Aqueous aerosol and cloud droplets are susceptible to organic film formation at the air-water interface e.g. Donaldson (1999), Donaldson and Vaida (2006), Ellison et al. (1999), Husar and Shu (1975), McNeill et al. (2013) and Tervahattu et al. (2002). The presence of such a film on the original aerosol or cloud droplet may change the chemical and physical properties through (a) reducing the rate of evaporation from the aerosol or droplets e.g. Davies et al. (2013), Eliason et al. (2003), Kaiser et al. (1996) and McFiggans et al. (2005), (b) inhibiting the transport of chemicals from the gas to the liquid phase of the droplet or aerosol e.g. Donaldson (1999), (c) reducing the scavenging of the droplet or aerosol by larger cloud and ice particles e.g. Andreaea and Rosenfeld (2008) and Feingold and Chuang (2002), (d) alter the cloud condensation nuclei activation potential of the droplet or aerosol e.g. Cruz and Pandis (1998) and Ruehl and Wilson (2014), (e) change the optical properties of the droplet or aerosol e.g. Donaldson and Vaida (2006) and (f) alter the reactive uptake ability of the aerosol or droplet e.g. Enami et al. (2010). An organic film at the air-water interface is susceptible to oxidation owing to atmospheric chemistry e.g. Bernard et al. (2016), Ciuraru et al. (2015) and Rossignol et al. (2016), a consequence of which is film ageing e.g. Pfrang et al. (2014). The aerosol can be considered to behave as an uncoated aerosol or a coated aerosol if the oxidation lifetime of the chemical film is less than a few seconds or greater than a few days respectively. A thin film with an oxidation lifetime between the two extremes can be considered a changing system, and the solar light scattering and absorbing properties of the aerosol will therefore alter as the film ages. Consequently, understanding how the film alters is paramount for accuracy in climate modelling.

Despite vast developments in our knowledge of atmospheric aerosol, current understanding of the physical and chemical characteristics is still limited e.g. Fuzzi et al. (2005) and Prather et al. (2008). The present study broadens knowledge of organic films on atmospheric aerosols by directly investigating the oxidation with gas-phase OH radicals of films from urban atmospheric aerosol sourced at Royal Holloway, University of London, remote atmospheric aerosol sourced from Antarctica and wood smoke aerosol. Alongside the remote atmospheric aerosol, organic extracts from Antarctic seawater were also collected. The sea-surface micro-layer and sub-surface layer contain many natural and anthropogenic organic materials e.g. Cincinelli et al. (2001), Cincinelli et al. (2005), Ciuraru et al. (2015), Fu (2015), Knulst et al. (2003) and Knulst and Södergren (1994) that will enter the atmosphere through bubbles bursting when waves break or from surface wind generating aerosol droplets e.g. Blanchard (1964), Donaldson and Vaida (2006), Gustafson and Dickhut (1997) and Cochran et al. (2016). The four samples may be interpreted as being from polluted urban, biomass burning, remote marine atmospheric aerosols and seawater.

Thin films present at air-water interfaces have been studied by a variety of techniques including x-ray and neutron studies e.g. King et al. (2009), Lu et al. (2000), Pfrang et al. (2014) and Thompson et al. (2010) and laser studies e.g. Tinel et al. (2016), Voss et al. (2007) and Voss et al. (2006). In the present work, neutron reflectivity was used to study oxidation of thin films extracted from atmospheric samples at the air-water interface. Oxidation chemistry of proxy-organic films have been studied previously, examples include the oxidation of oleic acid e.g. Dennis-Smith et al. (2012), González-Labrada et al. (2007), King et al. (2009), Pfrang et al. (2010), pinonic acid e.g. Enami and Sakamoto (2016), anthracene e.g. Mmereki and Donaldson (2003) and methyl oleate e.g. Pfrang et al. (2014). The use of OH radicals as the atmospheric oxidant has

additionally featured in a number of studies, such as those of Cappa et al. (2011) and Enami et al. (2014). The present study will extend previous work by investigating the oxidation kinetics of material extracted from the atmosphere as a thin film at the air-water interface as opposed to compounds that are proxies for atmospheric aerosol.

Once the films had formed at the air-water interface, the neutron scattering length density and thickness of the film were determined by measurement of the neutron reflectivity: the scattering length density of a material is dependent on its elemental composition and density. In addition, the reaction kinetics for the films when oxidized by gas-phase OH radicals was determined. The oxidation reaction was followed through continuous collection of neutron reflectivity profiles that allowed the neutron scattering length density per unit area of the interfacial layer to be followed with time. A rate constant for the oxidation was determined, and then the chemical lifetime of the film with respect to OH radical oxidation in the atmosphere was calculated. OH radicals are a very reactive lower atmospheric oxidant during the daytime e.g. Finlayson-Pitts and Pitts (1997) and Prinn et al. (2001), and will therefore react with saturated and unsaturated organic material e.g. Kolesar (2014). The reaction between the deuterated lipid 1,2-distearoyl-*sn*-glycero-3-phosphocholine (DSPC) and gas-phase OH radicals was studied to determine whether DSPC could be used as a proxy compound for organic films extracted from atmospheric matter and as a model reaction substrate.

2. Experimental

The study focuses on the oxidation of organic films sourced from atmospheric aerosol at the air-water interface. The interface was formed in a shallow PTFE trough enclosed in a Tedlar bag; the Tedlar bag was sealed to allow the development of the appropriate gaseous oxidizing environment above the film. Thickness and neutron scattering length density of the atmospheric aerosol film and how the film alters upon oxidation with gas-phase OH radicals was studied with neutron reflection techniques e.g. King et al. (2009).

2.1. Sample Collection & Extraction of Atmospheric Aerosol

Urban, remote and wood smoke atmospheric aerosol extracts as well as remote seawater samples were collected. Urban aerosol was collected at 15 m above the ground on the campus of Royal Holloway, University of London; urban aerosol was continuously collected for over a year in 30-day periods. The aerosols collected from the sampling point represent aerosols likely to be found in polluted air from London. Additionally owing to Royal Holloway's proximity to three major motorways M25, M40 and M4 (approximately 5 km away) and the large international airport Heathrow (approximately 15 km away), the samples were categorized as urban. Remote aerosol and seawater samples were collected from coastal Antarctica; two Antarctica aerosol filter samples were collected at the Halley Clean Air Sector Laboratory operated by the British Antarctic Survey during the 2015 and 2016 southern hemisphere summers (Jones et al., 2008). For each sample, atmospheric aerosol was continuously extracted for approximately 60 days. A sample of Antarctic seawater was collected on a sea ice cruise ship in the Weddell Sea (Antarctica) during the southern summer of 2014. Wood smoke aerosol was collected from the chimney

of a domestic wood burner; the fire was kept burning for six hours with aerosol being collected continuously. For all samples, analytical blanks were collected to account for any filter contamination. To ensure there was an accurate representation of all possible contamination, the analytical blanks travelled to sample sites.

To collect the urban atmospheric aerosol extract, air was pulled through short sections of clean stainless steel pipelines into a filter holder using an air pump at a flow of 30 L min^{-1} at local ambient temperature and pressure caught on pre-combusted 47 mm quartz filters (SKC) encased within PFA Savillex filter holders, whilst to collect remote atmospheric aerosol extracts ambient air was sampled from a half metre length of quarter inch PFA Teflon tubing onto a filter holder using a Staplex low volume air sampler (Model VM-4) at a flow rate of 20 L min^{-1} at local ambient temperature and pressure. Wood smoke samples were collected on the same filters, but housed in aluminium and steel filter holders machined at Royal Holloway, University of London that had the same internal dimensions as the PFA Savillex commercial filter holder. A different filter holder was required to collect wood smoke aerosol owing to the likely high temperature of sample collected. All instrumentation used in sample collection was cleaned with ultrapure water ($<18 \text{ M}\Omega \text{ cm}^{-1}$) and chloroform (Sigma-Aldrich, 0.5-1 % ethanol as stabilizer) multiple times and were assembled and disassembled in a clean glove bag. Upon collection, sample plus filter were stored in the dark at -18°C in clean glass Petri dishes until extraction.

To prepare the samples for use in the neutron reflection experiments, each filter paper was cut in half in a glove bag to avoid contamination. One half was for experimental use, the other half was stored at -18°C and kept for reference. The experimental filter half was placed in a sealed glass conical flask with 10 ml of chloroform and 10 ml of water and sonicated for five minutes and then filtered to remove the filter paper. The organic material likely to form insoluble organic films at the air-water interface was a solute in the chloroform (MacIntyre, 1974). The chloroform was separated from the water and subsequently evaporated under nitrogen leaving behind the organic atmospheric aerosol extract as a wax or oily residue, depending on aerosol source. To the residue, 2 ml of chloroform was added. The sample was stored in amber glass bottles at -18°C in the dark until use on the beam line.

Approximately 1 L of remote seawater was pumped from a water depth of $\sim 10 \text{ m}$ using the ship's continuous water sampling. The water was collected in a prepared PTFE travel jar, which was subsequently sealed and frozen at -18°C until analysis in the UK. Detritus was separated from the seawater samples by first filtering the water into a clean glass beaker. The water sample was subsequently shaken and extracted with chloroform in the method applied for atmospheric aerosol. To the resultant residue, again 2 ml of chloroform was added and the sample stored in amber glass bottles at -18°C in the dark until use on the beam line. All glassware was cleaned with ultrapure water and chloroform before use and all sample preparation was conducted in a clean environment.

2.2. Neutron Reflection

Using the neutron reflectometer INTER at ISIS Pulsed Neutron and Muon Source, Rutherford Appleton Laboratory, Oxfordshire (Webster et al., 2006), specular neutron reflectivity as a function of momentum transfer was used to collect

neutron reflectivity profiles. Reflectivity is the ratio of intensity in the reflected beam to that in the incident beam, whilst neutron momentum, Q , is defined as (Lu et al., 2000):

$$Q = \frac{4\pi \sin \theta}{\lambda}, \quad (1)$$

where λ is the wavelength of a neutron and θ the incident angle of the neutron beam to the interface of study. In the present study, the film thickness and neutron scattering length density of the atmospheric aerosol extract films were determined e.g. King (2009). The neutron scattering length density is defined as (Lu et al., 2000):

$$\rho = \sum n_i b_i, \quad (2)$$

where b_i is the neutron scattering length of the i^{th} element and n_i is the number density of the i^{th} element. The neutron scattering length is related to the interaction of the neutrons with the nuclei of the material under study and can be different for different isotopes of the same element, for example the neutron scattering length for hydrogen (^1H) is $-3.74 \times 10^{-5} \text{ \AA}$ and for deuterium (^2H) is $6.67 \times 10^{-5} \text{ \AA}$ e.g. Lu et al., 2000.

A film of atmospheric aerosol extract was placed at the air-water interface. The sub-phase was a mixture of water and deuterium oxide. Owing to the differences in neutron scattering length of hydrogen and deuterium, a 91.9:8.1 ratio of water and deuterium oxide forms a solution with an effective neutron scattering length density of zero. The solution is called air-contrast-matched-water and was used as the sub-phase for all experiments. All neutron reflection measurements were divided by a transmission data set, taken through the windows of the reaction chamber. This corrected the sample measurements for the incident neutron wavelength distribution and window transmission resulting in a normalised data set, which could be fitted as described below.

To obtain thickness and neutron scattering length density data, neutron reflection at two angles of the neutron beam in the vertical plane were used: 0.8° and 2.3° . This yielded a total momentum transfer range of $Q = 0.015$ to 0.33 \AA^{-1} . For the time resolved measurements of the oxidation reaction, the single angle 2.3° was used over a momentum transfer range of $Q = 0.03$ to 0.33 \AA^{-1} . For all experiments, reflected neutrons as a function of momentum transfer were counted for 15-minute time intervals.

The experimentally determined neutron reflectivity profiles were simulated using an optical formalism (Abelès, 1950) that depends on the film thickness, δ , and neutron scattering length density, ρ . These parameters are related to the surface coverage, Γ , in the relationship:

$$\Gamma b = \delta \rho, \quad (3)$$

where Γ is the surface coverage number of molecules per unit area in a film at the air-water interface composed of molecules with an average scattering length, b . The neutron scattering length cannot be known for a mixture of unknown molecules or reacting molecules at the air-water interface, especially where molecules leave or join the interface during a reaction. Therefore, in the study presented here the neutron scattering length per unit area of the interface, i.e. the quantity, $\delta \rho$, will be followed with time during every oxidation reaction; thus for the kinetics studied in this work the quantity $\frac{\rho_t \delta_t}{\rho_{t=0} \delta_{t=0}}$ is followed as a function of time, as in previous studies e.g. King (2009).

Abelès formalism as implemented in the software Motofit (Nelson, 2006), was used to calculate reflectivity and fit models. The films of atmospheric aerosol extract at the air-water interface were simulated as a single layer lying between two layers of infinite thickness. The regions of infinite thickness represent the aqueous sub-phase below the film, and the air above the film, and the neutron scattering length density of both of these was held at zero. In addition, the roughness of each layer was held at 3 Å and the background on the magnitude of 1×10^6 .

For the lipid, DSPC, a more ordered structure was simulated as a two layer system: one layer at the water interface representing the phosphocholine head groups of the lipid, and a second layer at the air interface representing the tail (hydrocarbon chains) of the lipid. Neutron scattering length densities and film thicknesses from Dabkowska et al. (2013) were used in the study to simulate the DSPC lipid.

2.3. Experimental Procedure

To record the neutron reflectivity profile of the films, two PTFE troughs were used. The first trough was a Langmuir trough with an approximate volume of 350 cm³ and PTFE barriers with a surface pressure sensor. The second trough was custom made to facilitate the production of an atmosphere of OH radicals above the trough and consists of a PTFE trough enclosed in a Tedlar bag with a UV photolysis lamp. The setup had two windows through which the neutron beam passed through. The volume of the trough was approximately 90 cm³; a small trough was used due to limited sample. Each trough was cleaned with chloroform and then filled with air-contrast-matched-water to create an air-water interface.

Between 100 and 400 µl of atmospheric aerosol extract suspended in chloroform was added to the air-water interface using a Hamilton syringe. The amount of material added was typically a few microliters less than that which would produce visible lens formation. After preparing the film, the thickness and neutron scattering length density of the film were determined from measurements prior to the OH radical oxidation.

UV lamps were required to create gas-phase OH radicals. The UV lamps were fluorescent germicidal lamps with an output wavelength of 254 nm. The lamps were suspended 9 cm above the trough and provided even illumination. The Langmuir trough and lamps were enclosed within a Tedlar bag to create a sealed environment. Gas-phase OH radicals were generated by the photolysis of gas-phase ozone in the presence of water vapour (Finlayson-Pitts and Pitts, 1997). An atmosphere of ozone and water vapour was generated by bubbling oxygen through air-contrast-matched-water at a flow rate of 1 L min⁻¹. The flow was then directed through an ozonizer (Ultra-Violet Products Ltd) that generated ozone by photolysis of oxygen with a Mercury pen-ray lamp. Subsequently, the flow passed into the Tedlar bag that had an approximate volume of 25 L with a gaseous mixing time of 25 minutes, assuming mixing in the Tedlar bag was efficient. To ensure the relative humidity of the experiment environment was maintained, a water reservoir with an approximate volume of 5×10^{-5} m³ was included within the Tedlar bag.

Measurements of experimental blanks were made for each film at the air-water interface. One experimental control for each sample was measuring whether the film would alter when exposed to just ozone. The second experimental control

was a measurement with only oxygen conducted with the ozonizer switched off. However, oxygen is likely to photolyse in the presence of UV light forming OH radicals and hence alteration in the film may be observed.

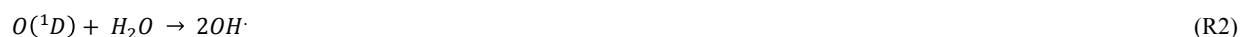
2.4. Estimation of OH Radical Concentration

To accurately estimate the concentration of the OH radicals produced, firstly the concentration of ozone had to be estimated.

- 5 The concentration of ozone was calculated to be 0.85 ppm by obtaining the UV-VIS spectrum of ozone in a 10 cm path length glass cell. Then the photolysis rate of ozone, $J_1(O(^1D))$, was measured directly by a Metcon radiometer normally used for measuring photolysis rates in the atmosphere.

- 10 The oxygen from which the ozone was produced from was saturated with water vapour; the concentration of water vapour was based on the vapour pressure of water (2.34 kPa at 20°C from Haynes, 2016). The rate constant value used for the photolysis of molecular oxygen was the value for ozone, scaled by the product of the absorption cross-sections and the quantum yields.

- 15 To estimate the concentration of gas-phase OH radicals in the Tedlar bag, kinetic modelling was based on a series of first-order differential equations using a Runge-Kutta algorithm e.g. Press et al. (2007) and Sandu and Sander (2006). Atkinson et al. (2003) covers the basic HO_x and O_x reactions occurring in the photolysis of ozone in the presence of water vapour in their reactions 1 to 30. The key reactions are outlined below:

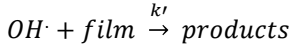


In the study presented a first-order wall loss with regard to OH radicals (R4) was added using the method outlined by Dilbeck and Finlayson-Pitts (2013). The wall loss was calculated to be 2 s^{-1} , assuming the Tedlar bag maintained a volume of 25 L and surface area of 0.612 m^2 upon experimental setup and the reaction probability for OH radicals on Tedlar was similar to halocarbon wax ($\gamma = 6 \times 10^{-4}$) e.g. Bertram et al. (2001).

- 25 Overall, the concentration of OH radicals present in the Tedlar bag was estimated to be $7 \times 10^6 \text{ molecule cm}^{-3}$. A sensitivity test was conducted on the model used; the initial starting concentration or the rate constant for each reaction step was increased and decreased by a factor of two and the effect on the final OH radical concentration analysed. It was determined that the OH radical concentration was most affected by the lamp intensity, initial ozone concentration and the water vapour concentration, each had a relative percentage error of 0.5%, 2 % and 1.7 % respectively on the OH radical
30 concentration.

2.5. Calculation of Atmospheric Aerosol Extract Lifetime.

To estimate the lifetime of the atmospheric aerosol extracts in the atmosphere upon exposure to gas-phase OH radicals, the bimolecular rate constant, k' , had to be calculated for Reaction 5:



The surface coverage of the aerosol extracts at the air-water interface is related to time by the following equation:

$$5 \quad \frac{d\Gamma_{film}}{dt} = -k'[OH\cdot]\Gamma_{film}, \quad (4)$$

where Γ_{film} represents the surface coverage of the film, t time and k' the pseudo first-order rate constant. Assuming the production of OH radicals to be continuous (and therefore $[OH\cdot]$ could be assumed to be a constant) and taking the change in the surface coverage of the film to be given by the product of the neutron scattering length density and film thickness, the following relationship could be used to model the neutron reflection profiles:

$$10 \quad \frac{\Gamma_{film}}{\Gamma_{film}^{t=0}} = \frac{\rho_t \delta_t}{\rho_{t=0} \delta_{t=0}} = e^{-k'[OH\cdot]t}, \quad (5)$$

A graph of $\frac{\rho_t \delta_t}{\rho_{t=0} \delta_{t=0}}$ versus time can then be plotted, and subsequently fitted to an exponential decay of the form e^{-kt} . The bimolecular rate constant, k , and atmospheric lifetime, τ , of the film was then calculated by applying the following two equations:

$$k = k'[OH\cdot], \quad (6)$$

$$15 \quad \tau = \frac{1}{k[OH\cdot]_{atm}}, \quad (7)$$

Atmospheric concentrations of OH radicals have been reported to range between 2 to 4×10^6 molecule cm^{-3} for a clean environment (Frost et al., 1999), and 4 to 6×10^6 molecule cm^{-3} for a polluted environment (George et al., 1999). In the presented study, a concentration of 4×10^6 molecule cm^{-3} has been used as $[OH\cdot]_{atm}$. The values for k , k' and τ determined in the study are shown in Table 1.

20 3. Results and Discussion

Material extracted from atmospheric aerosol and seawater successfully formed films at the air-water interface, and the thickness and neutron scattering length density of the films were determined by neutron reflection measurements. The oxidation of the films by gas-phase OH radicals was subsequently followed by continuously measuring neutron reflectivity for known time periods.

3.1. Atmospheric Aerosol Films

Typical neutron reflectivity data for the thin films at an air-water interface are depicted in Fig. 1. The neutron reflection results for the atmospheric aerosol extracts are distinguishable from the sub-phase and it can be inferred that films at the air-water interface were successfully formed.

Included in Fig. 1 is the neutron reflectivity profile obtained for the remote seawater extract. The neutron scattering length density and film thickness values obtained for the organic content of remote seawater (and displayed in Table 1) are slightly larger than values obtained for remote aerosol extracts. The source for remote aerosol is likely to be marine organic material (Legrand, 1998), however material extracted from the atmosphere has been exposed to oxidants and hence remote aerosol may differ slightly in composition to Antarctic seawater organic content. Kieber et al. (2016) demonstrated the potential for dissolved oceanic organic content to photochemically oxidize once in the atmosphere.

From Figs. 1a to 1d, it can be observed that the analytical blanks for each sample are indistinguishable from the neutron reflectivity profile of the sub-phase air-contrast-matched-water, thereby showing that the analytical blanks do not form films. Lack of signal for the analytical blanks demonstrates the success of collecting atmospheric aerosol by the method described in the study. The use of pre-combusted quartz filters and scrupulous clean working conditions contributed to the lack of contamination in all samples.

The neutron scattering length density determined by fitting models to the neutron reflectivity profile for urban and remote aerosol films lies below $1 \times 10^{-6} \text{ \AA}^{-2}$, whilst the wood smoke films had a higher neutron scattering length density of nearly $1.7 \times 10^{-6} \text{ \AA}^{-2}$. The neutron scattering length density may be used to indicate the possible composition of the films through comparing the experimentally obtained value for a film of the atmospheric aerosol extracts to those for various pure compounds, as depicted in Fig. 2. Classes of chemicals tend to fall into certain ranges, for example $-0.5 \times 10^{-6} \text{ \AA}^{-2}$ for saturated alkanes, $1 \times 10^{-6} \text{ \AA}^{-2}$ for aromatic groups and 1.5 to $2 \times 10^{-6} \text{ \AA}^{-2}$ for polysaccharides. Compounds chosen for the comparison directly relate to the aerosols studied in the work presented here: levoglucosan is a common tracer species of biomass burning aerosol e.g. Engling (2006), whilst methyl oleate, oleic acid and linoleic acid are common compounds used as aerosol-proxies e.g. Garland et al. (2008), King et al. (2009), Nah et al. (2013) and Pfrang et al. (2014).

It is necessary to consider that the neutron scattering length density obtained experimentally for atmospheric aerosol extracts is (a) probably that of a mixture of compounds with a range of individual neutron scattering length densities and (b) smaller than the values listed in Fig. 2 owing to the sample not packing densely at the air-water interface. Fig. 2 clearly demonstrates that the atmospheric aerosol films have scattering length densities greater than fatty acids, and indicates that the content of urban and remote aerosol might be similar in composition to organic compounds containing a small amount of oxygen, phosphorous or nitrogen atoms. The composition of wood smoke might be similar to polymers such as cellulose or levoglucosan (a common pyrolysis product of cellulose).

Fitting models to the neutron reflectivity data allowed the film thickness to be determined; aerosol extracts sourced from urban and remote locations had film thicknesses that did not exceed 11 \AA , however the wood smoke extract formed a

much thicker film of approximately 19 Å. In the absence of other data sources, the thickness determined in the study could be used in atmospheric modelling of core-shell aerosols.

The organic films were further studied by changing the surface pressure of the air-water interface. Closing and opening the barriers of the Langmuir trough compressed and expanded the film. Figure 3 depicts the compression and relaxation of an atmospheric aerosol extract film and the data is shown as a function of surface pressure rather than area per molecule because the sample was composed of an unknown complex mixture and therefore the number of molecules at the interface could not be determined. At each new surface pressure, a neutron reflectivity profile was collected and the film thickness determined by the method described in the Sect. 2.2. Owing to limited sample and neutrons being a limited resource, the experiment was conducted on just one sample: urban aerosol. An increase in surface pressure caused an increase in surface thickness as the molecules rearranged at the air-water interface to reduce the area they occupied. Expansion of the barriers caused surface pressure and surface thickness to reduce. Upon complete expansion, the film thickness was lower than the thickness measured prior to the compression and expansion of the film, indicating that material may have been lost from the interface or altered.

3.2. Kinetics of Atmospheric Aerosol Oxidation

Oxidation kinetics of proxy aerosol samples have been well studied e.g. Chapleski et al. (2016), commonly using ozone e.g. King et al. (2009), Pfrang et al. (2010) and Pfrang et al. (2014), OH radicals e.g. Cappa et al. (2011), George et al. (2009), Nah et al. (2013), Ruehl et al. (2013) Slade and Knopf et al. (2013) and Vlasenko et al. (2008) or nitrate radicals e.g. Knopf et al. (2011), Lee et al. (2013), Moise et al. (2002) and Zhang et al. (2014) as the oxidants. In the study presented here, films of aerosol extract formed at the air-water interface were oxidized through exposure to gas-phase OH radicals. The resultant decay of the relative quantity of $\frac{\rho_t \delta_t}{\rho_{t=0} \delta_{t=0}}$ as a function of time suggests the interface was changing to look more like water, and may indicate that either the surface material is becoming more hydrated or material is being lost from the interface. The alteration in $\frac{\rho_t \delta_t}{\rho_{t=0} \delta_{t=0}}$ as a function of time is shown in Figs. 4, 5 and 6. Error was determined by calculating the propagation of error as described by Bevington and Robinson (2002).

The decay profiles could be fitted to exponential curves. Figure 4 depicts the decay for the two urban aerosol extracts, the rate constants for the two urban aerosol extracts (extracted during the months of May and January) are the same within error, suggesting that the reactivity of the aerosol material sourced from the urban site with OH radicals may not be seasonally dependent, although further study is needed. The decay rate of $\frac{\rho_t \delta_t}{\rho_{t=0} \delta_{t=0}}$ for the remote aerosol extract collected in 2015 and 2016 are shown in Fig. 5 and overlap within error and the same rate constants may be used to describe both Antarctic atmospheric aerosols.

Interestingly, Figs. 4(a) and 5(a) both show a slower decay of the films when the films are exposed to oxygen and the UV lamps, owing to a lower ozone concentration present under these conditions reducing the concentration of OH

radicals, and thus slowing the rate of reaction. Importantly, the decrease in decay illustrates the film is not decaying solely from UV lamp damage. Neither the urban nor the remote aerosol extracts demonstrated a reaction with ozone.

Water insoluble wood smoke aerosol extracts have a decay of the same magnitude as urban and remote aerosol extract (Fig. 6), demonstrating a similar reactivity. In contrast, the wood smoke aerosol extract decays when exposed to ozone only. The extract was collected directly from the smoke plume and therefore had not been atmospherically processed and may contain unsaturated material. Goncalves et al. (2011) and Zhou et al. (2014) have investigated the oxidation kinetics of natural sea-surface material when exposed to gas-phase ozone, and observed a decrease in coverage. The decrease in coverage was attributed to unsaturated compounds present in the layer reacting with the ozone and products leaving the air-water interface.

Water insoluble surface-active extracts sourced from urban and remote locations did not react with ozone. For approximately 10000 seconds the neutron scattering length density per unit area of the material did not change, demonstrating the stability of the urban and remote aerosol extracts at the air-water interface. The extracts may not have decayed with ozone because either they contain a small mass ratio of unsaturated organic compounds to saturated material or the unsaturated content of the extract had been removed by atmospheric processing before collection. The latter suggestion is usually applied to extracts sourced from urban locations, as demonstrated by Jones et al. (2017). Results obtained from the study demonstrate a need for research that focuses on the ageing of saturated aerosol films; a number of studies have focused on the oxidation of films at the air-water interface e.g. Kinget al. (2009) and Pfrang et al. (2014), however the studies predominantly concentrated on the oxidation kinetics of films containing unsaturated functional groups.

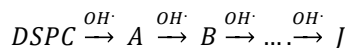
3.3. Oxidation Kinetics of a Proxy Atmospheric Aerosol

A film of DSPC, a phosphocholine lipid with saturated organic tails, was formed at the air-water interface and oxidized by gas-phase OH radicals. Lipids are commonly used as proxies for films on atmospheric aerosols, e.g. Garland et al. (2008), Jain et al. (2008), Morris et al. (2002), Nah et al. (2013), Smith et al. (2002) and Voss et al. (2007). Hence through comparing the reaction kinetics of DSPC with atmospheric aerosol extract under the same conditions, the validity of using lipids as proxy aerosols could be probed. The effect of the OH radicals on both the head and tail region of the lipid DSPC could be estimated from the neutron data individually, however to understand the decay process undergone by DSPC films the $\frac{\rho_t \delta_t}{\rho_{t=0} \delta_{t=0}}$ of the head and tail layer regions were combined by adding weighted values. An example is displayed as a function of time in Fig. 7. Three different films of DSPC at the air-water interface were exposed to gas-phase OH radicals, and all showed similar decay profiles.

The thin films of DSPC at the air-water interface displayed a decay that was characteristic of a step-wise degradation mechanism when exposed to gas-phase OH radicals (Enami, 2015), whereas the atmospheric-aerosol extracts demonstrated an exponential decay. A simulated fit for the decay of $\frac{\rho_t \delta_t}{\rho_{t=0} \delta_{t=0}}$ versus time was found by using a kinetic model based on a differential equation solved by a Runge-Kutta algorithm. The product of neutron scattering length density and

film thickness of the DSPC film at the air-water interface taken as a weighted sum of the products A to J . The algorithm used a weighting in each step of the reaction to ensure an accurate fit between the experimental and simulated data. The first product was weighted as 0.95, and each further product as 0.05 less, representing a loss of 5 percent of the molecules at the interface for each subsequent attack by the OH radicals until the film was no longer surface active. The degradation mechanism could be modelled accurately using ten overlapping kinetic steps, with the product of the first nine steps remaining at the air-water interface. The kinetic steps are outlined by the following scheme:

Scheme 2: The kinetic scheme of thin films composed of DSPC at the air-water interface degrading upon exposure to OH radicals.



where A to I represent the surface active products of the first nine reaction steps and J a gaseous or water soluble species that is lost from the interface. Table 2 lists the rate for each of the ten kinetic steps for three different DSPC films; analysis of the rate constants shows that an initial fast step is followed by a series of slower steps.

A series of checks were carried out to ensure that the degradation mechanism fully represented the method of decay for DSPC thin films at the air-water interface. First, the weighting of each kinetic step was adjusted and the alteration in quality of fit quantitatively determined by-eye. For the first three kinetic steps, the weight contribution could be varied by 5 percent whilst maintaining a reasonable fit, whereas for the following kinetic steps a variation of 15 percent in the weight of the contribution maintained an adequate fit. The result from the analysing the weight contribution demonstrates the importance of the first few kinetic steps in determining an accurate fit to the decay. Additionally, the importance in the number of required kinetic steps was determined iteratively by altering the number of steps, manually adjusting the rate constants to allow a reasonable fit and then determining the quality of the fit with a χ^2 test, that used Eq. 8:

$$\chi^2 = \sum \frac{(O_i - E_i)^2}{E_i}, \quad (8)$$

where O is the unchanged experimental value and E the value obtained after altering the number of kinetic steps. Figure 8 depicts the results for the weight contribution test and demonstrates that at least eight reaction steps are required.

In addition, two experimental blanks were carried out. DSPC films at the air-water interface were exposed to ozone only or UV light with oxygen. The DSPC films did not show a change when exposed to ozone only, however the chain region of the film did show a gradual decay when exposed to UV light in the presence of oxygen while the head region did not alter.

From comparing the decay of a film of DSPC at the air-water interface to films composed of atmospheric aerosol extract, it can be inferred that a phospholipid may not be a good representation of atmospheric aerosols owing to the difference in decay.

3.4. Atmospheric Implications

Simulations of neutron reflectivity profiles of the aerosol films at the air-water interface allowed an estimate of the film thickness. Use of a measured film thickness in light scattering calculations will aid the accurate modelling of scenarios in the atmosphere. The decay of the atmospheric film when exposed to OH radicals took the form of an exponential curve. The atmospheric lifetime of the film was estimated from Eq. 7 and is displayed in Table 2: the lifetime of the atmospheric aerosol extract is very short (on the timescale of minutes). Studies using proxy aerosol material have found the lifetime to vary from minutes e.g. Pfrang et al. (2014) to hours e.g. Donaldson and Valsaraj (2010), Gilman et al. (2004), King et al. (2009) and Thompson et al. (2010) and even to days e.g. Morris et al. (2002); the range in aerosol lifetime is likely caused by the phase and composition of the aerosol (Morris et al., 2002). The lifetime is relatively short in comparison to the typical lifetime of tropospheric aerosol (days), and consequently determining the presence of atmospheric thin films in the atmosphere may be difficult.

4. Conclusions

Material extracted from atmospheric aerosol was used to form films successfully at the air-water interface, from which the neutron scattering length density and thickness of the film could be resolved, demonstrating that neutron reflectivity is a useful technique for the study of aerosol extract films at the air-water interface. Urban and remote water insoluble surface active material extracted from aerosol formed films at the air-water interface with a neutron scattering length density value lying between 0.6 to $0.8 \times 10^{-6} \text{ \AA}^{-2}$ and a film thickness lying between 3 and 11 \AA , whilst wood smoke aerosol films were thicker (approximately 18 \AA) and had higher neutron scattering length density ($1.7 \times 10^{-6} \text{ \AA}^{-2}$).

Neutron reflectivity measurement allowed the thickness of interfacial films to be determined and it also permitted observation of the decay of the organic film when subjected to oxidizing conditions. The gas-phase oxidation demonstrated an exponential decay and not a step-wise degradation mechanism for all the aerosol films. The bimolecular rate constant obtained from the decay ranged from 5.2 to $10.0 \times 10^{-11} \text{ molecule cm}^{-3} \text{ s}^{-1}$ and was used to determine typical atmospheric lifetime of the aerosol. The lifetime of the atmospheric aerosol extracts is on the timescale of minutes, and is short in terms of lifetime in the atmosphere. It is therefore essential that the presence of a film and its change with time is considered in atmospheric modelling studies. The potential atmospheric aerosol proxy DSPC demonstrated different kinetics to samples extracted from the atmosphere, and thus should not be used as a proxy in future atmospheric experiments and simulations: asaturated lipid might be a better proxy-atmospheric aerosol.

Data Availability

Data is available at 10.5286/ISIS.E.61784247, 10.5286/ISIS.E.67767756, 10.5286/ISIS.E.81474355 and 10.5286/ISIS.E.79107195.

Appendix A

DSPC lipid films at the air-water interface have been modelled as a two-layer system in the study presented, however, the DSPC films could be fitted as a one-layer system. A neutron scattering length density of $7.07 \times 10^{-6} \text{ \AA}^{-2}$ as taken from the works of Hollinshead et al. (2009) and film thickness of approximately 20 Å were used to simulate the DSPC film as a monolayer before oxidation. The DSPC film could then be modelled as a monolayer as it decayed upon exposure to the gas-phase OH radicals. Interestingly, the decay profiles for each DSPC film when exposed to OH radicals were again not exponential, demonstrating that the DSPC film decays by a different mechanism to atmospheric aerosol extract.

Appendix B

The neutron scattering length density and film thickness values displayed in Table 1 were obtained by comparing a simulated neutron reflectivity profile to an experimentally obtained neutron reflectivity profile by eye. Applying a χ^2 test provided a means of demonstrating the level of accuracy provided by the fitting procedure.

To execute the χ^2 test, the film thickness of the aerosol extract film was held constant whilst the neutron scattering length density was adjusted. Subsequently, the film thickness was adjusted twice more and the process repeated. Figure 9 depicts χ^2 as a function of neutron scattering length density, for each plot a clear minimum is shown. Figure 9 suggests that the neutron scattering length density can be fitted to $\pm 0.05 \times 10^{-6} \text{ \AA}^{-2}$ accuracy. The neutron scattering length density and film thickness displayed in Table 1 correspond to the lowest minima. Note that the neutron scattering length density does not change with the value of film thickness.

Author Contributions

Rosalie H. Shepherd conducted all experiments, extracted all atmospheric aerosol extracts, analysed and interpreted the data and wrote the paper. Martin D. King, Andrew D. Ward and Adrian R. Rennie conceived the experiment idea and assisted in data collection and interpretation. In addition, Martin D. King collected the urban atmospheric aerosol extracts and Markus M. Frey and Neil Brough collected the remote atmospheric aerosol extracts. Max Skoda assisted in data collection.

Competing Interests

The authors declare that they have no conflict of interest.

Acknowledgements

The authors wish to thank STFC ISIS for awarding the beam time grants RB1510455, RB1520410 and RB1610119. Rosalie H. Shepherd would like to thank STFC for funding the student grant ST/L504279/1.

References

- 5 Abelès, F., (1950) 'La détermination de l'indice et de l'épaisseur des couches minces transparentes', *Le Journal de Physique et le Radium*, 11, pp. 307–310, doi: 10.1051/jphysrad:01950001107031000.
- Alley, R., Berntsen, T., Bindoff, N. L., Chen, Z., Chidthaisong, A., Friedlingstein, P., Gregory, J., Hegerl, G., Heimann, M., Hewitson, B., Hoskins, B., Joos, F., Jouzel, J., Kattsov, V., Lohmann, U., Manning, M., Matsuno, T., Molina, M., Nicholls, N., Overpeck, J., Qin, D., Raga, G., Ramaswamy, V., Ren, J., Rusticucci, M., Solomon, S., Somerville, R., Stocker, T. F.,
- 10 Stott, P., Stouffer, R. J., Whetton, P., Wood, R. A. and Wratt D., (2007) 'Climate Change 2007: The Physical Science Basis' Andreeva, M. O. and Rosenfeld, D., (2008) 'Aerosol–cloud–precipitation interactions. Part 1. The nature and sources of cloud-active aerosols', *Earth Science Reviews*, 89(1–2), pp. 13–41, doi: 10.1016/j.earscirev.2008.03.001.
- Atkinson, R., Baulch, D. L., Cox, R. A., Crowley, J. N., Hampson, R. F., Hynes, R. G., Jenkin, M. E., Rossi, M. J. and Troe, J., (2003) 'Evaluated kinetic and photochemical data for atmospheric chemistry: Part 1 - gas phase reactions of Ox, HOx, NOx and SOx species', *Atmospheric Chemistry and Physics Discussions*, 3(6), pp. 6179–6699, doi: 10.5194/acpd-3-6179-2003.
- 15 Bernard, F., Ciuraru, R., Boreave, A. and George, C., (2016) 'Photosensitized formation of secondary organic aerosols above the air/water interface', *Environmental Science & Technology*, 50, pp. 8678–8686, doi: 10.1021/acs.est.6b03520.
- Bertram, A. K., Ivanov, A. V., Hunter, M., Molina, L. T. and Molina, M. J., (2001) 'The Reaction Probability of OH on Organic Surfaces of Tropospheric Interest', *The Journal of Physical Chemistry A*, 105(41), pp. 9415–9421, doi: 10.1021/jp0114034.
- Bevington, P. and Robinson, K., (2002) 'Data Reduction and Error Analysis for the Physical Sciences', McGraw-Hill Education.
- Blanchard, D. C., (1964) 'Material, Sea-to-Air Transport of Surface Active', *Science*, 146, pp. 396–397, doi: 10.1126/science.146.3642.396.
- 25 Burkholder, J. B., Abbatt, J. P. D., Barnes, I., Roberts, J. M., Melamed, M. L., Ammann, M., Bertram, A. K., Cappa, C. D., Carlton, A. M. G., Carpenter, L. J., Crowley, J. N., Dubowski, Y., George, C., Heard, D. E., Herrmann, H., Keutsch, F. N., Kroll, J. H., McNeill, V. F., Ng, N. L., Nizkorodov, S. A., Orlando, J. J., Percival, C. J., Picquet-Varraut, B., Rudich, Y., Seakins, P. W., Surratt, J. D., Tanimoto, H., Thornton, J. A., Zhu, T., Tyndall, G. S., Wahner, A., Weschler, C. J., Wilson, K.
- 30 R. and Ziemann, P. J., (2017) 'The Essential Role for Laboratory Studies in Atmospheric Chemistry', *Environmental Science & Technology*, 51, pp. 2519–2528, doi: 10.1021/acs.est.6b04947.
- Cappa, C. D., Che, D. L., Kessler, S. H., Kroll, J. H. and Wilson, K. R., (2011) 'Variations in organic aerosol optical and

- hygroscopic properties upon heterogeneous OH oxidation', *Journal of Geophysical Research: Atmospheres*, 116(15), pp. 1–12, doi: 10.1029/2011JD015918.
- Chapleski, R. C., Zhang, Y., Troya, D. and Morris, J. R., (2016) 'Heterogeneous chemistry and reaction dynamics of the atmospheric oxidants, O₃, NO₃, and OH, on organic surfaces', *Chemical Society Review*, 45(3), pp. 3731–3746, doi: 10.1039/C5CS00375J.
- Cincinelli, A., Stortini, A. M., Checchini, L., Martellini, T., Del Bubba, M. and Lepri, L., (2005) 'Enrichment of organic pollutants in the sea surface microlayer (SML) at Terra Nova Bay, Antarctica: influence of SML on superficial snow composition.', *Journal of Environmental Monitoring*, 7(12), pp. 1305–1312, doi: 10.1039/b507321a.
- Cincinelli, A., Stortini, A. M., Perugini, M., Checchini, L. and Lepri, L., (2001) 'Organic pollutants in sea-surface microlayer and aerosol in the coastal environment of Leghorn - (Tyrrhenian Sea)', *Marine Chemistry*, 76(1-2), pp. 77–98, doi: 10.1016/S0304-4203(01)00049-4.
- Ciuraru, R., Fine, L., van Pinxteren, M., D'Anna, B., Herrmann, H. and George, C., (2015) 'Photosensitized production of functionalized and unsaturated organic compounds at the air-sea interface.', *Scientific reports*. 5(8), pp. 1-10, doi: 10.1038/srep12741.
- Ciuraru, R., Fine, L., Pinxteren, M. Van, D'Anna, B., Herrmann, H. and George, C., (2015) 'Unravelling New Processes at Interfaces: Photochemical Isoprene Production at the Sea Surface', *Environmental Science and Technology*, 49(22), pp. 13199–13205, doi: 10.1021/acs.est.5b02388.
- Cochran, R. E., Laskina, O., Jayarathne, T., Laskin, A., Laskin, J., Lin, P., Sultana, C., Lee, C., Moore, K. A., Cappa, C. D., Bertram, T. H., Prather, K. A., Grassian, V. H. and Stone, E. A., (2016) 'Analysis of Organic Anionic Surfactants in Fine and Coarse Fractions of Freshly Emitted Sea Spray Aerosol', *Environmental Science and Technology*, 50(5), pp. 2477–2486, doi: 10.1021/acs.est.5b04053.
- Cruz, C. N. and Pandis, S. N., (1998) 'The effect of organic coatings on the cloud condensation nuclei activation of inorganic atmospheric aerosol', *Journal Of Geophysical Research*, 103, pp. 13111–13123. doi: 10.1029/98JD00979.
- Dabkowska, A. P., Talbot, J. P., Cavalcanti, L., Webster, J. R. P., Nelson, A., Barlow, D. J., Fragneto, G. and Lawrence, M. J., (2013) 'Calcium mediated interaction of calf-thymus DNA with monolayers of distearoylphosphatidylcholine: a neutron and X-ray reflectivity study', *Soft Matter*, 9(29), pp. 7095–7105, doi: 10.1039/C3SM50350J.
- Davies, J. F., Miles, R. E. H., Haddrell, A. E. and Reid, J. P., (2013) 'Influence of organic films on the evaporation and condensation of water in aerosol.', *Proceedings of the National Academy of Sciences of the United States of America*, 110(22), pp. 8807–12, doi: 10.1073/pnas.1305277110.
- Dennis-Smith, B. J., Miles, R. E. H. and Reid, J. P., (2012) 'Oxidative aging of mixed oleic acid/sodium chloride aerosol particles', *Journal of Geophysical Research: Atmospheres*, 117(20), pp. 1–13, doi: 10.1029/2012JD018163.
- Dilbeck, C. W. and Finlayson-Pitts, B. J., (2013) 'Hydroxyl radical oxidation of phospholipid-coated NaCl particles', *Physical Chemistry Chemical Physics*, 15, pp. 9833–9844, doi: 10.1016/j.cognition.2008.05.007.
- Donaldson, D. J., (1999) 'Adsorption of Atmospheric Gases at the Air–Water Interface. I. NH₃', *Journal of Physical*

- Chemistry A, 103(1), pp. 62–70, doi: 10.1021/jp9833247.
- Donaldson, D. J. and Vaida, V., (2006) ‘The influence of organic films at the air-aqueous boundary on atmospheric processes’, *Chemical Reviews*, 106(4), pp. 1445–1461, doi: 10.1021/cr040367c.
- Donaldson, D. J. and Valsaraj, K. T., (2010) ‘Adsorption and reaction of trace gas-phase organic compounds on atmospheric water film surfaces: A critical review’, *Environmental Science and Technology*, 44(3), pp. 865–873, doi: 10.1021/es902720s.
- Eliason, T. L., Aloisio, S., Donaldson, D. J., Cziczo, D. J. and Vaida, V., (2003) ‘Processing of unsaturated organic acid films and aerosols by ozone’, *Atmospheric Environment*, 37(16), pp. 2207–2219, doi: 10.1016/S1352-2310(03)00149-3.
- Ellison, G. B., Tuck, A. F. and Vaida, V., (1999) ‘Atmospheric processing of organic aerosols’, *Journal of Geophysical Research*, 104(D9), pp. 11633. doi: 10.1029/1999JD900073.
- Enami, S., Hoffmann, M. R. and Colussi, A. J., (2010) ‘Molecular control of reactive gas uptake “on water”’, *Journal of Physical Chemistry A*, 114(18), pp. 5817–5822, doi: 10.1021/jp1019729.
- Enami, S., Hoffmann, M. R. and Colussi, A. J., (2014) ‘In situ mass spectrometric detection of interfacial intermediates in the oxidation of RCOOH(aq) by gas-phase OH-radicals’, *Journal of Physical Chemistry A*, 118(23), pp. 4130–4137, doi: 10.1021/jp503387e.
- Enami, S., Hoffmann, M. R. and Colussi, A. J., (2015) ‘Stepwise oxidation of aqueous dicarboxylic acids by gas-phase OH radicals’, *Journal of Physical Chemistry Letters*, 6(3), pp. 527–534, doi: 10.1021/jz502432j.
- Enami, S. and Sakamoto, Y., (2016) ‘OH-Radical Oxidation of Surface-Active cis-Pinonic Acid at the Air-Water Interface’, *Journal of Physical Chemistry A*, 120(20), pp. 3578–3587, doi: 10.1021/acs.jpca.6b01261.
- Engling, G., Carrico, C. M., Kreidenweis, S. M., Collett, J. L., Day, D. E., Malm, W. C., Lincoln, E., Min Hao, W., Iinuma, Y. and Herrmann, H., (2006) ‘Determination of levoglucosan in biomass combustion aerosol by high-performance anion-exchange chromatography with pulsed amperometric detection’, *Atmospheric Environment*, 40(SUPPL. 2), pp. 299–311, doi: 10.1016/j.atmosenv.2005.12.069.
- Feingold, G. and Chuang, P. Y. (2002) ‘Analysis of the Influence of Film-Forming Compounds on Droplet Growth: Implications for Cloud Microphysical Processes and Climate’, *Journal of the Atmospheric Sciences*, 59(12), pp. 2006–2018. doi: 10.1175/1520-0469(2002)059.
- Finlayson-Pitts, B. J. and Pitts, J. N., (1997) ‘Tropospheric air pollution: ozone, airborne toxics, polycyclic aromatic hydrocarbons, and particles.’, *Science*, 276(5315), pp. 1045–1052, doi: 10.1126/science.276.5315.1045.
- Frost, G. J., Trainer, M., Mauldin, R. L., Eisele, F. L., Prevot, A. S. H., Flocke, S. J., Madronich, S., Kok, G., Schillawski, R. D., Baumgardner, D. and Bradshaw, J., (1999) ‘Photochemical modeling of OH levels during the first aerosol characterization experiment (ACE 1)’, *Journal of Geophysical Research-Atmospheres*, 104(D13), pp. 16041–16052, doi: 10.1029/1999JD900171.
- Fu, H., Ciuraru, R., Dupart, Y., Passananti, M., Tinel, L., Rossignol, S., Perrier, S., Donaldson, D. J., Chen, J. and George, C., (2015) ‘Photosensitized Production of Atmospherically Reactive Organic Compounds at the Air/Aqueous Interface.’,

- Journal of the American Chemical Society, 137(26), pp. 8348–8351, doi: 10.1021/jacs.5b04051.
- Fuzzi, S., Andreae, M. O., Huebert, B. J., Kulmala, M., Bond, T. C., Boy, M., Doherty, S. J., Guenther, A., Kanakidou, M., Kawamura, K., Kerminen, V. M., Lohmann, U., Russell, L. M. and Pöschl, U., (2005) ‘Critical assessment of the current state of scientific knowledge, terminology, and research needs concerning the role of organic aerosols in the atmosphere, climate, and global change’, *Atmospheric Chemistry and Physics Discussions*, 5(6), pp. 11729–11780, doi: 10.5194/acpd-5-11729-2005.
- Fuzzi, S., Baltensperger, U., Carslaw, K., Decesari, S., Denier Van Der Gon, H., Facchini, M. C., Fowler, D., Koren, I., Langford, B., Lohmann, U., Nemitz, E., Pandis, S., Riipinen, I., Rudich, Y., Schaap, M., Slowik, J. G., Spracklen, D. V., Vignati, E., Wild, M., Williams, M. and Gilardoni, S., (2015) ‘Particulate matter, air quality and climate: lessons learned and future needs’, *Atmospheric Chemistry and Physics*, 15(14), pp. 8217–8299, doi: 10.5194/acp-15-8217-2015.
- Garland, E. R., Rosen, E. P., Clarke, L. I. and Baer, T., (2008) ‘Structure of submonolayer oleic acid coverages on inorganic aerosol particles: evidence of island formation.’, *Physical Chemistry Chemical Physics*, 10(21), pp. 3156–3161, doi: 10.1039/b718013f.
- George, I. J., Chang, R. Y. W., Danov, V., Vlasenko, A. and Abbatt, J. P. D., (2009) ‘Modification of cloud condensation nucleus activity of organic aerosols by hydroxyl radical heterogeneous oxidation’, *Atmospheric Environment*, 43(32), pp. 5038–5045, doi: 10.1016/j.atmosenv.2009.06.043.
- George, L. A., Hard, T. M. and O’Brien, R. J., (1999) ‘Measurement of free radicals OH and HO₂ in Los Angeles smog’, *Journal Of Geophysical Research-Atmospheres*, 104(D9), pp. 11643–11655, doi: 10.1029/1998JD100113.
- Gilman, J. B., Eliason, T. L., Fast, A. and Vaida, V., (2004) ‘Selectivity and stability of organic films at the air-aqueous interface’, *Journal of Colloid and Interface Science*, 280(1), pp. 234–243, doi: 10.1016/j.jcis.2004.07.019.
- Goncalves, C., Alves, C., Fernandes, A. P., Monteiro, C., Tarelho, L., Evtyugina, M. and Pio, C., (2011) ‘Organic compounds in PM_{2.5} emitted from fireplace and woodstove combustion of typical Portuguese wood species’, *Atmospheric Environment*, 45, pp. 4533–4545, doi: 10.1016/j.atmosenv.2011.05.071.
- González-Labrada, E., Schmidt, R. and DeWolf, C. E. (2007) ‘Kinetic analysis of the ozone processing of an unsaturated organic monolayer as a model of an aerosol surface’, *Physical Chemistry Chemical Physics*, 9(43), p. 5814-5821, doi: 10.1039/b707890k.
- Gustafson, K. E. and Dickhut, R. M., (1997) ‘Particle/gas concentrations and distributions of PAHs in the atmosphere of southern Chesapeake Bay’, *Environmental Science and Technology*, 31(1), pp. 140–147, doi: 10.1021/es9602197.
- Haynes, W. (2016) 'Handbook of Chemistry and Physics', CRC Press.
- Hollinshead, C. M., Harvey, R. D., Barlow, D. J., Webster, J. R. P., Hughes, A. V., Weston, A. and Lawrence, M. J., (2009) ‘Effects of surface pressure on the structure of distearoylphosphatidylcholine monolayers formed at the air/water interface’, *Langmuir*, 25(7), pp. 4070–4077, doi: 10.1021/la8028319.
- Husar, R. B. and Shu, W. R., (1975) ‘Thermal analyses of the LA smog aerosol’, *Journal of Applied Meteorology*, 14, pp. 1558–1565, doi: 10.1175/1520-0450(1975)014.

- Jain, K., Siddam, A., Marathi, A., Roy, U., Falck, J. R. and Balazy, M., (2008) 'The mechanism of oleic acid nitration by radical NO₂', *Free Radical Biology and Medicine*, 45(3), pp. 269–283, doi: 10.1016/j.freeradbiomed.2008.04.015.
- Jones, A. E., Wolff, E. W., Salmon, R. A., Bauguutte, S. J. B., Roscoe, H. K., Anderson, P. S., Ames, D., Clemitshaw, K. C., Fleming, Z. L., Bloss, W. J., Heard, D. E., Lee, J. D., Read, K. A., Hamer, P., Shallcross, D. E., Jackson, A. V., Walker, S. L., Lewis, A. C., Mills, G. P., Plane, J. M. C., Saiz-Lopez, A., Sturges, W. T. and Worton, D. R., (2008) 'Chemistry of the Antarctic Boundary Layer and the Interface with Snow: an overview of the CHABLIS campaign', *Atmospheric Chemistry and Physics*, 8(14), pp. 3789–3803, doi: 10.5194/acp-8-3789-2008.
- Jones, S. H., King, M. D., Ward, A. D., Rennie, A. R., Jones, A. C. and Arnold, T. (2017) 'Are organic films from atmospheric aerosol and sea water inert to oxidation by ozone at the air-water interface', *Atmospheric Environment*, 161, pp. 274–287, doi: 10.1016/j.atmosenv.2017.04.025.
- Kaiser, T., Roll, G. and Schweiger, G. (1996) 'Investigation of coated droplets in an optical trap: raman-scattering, elastic-light-scattering, and evaporation characteristics.', *Applied optics*, 35(30), pp. 5918–5924, doi: 10.1364/AO.35.005918.
- Kieber, D. J., Keene, W. C., Frossard, A. A., Long, M. S., Maben, J. R., Russell, L. M., Kinsey, J. D., Tyssebotn, I. M. B., Quinn, P. K. and Bates, T. S., (2016) 'Coupled ocean-atmosphere loss of marine refractory dissolved organic carbon', pp. 43, 2765–2772, doi: 10.1002/2016GL068273.Received.
- King, M. D., Rennie, A. R., Thompson, K. C., Fisher, F. N., Dong, C. C., Thomas, R. K., Pfrang, C. and Hughes, A. V., (2009) 'Oxidation of oleic acid at the air-water interface and its potential effects on cloud critical supersaturations.', *Physical Chemistry Chemical Physics*, 11(35), pp. 7699–7707, doi: 10.1039/b906517b.
- Knopf, D. A., Forrester, S. M. and Slade, J. H., (2011) 'Heterogeneous oxidation kinetics of organic biomass burning aerosol surrogates by O₃, NO₂, N₂O₅, and NO₃', *Physical Chemistry Chemical Physics*, 13(47), p. 21050–21062, doi: 10.1039/c1cp22478f.
- Knulst, J. C., Rosenberger, D., Thompson, B. and Paatero, J., (2003) 'Intensive Sea Surface Microlayer Investigations of Open Leads in the Pack Ice during Arctic Ocean 2001 Expedition', *Langmuir*, 19(24), pp. 10194–10199, doi: 10.1021/la035069+.
- Knulst, J. and Södergren, A., (1990) 'Occurrence and toxicity of persistent pollutants in surface microlayers near an incineration plant', *Cancer Letters*, 29, pp. 1339–1347, doi: 10.1016/0045-6535(94)90264-X.
- Kolesar, K. R., Buffaloe, G., Wilson, K. R. and Cappa, C. D., (2014) 'OH-initiated heterogeneous oxidation of internally-mixed squalane and secondary organic aerosol', *Environmental Science and Technology*, 48(6), pp. 3196–3202, doi: 10.1021/es405177d.
- Lee, L., Wooldridge, P., Nah, T., Wilson, K. and Cohen, R., (2013) 'Observation of rates and products in the reaction of NO₃ with submicron squalane and squalene aerosol.', *Physical Chemistry Chemical Physics*, 15(3), pp. 882–982, doi: 10.1039/c2cp42500a.

- Legrand, M., Ducroz, F., Wagenbach, D., Mulvaney, R. and Hall, J., (1998) 'Amonium in coastal Antarctica and snow: Role of polar ocean and penguin emissions', *Journal of Geophysical Research*, 103(D9), pp. 11043–11056, doi: 10.1029/97JD01976.
- Lu, J. R., Thomas, R. K. and Penfold, J., (2000) 'Surfactant layers at the air/water interface: Structure and composition', *Advances in Colloid and Interface Science*, 84(1), pp. 143–304, doi: 10.1016/S0001-8686(99)00019-6.
- MacIntyre, F., (1974) 'The top millimeter of the ocean', *Scientific American*, 230, pp. 62–77, doi: 10.1038/scientificamerican0574-62.
- McFiggans, G., Artaxo, P., Baltensperger, U., Coe, H., Facchini, M. C., Feingold, G., Fuzzi, S., Gysel, M., Laaksonen, A., Lohmann, U., Mentel, T. F., Murphy, D. M., O'Dowd, C. D., Snider, J. R. and Weingartner, E., (2005) 'The effect of physical and chemical aerosol properties on warm cloud droplet activation', *Atmospheric Chemistry and Physics Discussions*, 5(5), pp. 8507–8646, doi: 10.5194/acpd-5-8507-2005.
- McNeill, V. F., Sareen, N. and Schwier, A. N., (2013) 'Surface-Active Organics in Atmospheric Aerosols', *Atmospheric and Aerosol Chemistry*, 339, pp. 201–259.
- Mmereki, B. T. and Donaldson, D. J., (2003) 'Direct Observation of the Kinetics of an Atmospherically Important Reaction at the Air-Aqueous Interface', *Journal of Physical Chemistry A*, 107(50), pp. 11038–11042, doi: 10.1021/jp036119m.
- Moise, T., Talukdar, R. K., Frost, G. J., Fox, R. W. and Rudich, Y., (2002) 'Reactive uptake of NO₃ by liquid and frozen organics', *Journal of Geophysical Research-Atmospheres*, 107, pp. 1-9, doi: 4014 10.1029/2001jd000334.
- Morris, J. W., Davidovits, P., Jayne, J. T., Jimenez, J. L., Shi, Q., Kolb, C. E., Worsnop, D. R., Barney, W. S. and Cass, G., (2002) 'Kinetics of submicron oleic acid aerosols with ozone: A novel aerosol mass spectrometric technique', *Geophysical Research Letters*, 29(9), p. 1357. doi: 10.1029/2002GL014692.
- Nah, T., Kessler, S. H., Daumit, K. E., Kroll, J. H., Leone, S. R. and Wilson, K. R., (2013) 'OH-initiated oxidation of sub-micron unsaturated fatty acid particles.', *Physical Chemistry Chemical Physics*, 15(42), pp. 18649–18663, doi: 10.1039/c3cp52655k.
- Nah, T., Zhang, H., Worton, D. R., Ruehl, C. R., Kirk, B. B., Goldstein, A. H., Leone, S. R. and Wilson, K. R., (2014) 'Isomeric Product Detection in the Heterogeneous Reaction of Hydroxyl Radicals with Aerosol Composed of Branched and Linear Unsaturated Organic Molecules', *The Journal of Physical Chemistry A*, 118, pp. 11555–11571, doi: 10.1021/jp508378z.
- Nelson, A., (2006) 'Co-refinement of multiple-contrast neutron/X-ray reflectivity data using MOTOFIT', *Journal of Applied Crystallography*, 39(2), pp. 273–276, doi: 10.1107/S0021889806005073.
- Pfrang, C., Sebastiani, F., Lucas, C. O. M., King, M. D., Hoare, I. D., Chang, D. and Campbell, R. A., (2014) 'Ozonolysis of methyl oleate monolayers at the air-water interface: oxidation kinetics, reaction products and atmospheric implications', *Physical Chemistry Chemical Physics*, 16(26), pp. 13220–13228, doi: 10.1039/c4cp00775a.
- Pfrang, C., Shiraiwa, M. and Pöschl, U., (2010) 'Coupling aerosol surface and bulk chemistry with a kinetic double layer model (K2-SUB): Oxidation of oleic acid by ozone', *Atmospheric Chemistry and Physics*, 10(10), pp. 4537–4557, doi:

10.5194/acp-10-4537-2010.

- Prather, K. A., Hatch, C. D. and Grassian, V. H., (2008) 'Analysis of atmospheric aerosols', *Annual Review of Analytical Chemistry*, 1, pp. 485–514, doi: 10.1146/annurev.anchem.1.031207.113030.
- Press, W. H., Teukolsky, S. A., Vetterling, W. T. and Flannery, B. P., (2007) *Numerical Recipes: The Art of Scientific Computing*, Cambridge University Press.
- Prinn, R. G., Huang, J., Weiss, R. F., Cunnold, D. M., Fraser, P. J., Simmonds, P. G., McCulloch, A., Salameh, P., O'Doherty, S., Wang, R. H. J., Porter, L. and Miller, B. R., (2001) 'Evidence for substantial variation of atmospheric hydroxyl radicals in the past two decades', *Science*, 292(6), pp. 1882–1888, doi: 10.1126/science.1058673.
- Rossignol, S., Tinel, L., Bianco, A., Passananti, M., Brigante, M., Donaldson, D. J. and George, C., (2016) 'Atmospheric photochemistry at a fatty acid-coated air-water interface.', *Science*, 353(6300), pp. 699–702, doi: 10.1126/science.aaf3617.
- Ruehl, C. R., Nah, T., Isaacman, G., Worton, D. R., Chan, A. W. H., Kolesar, K. R., Cappa, C. D., Goldstein, A. H. and Wilson, K. R., (2013) 'The influence of molecular structure and aerosol phase on the heterogeneous oxidation of normal and branched alkanes by OH', *Journal of Physical Chemistry A*, 117(19), pp. 3990–4000, doi: 10.1021/jp401888q.
- Ruehl, C. R. and Wilson, K. R., (2014) 'Surface organic monolayers control the hygroscopic growth of submicrometer particles at high relative humidity', *Journal of Physical Chemistry A*, 118(22), pp. 3952–3966, doi: 10.1021/jp502844g.
- Sandu, A. and Sander, R., (2006) 'Technical Note : Simulating chemical systems in Fortran90 and Matlab with the Kinetic PreProcessor KPP-2.1', *Atmospheric Chemistry*, 6, pp. 187–195, doi: 10.5194/acp-6-187-2006.
- Sears, V. F., (1992) 'Neutron scattering lengths and cross sections', *Neutron News*, 3(3), pp. 26–37, doi: 10.1080/10448639208218770.
- Sebastiani, F., Campbell, R. A. and Pfrang, C., (2015) 'Complementarity of neutron reflectometry and ellipsometry for the study of atmospheric reactions at the air–water interface', *Royal Society of Chemistry*, 5(129), pp. 107105–107111, doi: 10.1039/C5RA22725A.
- Slade, J. H. and Knopf, D. A., (2013) 'Heterogeneous OH oxidation of biomass burning organic aerosol surrogate compounds: assessment of volatilisation products and the role of OH concentration on the reactive uptake kinetics', *Physical Chemistry Chemical Physics*, 15(16), pp. 5898–915, doi: 10.1039/c3cp44695f.
- Slade, J. H. and Knopf, D. A., (2014) 'Multiphase OH oxidation kinetics of organic aerosol: The role of particle phase state and relative humidity', *Geophysical Research Letters*, 41(14), pp. 5297–5306, doi: 10.1002/2014GL060582.
- Smith, G. D., Woods, E., DeForest, C. L., Baer, T. and Miller, R. E., (2002) 'Reactive uptake of ozone by oleic acid aerosol particles: Application of single-particle mass spectrometry to heterogeneous reaction kinetics', *Journal of Physical Chemistry A*, 106(35), pp. 8085–8095, doi: 10.1021/jp020527t.
- Stocker, T. F., Qin, D. and Plattner, G. K., (2013) 'Climate Change 2013: The Physical Science Basis (Technical Summary)', *Climate Change 2013: The Physical Science Basis*, pp. 33–115. doi: 10.1017/CBO9781107415324.005.
- Tervahattu, H., Hartonen, K., Kerminen, V., Kupiainen, K., Aarnio, P., Koskentalo, T., Tuck, A. and Vaida, V. (2002) 'New evidence of an organic layer on marine aerosols', *Journal of Geophysical Research*, 107(D7), pp. 1-8, doi:

- Thompson, K. C., Rennie, A. R., King, M. D., Hardman, S. J. O., Lucas, C. O. M., Pfrang, C., Hughes, B. R. and Hughes, A. V., (2010) 'Reaction of a phospholipid monolayer with gas-phase ozone at the air-water interface: Measurement of surface excess and surface pressure in real time', *Langmuir*, 26(22), pp. 17295–17303, doi: 10.1021/la1022714.
- 5 Tinel, L., Rossignol, S., Bianco, A., Passananti, M., Perrier, S., Wang, X., Brigante, M., Donaldson, D. J. and George, C. (2016) 'Mechanistic Insights on the Photosensitized Chemistry of a Fatty Acid at the Air/Water Interface', *Environmental Science and Technology*, 50(20), pp. 11041–11048. doi: 10.1021/acs.est.6b03165.
- Toon, O. B. and Pollack, J. B. (1980) 'Atmospheric Aerosols and Climate: Small particles in the Earth's atmosphere interact with visible and infrared light, altering the radiation balance and the climate', *American Scientist*.
- 10 Vlasenko, A., George, I. J. and Abbatt, J. P. D. (2008) 'Formation of volatile organic compounds in the heterogeneous oxidation of condensed-phase organic films by gas-phase OH', *Journal of Physical Chemistry A*, 112(7), pp. 1552–1560. doi: 10.1021/jp0772979.
- Voss, L. F., Bazerbashi, M. F., Beekman, C. P., Hadad, C. M. and Allen, H. C., (2007) 'Oxidation of oleic acid at air/liquid interfaces', *Journal of Geophysical Research Atmospheres*, 112(6), pp. 1–9, doi: 10.1029/2006JD007677.
- 15 Voss, L. F., Hadad, C. M. and Allen, H. C., (2006) 'Competition between atmospherically relevant fatty acid monolayers at the air/water interface', *Journal of Physical Chemistry B*, 110(39), pp. 19487–19490, doi: 10.1021/jp062595b.
- Webster, J., Holt, S. and Dalgliesh, R. (2006) 'INTER the chemical interfaces reflectometer on target station 2 at ISIS', *Physica B: Condensed Matter*, 385–386(April 2006), pp. 1164–1166, doi: 10.1016/j.physb.2006.05.400.
- Zhang, Y., Chapleski, R. C., Lu, J. W., Rockhold, T. H., Troya, D. and Morris, J. R., (2014) 'Gas-surface reactions of nitrate radicals with vinyl-terminated self-assembled monolayers', *Physical Chemistry Chemical Physics*, 16(31), pp. 16659–16670. doi: 10.1039/c4cp01982b.
- Zhou, S., Gonzalez, L., Leithead, A., Finewax, Z., Thalman, R., Vlasenko, A., Vagle, S., Miller, L. A., Li, S. M., Bureekul, S., Furutani, H., Uematsu, M., Volkamer, R. and Abbatt, J., (2014) 'Formation of gas-phase carbonyls from heterogeneous oxidation of polyunsaturated fatty acids at the air-water interface and of the sea surface microlayer', *Atmospheric Chemistry and Physics*, 14(3), pp. 1371–1384, doi: 10.5194/acp-14-1371-2014.
- 25

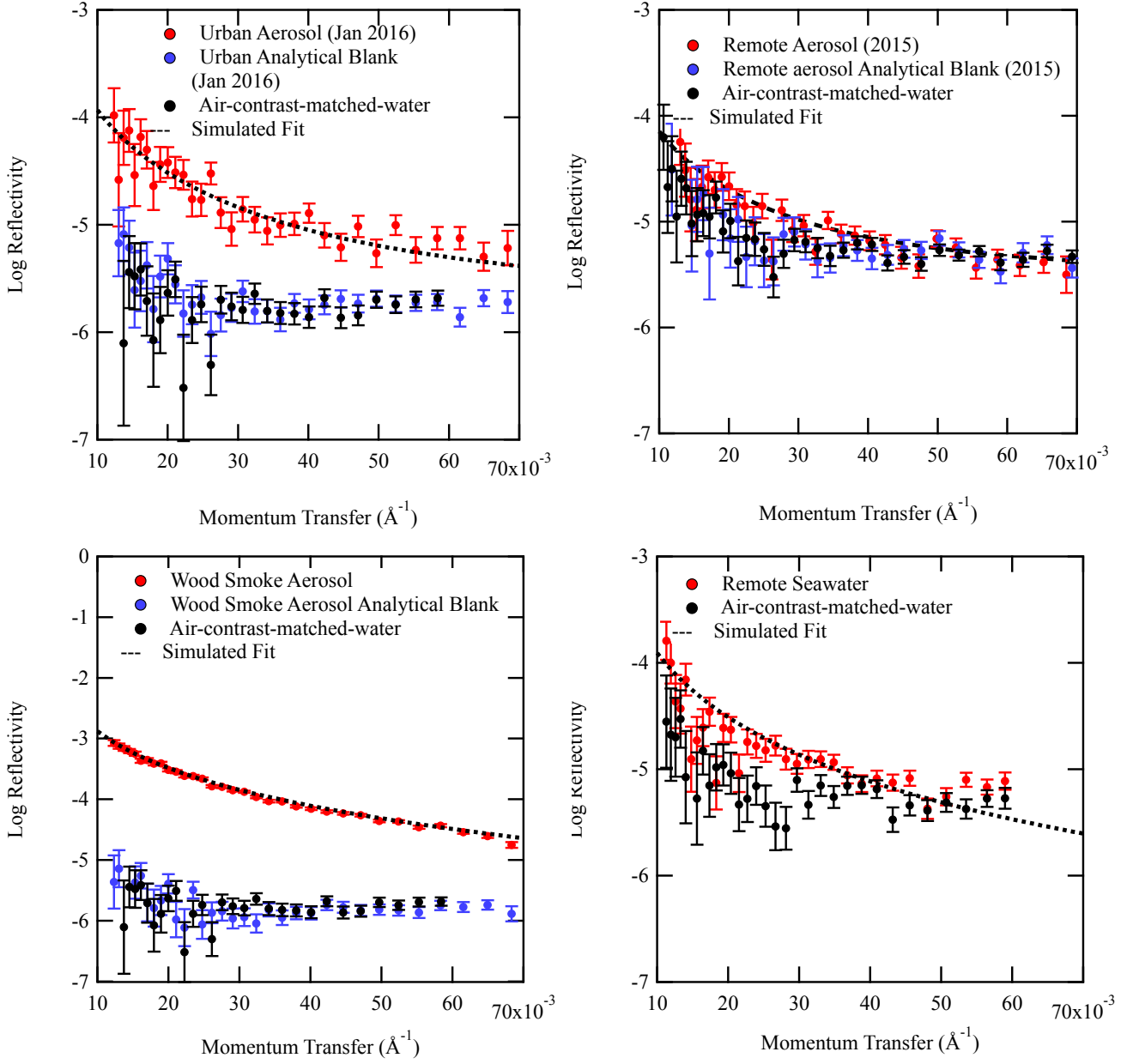


Figure 1: Neutron reflectivity profiles for films of (a) urban, (b) remote, (c) wood smoke and (d) remote seawater extract at the air-water interface, compared to the interface without a film present. The uncertainty displayed in Fig. 1 originates from a neutron reflectivity profile formed from histogram data; therefore neutrons between two momentum ranges can be described as counting statistics.

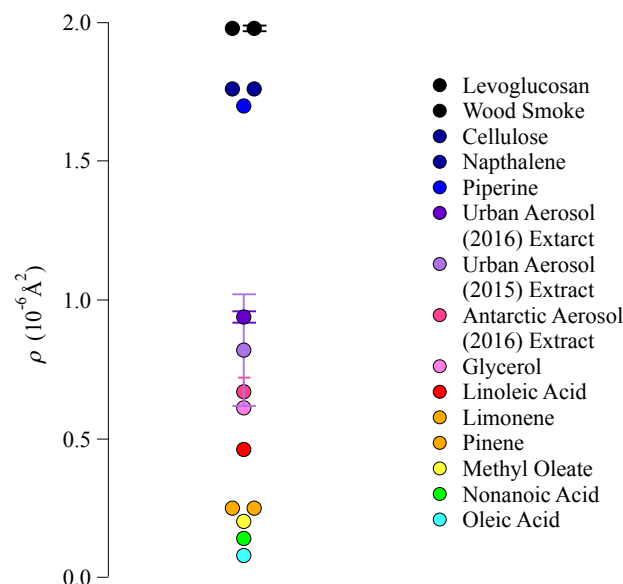


Figure 2: The neutron scattering length density of pure compounds calculated using the chemical composition and assumed density of various materials compared to the neutron scattering length density of films of the aerosol and seawater extracts collected in the present study (Sears, 1992). The density for the materials is assumed owing to the phase of the materials ranging from liquids to crystals.

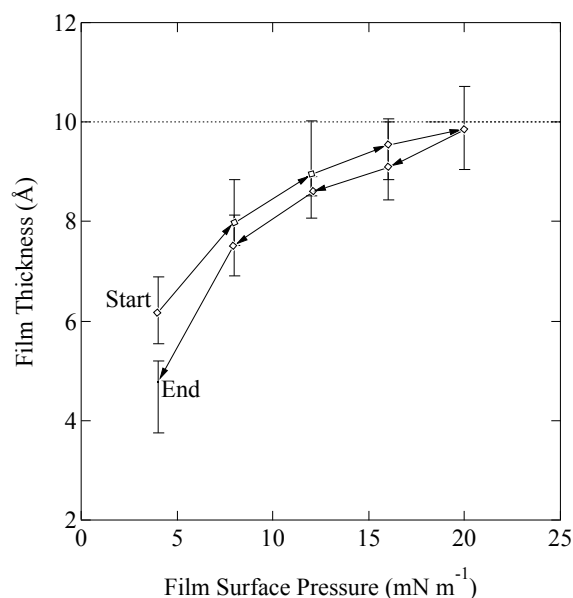


Figure 3: The change in film thickness of a film composed of urban aerosol extract at the air-water interface of a Nina Langmuir trough as the surface pressure of the trough is increased and decreased by changing the barrier position. A surface pressure higher than 20 mN m⁻¹ was not reached due to limited sample supplies. Error is represented as the maximum and minimum film thickness values that facilitated a fit.

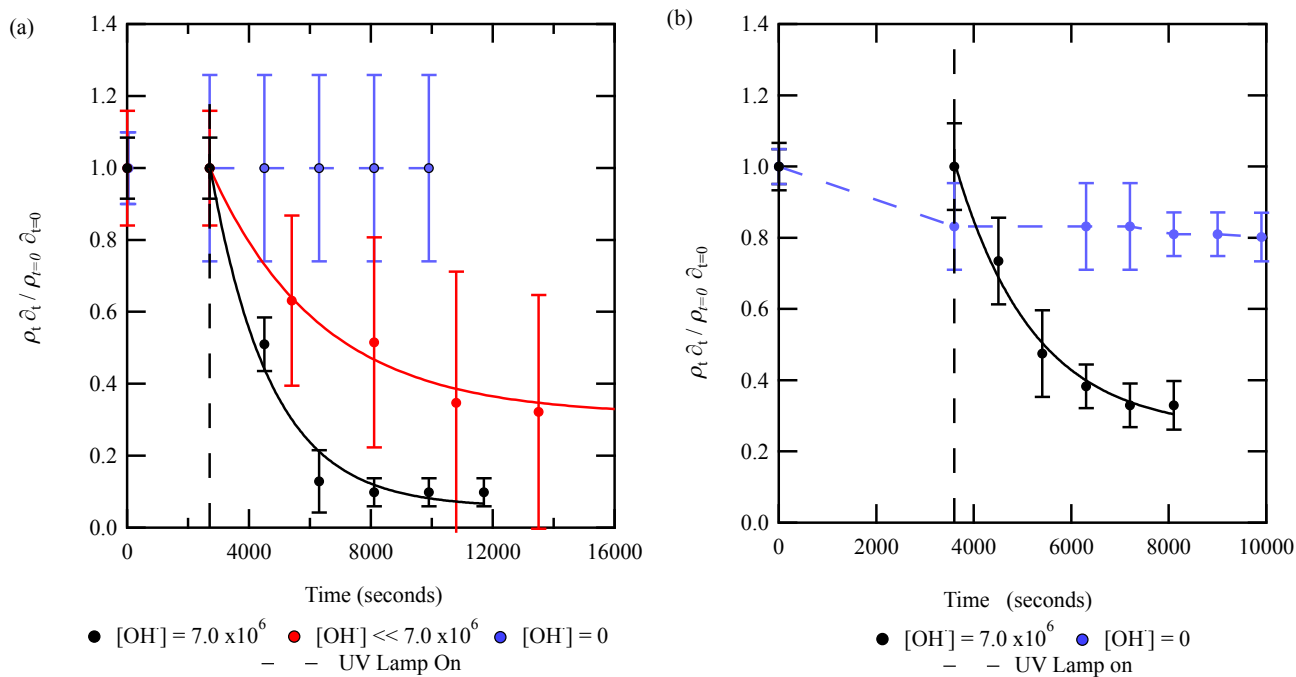


Figure 4: Oxidation of urban aerosol extract at the air-water interface for aerosol extract collected during (a) May 2015 and (b) January 2016. The May 2015 aerosol extract demonstrated an exponential decay of 0.03 min^{-1} when exposed to OH radicals at a concentration of $7.0 \times 10^6 \text{ molecule cm}^{-3}$, and an exponential decay of 0.017 min^{-1} when exposed to OH radicals at a much lower concentration. The UV lamp was turned on after (a) 2700 or (b) 3600 seconds. Error is displayed as the propagation of error between neutron scattering length density and film thickness.

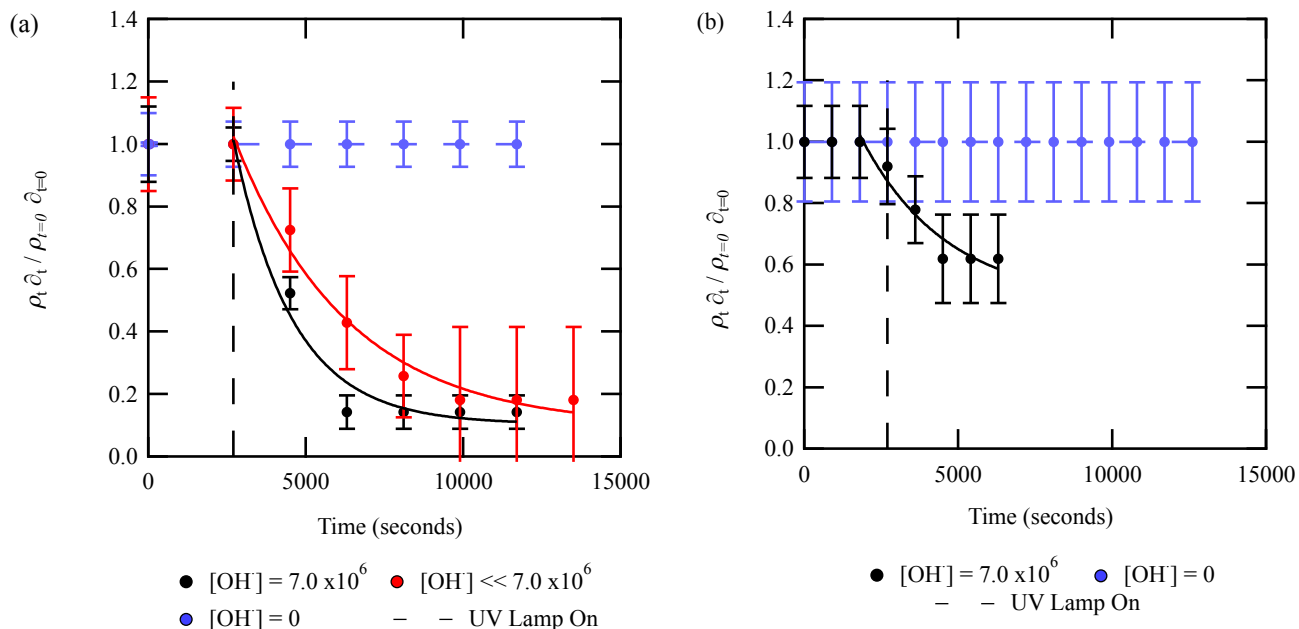


Figure 5: The reaction of a film of remote aerosol extract collected in (a) 2015 and (b) 2016 with gas-phase OH radicals. The remote aerosol extract collected in 2015 demonstrated an exponential decay of 0.032 min^{-1} when exposed to OH radicals at a concentration of $7.0 \times 10^6 \text{ molecule cm}^{-3}$ and an exponential decay of 0.011 min^{-1} when exposed to OH radicals at a much lower concentration. For all experiments, the UV lamps were turned on after 2700 seconds. Error is displayed as the propagation of error between neutron scattering length density and film thickness.

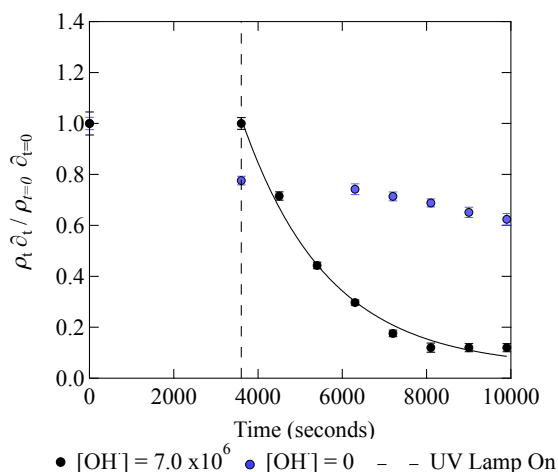


Figure 6: Insoluble wood smoke aerosol extract at the air-water interface decayed with a rate constant of $0.030 \pm 0.003 \text{ min}^{-1}$ when exposed to $[OH] = 7.0 \times 10^6 \text{ molecule cm}^{-3}$. The UV lamps were turned on after 3600 seconds. Error is displayed as the propagation of error between neutron scattering length density and film thickness.

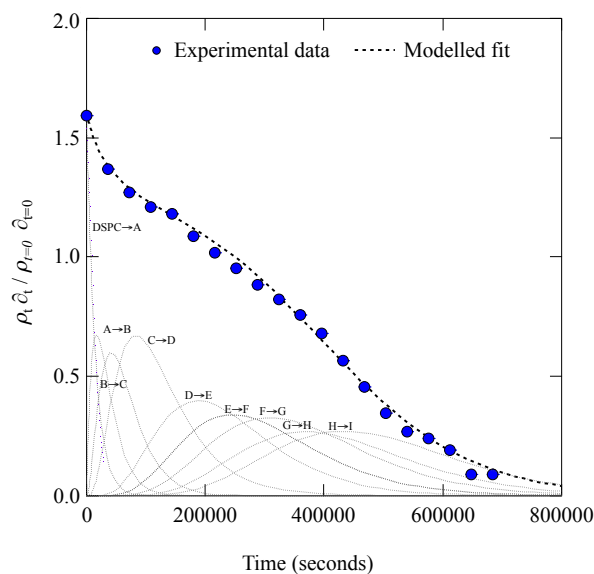


Figure 7: A typical decay profile for the head and tail region when added together for a film of DSPC at the air-water interface when exposed to OH radicals at a concentration of 7.0×10^6 molecule cm^{-3} . Ozone was present throughout the data collection, whilst the UV lamps were turned on after 2700 seconds. The decay was fitted to a step-wise degradation mechanism.

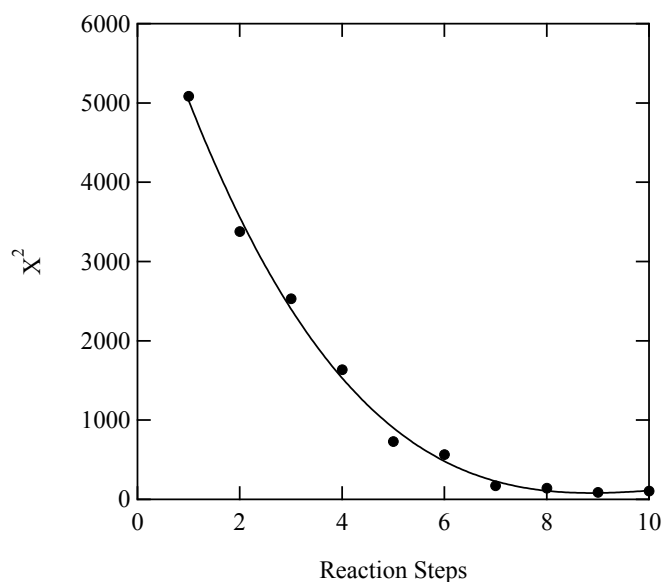


Figure 8: To determine the uncertainty in the proposed decay mechanism the weight contribution for each kinetic step and the importance of including ten kinetic steps was calculated through altering either the weight contribution or number of steps and adjusting the fit manually. The quality in the resultant fit was determined quantitatively by making a chi-squared test; a line to guide the eye has been added to the figure.

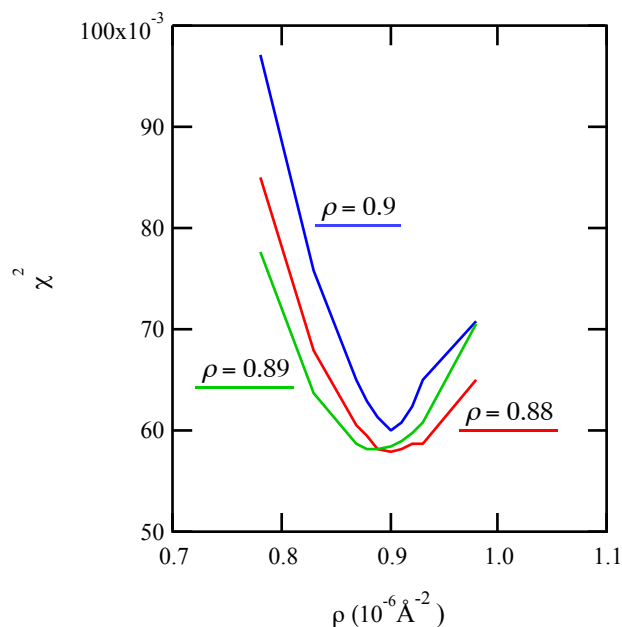


Figure 9: To study the level of accuracy in the simulation of the neutron reflection profile a χ^2 test was executed.

Table 1: The atmospheric aerosol extract formed films at the air-water interface. The table lists the neutron scattering length density and thickness of the each film studied at the air-water interface, as well as listing the oxidation kinetics of the film if exposed to OH radicals.

Aerosol Extract	δ (Å)	ρ (10^{-6} Å^{-2})	[OH] (molecule $\text{cm}^{-3} \text{ s}^{-1}$)	k' (min^{-1})	k (molecule $\text{cm}^{-3} \text{ s}^{-1}$)	τ (minutes)
Urban (May 2015)	6.10±0.36	0.83±0.06	<i>Film not exposed to OH radicals</i>			
	3.64±0.18	0.68±0.05	7.0×10^6	0.030	7.1×10^{-11}	58.3
Urban (January 2016)	10.18±0.26	0.89±0.05	7.0×10^6	0.037	8.8×10^{-11}	47.3
Remote (Summer 2015)	8.96±0.81	0.62±0.05	<i>Film not exposed to OH radicals</i>			
	7.59±0.30	0.67±0.05	7.0×10^6	0.032	7.6×10^{-11}	54.7
Remote (Summer 2016)	10.50±0.38	0.67±0.05	7.0×10^6	0.022	5.2×10^{-11}	79.5
Wood Smoke (Winter 2016)	18.61±0.54	1.72±0.05	7.0×10^6	0.042	1.0×10^{-10}	41.7
Remote Seawater (Summer 2015)	11.34±0.44	0.79±0.06	<i>Film not exposed to OH radicals</i>			

Table 2: The steady-state rate constants (k'_{1-10}) for the degradation mechanism comprising of ten kinetic steps fitted to the film of DSPC at the air-water interface when exposed to OH radicals, the uncertainty displayed was determined by altering the rate constant until the fit between experimental and simulated data was lost as judged by eye. Three different films of DSPC at the air-water interface (A-C) were exposed to OH radicals under the same conditions and subsequently fitted.

$k' \text{ (s}^{-1}\text{)}$	Film A	Film B	Film C
k'_1	0.004±0.002	0.0013±0.0006	0.006±0.003
k'_2	0.003±0.001	0.002±0.001	0.005±0.001
k'_3	0.002±0.001	0.001±0.001	0.001±0.001
k'_4	0.001±0.0005	0.002±0.001	0.001±0.001
k'_5	0.0011±0.0002	0.0011±0.0002	0.0015±0.0002
k'_6	0.001±0.0005	0.001±0.0005	0.001±0.0005
k'_7	0.001±0.0005	0.001±0.0005	0.0005±0.0003
k'_8	0.0009±0.0002	0.002±0.0005	0.0004±0.0002
k'_9	0.001±0.0005	0.002±0.0005	0.001±0.0005
k'_{10}	0.0009±0.0002	0.001±0.0005	0.001±0.0005

5

Paper 5: The reaction between gas-phase OH radicals and organic films extracted from atmospheric aerosol at the air-water interface: an x-ray reflectivity and atmospheric lifetime study

Rosalie H. Shepherd, Martin D. King, Andrew D. Ward, Neil Brough and Thomas Arnold

To be submitted to the Journal of Atmospheric Chemical Society: Earth and Space Chemistry.

I declare I have made the following contributions to the piece of co-authored work:

- Helped with the collection of urban aerosol extracts
- Extracted atmospheric aerosol from the collection filters
- Conducted the experiments, and collected and analysed all data collected
- Contributed to the conclusions drawn from the experiments conducted
- Authored the paper

The reaction between gas-phase OH radicals and organic films extracted from atmospheric aerosol at the air-water interface: an x-ray reflectivity and atmospheric lifetime study

Rosalie H. Shepherd^{1,2}, Martin D. King^{1}, Andrew D. Ward², Neil Brough³ and Thomas Arnold⁴*

¹Department of Earth Sciences, Royal Holloway, University of London, Egham, Surrey, TW20 0EX, UK

²Central Laser Facility, Rutherford Appleton Laboratory, Harwell, Science Campus, Chilton, Didcot, Oxfordshire, OX11 0FA, UK

³British Antarctic Survey, Natural Environmental Research Council, High Cross, Madingley Road, Cambridge, CB3 0ET, UK

⁴Diamond Light Source, Harwell, Science Campus, Chilton Didcot, Oxfordshire, OX11 0DE, UK

Atmospheric aerosol, x-ray reflection, OH radicals, oxidation, air-water interface

Water insoluble organic material extracted from atmospheric aerosol collected in urban (Royal Holloway, University of London, UK) and remote (Halley, Antarctica) locations formed stable thin films at an air-water interface and reacted with gas-phase OH radicals. Bimolecular rate

constants for gas-phase OH radical oxidation of urban or remote aerosol extracts were typically of the order 1×10^{-11} to 1×10^{-10} molecule⁻¹ cm³ s⁻¹, giving atmospheric lifetimes of the film with respect to gas-phase OH radical oxidation of 8 to 80 minutes. The lifetimes are short relative to the typical residence time of atmospheric aerosols.. Thin organic films at the air-water interface of atmospheric aerosol or cloud droplets may alter the residence lifetime and light scattering properties of the aerosol. X-ray reflectivity measurements of atmospheric aerosol film material at the air-water interface resulted in calculated film thickness values to be either 10 Å or 17 to 18 Å for remote or urban aerosol extracts respectively. The x-ray reflectivity measurements additionally indicate that the film may be consistent with having a structure with increased electron density of film molecules towards the water, suggesting amphiphilic behavior.

1. Introduction

Atmospheric aerosols significantly contribute to the Earth's climate¹ and directly influence the proportion of solar energy reaching the Earth's surface by scattering or absorbing incoming solar radiation,¹ and indirectly through acting as cloud condensation nuclei.²⁻⁴ Current understanding of the effect of atmospheric aerosols upon climate is considered low.^{1,5,6}

The complex chemical composition and variable physical properties associated with atmospheric aerosols makes it difficult to obtain complete chemical information on aerosols,⁷ and is consequently a contributory factor to the uncertainty surrounding atmospheric aerosols. An atmospheric aerosol may be composed of several different substituents that may form separate phases in an individual aerosol,^{8,9} often resulting in the formation of a thin organic film forming around a core aerosol droplet or particle.¹⁰⁻¹⁴ The resultant morphology is often referred to as core-shell. The presence of a thin organic film may alter the chemical and physical

properties of the core-shell aerosol through (a) altering the transport of chemicals from the gas to liquid phase and vice versa,^{15,16} (b) reducing the rate of evaporation from the core aerosol,^{17–20} (c) altering the cloud condensation nuclei activation potential,^{21,22} (d) reducing the scavenging of the core aerosol by larger cloud and ice particles^{23,24} and (e) changing the core-shell aerosol optical properties and thus the light scattering properties of the aerosol.²⁵

The organic-coated aerosol is susceptible to atmospheric oxidation^{18,26} and as a result may change both chemically and physically. Many oxidant species exist in the atmosphere and hydroxyl, OH, radicals are one of the dominant oxidizing chemicals in the lower atmosphere.²⁷ Understanding the behavior of organic aerosol upon exposure to OH radicals is paramount for determining the atmospheric chemical lifetime of the aerosol and subsequently a number of studies have focused on the oxidation of atmospheric aerosols when exposed to OH radicals. For example, McNeill et al.²⁸ studied the oxidation between submicron aqueous aerosols containing mixtures of sodium oleate, sodium dodecyl sulfate and inorganic salts when exposed to OH radicals, Nah et al.²⁹ studied the heterogeneous reaction between OH radicals and sub-micron unsaturated fatty acid particles, Enami et al.³⁰ studied the oxidation of alkanolic acids at the air-water interface by OH radicals, whilst Richards-Henderson et al.³¹ investigated the effect of sulfur dioxide on the oxidation rate of organic aerosol by OH radicals.

The oxidation of proxy organic atmospheric aerosols as thin films at the air-water interface has also been extensively studied.^{32–41} A number of studies that focused on organic films at the air-water interface have employed neutron reflection techniques, for example King et al.⁴² studied the oxidation of a film of oleic acid at the air-water interface with gas-phase ozone, whilst Pfrang et al.⁴³ investigated the oxidation of methyl oleate thin films with gas-phase ozone. Other techniques have also been successfully applied to study thin films at the air-water interface:

González-Labrada et al.³⁶ recorded the change in surface tension of a film composed of oleic acid when exposed to ozone using a surface tensiometer, whilst Wadia et al.⁴⁴ studied unsaturated and saturated phospholipids by using an atmospheric pressure ionization mass spectrometer.

Studies using atmospheric aerosol extracted from the atmosphere are sparse. Examples of such studies include Zhou et al.⁴⁵ who studied the heterogeneous oxidation of seawater polyunsaturated fatty acids at the air-water interface; a study relevant to aerosol research owing to the material at the surface of the ocean becoming incorporated into atmospheric aerosol,^{46–48} whilst Jones et al.⁴⁹ applied x-ray reflection techniques to study the oxidation of thin films extracted from atmospheric aerosol extracts collected at Royal Holloway, University of London and seawater extracts collected from the English Channel. The thin films were oxidized by aqueous-phase OH oxidation and gas-phase ozone oxidation.

The purpose of the study described here is two-fold: firstly to determine the film thickness for organic matter extracted from atmospheric aerosol at the air-water interface and secondly to determine the lifetime of a film of atmospheric aerosol extract at the air-water interface. The study will yield morphological data about the film at the air-water interface through calculating film thickness to Angstrom precision: accurate estimation of film thickness is paramount to model films likely to be found in the atmosphere. The lifetime will be calculated by measuring the bimolecular rate constant for the reaction between gas-phase OH radicals and the thin films of aerosol extracts at the air-water interface.

2. Experimental Methods

X-ray reflectivity was applied to study a thin film of atmospheric aerosol at the air-water interface upon exposure to gas-phase OH radicals; the following section introduces the x-ray reflectivity technique and the subsequent calculation of oxidation lifetime. Additionally, the method applied to extract and prepare atmospheric aerosol extracts for use on the x-ray beamline is described.

2.1. Extraction of atmospheric aerosol

Organic material from atmospheric aerosols was extracted from filters collected at two locations: the campus of Royal Holloway, University of London during the months of September 2015 and January 2016, and at the Halley Clean Air Sector Laboratory operated by the British Antarctic Survey⁵⁰ over the Antarctic summers of 2015 and 2016. The aerosol extract collected from Royal Holloway, University of London has been classified as urban owing to the proximity of the city of London, major motorways such as the M25 and M4, and the international airport, Heathrow all lying within a radius of 30 km. In contrast, because of the physical remoteness from other continents Antarctica is considered a clean environment, and therefore for the purpose of the study Antarctic aerosol extract is described as remote. The urban aerosol extracts were each collected over an approximately 30-day period, whilst the remote aerosol extracts were collected over approximately 60 days.

For the urban sampling sites, the aerosol was extracted from the atmosphere through an air pump that pulled air through clean stainless pipelines at a flow of 30 L min^{-1} , whilst remote aerosol was sampled by pulling air through a short length (10 cm) of quarter inch O.D. PFA Teflon tubing by applying a low volume air sampler (Model VM-4) with a flow rate of 20 L min^{-1} . In both sampling sites, the pipelines led to a PFA Savillex commercial filter holder, in which a pre-combusted 47 mm diameter quartz filter was encased. Atmospheric aerosol extract was

collected upon the filter. To separate the insoluble organic material from the filter, the filter was sonicated for 10 minutes in a solution consisting of 10 ml ultrapure water ($<18\text{ M}\Omega$) and 10 ml chloroform (Sigma-Aldrich, 0.5 to 1 % ethanol as stabilizer); sonication commonly reduced the filter to a pulp. The sonicated pulp was subsequently filtered with another pre-combusted quartz filter to remove the filter paper: the pulp was washed with ultrapure water and chloroform several times to maximize the amount of aerosol extract collected. The resulting filtrate consisted of a chloroform layer in which the material likely to form insoluble films at an air-water interface resided⁵¹ and an aqueous layer. The chloroform layer was separated from the aqueous layer by passing the filtrate through a separating funnel. The chloroform was then removed from the atmospheric aerosol extract by evaporative blow-down leaving an oily residue behind. The residual material was stored in 2 ml of fresh chloroform at $-18\text{ }^{\circ}\text{C}$ in the dark until use on the beam line. All glassware used in the extraction process was thoroughly cleaned with ultrapure water and chloroform prior to use and the extraction process was carried out in a clean glove bag. Analytical blanks were filters extracted in the same manner as filters used to collect atmospheric aerosol. The blanks travelled to and from the collection sites under the same conditions as the filters used to collect atmospheric aerosol.

Analytical filter blanks were likewise extracted in exactly the same manner. The analytical blanks provided a method of determining the level of contamination resulting from the extraction process and the level of contamination resulting from travelling to and from the collection site: especially important for the remote aerosol extracts.

2.2. Experimental setup

The air-water interface was created by using a PTFE trough, with a volume of 90 cm^3 , mounted onto an anti-vibration table. Owing to the small size and geometry of the trough in relation to the

x-ray beam footprint on the water surface, the trough was used without barriers or a surface tension sensor. The small trough was a compromise between the x-ray beam footprint and the limited amount of aerosol extract. A UV lamp containing two fluorescent germicidal lamps, each with an output wavelength centered on 254 nm, was suspended above the trough. To encase the experimental environment and to allow the production of an atmosphere containing OH radicals, the trough and UV lamp were enclosed within a Tedlar bag. Two thin Kapton windows at either end of the trough facilitated travel of the x-ray beam into and out of the enclosed environment. The Tedlar bag had a stainless-steel inlet and exhaust to allow gas to enter and leave. The bag had an approximate volume of 25 L and a surface area of 0.612 m². Generation of gas-phase OH radicals required a saturated atmosphere of water vapor. To ensure the relative humidity of the experiment environment was maintained, a water reservoir with an approximate volume of 0.05 L was included within the Tedlar bag.

For each experimental run the trough was cleaned with ultrapure water and chloroform before a fresh 90 cm³ volume of ultra pure water (<18 MΩ cm⁻¹) was poured into the trough. Between 100 to 200 µl of atmospheric aerosol extract in chloroform was added to the air-water interface using a Hamilton syringe.

2.3. X-ray reflectivity

The surface specular x-ray reflectometer at Diamond Light Source, I07, was applied to study the film of atmospheric aerosol extract at the air-water interface. I07 is described in detail by Nicklin et al.⁵² and Arnold et al.,⁵³ and the x-ray reflectivity technique is described in detail by Chateigner,⁵⁴ however a brief description will be given here. The x-ray beam had a wavelength of 0.992 Å, and was specularly reflected off the interface and onto a Pilatus detector, where the beam was measured as a function of momentum transfer, Q , defined as:

$$Q = \frac{4\pi \sin \theta}{\lambda}, \quad \text{Eq. 1}$$

versus reflectivity, R , which is defined as

$$R = \frac{16\pi^2}{Q^4} (2\rho)^2 \sin\left(\frac{Q\delta}{2}\right)^2, \quad \text{Eq. 2}$$

from Equation 1, λ is defined as the wavelength of an x-ray and θ the incident angle of the x-ray beam onto the interface of study, whilst δ is the film thickness and ρ the x-ray scattering length density. X-ray scattering length density is defined by the electron density of the interface, therefore heavier atoms that have a greater number of electrons will have a larger electron density and thus a greater x-ray scattering length density.⁴⁹ The profile of momentum transfer versus reflectivity will be called an x-ray reflection profile henceforth in the paper. To optimize signal relative to time, x-ray reflection profiles were collected over a time period of eight minutes.

To determine precise values of x-ray scattering length density and film thickness, the experimentally collected x-ray reflection profiles were simulated by Abelès formalism⁵⁵ in the computer software Motofit.⁵⁶ The Abelès formalism used a model of the atmospheric aerosol extract at the air-water interface, including parameters for the x-ray scattering length density, film thickness and film roughness to simulate the experimentally determined x-ray reflectivity profile. The values were initially estimated and then refined until a fit between experimental and simulated data was determined by eye. Application of a χ^2 test ensured the final value provided the best fit. Equation 3 displays the formula for the χ^2 test:

$$\chi^2 = \sum \frac{(O_i - E_i)^2}{E_i}, \quad \text{Eq. 3}$$

where O is the unchanged experimental value and E is the value observed after changing the x-ray scattering length density or film thickness.

Typically for a film of known composition at an air-water interface the surface coverage (number of molecules per unit area) can be calculated by $\frac{\rho\delta}{b}$ where b is the scattering length of a molecule. However in the study presented here the organic film is (a) a complex mixture of unknown materials and (b) a reaction system producing unknown surface-active product molecules at the air-water interface. Thus the scattering length, b , of the molecules in the film is not known. For the atmospheric aerosol extracts films exposed to gas-phase OH radicals, scattering length density per unit area, $\delta\rho$, was plotted as a function of time.⁴⁹ Such plots allowed the change in the film to be monitored and for $\delta\rho$ to be used as a variable. Each point on the plots corresponds to a new x-ray reflection profile; continuous collection of subsequent profiles allowed a temporal graph of $\delta\rho$ as a function of time to be plotted. In contrast to the preliminary study conducted by Jones et al.,⁴⁹ the study described here split the organic layer into two separate layers with differing scattering length densities and thicknesses to better reproduce the experimental x-ray reflection profiles. Upgrades in the beamline allowed for the refinement in the reflectivity profiles. In the study presented here the quantity, $\frac{\delta_t\rho_t}{\delta_{t=0}\rho_{t=0}}$, was followed as a function of time.

2.4. Gas-phase OH radical generation

Gas-phase OH radicals were formed from the photo-oxidation of ozone in the presence of water vapor; humidified oxygen was flowed at 1 L min⁻¹ through a photolytic ozonizer (Ultra-Violet Products Ltd) to produce ozone at 0.85 ppm (approximately 2.1×10^{13} molecule cm⁻³). The concentration of ozone within the bag was measured by UV-VIS spectrometry by sampling ozone in a 10 cm glass cell. The oxygen was saturated with water vapor prior to passing through the ozonizer by bubbling through water. The concentration of water vapor was based on the vapor pressure of water⁵⁷ to be 2.34 kPa at 20°C. The photolysis rate constants for the photolysis

of ozone, $J_1(O(^1D))$, was determined with an intensity calibrated Metcon radiometer (normally used for measurements of atmospheric photolysis reactions).⁵⁸ To determine the rate constant for the photolysis of molecular oxygen, the rate constant for ozone was scaled from the product of the absorption cross-sections and the quantum yields.

The gas-phase concentration of OH radicals in the Tedlar bag was estimated to be 6×10^6 molecule cm^{-3} . The concentration was calculated by kinetically modeling (a series of first-order differential equations using a Runge-Kutta Solver^{59,60}) reactions 1 to 30 in Atkinson et al.⁶¹ that cover the basic HO_x and O_x reactions occurring in the photolysis of ozone in the presence of water vapor. The key reactions are:



A first-order wall loss of OH radicals was added (R4) using the method outlined in Dilbeck and Finlayson-Pitts,⁶² based on a 25 L Tedlar bag with a surface area of 0.612 m^2 and assuming the reaction probability for OH radicals on Tedlar was similar to halocarbon wax ($\gamma = 6 \times 10^{-4}$).⁶³ The wall loss was calculated to be 2 s^{-1} .

A sensitivity test was conducted on the model used to determine the OH radical concentration; the initial starting concentration or the rate constant for each reaction step was increased and decreased by a factor of 2 and the effect on the final OH radical concentration analyzed. It was determined that the OH radical concentration was affected by the lamp intensity, initial ozone

concentration and the water vapor concentration, each with a relative percentage error of 0.5%, 2 % and 1.7 % respectively on the OH radical concentration.

The reflectivity of an atmospheric aerosol extract at the air-water interface was recorded three times prior to oxidation to establish that (a) the film was initially stable at the air-water interface and (b) to provide good signal to noise x-ray reflection profiles to allow precise determination of x-ray scattering length density and film thickness. After the three measurements, the film was exposed to gas-phase OH radicals. Continuous collection of x-ray reflection profiles during the exposure of the atmospheric aerosol extract to gas-phase OH radicals allowed the change in the film to be analyzed as a function of time.

2.5. Kinetic analysis

A central aim of the project was to estimate the atmospheric lifetime, τ , of the atmospheric aerosol extract upon exposure to gas-phase OH radicals. The rate of loss of atmospheric aerosol extract is outlined in Reaction 1:



with time was described by Equation 4:

$$\frac{d\Gamma_{film}}{dt} = -k'[OH\cdot]\Gamma_{film} , \quad Eq. 4$$

where Γ_{film} represents the surface coverage of the film at the air-water interface, $[OH\cdot]$ the concentration of gas-phase OH radicals and k' the pseudo first-order rate constant for Reaction 1.

Solving Equation 4 gives Equation 5:

$$\frac{\Gamma_{film}}{\Gamma_{film}^{t=0}} = e^{-kt} , \quad Eq. 5$$

where k is the bimolecular rate constant. By substituting $\frac{\rho_t \delta_t}{\rho_{t=0} \delta_{t=0}}$ for $\frac{\Gamma_{film}}{\Gamma_{film}^{t=0}}$ gives Equation 6:

$$\frac{\rho_t \delta_t}{\rho_{t=0} \delta_{t=0}} = e^{-kt} , \quad Eq. 6$$

the relative change in organic film surface coverage can be represented by the relative change in the measured scattering length per unit area, $\frac{\rho_t \delta_t}{\rho_{t=0} \delta_{t=0}}$. In Equations 5 and 6, t represents time and k' the pseudo first-order rate constant. The value of k' was determined by plotting $\frac{\rho_t \delta_t}{\rho_{t=0} \delta_{t=0}}$ as a function of time and fitting the subsequent plot to an exponential decay (e^{-kt}).

The atmospheric lifetime, τ , of the film with respect to oxidation by gas-phase OH radicals in the atmosphere can be calculated from the bimolecular rate constant, k , and a typical gas-phase concentration of OH radicals in the atmosphere, $[OH]_{atm}$ as shown in Equation 7:

$$\tau = \frac{1}{k[OH]_{atm}}, \quad \text{Eq. 7}$$

Ozone-only blank experiments were performed in the absence of UV light to demonstrate no apparent loss of film material owing to reaction with gas-phase ozone (as opposed to the hydroxyl radical). A blank kinetic run with oxygen only (no ozone or UV light present) was not required as no loss of film was observed with ozone-oxygen mixtures. A blank run with UV illumination only (i.e. no ozone) is not reported as the UV lamps generate ozone from the photolysis of molecular oxygen.

3. Results & Discussion

The results and discussion of the x-ray reflectivity of thin films of material extracted from atmospheric aerosol at the air-water interface are presented, followed by a kinetic analysis of its oxidation with gas-phase OH radicals.

3.1. X-ray reflection

Organic thin films composed of aerosol extracted from the atmospheric aerosol were studied at the air-water interface. Figure 1 depicts the x-ray reflection profiles for aerosol extracts sourced from (a) urban and (b) remote locations along with the corresponding analytical blank and clean

air-water interface. The figure demonstrates a definite change in the reflectivity profile with the atmospheric aerosol extract present at the air-water interface. The figure also demonstrates the analytical blanks are effectively indistinguishable from the clean air-water interface. Very close inspection of Figure 1b suggests the analytical blank may have received a tiny quantity of contamination on its long return journey from Antarctica. However, the changes in the x-ray reflectivity profile relative to the clean air-water interface are many orders of magnitude smaller than the loaded sample. The agreement is remarkable. Figure 1 demonstrates the essential requirement for these experiments to be performed at x-ray synchrotrons as the difference between aerosol extract and no aerosol extract at the air-water interface requires a large signal to noise ratio in reflectivity at large values of momentum transfer values. A commercial x-ray reflectometer is generally unlikely to achieve sufficient signal-to-noise ratios at the larger values of momentum transfer in timescales important for studying kinetics.

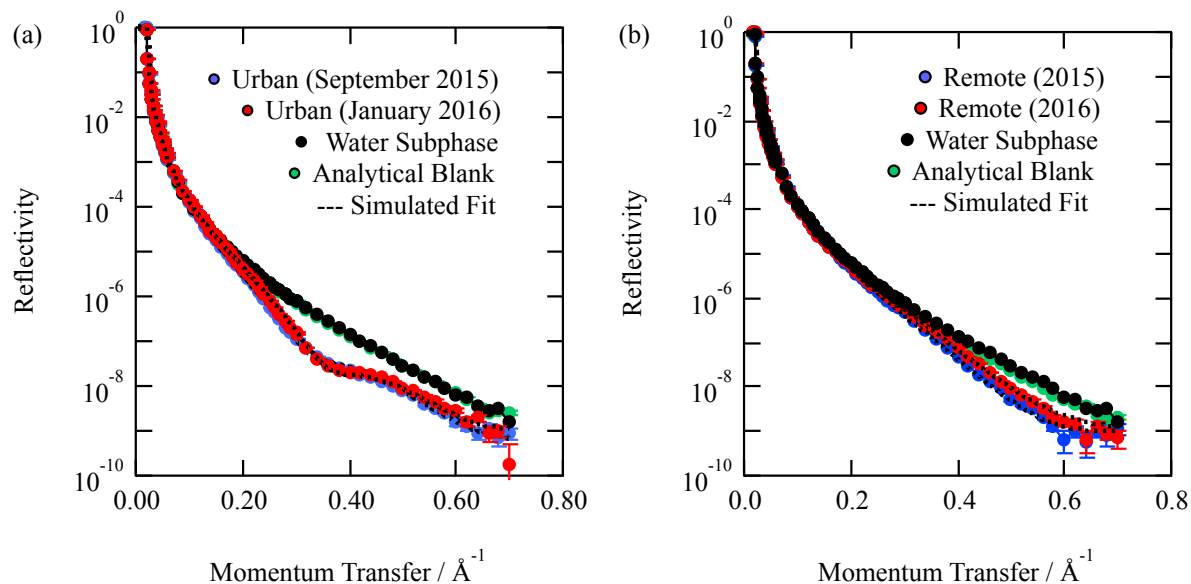


Figure 1. Depiction of the typical x-ray reflection profiles for (a) urban atmospheric aerosol extract and (b) remote atmospheric aerosol extract. A corresponding analytical blank is displayed in each figure. In both graphs, the analytical blank is indistinguishable from the water sub-phase

with a clean-air water interface within error. The error bars represent statistical counting errors from the accumulation and binning of photons, and are generally smaller than the points depicted.

Application of Abelès formalism allowed the x-ray scattering length density and film thickness of the aerosol extract film to be calculated. Additionally, more detailed structural information of the extract at the air-water interface was determined; the urban and remote aerosol extracts both demonstrated a good fit between experimental and calculated x-ray reflectivity profile to a two-layer system (as opposed to a one or three-layer system). It was not possible to achieve a realistic reproduction of the experimental reflectivity profile with one layer at the air-water interface and although a three-layer system provided a good visual fit it did not lower the value of the fitting metric, χ^2 . The two-layer system may be indicative of a film that might have a structure with increased electron density of film molecules towards the water, suggesting amphiphilic behavior.

Table 1. Table of the x-ray scattering length density (ρ) and film thickness (δ) for urban and remote atmospheric aerosol extract thin films at the air-water interface.

Aerosol Extract		Layer	ρ (10^{-6}\AA^{-2})	δ (\AA)
Urban	September 2015	Air interface	4.88 \pm 0.06	11.64 \pm 0.18
		Water interface	13.70 \pm 0.05	5.85 \pm 0.20
	January 2016	Air interface	5.33 \pm 0.9	9.82 \pm 0.58
		Water interface	13.96 \pm 0.18	6.61 \pm 0.37
Remote	2015	Air interface	2.55 \pm 0.05	4.45 \pm 0.26
		Water interface	10.91 \pm 0.17	6.19 \pm 0.09
	2016	Air interface	2.84 \pm 0.08	5.44 \pm 0.24
		Water interface	10.96 \pm 0.05	4.25 \pm 0.05

The layers of the two-layer system will be described as a layer beside the air interface, “air interface” and a layer at the water interface, “water interface”. The x-ray scattering length densities and film thickness determined for urban and remote atmospheric aerosol extracts are displayed in Table 1. Uncertainty in the values displayed in Table 1 was determined by adjusting the scattering length density or film thickness in turn until the simulated data no longer resembled the experimental data, as determined by-eye. Application of a χ^2 test (see Equation 3) ensured the x-ray scattering length density and film thickness values displayed were the values that gave the best fit. A demonstration of the robustness of the fitting procedure is given in Figure 2. Figure 2 is the value of the fitting metric, χ^2 , presented as a function of the x-ray scattering length density for three different film thickness. Figure 2 demonstrates a well-defined almost symmetrical minimum. Note the minimum of these curves is independent of thickness near the “best fit”. The left-hand panel is for the layer of aerosol extract at the air interface and the right hand panel is for the layer at the water interface. Each layer was investigated independently and the data presented in Figure 2 is from the urban aerosol extract. Figure 2 suggests the x-ray scattering length density can be fitted to $\pm 0.05 \times 10^{-6} \text{ \AA}^{-2}$ accuracy.

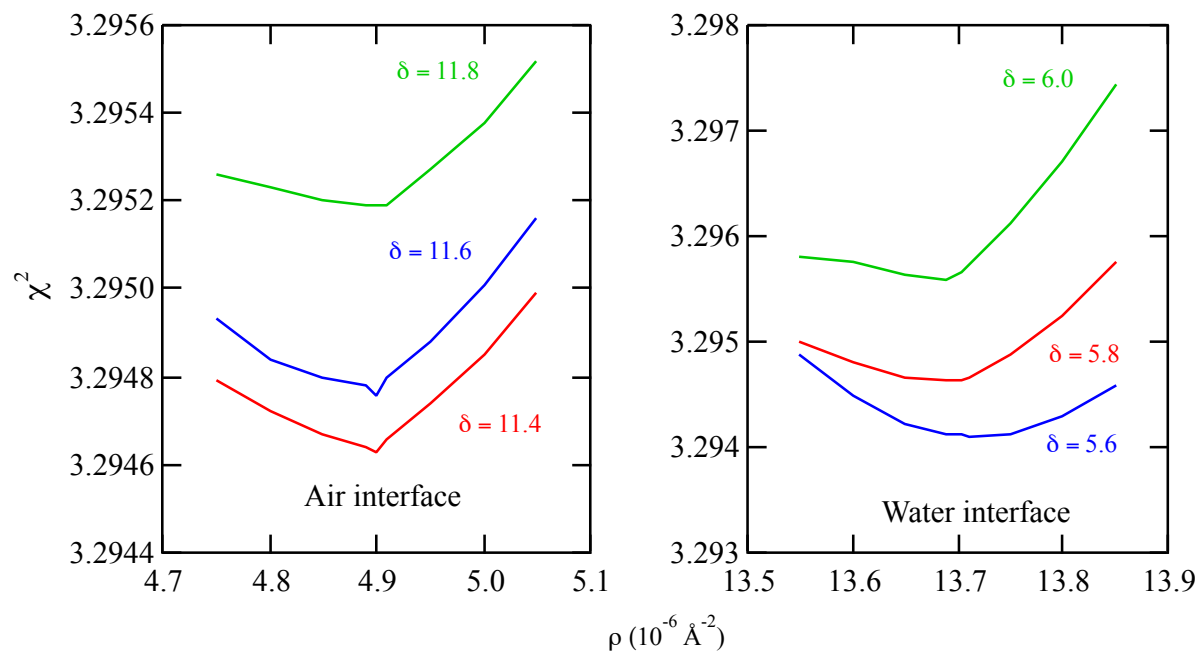


Figure 2. Figure 2 displays typical χ^2 plots, determined by investigating the robustness of the fitting procedure to find values of ρ and δ . The plots are for urban atmospheric aerosol collected during September 2015. It ought to be noted that the values of ρ and δ of the layer not under analysis were kept fixed.

The number of aerosol extracts studied is small owing to limited access to the x-ray synchrotron source and limited sample from atmospheric aerosol (the remote aerosol extract was completely consumed in these studies). However, inspection of Table 1 demonstrates the thickness and scattering length density are consistent between aerosol extracts from the same source. The remote aerosol extract is indicative of background polar/marine aerosol⁶⁴ and is a thinner film with a smaller electron density than the urban aerosol extract. The urban aerosol extract is most likely characterized by the close proximity of the mega city London, the major international airport Heathrow and the junction of three major arterial motorways.

The separation of the atmospheric aerosol extract into two layers indicates that the extract may contain hydrophobic and hydrophilic components. For both urban and remote extracts, the x-ray scattering length density and film thickness for the layer at the water interface is higher than the x-ray scattering length density for the layer at the air interface. Literature reports similar trends in x-ray scattering length density of thin films composed of molecules containing hydrophobic and hydrophilic regions, for example Dabkowska et al.⁶⁵ studied monolayer films of the lipid distearoylphosphatidylcholine (DSPC) at the air-water interface and report a x-ray scattering length density $5.55 \times 10^{-6} \text{ \AA}^{-2}$ higher for the hydrophilic head group region than for the hydrophobic chain region of the lipid.

Previous studies have used a film thickness ranging from 10 to 20 Å for a thin film at the air-water interface, whilst thicker coatings have been used at air-solid interfaces.^{11,42,43,49,66} In the study presented, the total thickness of the atmospheric aerosol extract films did not exceed 18 Å for urban aerosol extracts or 10 Å for remote aerosol extracts, agreeing with previous measurements. These thickness are important for atmospheric and core-shell morphology atmospheric modeling.²⁵

3.2. Oxidation of atmospheric aerosol

The films of atmospheric aerosol extract at the air-water interface were exposed to gas-phase OH radicals with a concentration of $7.0 \times 10^6 \text{ molecules cm}^{-3}$. The change in x-ray reflectivity was followed continuously in eight-minute intervals. Figure 3 depicts the change in the x-ray reflection profile with time as atmospheric aerosol extracts at the air water interface were exposed to gas-phase OH radicals.

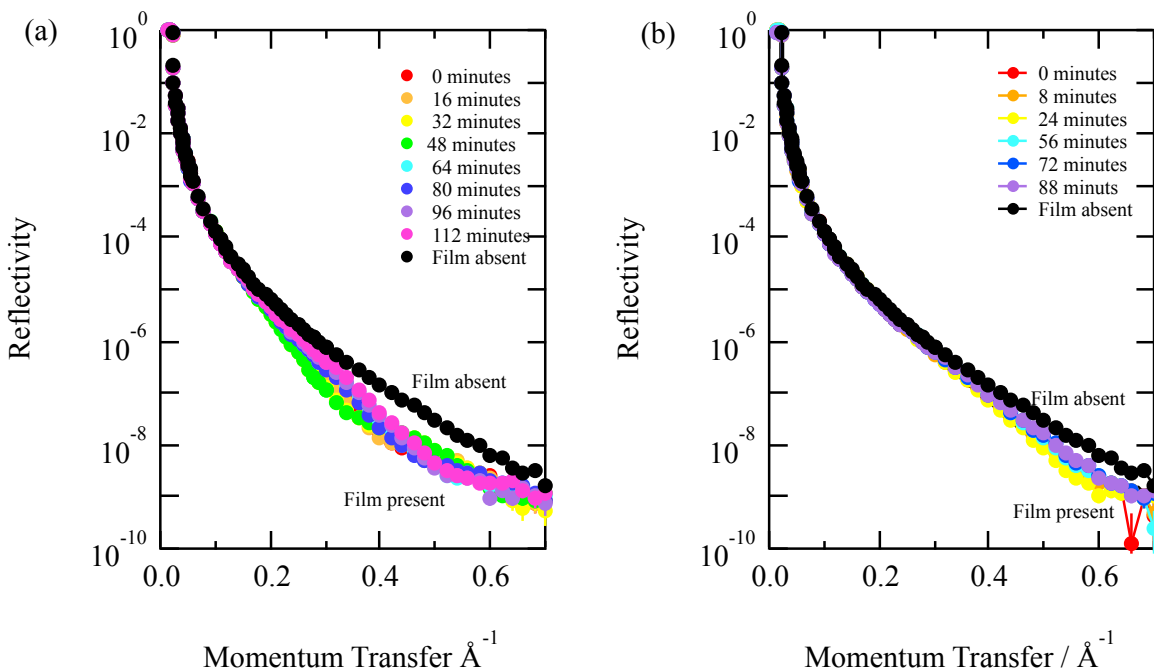


Figure 3. X-ray reflection profiles of two films when exposed to gas-phase OH radicals. The two films represent (a) urban atmospheric aerosol collected in September 2015 and (b) remote atmospheric aerosol collected during the Antarctic summer of 2016. Upon exposure to gas-phase OH radicals, the reflectivity of the film alters indicating a reaction is occurring at the air-water interface.

Each x-ray reflection profile collected was simulated and fitted with a calculated reflection profile to determine the x-ray scattering length density and film thickness as a function of time. The experimental x-ray reflectivity profiles of the reacting system were calculated and fitted as a function of time as one and two layer systems. The two-layer calculation of the x-ray reflectivity profile gave a superior fit to the experimental data throughout the oxidation reaction. The values of the scattering length density, ρ , and thickness, δ , are plotted as $\frac{\rho_t \delta_t}{\rho_{t=0} \delta_{t=0}}$ versus time in Figures 4, 5 and 6. Figure 4 depicts the kinetic decay observed for the films composed of urban aerosol

extract upon exposure to gas-phase OH radicals, whilst Figure 5 depicts the kinetic decay observed for the films composed of remote aerosol extracts upon exposure to gas-phase OH radicals. Uncertainty bars in Figures 4, 5 and 6 represent the propagated error from the in x-ray scattering length density and film thickness.⁶⁷

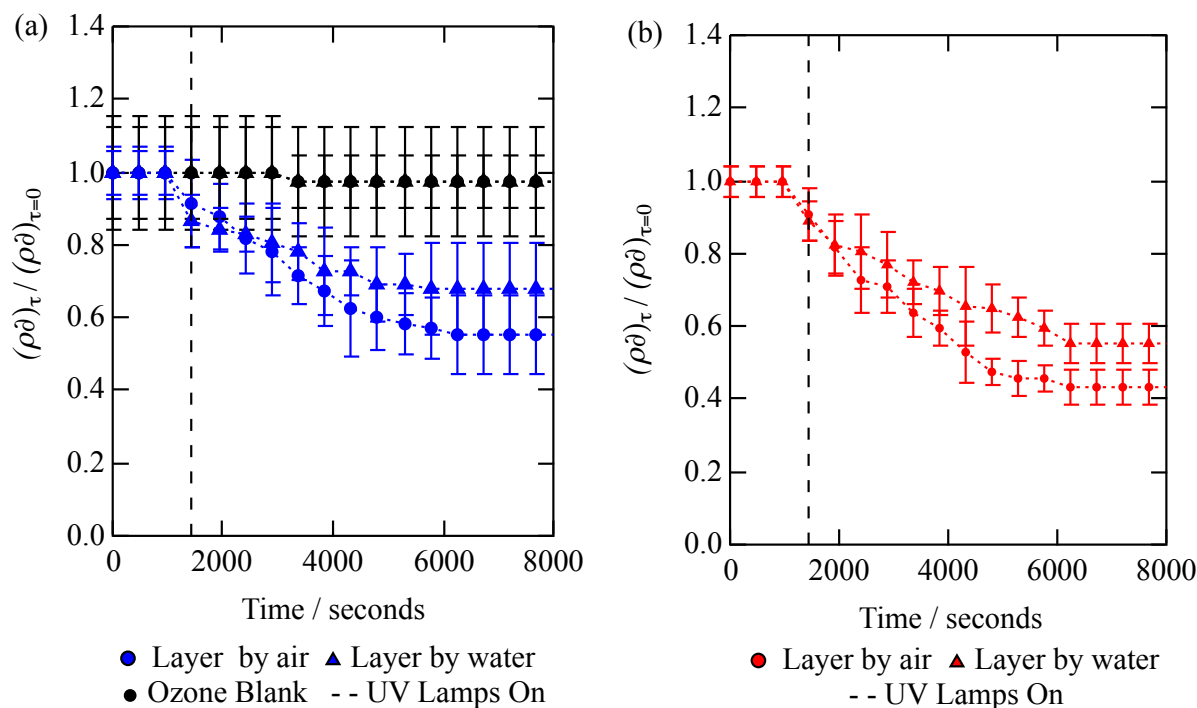


Figure 4. Urban atmospheric aerosol extract collected during (a) September 2015 and (b) January 2016 decayed when exposed to $[\text{OH}] = 7.0 \times 10^6 \text{ molecule cm}^{-3}$. UV lamps were turned on after 1440 seconds (dotted vertical lines).

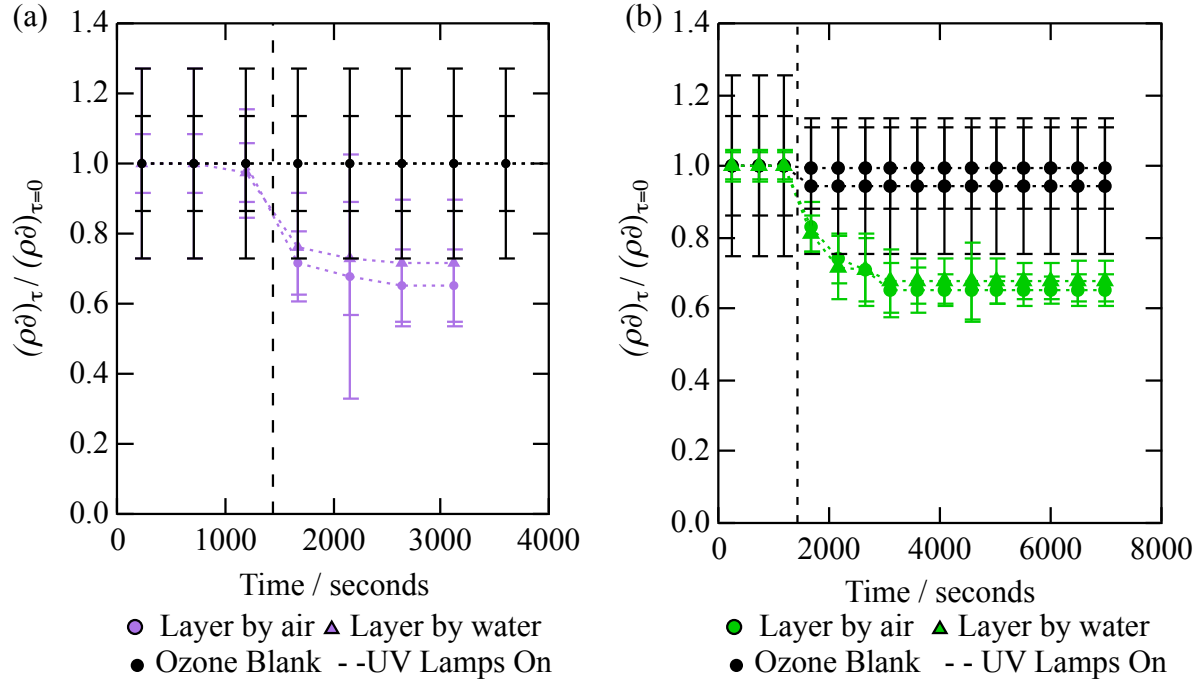


Figure 5. Remote atmospheric aerosol extract collected during (a) 2015 Antarctic summer and (b) 2016 Antarctic summer when exposed to $[\text{OH}] = 7.0 \times 10^6 \text{ molecule cm}^{-3}$. UV lamps were turned on after 1440 seconds (dotted vertical lines).

Both Figures 4 and 5 demonstrate an exponential decay in the scattering length per unit area, $\frac{\rho_t \delta_t}{\rho_{t=0} \delta_{t=0}}$ when each thin film was exposed to OH radicals. It can be observed that the rate of decay for the two layers that each film is comprised of lies within error of each other, apart from the January 2016 urban aerosol extract depicted in Figure 4b: between 4000 and 6000 seconds the decay for the two layers is notably different. The decay in $\frac{\rho_t \delta_t}{\rho_{t=0} \delta_{t=0}}$ as a function of time shows that the interface is becoming more like pure water upon exposure to OH radicals, suggesting that either the interface is becoming hydrated or material is being lost from the interface.

Figures 4 and 5 both demonstrate that urban and remote aerosol extracts do not change when exposed to ozone only, therefore the change observed in the two figures when the atmospheric aerosol extracts were exposed to gas-phase OH radicals might be described as a reaction. Jones et al.⁴⁹ observed no reactivity to gas-phase ozone when films of seawater extracts and atmospheric aerosol extracts were exposed to ozone.

To calculate the value of the bimolecular rate constant for Reaction 1, $\rho\delta$ for the two layers was averaged and the decay fitted to an exponential curve of the form $e^{-kt} + c$. Figure 6 depicts the kinetic decay profiles for the reaction of the two urban and two remote atmospheric aerosol extracts with gas-phase OH radical.

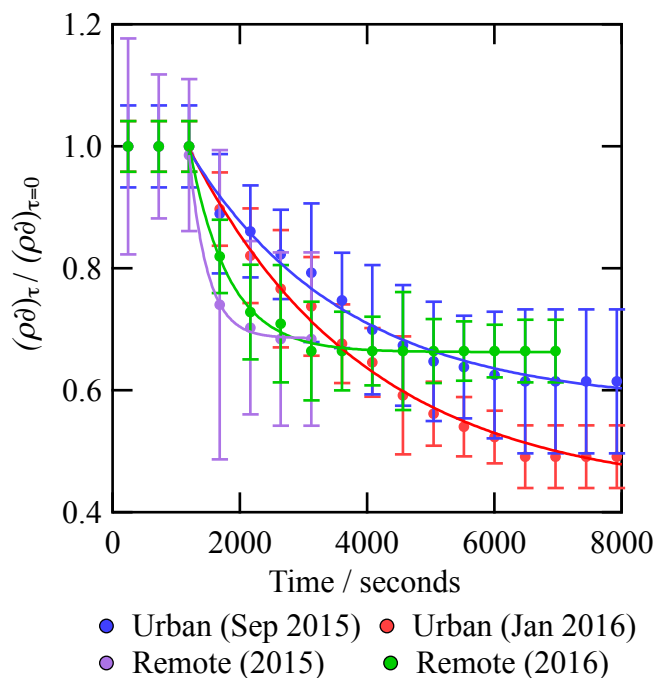


Figure 6. The decay in $\frac{\rho_t\delta_t}{\rho_{t=0}\delta_{t=0}}$ for urban and remote atmospheric aerosol extracts at the air-water interface reacts when exposed to gas-phase OH radicals as a function of time. The solid line drawn on the figure represents the exponential decay.

The pseudo first-order rate constants calculated from Figure 6 are displayed in Table 2, alongside the modeled concentration of gas-phase OH radicals above the film. The bimolecular rate constant, k , for Reaction 1 is calculated from $k = k'[OH]$.

Table 2. Pseudo first-order and bimolecular rate constants as well as atmospheric film lifetime for the reaction between atmospheric aerosol extract and gas-phase OH radicals. To determine the lifetime of the atmospheric aerosol extracts when in the atmosphere, the concentration of $[OH]_{atm}$ was determined from literature to be $4 \times 10^6 \text{ cm}^{-3}$.^{68,69}

	Aerosol Extract	Reaction	k' min ⁻¹	$[OH]_{bag}$ molecule cm ⁻³	k molecule ⁻¹ cm ³ s ⁻¹	τ minutes
Urban	September 2015	Y	0.024±0.002	7.0×10^6	5.7×10^{-11}	72.9
	September 2015 blank	N	/	/	/	/
	January 2016	Y	0.022±0.002	7.0×10^6	5.2×10^{-11}	79.5
	January 2016 blank	N	/	/	/	/
Remote	2015	Y	0.208±0.015	7.0×10^6	5.0×10^{-10}	8.4
	2015 blank	N	/	/	/	/
	2016	Y	0.097±0.004	7.0×10^6	2.3×10^{-10}	18.0
	2016 blank	N	/	/	/	/

The reaction probability, γ , is the fraction of collisions between gas-phase molecules and a surface that results in a reactive loss. The reaction probability can be estimated as $\gamma \sim 1$ for Reaction 1. The reaction probability is calculated by assuming all reactions occur at the interface⁷⁰ i.e. the rate of the surface reaction $\frac{d\Gamma_{film}}{dt} = k[OH]\Gamma_{film}$ normalized by a gas-surface collision frequency as displayed in Equation 8:

$$\gamma = \frac{\frac{d\Gamma_{film}}{dx}}{\frac{1}{4}[OH]\bar{c}} = \frac{4k\Gamma_{film}}{\bar{c}}, \quad \text{Eq. 8}$$

where Γ_{film} is the surface coverage of the atmospheric aerosol extract, estimated as 1.5×10^{18} molecule m^{-2} by King et al.,⁴² \bar{c} is the average molecular speed of an OH radical (600 ms^{-1}), and k is the bimolecular rate constant. Smith et al.⁷¹ showed that the oxidation of squalene with gas-phase OH radicals has a reaction probability of 0.3 ± 0.1 , whilst George et al.³⁵ and Hearn and Smith⁷² measured the reaction probability of 1.3 ± 0.4 and 2.0 ± 0.6 respectively for gas-phase OH radicals reacting with bis(2-ethylhexyl)sebacate. McNeill et al.⁷³ measured the reaction probability of gas-phase OH radical on solid palmitic acid particles as $\gamma = 0.3$ to 1 for solid particles and $\gamma = 0.05$ for palmitic acid on water. Finally Bertram et al.⁶³ measured reaction probabilities for a variety of substrates reacting with OH radical including paraffin wax ($\gamma = 0.34$), a methyl terminated monolayer ($\gamma = 0.29$), stearic-palmitic acid ($\gamma = 0.32$), a vinyl terminated monolayer ($\gamma = 0.6$), pyrene ($\gamma = 0.32$) and soot ($\gamma = 0.88$).

The calculated bimolecular rate constants are based upon gas kinetics and are relatively fast. As a comparison, Hennigan et al.⁷⁴ measured the bimolecular rate constant for the reaction of gas-phase OH radicals with levoglucosan in simulated biomass burning particles to be $1.1 \pm 0.5 \times 10^{-11} \text{ molecule}^{-1} \text{ cm}^3 \text{ s}^{-1}$, whilst King et al.⁷⁵ calculated a bimolecular rate constant of the magnitude $1 \times 10^{-5} \text{ molecule}^{-1} \text{ cm}^3 \text{ s}^{-1}$ for the reaction between gas-phase ozone and optically trapped droplets. The bimolecular rate constants are susceptible to the gas-phase OH radical concentration being steady state.

It is useful to compare the chemical lifetime of the extracted material with respect to OH radical oxidation to typical lifetimes of atmospheric aerosol. If the chemical lifetime of the film is similar to the atmospheric lifetime of an atmospheric aerosol then the oxidation need to be considered in atmospheric models. The lifetime of an atmospheric aerosol can be governed by the relative humidity³⁹ of the environment, the presence¹³ and composition⁷⁶ of a film and by the

oxidants present in the surrounding environment.⁷⁷ Williams et al.⁷⁸ calculated a lifetime ranging from 1 to 10 days for an aerosol with a diameter of 0.1 μm at an altitude ranging from 0 to 8 km. George et al.⁷⁹ sampled ambient aerosol from Toronto (Canada) and oxidized it in the lab with OH radicals in a flow tube and found OH can oxidize this mater on the timescales of four days, Likewise Robinson et al. predicted the timescale for OH oxidation of organic aerosol to be 1 to 9 days. The chemical lifetime reported here is very small but in contrast to the studies of George et al.⁷⁹ and Robinson et al.⁸⁰ the reaction is a surface reaction only. The lifetime of the atmospheric aerosol extract in the study presented was calculated to lie between 8 to 80 minutes, the measured lifetime is very short in comparison to typical aerosol lifetime of 1 to 10 days.⁸¹ Hence, it can be concluded that atmospheric aerosol films composed of similar material may react very quickly in the atmosphere and consequently determining the presence of the atmospheric aerosol extract as a thin film in the atmosphere may be difficult. .

4. Conclusion

The study presented here demonstrates the successful formation of a thin film of atmospheric aerosol at the air-water interface from material extracted from atmospheric aerosol. The film was determined to compromise of a two-layer system; indicating aerosol extracts may produce a film thickness of below 17 to 18 \AA for urban extracts and 10 \AA for remote extracts. In the absence of other data sources, the film thickness determined in the study could be used in atmospheric radiative transfer models for core-shell systems. The two-layer system indicates that the atmospheric aerosol extracts may contain hydrophobic and hydrophilic regions.

The atmospheric aerosol extracts were exposed to gas-phase OH radicals at a concentration of $7.0 \times 10^6 \text{ molecule cm}^{-3}$ and showed an exponential alteration with first-order rate constants ranging from 0.022 min^{-1} for urban atmospheric aerosol extracts to 0.208 min^{-1} for atmospheric

aerosol extracts sourced from remote locations. Substituting the first-order rate constants into a series of equations allowed the bimolecular rate constants of the magnitude of 1×10^{-11} to 1×10^{-10} molecules⁻¹ cm³ s⁻¹ and lifetime of the atmospheric aerosol extract at the air-water interface to be calculated. The bimolecular rate constants were observed to be fast, and the lifetime of the films was determined to lie between 8 and 80 minutes depending on aerosol extract.

The determined film thickness and film lifetime presented in the work represent values for a large ensemble of molecules and give an estimate of the values. However, these values do not represent an average, the average macroscopic scale film properties at the air-water interface of a trough may not be statistically applicable to macroscopic areas of individual aerosol droplets. A further caveat of the work is that the process of extraction may change the availability of compounds that form films at the air-water interface.

Corresponding Author

Professor Martin King: martin.king@es.rhul.ac.uk

Author Contributions

Rosalie H. Shepherd conducted all experiments, extracted all atmospheric aerosol extracts, analyzed and interoperated data collected and wrote the paper. Martin D. King and Andrew D. Ward conceived the experiment idea and assisted during the experiment. Neil Brough collected aerosol extract from Antarctica. Thomas Arnold was the synchrotron beamline scientist who assisted with the experiment and reduced all data.

Acknowledgements

The authors would like to thank Diamond Light Source for granting access time on I07 under the experiment number SI13493. Rosalie H. Shepherd would like to thank STFC for funding the student grant STL504279\1.

Notes

Data is available at [10.5281/zenodo.817516](https://doi.org/10.5281/zenodo.817516)

References

- (1) Stocker, T. F., Qin, D. and Plattner, G. K., Climate Change 2013: The Physical Science Basis (Technical Summary). *The Intergovernmental Panel on Climate Change*. **2013**, 33–115.
- (2) Lohmann, U. and Feichter, J. Global Indirect Aerosol Effects : A Review. *Atmospheric Chemistry and Physics* **2005**, 5, 715–737.
- (3) Ramanathan, V., Crutzen, P. J., Kiehl, J. T. and Rosenfeld, D. Aerosols, Climate and the Hydrological Cycle. *Science*. **2001**, 294, 2119–2125.
- (4) Breon, F. M., Tanre, D. and Generoso, S. Aerosol Effect on Cloud Droplet Size Monitored from Satellite. *Science*. **2002**, 295, 834–839.
- (5) Prather, K. A., Hatch, C. D. and Grassian, V. H. Analysis of Atmospheric Aerosols. *Annual Review of Analytical Chemistry*. **2008**, 1, 485–514.
- (6) Burkholder, J. B., Abbatt, J. P. D., Barnes, I., Roberts, J. M., Melamed, M. L., Ammann, M., Bertram, A. K., Cappa, C. D., Carlton, A. M. G., Carpenter, L. J., Crowley, J. N.,

- Dubowski, Y., George, C., Heard, D. E., Herrmann, H., Keutsch, F. N., Kroll, J. H., McNeill, V. F., Ng, N. L., Nizkorodov, S. A., Orlando, J. J., Percival, C. J., Picquet-Varrault, B., Rudich, Y., Seakins, P. W., Surratt, J. D., Tanimoto, H., Thornton, J. A., Zhu, T., Tyndall, G. S., Wahner, A., Weschler, C. J., Wilson, K. R. and Ziemann, P. J. The Essential Role for Laboratory Studies in Atmospheric Chemistry. *Environmental Science Technology*. **2017**, 51, 2519-2528.
- (7) Jacobson, M. C. and Hansson, H. Organic Atmospheric Aerosols: Review and State of the Science. *Reviews of Geophysics*. **2000**, 38, 267–294.
- (8) Reid, J. P., Dennis-Smith, B. J., Kwamena, N. O. A., Miles, R. E. H., Hanford, K. L. and Homer, C. J. The Morphology of Aerosol Particles Consisting of Hydrophobic and Hydrophilic Phases: Hydrocarbons, Alcohols and Fatty Acids as the Hydrophobic Component. *Physical Chemistry Chemical Physics*. **2011**, 13, 15559–15572.
- (9) Russell, L. M., Steven, M. F. and Satish, M. C. B. Mapping Organic Coatings on Atmospheric Particles. *Geophysical Research Letters*. **2002**, 29, 1–4.
- (10) Wyslouzil, B. E., Wilemski, G., Strey, R., Heath, C. H. and Dieregswiler, U. Experimental Evidence for Internal Structure in Aqueous-Organic Nanodroplets. *Physical Chemistry Chemical Physics*. **2006**, 8, 54–57.
- (11) Donaldson, D. J. and Vaida, V. The Influence of Organic Films at the Air-Aqueous Boundary on Atmospheric Processes. *Chemical Reviews*. **2006**, 106, 1445–1461.
- (12) Ellison, G. B., Tuck, A. F. and Vaida, V. Atmospheric Processing of Organic Aerosols. *Journal of Geophysical Research*. **1999**, 104, 11633-11641.

- (13) Gill, P. S., Graedel, T. E. and Weschler, C. J. Organic Films on Atmospheric Aerosol Particles, Fog Droplets, Cloud Droplets, Raindrops, and Snowflakes. *Review of Geophysics*. **1983**, *21*, 903-920.
- (14) Tervahattu, H., Juhanaja, J. and Kupiainen, K. Identification of an Organic Coating on Marine Aerosol Particles by TOF-SIMS. *Journal of Geophysical Research: Atmospheres*. **2002**, *107*, 1-7.
- (15) Donaldson, D. J. Adsorption of Atmospheric Gases at the Air–Water Interface. I. NH₃. *Journal of Physical Chemistry A*. **1999**, *103*, 62–70.
- (16) Enami, S., Hoffmann, M. R. and Colussi, A. J. Molecular Control of Reactive Gas Uptake “on Water”. *Journal of Physical Chemistry A*. **2010**, *114*, 5817–5822.
- (17) Kaiser, T., Roll, G. and Schweiger, G. Investigation of Coated Droplets in an Optical Trap: Raman-Scattering, Elastic-Light-Scattering, and Evaporation Characteristics. *Applied Optics*. **1996**, *35*, 5918–5924.
- (18) Eliason, T. L., Aloisio, S., Donaldson, D. J., Cziczo, D. J. and Vaida, V. Processing of Unsaturated Organic Acid Films and Aerosols by Ozone. *Atmospheric Environment*. **2003**, *37*, 2207–2219.
- (19) Davies, J. F., Miles, R. E. H., Haddrell, A. E. and Reid, J. P. Influence of Organic Films on the Evaporation and Condensation of Water in Aerosol. *Proceedings of the National Acadamey of Sciences of the U. S. A.* **2013**, *110*, 8807–8812.
- (20) McFiggans, G., Artaxo, P., Baltensperger, U., Coe, H., Facchini, M. C., Feingold, G., Fuzzi, S., Gysel, M., Laaksonen, A., Lohmann, U., Mentel, T. F., Murphy, D. M.,

- O'Dowd, C. D., Snider, J. R. and Weingartner, E. The Effect of Physical and Chemical Aerosol Properties on Warm Cloud Droplet Activation. *Atmospheric Chemistry and Physics Discussions*. **2005**, 5, 8507–8646.
- (21) Ruehl, C. R. and Wilson, K. R. Surface Organic Monolayers Control the Hygroscopic Growth of Submicrometer Particles at High Relative Humidity. *Journal of Physics and Chemistry A*. **2014**, 118, 3952–3966.
- (22) Cruz, C. N. and Pandis, S. N. The Effect of Organic Coatings on the Cloud Condensation Nuclei Activation of Inorganic Atmospheric Aerosol. *Journal Of Geophysical Research*. **1998**, 107, 13111–13123.
- (23) Andreaea, M. O. and Rosenfeld, D. Aerosol–cloud–precipitation Interactions. Part 1. The Nature and Sources of Cloud-Active Aerosols. *Earth-Science. Reviews* **2008**, 89, 13–41.
- (24) Feingold, G. and Chuang, P. Y. Analysis of the Influence of Film-Forming Compounds on Droplet Growth: Implications for Cloud Microphysical Processes and Climate. *Journal of Atmospheric Science*. **2002**, 59, 2006–2018.
- (25) Jones, S. H., King, M. D. and Ward, A. D. Atmospherically Relevant Core–shell Aerosol Studied Using Optical Trapping and Mie Scattering. *Chemical Communications*. **2015**, 51, 4914–4917.
- (26) Mmereki, B. T. and Donaldson, D. J. Direct Observation of the Kinetics of an Atmospherically Important Reaction at the Air-Aqueous Interface. *Journal of Physical Chemistry A*. **2003**, 107, 11038–11042.
- (27) Prinn, R. G., Huang, J., Weiss, R. F., Cunnold, D. M., Fraser, P. J., Simmonds, P. G.,

- McCulloch, A., Salameh, P., O'Doherty, S., Wang, R. H. J., Porter, L. and Miller, B. R. Evidence for Substantial Variation of Atmospheric Hydroxyl Radicals in the Past Two Decades. *Science*. **2001**, 292, 1882–1888.
- (28) McNeill, V. F., Wolfe, G. M. and Thornton, J. A. The Oxidation of Oleate in Submicron Aqueous Salt Aerosols: Evidence of a Surface Process. *Journal of Physics and Chemistry A*. **2007**, 111, 1073–1083.
- (29) Nah, T., Kessler, S. H., Daumit, K. E., Kroll, J. H., Leone, S. R. and Wilson, K. R. OH-Initiated Oxidation of Sub-Micron Unsaturated Fatty Acid Particles. *Physical Chemistry Chemical Physics*. **2013**, 15, 18649–18663.
- (30) Enami, S., Hoffmann, M. R. and Colussi, A. J. In Situ Mass Spectrometric Detection of Interfacial Intermediates in the Oxidation of RCOOH(aq) by Gas-Phase OH-Radicals. *Journal of Physical Chemistry A*. **2014**, 118, 4130–4137.
- (31) Richards-Henderson, N. K., Goldstein, A. H. and Wilson, K. R. Sulfur Dioxide Accelerates the Heterogeneous Oxidation Rate of Organic Aerosol by Hydroxyl Radicals. *Environmental Science and Technology*. **2016**, 50, 3554–3561.
- (32) Chapleski, R. C., Zhang, Y., Troya, D and Morris, J. R. Heterogeneous Chemistry and Reaction Dynamics of the Atmospheric Oxidants, O₃, NO₃ and OH on Organic Surfaces. *Chemical Society Reviews*. **2016**, 45, 3731–3746.
- (33) Dennis-Smith, B. J., Miles, R. E. H. and Reid, J. P. Oxidative Aging of Mixed Oleic Acid/sodium Chloride Aerosol Particles. *Journal of Geophysical Research Atmospheres* **2012**, 117, 1–13.

- (34) Eliason, T. L., Gilman, J. B. and Vaida, V. Oxidation of Organic Films Relevant to Atmospheric Aerosols. *Atmospheric Environment*. **2004**, 38, 1367–1378.
- (35) George, I. J. Vlasenko, A., Slowik, J. G. and Abbatt, J. P. D. Heterogeneous Oxidation of Saturated Organic Aerosols by Hydroxyl Radicals: Uptake Kinetics and Condensed-Phase Products. *Atmospheric Chemistry and Physics Discussions*. **2007**, 7, 6803–6842.
- (36) González-Labrada, E., Schmidt, R. and DeWolf, C. E. Real-Time Monitoring of the Ozonolysis of Unsaturated Organic Monolayers. *Chemical Communications*. **2006**, 23, 2471–2473.
- (37) González-Labrada, E., Schmidt, R. and DeWolf, C. E. Kinetic Analysis of the Ozone Processing of an Unsaturated Organic Monolayer as a Model of an Aerosol Surface. *Physical Chemistry Chemical Physics* **2007**, 9, 5814.
- (38) Nakayama, T., Sato, K., Matsumi, Y., Imamura, T., Yamazaki, A. and Uchiyama, A. Wavelength and NO_x Dependent Complex Refractive Index of SOAs Generated from the Photooxidation of Toluene. *Atmospheric Chemistry and Physics* **2013**, 13, 531–545.
- (39) Slade, J. H. and Knopf, D. A. Multiphase OH Oxidation Kinetics of Organic Aerosol: The Role of Particle Phase State and Relative Humidity. *Geophysical Research Letters* **2014**, 41, 5297–5306.
- (40) Vieceli, J., Roeselov, M., Potter, N., Dang, L. X., Garrett, B. C. and Tobias, D. J. Molecular Dynamics Simulations of Atmospheric Oxidants at the Air-Water Interface: Solvation and Accommodation of OH and O₃. *Journal of Physics and Chemistry B* **2005**, 109, 15876–15892.

- (41) Voss, L. F., Hadad, C. M. and Allen, H. C. Competition between Atmospherically Relevant Fatty Acid Monolayers at the Air/water Interface. *Journal of Physical Chemistry B*. **2006**, *110*, 19487–19490.
- (42) King, M. D., Rennie, A. R., Thompson, K. C., Fisher, F. N., Dong, C. C., Thomas, R. K., Pfrang, C. and Hughes, A. V. Oxidation of Oleic Acid at the Air-Water Interface and Its Potential Effects on Cloud Critical Supersaturations. *Physical Chemistry Chemical Physics*. **2009**, *11* (35), 7699–7707.
- (43) Pfrang, C.; Sebastiani, F.; Lucas, C. O. M.; King, M. D.; Hoare, I. D.; Chang, D.; Campbell, R. A. Ozonolysis of Methyl Oleate Monolayers at the Air-Water Interface: Oxidation Kinetics, Reaction Products and Atmospheric Implications. *Phys. Chem. Chem. Phys.* **2014**, *16*, 13220–13228.
- (44) Wadia, Y., Tobias, D. J., Stafford, R. and Finlayson-Pitts, B. J. Real-Time Monitoring of the Kinetics and Gas Phase Products of the Reaction of Ozone with 1-Oleoyl-2-Palmitoyl-Sn-Glycero-3-Phosphocholine at the Air/Water Interface. *Langmuir*. **2003**, *16*, 9321–9330.
- (45) Zhou, S., Gonzalez, L., Leithead, A., Finewax, Z., Thalman, R., Vlasenko, A., Vagle, S., Miller, L. A., Li, S. M., Burekul, S., Furutani, H., Uematsu, M., Volkamer, R. and Abbatt, J. Formation of Gas-Phase Carbonyls from Heterogeneous Oxidation of Polyunsaturated Fatty Acids at the Air-Water Interface and of the Sea Surface Microlayer. *Atmospheric Chemistry and Physics*. **2014**, *14*, 1371–1384.
- (46) Blanchard, D. C. Material, Sea-to-Air Transport of Surface Active. *Science*. **1964**, *146*, 396–397.

- (47) Donaldson, D. J. and George, C. Sea-Surface Chemistry and Its Impact on the Marine Boundary Layer. *Environmental Science and Technology*. **2012**, *46*, 10385–10389.
- (48) Marty, J. C., Saliot, A., Buat-Ménard, P., Chesselet, R. and Hunter, K. A. Relationship between the Lipid Compositions of Marine Aerosols, the Sea Surface Microlayer, and Subsurface Water. *Journal of Geophysical Research Oceans*. **1979**, *84*, 5707–5716.
- (49) Jones, S. H., King, M. D., Ward, A. D., Rennie, A. R., Jones, A. C. and Arnold, T. Are Organic Films from Atmospheric Aerosol and Sea Water Inert to Oxidation by Ozone at the Air-Water Interface?. *Atmospheric Environment*. **2017**, *161*, 274-287.
- (50) Jones, A. E., Wolff, E. W., Salmon, R. A., Bauguitte, S. J. B., Roscoe, H. K., Anderson, P. S., Ames, D., Clemitshaw, K. C., Fleming, Z. L., Bloss, W. J., Heard, D. E., Lee, J. D., Read, K. A., Hamer, P., Shallcross, D. E., Jackson, A. V., Walker, S. L., Lewis, A. C., Mills, G. P., Plane, J. M. C., Saiz-Lopez, A., Sturges, W. T. and Worton, D. R. Chemistry of the Antarctic Boundary Layer and the Interface with Snow: An Overview of the CHABLIS Campaign. *Atmospheric Chemistry and Physics*. **2008**, *8*, 3789–3803.
- (51) MacIntyre, F. The Top Millimeter of the Ocean. *Scientific American*. **1974**, *230*, 62–77.
- (52) Nicklin, C., Arnold, T., Rawle, J. and Warne, A. Diamond Beamline I07: A Beamline for Surface and Interface Diffraction. *Journal of Synchrotron Radiation*. **2016**, *23*, 1245–1253.
- (53) Arnold, T., Nicklin, C., Rawle, J., Sutter, J., Bates, T., Nutter, B., McIntyre, G. and Burt, M. Implementation of a Beam Deflection System for Studies of Liquid Interfaces on Beamline I07 at Diamond. *Journal of Synchrotron Radiation*. **2012**, *19*, 408–416.

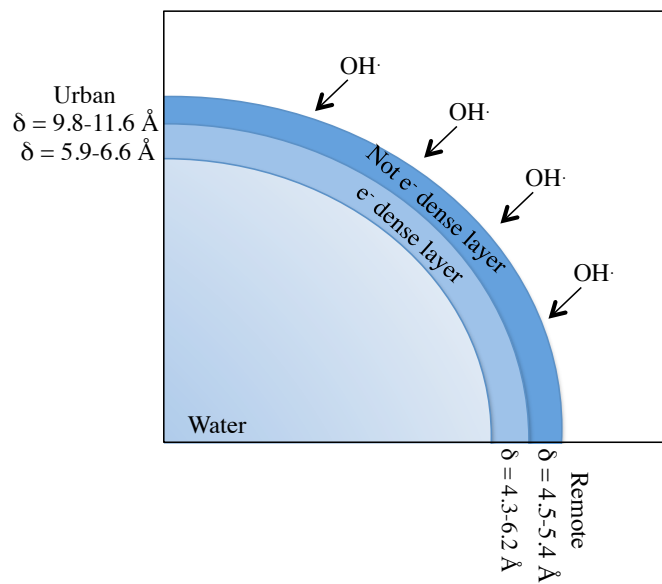
- (54) Chateigner, D. *Wiley-ISTE*. 2010.
- (55) Abelès, F. La Détermination de L'indice et de L'épaisseur Des Couches Minces Transparentes. *Journal Physique et Le Radium* **1950**, *11*, 307–310.
- (56) Nelson, A. Co-Refinement of Multiple-Contrast neutron/X-Ray Reflectivity Data Using MOTOFIT. *Journal of Applied Crystallography*. **2006**, *39*, 273–276.
- (57) Haynes, W. *CRC Press*. 2016.
- (58) Kukui, A., Legrand, M., Preunkert, S., Frey, M. M., Loisil, R., Gil Roca, J., Jourdain, B., King, M. D., France, J. L. and Ancellet, G. Measurements of OH and RO₂ Radicals at Dome C, East Antarctica. *Atmospheric Chemistry and Physics*. **2014**, *14*, 12373–12392.
- (59) Press, W. H., Teukolsky, S. A., Vetterling, W. T. and Flannery, B. P. *Cambridge University Press*. 2007.
- (60) Sandu, A. and Sander, R. Technical Note : Simulating Chemical Systems in Fortran90 and Matlab with the Kinetic PreProcessor KPP-2.1. **2006**, *6*, 187–195.
- (61) Atkinson, R., Baulch, D. L., Cox, R. A., Crowley, J. N., Hampson, R. F., Hynes, R. G., Jenkin, M. E., Rossi, M. J. and Troe, J. Evaluated Kinetic and Photochemical Data for Atmospheric Chemistry: Part 1 - Gas Phase Reactions of O_x, HO_x, NO_x and SO_x Species. *Atmospheric Chemistry and Physics Discussions*. **2003**, *3*, 6179–6699.
- (62) Dilbeck, C. W. and Finlayson-Pitts, B. J. Hydroxyl Radical Oxidation of Phospholipid-Coated NaCl Particles. *Physical Chemistry Chemical Physics*. **2013**, *15*, 9833–9844.
- (63) Bertram, A. K., Ivanov, A. V., Hunter, M., Molina, L. T. and Molina, M. J. The Reaction

- Probability of OH on Organic Surfaces of Tropospheric Interest. *Journal of Physical Chemistry A*. **2001**, *105*, 9415–9421.
- (64) Wolff, E. W. Signals of Atmospheric Pollution in Polar Snow and Ice. *Antarctic Science*. **1990**, *2*, 189–205.
- (65) Dabkowska, A. P., Talbot, J. P., Cavalcanti, L., Webster, J. R. P., Nelson, A., Barlow, D. J., Fragneto, G. and Lawrence, M. J. Calcium Mediated Interaction of Calf-Thymus DNA with Monolayers of Distearoylphosphatidylcholine: A Neutron and X-Ray Reflectivity Study. *Soft Matter*. **2013**, *9*, 7095–7105.
- (66) Takahama, S., Liu, S. and Russell, L. M. Coatings and Clusters of Carboxylic Acids in Carbon-Containing Atmospheric Particles from Spectromicroscopy and Their Implications for Cloud-Nucleating and Optical Properties. *Journal of Geophysical Research Atmospheres*. **2010**, *115*, 1–21.
- (67) Bevington, P. and Robinson, K. *McGraw-Hill Education*. **2002**.
- (68) George, L. A., Hard, T. M. and O'Brien, R. J. Measurement of Free Radicals OH and HO₂ in Los Angeles Smog. *Journal of Geophysical Research*. **1999**, *104*, 11643–11655.
- (69) Frost, G. J., Trainer, M., Mauldin, R. L., Eisele, F. L., Prevot, A. S. H., Flocke, S. J., Madronich, S., Kok, G., Schillawski, R. D., Baumgardner, D. and Bradshaw, J. Photochemical Modeling of OH Levels during the First Aerosol Characterization Experiment (ACE 1). *Journal of Geophysical Research*. **1999**, *104*, 16041–16052.
- (70) Hanson, D. R. Surface-Specific Reactions on Liquids. *Journal of Physical Chemistry B*. **1997**, *101*, 4998–5001.

- (71) Smith, G. D., Woods, E., DeForest, C. L., Baer, T. and Miller, R. E. Reactive Uptake of Ozone by Oleic Acid Aerosol Particles: Application of Single-Particle Mass Spectrometry to Heterogeneous Reaction Kinetics. *Journal of Physical Chemistry A*. **2002**, *106*, 8085–8095.
- (72) Hearn, J. D., Lovett, A. J. and Smith, G. D. Ozonolysis of Oleic Acid Particles: Evidence for a Surface Reaction and Secondary Reactions Involving Criegee Intermediates. *Physical Chemistry Chemical Physics*. **2005**, *7*, 501–511.
- (73) McNeill, V. F., Yatavelli, R. L. N., Thornton, J. A., Stipe, C. B. and Landgrebe, O. The Heterogeneous OH Oxidation of Palmitic Acid in Single Component and Internally Mixed Aerosol Particles: Vaporization, Secondary Chemistry, and the Role of Particle Phase. *Atmospheric Chemistry and Physics Discussions*. **2008**, *8*, 6035–6068.
- (74) Hennigan, C. J., Sullivan, A. P., Collett, J. L. J. and Robinson, A. L. Levoglucosan Stability in Biomass Burning Particles Exposed to Hydroxyl Radicals. *Geophysical Research Letters*. **2010**, *37*, 1-4.
- (75) King, M. D., Thompson, K. C., Ward, A. D., Pfrang, C. and Hughes, B. R. Oxidation of Biogenic and Water-Soluble Compounds in Aqueous and Organic Aerosol Droplets by Ozone: A Kinetic and Product Analysis Approach Using Laser Raman Tweezers. *Faraday Discussions*. **2008**, *137*, 173–192.
- (76) Gilman, J. B., Eliason, T. L., Fast, A. and Vaida, V. Selectivity and Stability of Organic Films at the Air-Aqueous Interface. *Journal of Colloid and Interface Science*. **2004**, *280*, 234–243.

- (77) Knopf, D. A., Forrester, S. M. and Slade, J. H. Heterogeneous Oxidation Kinetics of Organic Biomass Burning Aerosol Surrogates by O_3 , NO_2 , N_2O_5 and NO_3 . *Physical Chemistry Chemical Physics*. **2011**, *13*, 21050-21062.
- (78) Williams, J., de Reus, M., Krejci, R., Fischer, H. and Ström, J. Application of the Variability-Size Relationship to Atmospheric Aerosol Studies: Estimating Aerosol Lifetimes and Ages. *Atmospheric Chemistry and Physics Discussions*. **2002**, *2*, 43–74.
- (79) George, I. J., Slowik, J. and Abbatt, J. P. D. Chemical Aging of Ambient Organic Aerosol from Heterogeneous Reaction with Hydroxyl Radicals. *Geophysical Research Letters*. **2008**, *35*, 1–5.
- (80) Robinson, A. L., Donahue, N. M. and Rogge, W. F. Photochemical Oxidation and Changes in Molecular Composition of Organic Aerosol in the Regional Context. *Journal of Geophysical Research Atmospheres*. **2006**, *111*, 1–15.
- (81) Kanakidou, M., Seinfeld, J. H., Pandis, S. N., Barnes, I., Dentener, F. J., Facchini, M. C., Van Dingenen, R., Ervens, B., Nenes, A., Nielsen, C. J., Swietlicki, E., Putaud, J. P., Balkanski, Y., Fuzzi, S., Horth, J., Moortgat, G. K., Winterhalter, R., Myhre, C. E. L., Tsigaridis, K., Vignati, E., Stephanou, E. G. and Wilson, J. Organic Aerosol and Global Climate Modelling: A Review. *Atmospheric Chemistry and Physics*. **2005**, *5*, 1053–1123.

For table of contents only:



Paper 6: Oxidation of a bilayer of DPPC on a mineral interface by aqueous-phase OH radicals to replicate atmospheric aerosol behaviour

Rosalie H. Shepherd, Martin D. King, Adrian R. Rennie, Andrew D. Ward, Rebecca Welbourn and Christy Kinane

To be submitted as a letter to the Journal of American Chemical Society.

I declare I have made the following contributions to the piece of co-authored work:

- Conducted the experiments, and collected and analysed all data collected
- Contributed to the conclusions drawn from the experiments conducted
- Authored the paper

Oxidation of a bilayer of DPPC on a mineral interface by aqueous-phase OH radicals to replicate atmospheric aerosol behavior

Rosalie H. Shepherd^{1, 2}, Martin D. King^{1*}, Adrian R. Rennie³, Andrew D. Ward², Rebecca Welbourn⁴ and Christy Kinane⁴

¹Department of Earth Sciences, Royal Holloway, University of London, Egham, Surrey, TW20 0EX, UK

²Central Laser Facility, Research Complex, STFC Rutherford Appleton Laboratory, Oxford

³Centre for Neutron scattering, Uppsala University, 75120, Uppsala, Sweden

⁴ISIS Neutron and Muon Source, Science and Technology Facilities Council, Rutherford Appleton Laboratory, Harwell Oxford, Didcot, OX11 0QX, UK

Atmospheric aerosols may be coated with an organic thin film. It is crucial to characterize the organic thin film in terms of optical properties and film thickness to correctly understand current climate scenarios and to accurately predict future climate change. Owing to the high level of oxidants present in the atmosphere, organic films may undergo considerable change. Bilayers of deuterated 1,2-dipalmitoyl-sn-glycero-3-phosphocholine (DPPC) were deposited at a silica-water interface to mimic the presence of an organic bilayer on mineral atmospheric dust aerosol. Neutron reflectivity was used initially to characterize the bilayer in terms of composition and layer thickness. To investigate the bilayer degradation, neutron reflectivity profiles were collected continuously as the bilayer was exposed to aqueous-phase OH radicals. The results showed the bilayer decayed until the majority of material had left the silica surface. The decay could be simulated by a degradation mechanism comprising of seven or nine kinetic steps. The degradation had a bimolecular rate constant on the magnitude of 10^{-12} molecule⁻¹ cm³ s⁻¹, and the bilayer had a atmospheric lifetime of some hours, which is on a similar timescale to some removal processes in the atmosphere. Understanding the changes that an organic film may undergo in the atmosphere and their inclusion into models is paramount for the calculation of accurate climate estimations.

1. INTRODUCTION

Atmospheric aerosol contributes to global temperatures and climate directly by scattering or absorbing incoming solar radiation;¹⁻³ and indirectly by acting as cloud condensation nuclei.³⁻⁵ Cloud droplets form by the nucleation of water on aerosol.⁶ Large uncertainty exists regarding the extent to which aerosol, including oxidized aerosol, effects global temperatures. More research focused on understanding atmospheric aerosol properties is urgently required e.g. Stocker et al.⁷

Owing to the high concentration of aerosol present in the atmosphere, atmospheric aerosol and cloud droplets are susceptible to the development of a thin film of organic matter on their surface e.g. Tervahattu et al.⁸ and Gill et al.⁹ The presence of a thin film presents additional challenges for scientists trying to understand atmospheric aerosols, and consequently a number of studies

have focused on aerosol films e.g. McNeill et al.¹⁰ and Gill et al.⁹ In particular, Jones et al. and Liu et al. have both studied the optical properties of aerosol thin films,^{11,12} Davies et al. Ruehl et al. and Donaldson et al. investigated the impact of thin films upon atmospheric processes such as evaporation,¹³⁻¹⁵ whilst Nieto-Gligorovski et al., Voss et al. and Eliason et al. probed the alteration of the core aerosol's reaction chemistry upon film formation.¹⁶⁻¹⁹

The oxidation of an organic film at the air-water interface has previously been studied by applying neutron or x-ray reflection techniques e.g. King et al., Pfrang et al. and Jones et al.,²⁰⁻²² such studies have investigated the oxidation of proxy organic surfactant films. However, surface active material may collect at the solid-liquid interface of an aqueous aerosol and hence the presented study extends such experiments by replicating and understanding the behavior and reactivity traits of an organic film at a silica-water interface by applying neutron reflectometry e.g. Penfold and Thomas²³ and Lu et al.²⁴ Silica was chosen as the material to replicate the core aerosol as minerals make up a large proportion of atmospheric aerosol (atmospheric loading of 1000 to 5000 Mt/year)^{25,26} and has been proven to exist in the atmosphere with a film of material present e.g. Falkovich et al.,²⁷ whilst 1,2-dipalmitoyl-sn-glycero-3-phosphocholine (DPPC) was used as the proxy atmospheric thin film owing to lipids known to be highly abundant aerosols e.g. Ciuraru et al.²⁸ and Marty et al.²⁹

Probing the reaction chemistry of the oxidation of organic materials is paramount not only for understanding climate scenarios, but also for characterizing membranes in biology. DPPC has featured in a small number of oxidation studies. For example, Dilbeck and Finlayson-Pitts⁴⁷ studied the oxidation of a DPPC bilayer on a salt product and determined a number of the oxidation products, whilst Wadia et al.³⁰ exposed DPPC monolayers at the air-water interface to ozone.

A variety of oxidants have been used in experiments replicating the atmosphere. Gas-phase ozone^{23,33-37} and OH radicals^{17,33-45} are two commonly used oxidants. Studies including OH radicals as the oxidant include Karagulian et al.⁴⁶ who used OH radicals to oxidize the phospholipid OPPC, Cappa et al.³³ who oxidized the

model aerosol compounds squalane and azelic acid with OH radicals, Nah et al.³⁴ who probed the reaction between OH radicals and unsaturated fatty acids and Slade et al.³⁵ who determined the oxidation kinetics for levoglucosan and methyl-nitrocatechol upon exposure to OH radicals.

DPPC has demonstrated the ability to form robust and reproducible bilayers in previous studies e.g. Koenig et al., Smith et al. and Charitat et al.⁴⁸⁻⁵⁰ In the presented study, bilayers of DPPC were formed at the silica-water interface and were subsequently oxidized by aqueous-phase OH radicals. Experiments were conducted on the neutron reflectometer polREF at ISIS Neutron and Muon Source, Rutherford Appleton Laboratories. Neutron reflectometry was measured as a function of momentum transfer and the resultant graph will be called a neutron reflection profile henceforth. Simulation of the neutron reflection profiles for the bilayer at the silica-water interface allowed the neutron scattering length density and layer thickness to be determined for the bilayer at the silica-water interface. Aqueous OH radicals then oxidized the bilayer and the reaction was followed by continuously collecting neutron reflection profiles. A plot of $\frac{\delta_t \rho_t}{\delta_{t=0} \rho_{t=0}}$ as a function of time could then be drawn. Fits allowed the mechanism of decay to be estimated and the bimolecular rate constant and lifetime of the bilayer under atmospheric conditions to be calculated.

2. RESULTS AND DISCUSSION

A polished silica crystal was used as the window and interface for the bilayer to form upon. The bilayers of DPPC were formed on the silica surface by using the well-known vesicle fusion method.⁵¹ The silica window was separated from the PMMA back by a PTFE spacer 2 mm thick.⁵² An aqueous subphase consisting of silica contrast matched water formed from 69 percent D₂O and 31 percent H₂O was pumped into and through the space created by the PTFE spacer between the silica window and the cell back.

The cell was illuminated by a 254 nm UV light placed 16 mm from the crystal. The UV lamps were switched on remotely to ensure the bilayer was exposed to UV light at a specific time. To generate the OH radicals, hydrogen peroxide was added at 2.5 percent by volume into the subphase that flowed through the cell at 1 ml min⁻¹. The hydrogen peroxide was subsequently photolysed by the UV light. The concentration of hydrogen peroxide was chosen to ensure that the concentration of hydrogen peroxide was maintained throughout the experimental apparatus, thereby providing pseudo first-order conditions.

Three neutron data sets were collected prior to oxidation to enable characterization of the initial bilayer. During the oxidation of the bilayer with OH radicals, neutron reflection profiles were collected every 40 minutes. In addition, two experimental controls were measured for the bilayers where either hydrogen peroxide or only UV illumination present.

2.1. Fitting neutron reflection data to the bilayer

The neutron reflection profiles of the bilayer at the silica-water interface could be simulated as a six-layer system (1. crystalline silica 2. silica interface 3. bilayer head layer 4. bilayer tail layer 5. a second bilayer head layer 6. aqueous

subphase) using neutron scattering length density and thickness literature values for the head and tail layers of the bilayers.^{48,53} Figure 1 displays a diagram of the layered system, whilst Table 1 displays the values used in the simulation. During the oxidation reaction, the silica interface may have aged and was therefore analyzed by comparing the neutron reflection profiles for the same silica crystal at an interface with aqueous D₂O, H₂O and mixtures of. The neutron scattering length density was observed to be different to the neutron scattering length density of silica and hence an extra layer (the silica interface) was included.

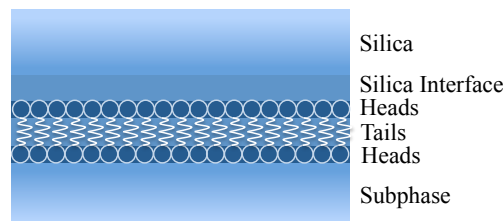


Figure 1: Depiction of the layers of the system under study.

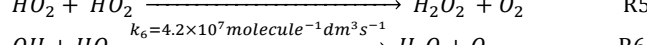
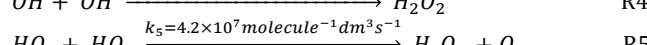
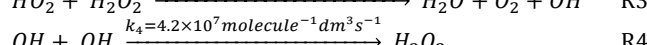
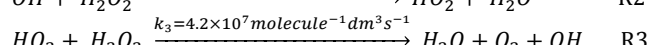
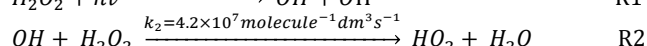
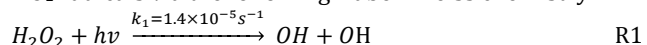
In addition, water penetration is a well-documented phenomenon for lipid bilayers^{54,55} and Table 1 outlines the proportion of water found in the three-layer bilayer system. Solvent percentage (volume/volume) and layer thickness were varied until a good fit, as judged by eye, was obtained between simulated and experimental neutron reflection profiles.

Table 1. The scattering length density (ρ) and thickness (δ) of the layers used to fit the neutron reflection profile of a bilayer of DPPC at the silica-water interface. The scattering length densities of layers 3 to 5 were obtained from literature.^{48,53}

Layer	ρ 10 ⁻⁶ Å ⁻²	δ Å	Solvent % v/v
2.Silica interface	3.62±0.5	49.26±0.5	5±1
3.Silica interface heads	1.73	12±0.5	15±2
4.Tails	-0.37	35±0.5	5±2
5.Water interface heads	1.73	12±0.5	15±2

2.2. Bilayer oxidation

The OH radicals were generated by the photolysis of 2.5 percent by volume aqueous solution of hydrogen peroxide. The photolysis of hydrogen peroxide produced OH and HO₂ radicals via the following Haber-Weiss chemistry:⁵⁶



Through treating reactions R1 to R6 as a series of first-order differential equations and solving numerically with a Runge-Kutta method,⁵⁷ the steady-state concentrations of the OH and HO₂ radicals were calculated. Owing to Yu and Barker providing an in-depth investigation into the model-

ing of each reaction step, a sensitivity test was not required.⁵⁶

The value of k_1 was dependent on the intensity of the UV lamp, the geometry of the cell and the optical properties of the silica windows. An offline experiment was applied to determine k_1 . Four 0.003 mol dm⁻³ solutions of aqueous hydrogen peroxide solutions were photolysed for known time periods. The concentration of hydrogen peroxide was determined by UV-VIS spectroscopy (using the absorption cross section provided by Chu and Anastasio.⁵⁸ To ensure any changes in the absorption signal was observed, a less concentrated solution of hydrogen peroxide had to be used. The decay in the concentration of hydrogen peroxide with photolysis time could be plotted and simulated by modeling R1 to R6 and varying k_1 until a line could be drawn through the plotted points, as depicted in Figure 2.

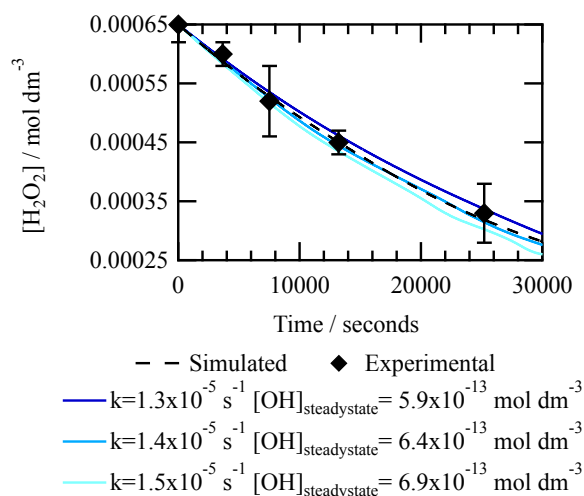


Figure 2. The decay in the concentration of H_2O_2 in H_2O owing to photolysis by the UV illumination. The error bars displayed on the experimental data was calculated by repeating measurements on the UV-VIS spectrometer. The reactions R1-R6 were numerically simulated as a series of first-order differential equations to calculate $[\text{H}_2\text{O}_2]$ as a function of photolysis time: the value of k_1 was varied until a good fit (as judged by-eye) was observed between simulated and experimental data. As shown in the figure, a value of $k_1 = 1.4 \times 10^{-5} \text{ s}^{-1}$ was used.

The oxidation of the bilayers was conducted in a solution comprising of a silica contrast matched solution formed from 69 percent D_2O and 31 percent H_2O volume/volume. The presence of D_2O would cause an increase in the steady-state concentration of hydroxyl radicals (OH and OD) as a kinetic isotope effect will reduce the value of the rate constant by approximately a factor of five for the reactions R2, R3, R5 and R6 owing to the abstraction of a C-D bond.⁵⁹ The steady-state concentrations of OH and HO_2 radicals in the neutron cell were calculated to be $6.9 \times 10^{-10} \text{ molecule cm}^{-3}$ and $2.2 \times 10^{-3} \text{ molecule cm}^{-3}$ respectively assuming no D_2O was present, whilst the steady-state concentrations of OD and DO_2 radicals in the neutron cell were calculated as $3.0 \times 10^{-9} \text{ molecule cm}^{-3}$ and $4.8 \times 10^{-3} \text{ molecule cm}^{-3}$ respectively during

the bilayer oxidation assuming that H_2O was not present. The actual steady state concentrations of OH and HO_2 radicals were crudely estimated for the bilayer oxidation in a solution of 69 percent: 31 percent (volume/volume) D_2O : H_2O as $2.3 \times 10^{-9} \text{ molecule cm}^{-3}$ and $4.0 \times 10^{-3} \text{ molecule cm}^{-3}$ respectively. The determined concentration of OH radicals is of the same magnitude to aqueous-phase OH radicals present in cloud droplets as reported by Herrmann et al.⁶⁰

When the bilayers were exposed to the OH radicals, neutron reflection profiles were collected continuously for 40-minute periods. Every neutron reflection profile collected was simulated as a six-layer system and Figure 3 depicts the neutron reflection profiles collected during the OH exposure, with the simulated fit overlaying the experimental neutron reflection profile. Simulation of the neutron reflection profiles allowed the change in neutron scattering length density and thickness of each layer to be determined.

From Figure 3, the bilayer was observed to decay when exposed to OH radicals, until 7200 seconds after initial exposure. The reaction may be over at 7200 seconds owing to the neutron reflection profiles collected from 7200 seconds onwards overlaying. Interestingly, Figure 3 shows that some material from the bilayers remained at the interface after 14400 seconds exposure to OH radicals, as shown by the final data not overlaying that for the bare silica-water interface. When the silica crystal was removed from the neutron beamline, material was observed to be still present upon the silica crystal owing to the crystal showing hydrophobic traits post experiment. The possibility that the silica-water interface had altered was ruled out by reusing the same silica crystal. Owing to OH radicals being powerful and unselective reactants, it can be assumed that only chemically inert material remains at the silica interface. Use of a complimentary technique such as FTIR-ATR could be used to provide clearer chemical information of the material remaining at the end of the oxidation reaction.

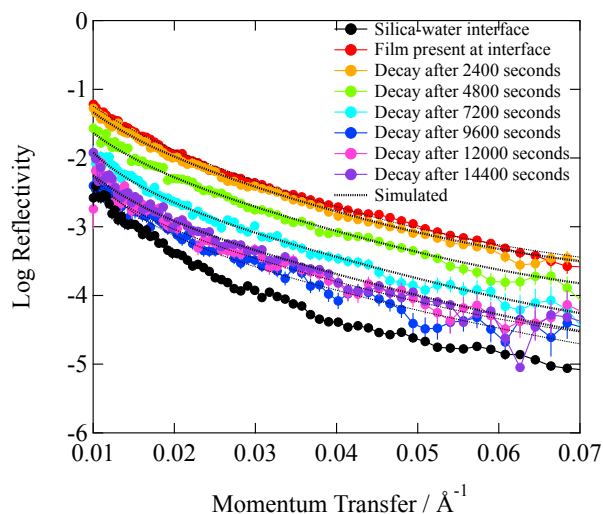


Figure 3. The loss in neutron reflectivity as the bilayers at the air-water interface was exposed to OH radicals at a concentration of $2.3 \times 10^{-9} \text{ molecule cm}^{-3}$. Simulated fits for chosen neutron reflection profiles are laid over the experimental data.

The OH radicals were formed from the photolysis of hydrogen peroxide with UV. From the experimental controls, it was observed that without both hydrogen peroxide and UV illumination present no measureable reaction was observed over a 15000 second time frame.

2.2. Bilayer oxidation kinetics

Once the neutron scattering length density and layer thicknesses were known for each neutron reflection profile collected during the oxidation process of the interface, a plot of relative neutron scattering length per unit area for each layer of the bilayer system could be plotted as a function of time. A typical plot is displayed in Figure 4. Figure 4 again demonstrates that material remains at the silica-water interface after exposure to OH radicals owing to the plateau of scattering length per unit area between 10000 and 15000 seconds. The uncertainty in each layer thickness at 10000 seconds is ± 0.3 , ± 0.3 and $\pm 0.2 \times 10^{-6} \text{ \AA}^{-2}$ for the bilayer heads at the silica interface, tails and heads at the water interface respectively. The small alteration in thickness suggests that the oxidation reaction is finished by 10000 seconds.

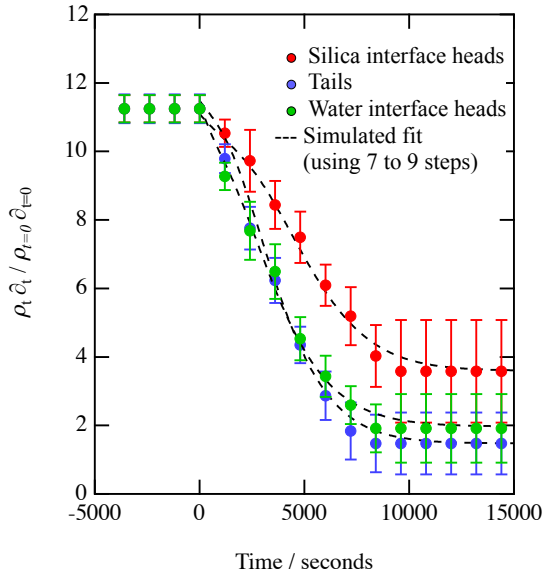
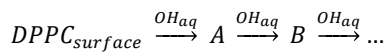


Figure 4. The step-wise degradation mechanism for each layer used to represent the bilayer at the silica-water interface. At time zero, the bilayer was exposed to OH radicals.

Interestingly the head layer nearest the silica interface has the largest value of scattering length per unit area at the reaction end point, indicating that oxidation of the head layers may be more difficult than oxidation of the tail layer. The other head layer was not directly tethered to the silica interface and may thus leave the interface more easily.

Scheme 1. The chemical reaction for the oxidation of the bilayer with OH radicals at the silica-water interface.



The chemical reaction for each layer could be fitted to a step-wise degradation mechanism comprising of seven or nine degradation steps (depending on the layer) the weighting of which decreased by five percent for each step. The pseudo first-order rate constants were then obtained for each step. Scheme 1 depicts the chemical reaction for the oxidation of the bilayer. To ensure the predicted degradation decay accurately resembled the oxidation reaction, a number of tests were run on (1) the weighting of each kinetic step and (2) the number of steps required (see Appendix B). The determined pseudo first-order rate constant could be used to determine the bimolecular rate constant through applying Equation 1:

$$k = k' [OH], \quad \text{Eq.1}$$

where k is the bimolecular rate constant and k' the pseudo first-order rate constant. Subsequent calculation of the lifetime (τ) dependent on chemical oxidation in the atmosphere could be calculated using Equation 2:

$$\tau = \frac{1}{k(OH)_{atm}}, \quad \text{Eq.2}$$

where $[OH]_{atm}$ is the concentration of OH radicals in the atmosphere. By using an atmospherically relevant concentration of OH radicals ($1 \times 10^6 \text{ molecule cm}^{-3}$ was used)⁶² the atmospheric lifetime of the bilayer could be calculated.

Table 2 displays the bimolecular rate constant and atmospheric lifetime values calculated for the bilayers. It ought to be noted that the slowest pseudo first-order rate constant was used to represent the oxidation of each layer of the bilayer, owing to the slowest step most likely being the rate-determining step of the overall reaction.

Table 2. The bimolecular rate constant (k) and lifetime with regard to atmospheric conditions (τ) for each kinetic step of the three-layers used to depict the bilayer at the silica-water interface.

Layer	k ($\text{molecule}^{-1} \text{ cm}^3 \text{ s}^{-1}$)	τ (hours)
Silica interface heads	$(4.6-9.2) \times 10^{-12}$	3 to 6
Tails	$(4.6-9.2) \times 10^{-12}$	3 to 6
Water interface heads	$(3.9-10.4) \times 10^{-12}$	3 to 7

The calculated bimolecular rate constants are similar to literature values. The bimolecular rate constants calculated by Slade et al.⁶³ for the reaction between OH radicals and laboratory generated levoglucosan and methyl-nitrocatechol aerosols, Slade and Knopf³⁹ who studied the reaction between OH radicals and biomass burning aerosols and Bejan et al.⁶⁴ who calculated gas-phase rate constants for the reaction between OH radicals and nitrophenols were all on the magnitude of 1×10^{-12} to $1 \times 10^{-13} \text{ molecule}^{-1} \text{ cm}^3 \text{ s}^{-1}$.

The lifetime of the bilayer in regard to atmospheric concentration of OH radicals was on the scale of hours. Contrastingly, Slade et al.³⁹ estimated a lifetime ranging from 2 days to 2 weeks for biomass burning aerosol particles when exposed to atmospheric background level OH radicals, whilst in a separate study Slade et al.³⁵ determined a lifetime of 3 to 27 days for proxy aerosols when exposed to atmospheric background level OH radicals at different relative humidity percentages. Additional-

ly, a number of studies have focused on estimating the atmospheric lifetime for organic aerosols when exposed to other oxidants, for example Knopf et al.⁶³ estimated a lifetime ranging from 1 to 112 minutes for organic aerosol when exposed to O₃, NO₂, N₂O₅ or NO₃. In the study presented, the lifetime of the bilayer was on the timescale of hours, which is on a similar timescale to some removal processes in the atmosphere.

CONCLUSION

Neutron reflectometry was applied to study a bilayer of DPPC at the silica-water interface. The bilayer could be simulated as a six-layer system, including a layer that represented the silica interface with a scattering length density of was $3.62 \pm 0.5 \times 10^{-6} \text{ Å}^{-2}$ and thickness $49.26 \pm 2 \text{ Å}$.

Aqueous-phase OH radicals oxidized the film. The change in the bilayer upon exposure to OH radicals could be simulated with a seven or nine step degradation decay. Knowledge of the mechanism describing the decay of the bilayer when exposed to OH radicals allowed the bimolecular rate constants to be calculated and subsequently lifetime of the bilayers with regard to atmospheric conditions to be estimated. The bimolecular rate constants were on the magnitude of $1 \times 10^{-12} \text{ molecule}^{-1} \text{ cm}^3 \text{ s}^{-1}$ without an enhancement in oxidation rate with regard to the bilayer being attached to the silica-water interface. The lifetime of the bilayers with regard to atmospheric conditions was hours, similar to the lifetime of atmospheric aerosol. Such information is paramount for accurate climate and global temperature estimations.

Experimental control measurements demonstrated that the bilayer did not decay when exposed to either hydrogen peroxide or UV light only.

AUTHOR INFORMATION

Corresponding Author

Professor Martin King: m.king@es.rhul.ac.uk

Notes

The authors declare no competing financial interests.

Data is available at 10.5286/ISIS.E.84763411.

ACKNOWLEDGMENT

The authors would like to thank the STFC ISIS for awarding the beam time grants RB1520395, RB1620309 and RB1610133. Rosalie H. Shepherd would like to thank STFC for funding the student grant ST/L504279/1.

Appendix A

The bilayer formed at the silica-water interface displayed a step-wise degradation decay when exposed to OH radicals. The three layers used to describe the bilayer at the silica-water interface could be fitted to different degradation decays and were hence analyzed separately. For each layer, the number of steps required for the degradation and the corresponding weighting (or overall contribution) of each step in the reaction was analyzed through applying chi-squared tests; the tests are outlined in Appendix B. Each step of the degradation decay was fitted to a pseudo first-order rate constant, which is outlined in Table 3. The

first-order rate constants were determined by simulating the experimental decay with a step-wise degradation, and altering the rate constants in turn until a by-eye fit was obtained. The number of steps and the weighting of each step was initially estimated and then refined through application of the chi-squared tests.

Table 3. The pseudo first-order rate constants (k') for each step of the step-wise degradation decay of each layer of the bilayer at the silica-water interface when exposed to aqueous-phase OH radicals. The rate constants are depicted as the average and standard deviation of four bilayers, when the rate constants did not change between bilayers the standard deviation is displayed as zero.

Silica interface-heads (s ⁻¹)	Tails (s ⁻¹)	Water interface-heads (s ⁻¹)
$(9.3 \pm 1.5) \times 10^{-4}$	$(8.0 \pm 0.1) \times 10^{-4}$	$(1.7 \pm 0.7) \times 10^{-3}$
$(8.4 \pm 1.1) \times 10^{-4}$	$(8.3 \pm 0.5) \times 10^{-4}$	$(3.1 \pm 1.4) \times 10^{-3}$
$(9.3 \pm 0.1) \times 10^{-4}$	$(1.2 \pm 0.6) \times 10^{-3}$	$(9.0 \pm 1.0) \times 10^{-4}$
$(1.0 \pm 0.1) \times 10^{-3}$	$(1.0 \pm 0.1) \times 10^{-3}$	$(8.0 \pm 1.0) \times 10^{-4}$
$(1.5 \pm 1.0) \times 10^{-3}$	$(3.0 \pm 1.0) \times 10^{-3}$	$(1.3 \pm 0.4) \times 10^{-3}$
$(3.0 \pm 1.0) \times 10^{-3}$	$(1.0 \pm 0.1) \times 10^{-1}$	$(9.5 \pm 1.0) \times 10^{-2}$
$(1.0 \pm 0.0) \times 10^{-2}$	$(1.0 \pm 0.1) \times 10^{-1}$	$(9.5 \pm 1.0) \times 10^{-2}$
$(1.0 \pm 0.1) \times 10^{-1}$	-	-
$(1.0 \pm 0.1) \times 10^{-1}$	-	-

Appendix B

A number of tests were run to (1) ensure the neutron scattering length density and layer thickness fully represented the bilayers and (2) the stepwise degradation mechanism fully described the decay observed for the bilayers upon exposure to OH radicals.

1. Bilayer fitting

To quantify the quality of the fits to the experimental neutron data for the bilayers, a metric χ^2 as a function of neutron scattering length density and layer thickness was calculated by simulating the experimentally collected neutron reflection profiles. Equation 3 was applied to determine χ^2 :

$$\chi^2 = \sum \frac{(R_{exp} - R_{calc})^2}{R_{calc}}, \quad \text{Eq. 3}$$

where R_{exp} is the experimental value and R_{calc} is the simulated value.

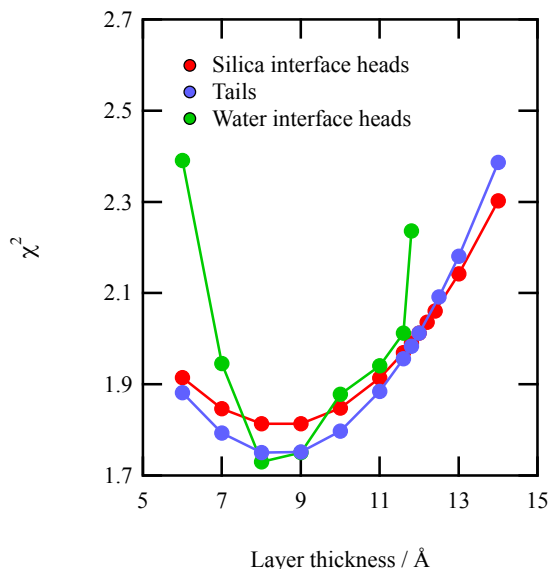


Figure 5. To quantify the quality of fit between simulated and experimental neutron reflection profiles, χ^2 tests were run. Figure 5 depicts χ^2 as a function of layer thickness.

χ^2 was determined individually for each layer used to describe the bilayers at the silica-water interface; for each layer the scattering length density from literature was held constant and the thickness of each layer was altered in turn. At each new thickness, χ^2 was determined. The results from the test displayed a clear minimum suggesting a fit could be determined with accuracy lying in the range ± 0.5 Å for layer thickness. The layer thicknesses that provided the points lying in the minima were used to simulate the bilayer. The χ^2 test for a neutron reflection profile collected after the bilayer had been exposed to the OH radicals for 144000 seconds is displayed in Figure 5. The minima displayed in Figure 5 do not lie near a layer thickness of 0 Å, demonstrating that a layer thickness of zero would not accurately represent the silica-water interface. The results indicate that there is some bilayer residual remaining after 144000 seconds exposure to OH radicals.

2. Bilayer oxidation kinetics

Evaluation of the determined degradation decay required two processes. Firstly, the weight of each kinetic step for each layer was adjusted and the alteration in the quality of fit determined by running a χ^2 test as described above. It was observed that the weighting of each kinetic step could vary by approximately twenty percent, however the observation was most exaggerated for the first few steps regardless of the layer under study.

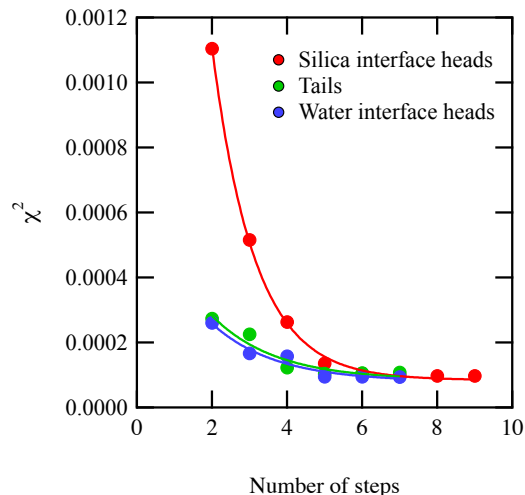


Figure 6. The requirement for seven or nine steps in the degradation decay was investigated by applying a χ^2 test. χ^2 as a function of number steps is displayed.

Secondly, the number of steps required in the degradation decay was investigated by altering the number of steps, manually adjusting the rate constants to keep a reasonable fit between simulated and experimental data and then determining the quality of fit with a χ^2 test. Figure 6 displays the results. From Figure 6 it can be observed that at least six steps are required. However, χ^2 continues to gradually decrease, demonstrating an improved fit can be obtained by including a greater number of kinetic steps.

Appendix C

The bilayer was simulated as a three-layer system consisting of a layer for the hydrocarbon region of the bilayer that separated two layers head group layers. However, when the bilayer was exposed to OH radicals and demonstrated decay, it was thought that the structure of the bilayer might alter and the clear distinction between the three layers might cease to exist. Consequently, fitting the bilayer as a one-layer system was attempted.

Figure 7 displays the simulated one-layer system neutron reflection profiles overlaying the experimental neutron reflection profiles. From the figure, it can be observed that the simulations are poorer at low values of momentum transfer. χ^2 values were determined for each fit and are at much higher values than for bilayers simulated as a three-layer system (see insert graphic in Figure 7). Therefore the bilayers were not simulated as one-layer systems. It can be consequently concluded that the structure of the bilayers are consistent with a layered structure upon exposure to OH radicals.

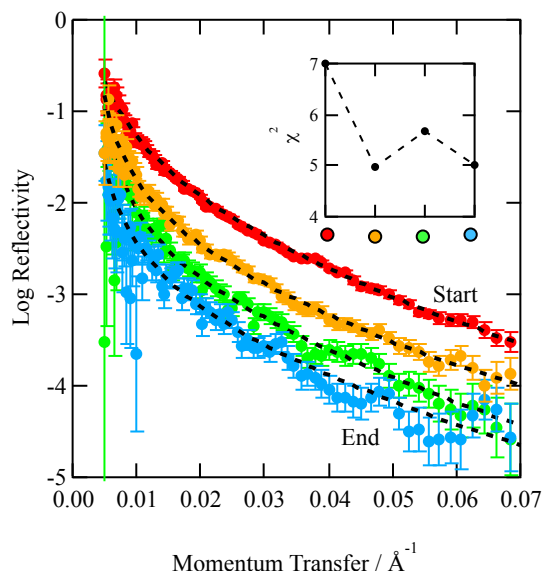


Figure 7. The bilayer at the silica-water interface simulated as a one-layer system. The simulated fits are overlaid the experimental neutron reflection plots (dotted lines). The inserted graphic displays χ^2 for each depicted neutron reflection plot.

REFERENCES

- Alley, R.; Berntsen, T.; Bindoff, N.L.; Chen, Z.; Chidthaisong, A.; Friedlingstein, P.; Gregory, J.; Hegerl, G.; Heimann, M.; Hewitson, B.; Hoskins, B.; Joos, F.; Jouzel, J.; Kattsov, V.; Lohmann, U.; Manning, M.; Matsuno, T.; Molina, M.; Nicholls, N.; Overpeck, J.; Qin, D.; Raga, G.; Ramaswamy, V.; Ren, J.; Rusticucci, M.; Solomon, S.; Somerville, R.; Stocker, T. F.; Stott, P.; Stouffer, R. J.; Whetton, P. and Wood R. A. *Intergovernmental Panel on Climate Change*, **2007**.
- Toon O. B. and Pollack, J. B. *American Science*, **1980**, 86(3), 268-278.
- Andreaea M. O. and Rosenfeld D., *Earth Science Reviews*, **2008**, 89, 13-41.
- Charlson, R. J.; Seinfeld, J. H.; Nenes, A.; Kulmala, M.; Laaksonen A. and Facchini M. C., *Science*, **2001**, 292, 2025-2026.
- Rosenfeld, D.; Lohmann, U.; Raga, G. B.; O'Dowd, C. D.; Kulmala, M.; Fuzzi, S.; Reissell A. and Andreaea M. O., *Science*, **2008**, 321, 1309-1313.
- Breon, F. M.; Tanre D. and Generoso, S. *Science*, **2002**, 295, 834-839.
- Stocker, T. F.; Qin D. and Plattner, G. K. *Intergovernmental Panel on Climate Change*, **2013**.
- Tervahattu, H.; Hartonen, K.; Kerminen, V.; Kupiainen, K.; Aarnio, P.; Koskentalo, T.; Tuck A. and Vaida, V. *Journal of Geophysical Research*, **2002**, 107, 1-7.
- Gill, P.S.; Graedel T. E. and Weschler, C. J. *Review of Geophysics*, **1983**, 21, 903.
- McNeill, V. F.; Sareen N. and Schwier, V. *Atmospheric Aerosol Chemistry*, **2013**, 339, 201-259.
- Jones, S. H.; King M. D. and Ward, A. D. *Chemical Communications*, **2015**, 51, 4914-4917.
- Liu, P.; Zhang Y. and Martin, S. T. *Environmental Science and Technology*, **2013**, 47, 13594-13601.
- Davies, J. F.; Miles, R. E. H.; Haddrell A. E. and Reid, J. P. *Proceedings of the National. Acadamey of Sciences of the U.S.A.*, **2013**, 110, 8807-8812.
- Donaldson D. J. and Vaida, V. *Chemical Reviews*, **2006**, 106, 1445-1461.
- Ruehl C. R. and Wilson, K. R. *Journal of Physical Chemistry A*, **2014**, 118, 3952-3966.
- Nieto-Gligorovski, L.; Net, S.; Gligorovski, S.; Zetzsch, C.; Jammoul, A.; D'Anna B. and George, C. *Physical Chemistry Chemical Physics*, **2008**, 10, 2964-2971.
- Eliason, T. L.; Gilman J. B. and Vaida, V. *Atmospheric Environment*, **2004**, 38, 1367-1378.
- T. L. Eliason, S. Aloisio, D. J. Donaldson, D. J. Cziczco and V. Vaida, *Atmos. Environ.*, **2003**, **37**, 2207-2219.
- L. F. Voss, M. F. Bazerbashi, C. P. Beekman, C. M. Hadad and H. C. Allen, *J. Geophys. Res. Atmos.*, **2007**, **112**, 1-9.
- M. D. King, A. R. Rennie, K. C. Thompson, F. N. Fisher, C. C. Dong, R. K. Thomas, C. Pfrang and A. V Hughes, *Phys. Chem. Chem. Phys.*, **2009**, **11**, 7699-7707.
- C. Pfrang, F. Sebastiani, C. O. M. Lucas, M. D. King, I. D. Hoare, D. Chang and R. A. Campbell, *Phys. Chem. Chem. Phys.*, **2014**, **16**, 13220-13228.
- Jones, S. H.; King, M. D.; Ward, A. D.; Rennie, A. R.; Jones A. C. and Arnold, T. *Atmospheric Environment*, **2017**, 161, 274-287.
- Penfold, J. and Thomas, R. K. *Journal of Physics and Condensed Matter*, **1990**, 2, 1369-1412.
- Lu, J. R.; Thomas R. K. and Penfold, J. *Advanced Colloid Interface Science*, **2000**, 84, 143-304.
- Cwiertny, D. M.; Young M. A. and Grassian, V. H. *Annual Review of Physical Chemistry*, **2008**, 59, 27-51.
- Dupart, Y.; King, S. M.; Nekat, B.; Nowak, A.; Wiedensohler, A.; Herrmann, H.; David, G.; Thomas, B.; Miffre, A.; Rairoux, P.; D'Anna B. and George, C. *Proceedings of the National Academy of Science of the U.S.A.*, **2012**, 109, 20842-20847.
- Falkovich, A. H.; Schkolnik, G.; Ganor E. and Rudich, Y. *Journal of Geophysical Research*, **2004**, 109, 1-19.
- Ciuraru, R.; Fine, L.; Van Pinxteren, M.; D'Anna, B.; Herrmann, H. and George, C. *Scientific Reports*, **2015**, 5, 12741.
- Marty, J. C.; Saliot, A.; Buat-Ménard, P.; Chesselet R. and Hunter, K. A. *Journal of Geophysical Research Oceans*, **1979**, 84, 5707-5716.
- Wadia, Y.; Tobias, D. J.; Stafford R. and Finlayson-Pitts, B. J. *Langmuir*, **2003**, 16, 9321-9330.
- Thompson, K. C.; Rennie, A. R.; King, M. D.; Hardman, S. J. O.; Lucas, C. O. M.; Pfrang, C.; Hughes, B. R. and Hughes, A. V. *Langmuir*, **2010**, 26, 17295-17303.
- Thompson, K. C.; Jones, S. H.; Rennie, A. R.; King, M. D.; Ward, A. D.; Hughes, B. R.; Lucas, C. O. M.; Campbell, R. A. and Hughes, A. V. *Langmuir*, **2013**, 29, 4594-4602.
- Cappa, C. D.; Che, D. L.; Kessler, S. H.; Kroll, J. H. and Wilson, K. R. *Journal of Geophysical Research Atmospheres*, **2011**, 116, 1-12.
- Nah, T.; Kessler, S. H.; Daumit, K. E.; Kroll, J. H.; Leone, S. R. and Wilson, K. R. *Physical Chemistry Chemical Physics*, **2013**, 15, 18649-18663.
- Slade, J. H. and Knopf, D. A. *Geophysical Research Letters*, **2014**, 41, 5297-5306.
- Charleski, R. C.; Zhang, Y.; Troya, D. and Morris, J. R. *Chemical Society Reviews*, **2016**, 45, 3731-3746.
- Ruehl, C. R.; Nah, T.; Isaacman, G.; Worton, D. R.; Chan, A. W. H.; Kolesar, K. R.; Cappa, C. D.; Goldstein, A. H. and Wilson, K. R. *Journal of Physical Chemistry A*, **2013**, 117, 3990-4000.
- Kolesar, K. R.; Buffaloe, G.; Wilson, K. R. and Cappa, C. D. *Environmental Scientific Technology*, **2014**, 48, 3196-3202.
- Slade J. H. and Knopf, D. A. *Physical Chemistry Chemical Physics*, **2013**, 15, 5898-5915.
- Nah, T.; Kessler, S. H.; Daumit, K. E.; Kroll, J. H.; Leone, S. R. and Wilson, K. R. *Journal of Physical Chemistry A*, **2014**, 118, 4106-4119.
- Vlasenko, A.; George, I. J. and Abbatt, J. P. D. *Journal of Physical Chemistry A*, **2008**, 112, 1552-1560.
- George, I. J.; Vlasenko, A.; Slowik, J. G. and Abbatt, J. P. D. *Atmospheric Chemistry and Physics*, **2007**, 7, 6803-6842.
- Atkinson, R. *Atmospheric Environment*, **2000**, 34, 2063-2101.
- Smith, J. D.; Kroll, J. H.; Cappa, C. D.; Che, D. L.; Liu, C. L.; Ahmed, M.; Leone, S. R.; Worsnop, D. R. and Wilson, K. R. *Atmospheric Chemistry and Physics*, **2009**, 9, 3209-3222.
- Atkinson, R.; Arey, J. and Aschmann, S. M. *Atmospheric Environment*, **2008**, 42, 5859-5871.
- Karagulian, F.; Dilbeck, C. W. and Finlayson-Pitts, B. J. *Journal of American Chemical Society*, **2008**, 130, 11272-11273.

- 47 Dilbeck, C. W. and Finlayson-Pitts, B. J. *Physical Chemistry Chemical Physics*, **2013**, 15, 9833-9844.
- 48 Koenig, B. W.; Krueger, S.; Orts, W. J.; Majkrzak, C. F.; Berk, N. F.; Silverton, J. V.; Gawrisch, K.; Koenig, B. W.; Krueger, S.; Orts, W. J.; Majkrzak, C. F.; Berk, N. F.; Silverton, J. V. and Gawrisch, K. *Langmuir*, **1996**, 12, 1343-1350.
- 49 Smith, H. L.; Howland, M. C.; Szmodis, A. W.; Qijuan, L.; Daemen, L. L.; Parikh, A. N. and Majewski, J. *Journal of American Chemistry Society*, **2009**, 131, 3631-3638.
- 50 Charitat, T.; Bellet-Amalric, E.; Fragneto, G. and Graner, F. *The European Physical Journal B*, **1999**, 8, 583-593.
- 51 Brian, A. A. and McConnell, H. M. *Proceedings of the National Academy of Science of the U.S.A.*, **1984**, 81, 6159-6163.
- 52 Rennie, A. R.; Hellsing, M. S.; Lindholm, E. and Olsson, A. *Review of Scientific Instruments*, **2015**, 86, 1-3.
- 53 Koutsoubas, A. *Journal of Physical Chemistry B*, **2016**, 120, 11474-11483.
- 54 Naumann, C.; Brumm, T.; Rennie, A. R.; Penfold, J. and Bayerl, T. M. *Langmuir*, **1996**, 11, 3948-3952.
- 55 Bayerl, T. M.; Thomas, R. K.; Penfold, J.; Rennie, A. R. and Sackmann, E. *Biophysical Journal*, **1990**, 57, 1095-1098.
- 56 Yu, X. Y. and Barker, J. R. *Journal of Physical Chemistry A*, **2003**, 107, 1313-1324.
- 57 Press, W. H.; Teukolsky, S. A.; Vetterling, W. T. and Flannery, B. P. *Cambridge University Press*, **2007**.
- 58 Chu, L. and Anastasio, C. *Journal of Physical Chemistry A*, **2005**, 109, 6264-6271.
- 59 Laidler, K. J. *Harper-Collins*, **1987**.
- 60 Herrmann, H.; Hoffmann, D.; Schaefer, T.; Bräuer, P. and Tilgner, A. *ChemPhysChem*, **2010**, 11, 3796-3822.
- 61 McNamee, C. E.; Kappl, M.; Butt, H. J.; Higashitani, K. and Graf, K. *Langmuir*, **2010**, 26, 14574-14581.
- 62 Whalley, L. K.; Stone, D.; George, I. J.; Mertes, S.; Van Pinxteren, D.; Tilgner, A.; Herrmann, H.; Evans, M. J. and Heard, D. E. *Atmospheric Chemistry and Physics*, **2015**, 15, 3289-3301.
- 63 Knopf, D. A.; Forrester, S. M. and Slade, J. H. *Physical Chemistry Chemical Physics*, **2011**, 13, 21050-21062.
- 64 Bejan, I.; Barnes, I.; Olariu, R.; Zhou, S.; Wiesena, P. and Bentera, T. *Physical Chemistry Chemical Physics*, **2007**, 9, 5686-5692.

Critical Evaluation

The work presented in the thesis uses optical trapping techniques as well as neutron and x-ray reflectivity to study atmospheric aerosols and thin films that form upon atmospheric aerosols or cloud droplets. The aim of the work presented was to understand the aerosol optical and chemical properties in terms of refractive index and thickness of thin films. Additionally, change in the aerosol or aerosol thin films were monitored upon exposure to atmospheric oxidants. Atmospheric and climate theoretical scientists can use the results presented in the thesis to further current understanding on how atmospheric aerosols affect climate. Examples of theoretical scientists using data similar to the data presented in this thesis includes work conducted by (a) Bellouin et al. (2011) who investigated aerosol forcing by applying refractive index values for seasalt, fossil fuel black carbon, biomass burning and mineral dust in the model HadGEM2-ES and (b) Anttila et al. (2006) who studied the reactive uptake of gaseous compounds by organic-coated aqueous aerosols. Anttila et al. (2006) applied a variation of the resistor model to account for the mechanism which layered organic coatings may slow the reactive uptake by aqueous aerosols; such a study required knowledge of film thickness.

3.1. Optical Trapping

Optical trapping applied simultaneously with Mie spectroscopy was used to determine the refractive index and radius of optically trapped aerosols. Three papers were written based on the optical trapping technique, and the papers are discussed in turn in the following section.

3.1.1. Evaluation of Paper 1: Mie scattering from optically levitated mixed sulfuric acid-silica core-shell aerosols: confirmation of core-shell morphology for atmospheric science

In Paper 1, optically trapping was successfully applied simultaneously with Mie spectroscopy to follow the formation of a thin film of sulfuric acid upon a silica core particle resulting in the creation of a core-shell morphology aerosol. Prior to film formation, the refractive index and

Critical Evaluation

radius of the core particle silica was determined, as well as the refractive index of optically trapped sulfuric acid droplets. Once the core and shell material had been characterised individually, a core-shell morphology aerosol was formed and the change in refractive index and radius during core-shell formation followed by continuously collecting Mie spectra throughout.

To determine the refractive index of the sulfuric acid droplets, the experimentally obtained Mie spectrum was compared to a computer-simulated spectrum. To obtain an accurate simulated Mie spectrum, several steps were employed. Firstly, the radius of the droplet was held constant whilst the three empirical Cauchy coefficients (A , B and C) were adjusted until a good fit was obtained. Then, the radius was iterated and the three Cauchy coefficients varied again until a fit between experimental and simulated data was obtained. For each new fit, the least squares fitting residual was calculated. The described process was repeated until a global minimum in the least squares fitting residual was observed. The method applied was able to determine the refractive index to ± 0.001 and radius to $\pm 0.005 \mu\text{m}$. A more detailed method of determining an accurate fit between the experimental and simulated Mie spectra would be to change the radius of the droplet as well as the three Cauchy coefficients, however such a technique is computer intensive and would not be practical when analysing a small number of Mie spectra; it remains an aim for future work. The iterative fit was determined to be an accurate method of determining the radius and refractive index of optically trapped sulfuric acid droplets owing to excellent fits obtained between experimental and simulated data.

Determining the refractive index of sulfuric acid droplets demonstrated that the concentration of all aqueous sulfuric acid droplets would be approximately the same despite the starting concentration of the sulfuric acid droplet. The phenomenon has been attributed to the sulfuric acid to water ratio being controlled by the local relative humidity of the aqueous droplet: in essence water evaporated from the droplet to maintain equilibrium with the

Critical Evaluation

surrounding microenvironment. From the observation, it was assumed that a sulfuric acid film would have the same concentration as the optically trapped aqueous sulfuric acid droplets.

The iterative fitting process could not be applied to the silica Mie spectra, because the optically trapped silica particles produced Mie spectra that contained noticeably fewer Mie resonances in comparison to the Mie spectra produced by sulfuric acid. A good fit between the experimentally obtained Mie spectra and the simulated Mie spectra was determined by eye, through manually adjusting the three Cauchy coefficients and particle radius. A larger silica particle or a particle with a higher refractive index would of provided a Mie spectrum containing more Mie resonances; however changing the core aerosol would of altered the atmospheric relevance of the study.

Having characterised the core and shell material, a core-shell morphology silica-sulfuric acid system was formed through colliding an optically trapped silica particle with sulfuric acid droplets. Mie spectra were collected throughout the film forming process, when a sulfuric acid droplet collided with the optically trapped silica particle a jump in the Mie spectra was observed. Figure 3 in Paper 1 depicts the change in Mie spectra for a silica particle as a film of sulfuric acid develops. The film thickness was determined by comparing the Mie resonances observed in the experimentally collected Mie spectra to simulated core-shell Mie spectra. The uncertainty in film thickness was $\pm 0.005 \mu\text{m}$.

The method applied to determine the film thickness assumed that the film of sulfuric acid was symmetrical around the core particle silica. If a very thick film of sulfuric acid had formed then it would have been possible for the core particle to be displaced from the centre of the film material. As explained by Kaiser et al. (1996), a core particle will be displaced if the densities between the core and shell material are different: a difference in density may cause each material to experience the force applied from the optics differently. Figure 1.6b depicts a potential geometry of the core-shell aerosol resulting from such an effect. The film of sulfuric acid reached a maximum thickness of $0.263 \mu\text{m}$, whilst the radius of the silica particle was $0.965 \mu\text{m}$. The thickness

Critical Evaluation

of the sulfuric acid film is small in comparison to the radius of the silica particle and hence core particle displacement is unlikely.

A third morphology composition is for the sulfuric acid to form lenses on the surface of the silica particle e.g. Reid et al. (2011), as depicted in Figure 1.6 image (c). The study of sulfuric acid droplets colliding with polystyrene outlined in section 3.4 in Paper 1 demonstrated a lens formation system, allowing the possibility that sulfuric acid formed a lens geometry aerosol upon collision with the optically trapped silica particle. From following the change in Mie spectra as sulfuric acid droplets collided with the polystyrene particle, a loss in number in Mie resonances was observed. Contrastingly, an increase in number of resonances was observed when sulfuric acid collided with a silica particle.

Additionally two other core particles, titania and alumina, were studied. Titania and alumina are two other mineral dust aerosol found in the stratosphere. However, upon optically trapping it was discovered that the refractive index of the two mineral dust particles lay below the expected refractive index. The refractive index was thought to be low owing to a low mass density resulting from the method of manufacture. Owing to the two mineral dust particles not representing mineral dust accurately it was decided to not pursue the study of sulfuric acid films forming on the mineral dust further.

3.1.2. Evaluation of Paper 2: Following the refractive index of squalene droplets during oxidative ageing

Paper 2 followed the change in refractive index of squalene, a naturally occurring atmospheric aerosol, upon exposure to 0.4 ppm ozone. The refractive index of squalene was determined prior, during and after oxidation.

A high number of Mie resonances was observed in all squalene Mie spectra, and hence the iterative least squares residual fitting procedure described in section 2.1.3.3 could be applied. Uncertainty in the refractive index was determined to be ± 0.0026 in Paper 2, whilst the uncertainty in Paper 1 (which used the same fitting procedure) was

Critical Evaluation

determined to be ± 0.001 . Paper 1 had a greater number of resonances per wavelength and hence a reduced uncertainty. In addition, owing to the oxidation sensitivity of squalene the refractive index of six newly trapped squalene droplets varied by 0.01 resulting in a small increase in uncertainty values. Additional offline experiments had to be conducted on a differential refractometer to determine whether the refractive index values determined by Mie spectroscopy for newly trapped squalene droplets lay within a realistic range, and as depicted by Figure 2 in Paper 2, the refractive index values do lie well within the calculated realistic range.

The optically trapped squalene droplets were exposed to ozone at the concentration of 0.4 ppm, and the change in Mie spectra continuously followed by collecting a spectra every three seconds. Owing to time constraints, a detailed fit was executed for a number of Mie spectra collected throughout the reaction by applying the iterative least squares residual fitting procedure, whilst the remainder spectra were fitted by eye through manually adjusting the three Cauchy coefficients and droplet radius. As a comparison, a simpler method of changing the Cauchy coefficient A and radius only was applied to the remainder spectra, but it was observed that the method prevented the remaining spectra from achieving the refractive index and radius values of the iterative fitted spectra and hence was not used.

Figures 3 and 5 in Paper 2 illustrates the overall refractive index increasing, whilst the radius decreases when squalene reacts with ozone or oxygen. Upon reaction with ozone, the composition of the optically trapped droplets will alter resulting in a change in refractive index: an increase in refractive index may occur from the oxidation causing a change in density of the optically trapped droplet. The density was observed to increase by 0.163 g mol^{-1} when a squalene droplet was exposed to ozone. Contrastingly, a decrease in radius was observed upon squalene reacting with ozone. A decrease in radius is most likely caused by the production of volatile by-products during the oxidation reaction that subsequently evaporate from the droplet.

3.1.3. Evaluation of Paper 3: Determination of the refractive index of insoluble organic material from atmospheric aerosol over the visible wavelength range using optical tweezers

In Paper 3, optical trapping was successfully applied to levitate aerosol extract sourced from the atmosphere and of humic acid salts. Extracts from atmospheric aerosol were collected from three aerosol sources: the campus of Royal Holloway, University of London was used to represent urban aerosol, whilst aerosol extracted from Antarctica was described as remote aerosol. In addition, aerosol was extracted from the smoke plume of a flaming fire.

Upon trapping, Mie spectroscopy was employed to determine the refractive index for the three aerosol samples extracted from the environment as well as commercially sourced humic acid. Owing to limited atmospheric aerosol extracts, small droplets (with a radius of approximately $0.6\ \mu\text{m}$) were optically trapped and consequently the collected Mie spectra had only a few Mie resonances. Theoretical fits of the Mie spectra were simulated by manually adjusting the Cauchy coefficients A, B and C and the radius until a good fit between simulated and experimental spectra was determined by-eye. Contrastingly, humic acid was sourced commercially and consequently there was plenty of sample available. Large aqueous humic acid droplets were optically trapped and the collected Mie spectra depicted a high number of resonances. The iterative least squares residual fitting procedure could be applied. The by-eye fitting procedure resulted in an uncertainty of ± 0.015 for the refractive index in comparison to an uncertainty of ± 0.001 (from Paper 1) in the refractive index when the iterative least squares residual fitting procedure was applied.

In addition, UV-VIS spectra for all samples studied in the paper were obtained and for the highly absorbing aerosol extract the absorption Ångström exponent and imaginary refractive index calculated. The method of calculating the absorption Ångström exponent is well documented in literature Chakrabarty et al. (2010) and Schuster et al. (2016), however again owing to the lack of Mie resonances in the atmospheric aerosol extracts Mie spectra, the

Critical Evaluation

absorption Ångstrom exponent determined ought to be used as a guideline value only.

In addition, the imaginary refractive index of the atmospheric aerosol extracts was determined from UV-VIS spectra using equations sourced from literature e.g. Liu (2015). The imaginary refractive index determined in the study presented lies between the refractive index of biomass burning aerosols as determined by Guyon et al. (2003) and brown carbon found in tar balls e.g. Chakrabarty et al. (2010). The humic acid aerosol used in the study was dissolved in water and consequently the imaginary refractive indices of the humic acid aqueous aerosol and the wood smoke aerosol extracts could not be directly compared.

Another limitation of the work depicted in the paper is the limited amount of atmospheric aerosol extracts. The Mie spectra for the atmospheric aerosol extracts only demonstrate a few Mie resonances and hence their Mie spectra had to be simulated by carrying out a by-eye fitting procedure.

In order to collect more atmospheric aerosol extracts, either an air pump with larger pre-combusted filters or higher flow rate could be used; either method would require additionally equipment that was unfortunately unavailable for the study presented. The wood smoke aerosol extract was the only aerosol extract that could be collected from a plentiful supply. However, the aerosol extract collection was the first attempt at such a collection and the filter became overloaded owing to the sampling point being placed too close to the fire; to resolve the problem a long chimney (i.e. over 1 m) could be used. Additionally, collecting aerosol from different sites along the chimney would allow an analysis of how the aerosols reactivity with oxidants changes with time.

3.1.4. Future work based on optical trapping experiments

Future work in the research field ought to involve further experiments based upon core-shell systems. Future work could firstly focus on the characterisation of static core-shell systems in terms of refractive index and film thickness. The work presented has

Critical Evaluation

successfully demonstrated the characterisation of a film of sulfuric acid on a silica core particle, however one example of future work is to increase the complexity of the system by forming a thin film comprising of two or more different compounds. The atmosphere is a chemically complex environment and it is highly unlikely that atmospheric aerosols consist of pure compounds. Forming a film consisting of extracts sourced from atmospheric aerosol (such as those described in Paper 3) on a mineral aerosol like silica is a possible idea for a future experiment, however the method of extracting atmospheric aerosol would need to be altered as more material would likely be required. Collecting aerosol extracts from other environments such as from forests, the middle of the ocean and perhaps the top of mountains would provide an interesting insight into how aerosol source affects aerosol chemistry. To improve aerosol extract sampling, the following sampling restrictions could be applied: (a) shorter filter sampling times to prevent or reduce aerosol oxidation once collected, (b) the use of denuders to address the same problem and (c) apply size selection of the aerosol with visual impactors.

Another avenue to explore for core-shell systems would be to investigate alternative core-shell morphologies; it is highly unlikely that atmospheric aerosol would be core-shell owing to the irregularity of core aerosol shapes. As described in section 3.1.1 other aerosol morphologies for mix-phase aerosols include lens formation or core-aerosol displacement. However, Mie theory requires a spherical system and therefore at the moment such experiments are not possible. A liquid-liquid core-shell morphology aerosol would provide a spherical system, however there are several problems preventing such a morphology from being created. For example, one problem is that the core and shell material would need to be selected such that they do not mix.

The thesis presented studied the consequence of atmospheric aerosol being exposed to the atmospheric oxidant ozone. As observed in Paper 2, upon exposure to ozone the refractive index and radius of the atmospheric aerosol squalene altered dramatically providing new

Critical Evaluation

detail upon the change in refractive index and aerosol radius of a reacting aerosol. Understanding the changes in chemical and physical properties of an atmospheric aerosol upon exposure to atmospheric oxidants is paramount for accurate climate modelling. Future work in the research field should concentrate on furthering current understanding of other oxidising systems. Such an experiment could follow on from the work presented in Paper 3, by studying the oxidisation of the atmospheric aerosol extracts.

Additionally, experiments could begin to explore the effects of exposing a core-shell morphology aerosol to atmospheric oxidants. It is expected that the film would alter in chemical composition and thickness, thus causing a change in refractive index. Such experiments could consider whether it would be possible to remove the film entirely by exposing the film to atmospheric oxidants. For such experiments, a core particle that does not oxidise would be required for initial experiments (until the oxidisation of the film is fully understood). Following the change in film thickness would also allow the kinetics of the oxidation of the film to be determined as well as the film's atmospheric lifetime.

Through studying the oxidation of core-shell morphology aerosols, a direct link between the optical trapping and neutron and x-ray reflectivity based work presented in the thesis would be made.

3.1.5. Summary on work based on optical trapping

Through applying optical trapping techniques, laboratory generated aerosols and aerosol extracts sourced from the atmosphere were optically levitated and studied by applying Mie spectroscopy simultaneously. The wavelength dependent refractive index and radius of the trapped aerosol were accurately determined. Additionally Mie spectroscopy was successfully applied to follow the change in refractive index and radius upon core-shell morphology formation and oxidation of a trapped aerosol. Future work in the research field could follow on from the work presented by studying the oxidation of a core-shell morphology aerosol.

3.2. Neutron and x-ray scattering

Neutron and x-ray reflectivity techniques were applied to study thin films at the air-water or silica-water interface. Two papers were written from experiments conducted at ISIS - a source of neutrons, whilst a third paper was written based on an experiment that used x-ray reflectivity.

3.2.1. Evaluation of Paper 4: Gas-phase OH radical oxidation of an organic film at the air-water interface using material extracted from urban, remote and wood smoke aerosol

Neutron reflectometry has been used to study thin films composed of atmospheric aerosol extract at the air-water interface. Extracts categorised as urban extracts were collected from the campus of Royal Holloway, University of London, whilst remote extracts were collected from Antarctica. Additionally, aerosol extracts from the smoke plume of a flaming fire were collected. The three aerosol extracts were all observed to be stable at the air-water interface.

Each film was characterised in terms of neutron scattering length density and film thickness. The neutron scattering length density for the urban and remote aerosol extracts both lay below $1 \times 10^{-6} \text{ \AA}^{-2}$, whilst the aerosol extracted from wood smoke had a much higher scattering length density of almost $2 \times 10^{-6} \text{ \AA}^{-2}$. The composition of the aerosol extracts was not known, and hence to try and determine possible constituents of the extracts the neutron scattering length density was compared to neutron scattering length densities of well-studied compounds. Through running a process of elimination it was concluded that the urban and remote aerosols might be similar in composition to organic compounds containing a small amount of oxygen, phosphorous and nitrogen atoms, whilst the composition of wood smoke aerosol extracts might be similar to polymers, for example cellulose.

The thickness of the atmospheric aerosol extract thin films studied was determined to not exceed 19 \AA , much thinner than the film thickness used in optical trapping experiments (263 nm). In the

Critical Evaluation

absence of other data sources the film thickness could be used in atmospheric modelling.

In addition to aerosol extracts, the organic content of Antarctic seawater was analysed at the air-water interface. The neutron scattering length density and film thickness are slightly higher than the values obtained for aerosol extracts sourced from Antarctica. Understanding seawater extracts is essential for understanding marine aerosol owing to the sea-surface microlayer acting as a source of atmospheric aerosol e.g. Blanchard et al. (1964), Blanchard and Woodcock (1957) and Donaldson and George (2012).

The study moved onto studying the change in the thin-films when exposed to the atmospheric oxidant, gas-phase OH radicals. Continuous collection of neutron reflectivity profiles allowed the alteration in the film upon exposure to OH radicals to be monitored throughout. For each atmospheric aerosol extract thin film exposed to OH radicals, a plot of $\frac{\rho_t \delta_t}{\rho_{t=0} \delta_{t=0}}$ as a function of time depicted the decay profile. In the plot, ρ represents scattering length density and δ film thickness. Results showed that the thin films were susceptible to gas-phase OH radical oxidation. For all atmospheric aerosol extracts, the decay profile could be fitted to an exponential decay of the form e^{-kt} , demonstrating first-order loss.

Kinetic analysis of the possible reaction steps allowed the concentration of the OH radicals to be determined, and thus a bimolecular rate constant for the reaction between atmospheric aerosol extract thin films and OH radicals to be calculated. The bimolecular rate constant showed that OH radical attack was quickest for extracts sourced from urban environments, whilst aerosol extracts from a remote environment were slowest. It ought to be noted that the differences between bimolecular rate constants are only marginal. Other techniques that could of helped determine the exact mechanism of degradation includes gas-chromatography analysis, the technique would of allowed the chemical composition of the film at the air-water interface to be determined.

Critical Evaluation

Once the bimolecular rate constant was calculated, the lifetime of the film could be determined. The concentration of atmospheric OH radicals was used to allow the lifetime of the aerosol extract in the atmosphere to be determined. The lifetime of the atmospheric aerosol extracts was determined to be on the timescale of minutes. The lifetime is relatively short in comparison to the typical lifetime of an aerosol in the troposphere (days) and hence determining the presence of atmospheric aerosol thin films in the atmosphere may be difficult because of their short lifetime.

Formation of the OH radicals in the study presented required oxygen to pass into an ozoniser and then into an enclosed environment where the ozone gas was exposed to UV light. Two reaction blanks were carried out where either the ozoniser or UV light was switched off. When the ozoniser was switched off, a plot of $\frac{\rho_t \delta_t}{\rho_{t=0} \delta_{t=0}}$ as a function of time demonstrated a decay, indicating that oxygen will convert into OH radicals that will react with the thin film present. It ought to be noted that the decay was not as fast as when the ozoniser was switched on, indicating that not as high an OH radical concentration was present.

Interestingly, the second reaction blank required the UV light to be switched off. The thin film was subsequently exposed to ozone gas only. A plot of $\frac{\rho_t \delta_t}{\rho_{t=0} \delta_{t=0}}$ as a function of time did not show a decay at all, indicating that the composition of the thin film at the air-water interface may consist of saturated molecules.

To compare the alteration of the atmospheric aerosol thin films when exposed to OH radicals, a possible atmospheric aerosol proxy was chosen. Lipids have frequently been used as atmospheric aerosol proxies, as shown in the work conducted by Smith et al. (2002) and Jones et al. (2015). Hence the lipid 1,2-distearoyl-sn-glycero-3-phosphocholine (DSPC) was used in the study presented. A layer of DSPC at the air-water interface was characterised in terms of neutron scattering length density and film thickness. Owing to extensive work having already concentrated on the structure and neutron scattering length density of DSPC at the air-water interface e.g. Dabkowska et al. (2013) and Hollinshead et al. (2009), DSPC was studied as a two layer

Critical Evaluation

system with a head-group layer and a tail-group layer. DSPC could have been studied as a monolayer, however to harmonise with other work presented in the thesis, DSPC was studied as a two-layer system.

DSPC films were subsequently exposed to gas-phase OH radicals of the same concentration as the OH radicals that were exposed to the atmospheric aerosol extract thin films. Again, a plot of $\frac{\rho_t \delta_t}{\rho_{t=0} \delta_{t=0}}$ as a function of time depicted the decay profile. However, unlike atmospheric aerosol extracts, the decay was not an exponential decay. The decay could be fitted to a multi-step degradation mechanism comprising of ten different steps. An analysis of the number of steps and the weighting (i.e. the contribution) of each step demonstrated that ten steps were required, with the first few steps having a high weighting parameter. The determined degradation mechanism demonstrated a fast initial step, followed by a number of successive slow steps before completing the reaction by a number of quick steps.

The difference in decay profiles for the atmospheric aerosol extracts and the lipid DSPC demonstrates that the atmospheric aerosol extracts are likely not composed of lipid molecules, and consequently a lipid may not be the best representative molecule for atmospheric aerosol. Owing to DSPC being an unlikely atmospheric aerosol proxy, repeating the experiment to validate the proposed reaction mechanism is not necessary.

3.2.2. Evaluation of Paper 5: The reaction between gas-phase OH radicals and organic films extracted from atmospheric aerosol at the air-water interface: an x-ray reflectivity and atmospheric lifetime study

In a separate study, x-ray reflectivity was applied to study thin films of atmospheric aerosol extracts at the air-water interface. As in Paper 4, aerosol collected from the campus of Royal Holloway, University of London was categorised as urban aerosol, whilst aerosol collected from Antarctica was categorised as remote aerosol. Both aerosol extracts were categorised as stable at the air-water interface.

Critical Evaluation

The thin films were characterised in terms of x-ray scattering length density and film thickness. Owing to x-ray beams being sensitive to electrons, the reflectivity profiles were much stronger than the neutron reflectivity profiles determined in Paper 4. Hence, fringes could be recognised in the reflectivity profiles, which helped aid the structure of the thin film to be determined.

The x-ray reflectivity profiles were accurately simulated with a two-layer model, with the layer closest to the air interface having a much lower x-ray scattering length density than the layer closest to the water interface for both urban and remote thin films. The total film thickness for urban thin films at the air-water interface is much thicker than determined in Paper 4, and could be because of either (a) more material added to the interface or (b) the sample becoming more concentrated. The work outlined in Paper 5 was conducted after the work in Paper 4 was completed; however the same samples were used. Each time the sample flask was opened solvent may have evaporated off leaving behind a slightly more concentrated sample.

As in paper 4, the atmospheric aerosol thin films were exposed to gas-phase OH radicals. Continuous collection of x-ray reflection profiles allowed a plot of $\frac{\rho_t \delta_t}{\rho_{t=0} \delta_{t=0}}$ as a function of time to be drawn, depicting the alteration of the film upon exposure to the oxidants. As with Paper 4, the film was shown to decay exponentially and could be fitted to a curve of the form e^{-kt} .

From the exponential fit, the bimolecular rate constant could be determined. Again, as with Paper 4, the bimolecular constant was highest for films composed of aerosol extracts sourced from urban environments in comparison to films composed of aerosol extracts sourced from remote environments.

Once the bimolecular constant was determined, the lifetime of the atmospheric aerosol extract films was determined. A concentration of atmospheric OH radicals was used in the calculation. As with Paper 4, the lifetime of the atmospheric aerosol extract films was on the timescale of minutes. Again, the lifetime is relatively short to the lifetime of tropospheric aerosols (days) and hence studying thin films in

Critical Evaluation

situ in the atmosphere may be consequently difficult. The lifetime of remote atmospheric aerosol extracts is comparatively short to urban atmospheric aerosol extracts. Air that reaches Antarctica has more than likely travelled the world, and hence the material has had a long time to oxidise and may have undergone chemical ageing already. The aerosol may not be as chemically complex as “fresh” urban aerosol and therefore the oxidation reaction may not be as complex and hence may be quicker.

Similarly to Paper 4, the UV experimental blank investigation was carried out. Without UV light present the OH radicals could not be formed and hence the atmospheric aerosol extract films were exposed to ozone only. As in Paper 4, the atmospheric aerosol extract films did not demonstrate a change upon exposure to ozone, indicating that the urban and remote aerosol extract did not contain unsaturated material.

3.2.3. Evaluation of Paper 6: Oxidation of a bilayer of DPPC on a mineral interface by aqueous-phase OH radicals to replicate atmospheric aerosol behavior

Neutron reflectivity was applied to study the aqueous phase OH radical oxidation of a proxy atmospheric aerosol thin film at the silica-water interface. The silica-water interface represented an aqueous mineral aerosol. A bilayer of the deuterated lipid 1,2-dipalmitoyl-sn-glycero-3-phosphocholine (DPPC) was formed at the interface. From the neutron reflection profiles, the bilayer could be characterised in terms of layer thickness and layer neutron scattering length density. DPPC has featured in numerous neutron reflection studies, and hence the neutron scattering length density and thickness of each layer of the bilayer is well known. Through applying values from literature and adjusting the solvent penetration percentage, an accurate simulation of the experimental neutron reflection profile could be obtained. The bilayer was simulated as a three-layer system consisting of head-tail-head layers.

The bilayer was exposed to aqueous-phase OH radicals at a concentration of $2.3 \times 10^{-12} \text{ mol dm}^{-3}$. In Papers 4 and 5, the

Critical Evaluation

concentration of gas-phase OH radicals was on a magnitude of 10^{-6} mol dm^{-3} . The difference in OH radical concentration reflects the atmospheric levels of the oxidant in the phase in which the oxidant was used.

During the oxidation of the lipid bilayer, the alteration in neutron scattering length density and thickness was followed by continuously collecting neutron reflection profiles. Upon simulation of the neutron reflection profiles, a plot of $\frac{\rho_t \delta_t}{\rho_{t=0} \delta_{t=0}}$ as a function of time could be drawn. Owing to a bilayer of DPPC being best represented by a three-layer system, a plot of $\frac{\rho_t \delta_t}{\rho_{t=0} \delta_{t=0}}$ as a function of time was drawn for each layer.

The alteration in $\frac{\rho_t \delta_t}{\rho_{t=0} \delta_{t=0}}$ as a function of time could be simulated by a 7 to 9 step degradation step, with the weighting of the step decreasing by five percent each time. The aerosol extracts studied in Papers 4 and 5 demonstrated a different decay mechanism consisting of an exponential decay upon exposure to OH radicals. The difference in decay profiles between the aerosol extracts and the lipid bilayer indicates that the aerosol extracts collected from the atmosphere do not contain lipids.

Once the decay profile had been accurately simulated, the bimolecular rate constant could be calculated from the pseudo first-order rate constant. The lipid bilayers demonstrated a bimolecular rate constant on the magnitude of 10^{-12} $\text{cm}^3 \text{ molecule}^{-1} \text{ s}^{-1}$ and consequently a lifetime of hours. Contrastingly, Papers 4 and 5 that used gas-phase OH radicals demonstrated bimolecular rate constants on the magnitude of 10^{-10} $\text{cm}^3 \text{ molecule}^{-1} \text{ s}^{-1}$ and a lifetime on the magnitude of minutes. The difference between the three experiments reflects (a) the reactivity of the sample and (b) the ability of the reacted material to leave the interface. The difference in accessibility between the aerosol extracts and the lipid bilayer was predominantly governed by the lipid bilayer having a less reactive head layer (as the head layer is more oxidised than the tail layer) directly beside the aqueous phase.

Critical Evaluation

As with Papers 4 and 5, experimental blanks were carried out. The lipid bilayer did not demonstrate any alteration when exposed to only UV or only H_2O_2 (the two variables required to form OH radicals).

3.2.4. Future work for neutron and x-ray reflectivity experiments

Future works focused on studying thin films of atmospheric aerosol extracts at the air-water interface ought to explore further the structure and oxidation of the thin films upon exposure to atmospheric oxidants. Examples of such studies include (a) using techniques such as Fourier transform infrared spectroscopy attenuated total reflectance (FTIR-ATR) and Sum Frequency Generation (SFG) to probe the structure and orientation of the thin films at the air-water interface in greater detail and (b) using alternate atmospheric oxidants. Use of alternate oxidants is particularly important following the work that demonstrated ozone did not cause a change in the thin film at the air-water interfaces.

In addition, such studies could focus on collecting a lot more atmospheric aerosol extracts. A greater amount of atmospheric aerosol extracts would mean that a thin film could be formed in the Langmuir trough that had a surface tensiometer sensor. Consequently, the change in surface pressure for a thin film composed of atmospheric aerosol extracts could be followed as the film is exposed to atmospheric oxidants. Such information would provide additional evidence for the loss of material at the interface during the oxidation reaction.

Future work for the project based on studying the oxidation of DPPC bilayers at the silica-water interface could include conducting the same experiment on a x-ray reflectometer. As demonstrated between Papers 4 and 5, x-rays can be a more sensitive technique that may provide more detail on the structure of the system under study. Neutron reflectivity provided a method of easily following the oxidation of the three layers of the bilayer, however x-ray reflection may be able to add extra certainty when determining the decay profiles for each layer when the bilayer is exposed to the oxidant.

Furthermore, another method to study the head or tail layer in depth would be to use a DPPC lipid that has either the head or tail

Critical Evaluation

deuterated. The liquid subphase could then be contrast matched to the non-deuterated layer so when the film is exposed to an oxidant the change in either the head or tail layer could be easily followed.

The oxidation of DPPC bilayers at a silica-liquid interface could be important for biological or atmospheric systems. However, the experiments presented in Paper 6 were conducted in standard laboratory conditions: a temperature of 20° C and a pressure of 1 atm. Atmospheric conditions could be better replicated by decreasing the temperature of the reaction cell. The decay of the bilayer upon exposure to atmospheric oxidants could be studied at a number of temperatures between 20 and -60° C, though condensation onto the silica interface and potential freezing may add difficulties. It ought to be noted that changing the temperature of the Langmuir based experiments would be much trickier as the experimental environment is not so tightly enclosed.

3.2.5. Summary of experiments based on neutron and x-ray reflectivity

Application of neutron and x-ray reflectivity techniques allowed thin films composed of atmospheric aerosol extract to be characterised in terms of neutron or x-ray scattering length density and film thickness.

In addition, neutron and x-ray reflectivity techniques were additionally used to study the oxidation of atmospheric thin films at the air-water interface. Comparing the decay between the atmospheric aerosol extracts and the lipid DSPC, a potential proxy atmospheric aerosol, it was observed that the decay profiles were very different: atmospheric aerosol extracts demonstrated an exponential decay whilst DSPC demonstrated a degradation mechanism decay. The oxidation reaction between DSPC and OH radicals was found to proceed via a multi-step degradation mechanism. Owing to the difference in decay profiles, it was concluded that a lipid is not a good proxy atmospheric aerosol.

Running a kinetic analysis of the atmospheric aerosol extract decay allowed the atmospheric lifetime of the extract to be calculated. For thin films studied with neutron and x-ray reflectivity it was

Critical Evaluation

observed that the lifetime of the aerosol extracts would be on the timescale of minutes.

In a separate study, a lipid bilayer at the silica-liquid interface was additionally characterised in terms of neutron scattering length density, film thickness and film structure by applying neutron reflectivity. The alteration of the lipid bilayer DPPC upon exposure to OH radicals was studied by applying neutron reflection. Applying kinetic analysis to the oxidation reaction, it was discovered that the film had a lifetime on the scale of hours. Determination of atmospheric aerosol thin film is paramount for the accurate modelling of the atmosphere.

Critical Evaluation References

- Anttila et al. *Journal of Physical Chemistry A* **110**, 10435-10443 (2006).
- Bellouin N. et al., *Journal of Geophysical Research: Atmospheres* **116**(D20), 1-25 (2011).
- Blanchard D. C., *Science* **146**, 396–397 (1964).
- Blanchard D. C. and A. H. Woodcock, 1957. *Tellus* **9**(2), 145–158 (1957).
- Chakrabarty R. K. et al., *Atmospheric Chemistry and Physics* **10**(13), 6363–6370 (2010).
- Dabkowska A. P. et al., *Soft Matter* **9**(29), 7095–7105 (2013).
- Donaldson D. J. and C. George, *Environmental Science & Technology* **46**(19), 10385–89 (2012).
- Guyon P. et al., *Journal of Aerosol Science* **34**(7), 883–907 (2003).
- Hollinshead C. M. et al., *Langmuir* **25**(7), 4070–4077 (2009).
- Jones S. H., M. D. King, and A. D. Ward, *Chemical Communications* **51**(23), 4914-4917 (2015).
- Kaiser T., G. Roll, and G. Schweiger, *Applied Optics* **35**(30), 5918–5924 (1996).
- Liu P. F. et al, *Atmospheric Chemistry and Physics* **15**(3), 1435–1446 (2015).
- Reid J. P. et al., *Physical Chemistry Chemical Physics* **13**(34), 15559–15572 (2011).
- Schuster G. L. et al., *Atmospheric Chemistry and Physics* **16**(3), 1587–1602 (2016).
- Smith, G. D. et al., *Journal of Physical Chemistry A* **106**(35), 8085–8095 (2002).

Summary and Conclusion

Optical trapping and neutron and x-ray reflectometry were applied to study atmospheric aerosols. Both techniques were applied to study atmospheric aerosol extracts collected from the atmosphere of three different environments. From applying optical trapping techniques, the refractive index was observed to range from 1.450 to 1.588 at 589 nm for the different samples. In addition, the Ångstrom exponent and imaginary refractive index was determined for the absorbing samples.

The atmospheric aerosol extracts were additionally used to form thin films at the air-water interface. Through applying neutron and x-ray reflectometry it was observed that the extracts successfully formed thin films at the air-water interface with a film thickness that did not exceed 18.6 Å. Aerosol thin films could also be studied through applying optical trapping techniques: aqueous films of sulfuric acid collided with optically trapped silica aerosols representing possible systems in the upper troposphere and lower stratosphere. The sulfuric acid spread on the silica aerosol to form films 263 nm thick. Upon film formation, it was observed the optical properties began to represent the film material and not the core aerosol.

Both optical trapping and reflectometry techniques were applied to study the oxidative changes of atmospheric aerosols. In particular, optical trapping was applied to follow the refractive index and radius change of the atmospheric aerosol squalene, whilst neutron or x-ray reflectometry was applied to determine the lifetime of thin films at the air-water or silica-water interface: lifetime was on the scale of minutes to hours. Reflectometry experiments demonstrated that material extracted from the atmosphere is resistant to ozone oxidation; thereby suggesting that atmospheric aerosol may contain a high-saturated content.

To further the work outlined in the thesis, possible directions for future work includes (a) optically trapping the atmospheric aerosol extract and oxidising the trapped droplet with OH radicals (an interesting extension of such a project would be to see if the droplet would alter upon exposure to ozone.), (b) forming a core-shell system

Summary and Conclusion

with the atmospheric aerosol extract as the shell material (as the shell material initially owing to Paper 3 modelling the extract as the shell) and (c) exposing the core-shell system formed in (b) to OH radicals. Moving aside from the atmospheric aerosol extracts, possible avenues would be to study different core-shell systems, e.g. liquid-liquid systems and using different atmospheric reactants such as nitrogen oxides.

In summary, optical trapping applied simultaneously with Mie spectroscopy is a valuable tool when determining the wavelength dependent refractive indices of atmospheric aerosol, either as a core-shell system, a reacting system or as an optically trapped aerosol. The complimentary use of neutron and x-ray reflectivity provides additional information for core-shell aerosol systems, such as film structure and thickness. Reflectivity studies have demonstrated the susceptibility of atmospheric aerosols to oxidation by certain atmospheric oxidants.